EPFL

Stress management in the context of induced seismicity in subsurface reservoirs

Barnaby Padraig FRYER

École
polytechnique
fédérale
de Lausanne

2020

Acknowledgements

I would like to thank my two advisors, Lyesse Laloui and Gunter Siddiqi, for their continued support and guidance. You have both shown me so much trust and on many occasions have gifted me the freedom and independence to explore both the topics and ideas that I wanted whilst ensuring that I only ever strayed an acceptable distance from reality. To be honest I'm not sure I would have enjoyed a PhD in any other form, and I feel that now, thanks to your guidance, I should have enough of the tools necessary to give me every chance of making the next step to becoming an independent researcher.

I wish to thank Mohamed Farhat for chairing my committee and David Dempsey, Annemarie Muntendam-Bos, and Brice Lecampion for reviewing my thesis.

Maybe it will seem a bit strange to some given the nature of most of our conversations, but I would like to acknowledge the significant contribution of both Mateo Acosta and Corentin Noël to this thesis. Just about every idea I've had during the last three years (unfortunately that includes the bad ones as well) was somehow influenced or even inspired by conversations with them and I don't think it is an exaggeration to say that this thesis would have been significantly harder without them. I would also like to thank the head of their laboratory, Marie Violay, for not only putting up with my continued presence in her students' offices but also for her helpful feedback on my candidacy exam. I would like to thank Chao Li and Aldo Madaschi for their help and especially their patience at the beginning of my study. More recently, I have benefited from collaborations which I feel have really helped me learn and improve and for which I am very grateful. For this I'd like to thank Xiaodong Ma, Haseeb Zia, and Brice Lecampion. I am also grateful to François Passelègue for his feedback on parts of the thesis.

This thesis also benefited from many external people who were kind enough to take time out of their days to help and advise me when they really stood to gain nothing themselves. For this I would like to thank people as Lauren Boyd, Mark Zoback, Jonathan Banks, Bettina Goertz-Allmann, Dimitrios Karvounis, Loes Buijze, Bogdan Orlic, Alberto Riva, Hans Veldkamp, Frank Schoof, Energie Beheer Nederland, Frédéric Guinot, Kayla Kroll, Jim Rutledge, Deb Rajdeep,

Acknowledgements

Abstract

The stress state of the subsurface has been shown to have an influence on a number of key processes. For example, the criticality of the stress state indicates how large stress changes need to be before a fault begins to slip, the mean effective stress controls compaction and permeability loss in hydrocarbon reservoirs, the differential stress has been seen in seismology to have a strong influence on the size distribution of earthquake catalogues, with stress state further influencing the affinity of a fault to slip either seismically or aseismically, and the stress state strongly influences the propagation of a hydraulic fracture, with stress jumps being capable of completely halting a fracture's propagation. For reasons such as these, it has long been recognized that the state of stress is an important parameter for subsurface industrial operations such as hydrocarbon production, Enhanced Geothermal System (EGS) stimulation, carbon storage, and hydraulic fracturing.

Generally, however, the state of stress does not remain constant during many of these operations. Decreasing effective stresses have led to induced seismicity during injection, fluid production has led to total stress changes which have induced seismicity, even in areas where pore pressure has decreased, temperature-induced stress changes have led to shear stimulation, and changes in total stress have led to so-called "frac-hits" where hydraulic fractures propagate towards depleted zones. These examples demonstrate an operator's ability to alter the state of stress, yet deliberate attempts to alter the stress state for the benefit of future operations have only been suggested a handful of times.

Here, this idea of altering the state of stress is extended through a series of investigations. It is shown that, because production-induced seismicity is caused by total stress changes associated with the gradient of the produced fluid pressure, a hydraulic fracture which reduces the gradient required for production will also reduce the resulting seismicity. Conversely, compaction which leads to permeability loss will result in higher pore pressure gradients and therefore more induced seismicity. Both of these studies, which also have implications for optimal horizontal wellbore orientation, are investigated through the use of a poroelastic reservoir simulator developed during the thesis. In a following study, it is suggested that high stress path reservoirs are attractive targets for fluid injection, as total stress changes will result in an increased stability despite increasing pore pressure. Further, the concept of stress preconditioning is introduced, such that operators alter the stress state of an EGS reservoir to promote more favorable earthquake distributions. These concepts, which make up the first three chapters of the thesis, all are forms of reservoir management that reduce the risk associated with induced seismicity. Following this, in a numerical study, the idea of stress

preconditioning is extended to allow for directed stimulation treatments in EGSs. Finally, the idea of inducing stress jumps through production such that hydraulic fractures do not propagate vertically is evaluated by means of scaling analyses and numerical simulation, with implications for carbon storage.
More than the individual propositions, this thesis promotes the mindset that, where appropriate, attempts should be made to alter the state of stress for the benefit of future operations.

Keywords: Induced seismicity, stress management, hydraulic fracturing, reservoir stimulation, Enhanced Geothermal Systems, state of stress, stress preconditioning, reservoir depletion, carbon storage, fluid injection

Résumé

L'état de contrainte du souterrain a été montré d'avoir une influence importante sur un nombre de processus clés. Par exemple, le niveau de criticité de contrainte indique les changements de contrainte nécessaires pour faire déclencher un séisme, la contrainte moyenne effective est responsable pour les changements de perméabilité liés à la compaction d'un réservoir souterrain, la contrainte différentielle a une influence majeure sur la distribution fréquence-magnitude de séismes, avec un effet supplémentaire de la contrainte normale sur la possibilité qu'une faille glisse d'une manière aséismique, et l'état de contrainte influence significativement la propagation d'une fracture hydraulique, avec les bonds de contrainte capable d'arrêter une fracture propageant. Pour des raisons comme celles-ci, il a longtemps été reconnu que l'état de contrainte est un paramètre important pour les opérations souterraines comme la production du pétrole, les Systèmes Géothermiques Stimulés (EGSs), le stockage carbone, et la fracturation hydraulique.

Généralement, par contre, l'état de contrainte ne reste pas constant pendant une opération. Des contraintes effectives diminuantes ont conduit jusqu'à la séismicité induite pendant l'injection de fluide, la production de fluide a causé de changements de contrainte en résultant dans la séismicité induite, même où la pression fluide a diminué, les changements de contrainte dus aux changements de la température ont causé la stimulation du réservoir, et des changements de contrainte totale ont été responsables pour des « frac-hits », où les fractures hydrauliques propagent vers les zones épuisées. Ces exemples démontrent la capabilité d'un opérateur d'altérer l'état de contrainte, cependant des essais délibérés d'influencer l'état de contrainte pour les bienfaits des opérations futures ont été suggérés que quelques fois.

Dans cette thèse, l'idée d'altérer l'état de contrainte a été étendu par un nombre de recherches. Il est montré que, vu que la séismicité induite pendant la production de fluide est liée au gradient de la pression fluide, une fracture hydraulique la réduirait. Réciproquement, la perte associée à la compaction résulte dans un gradient de pression fluide nécessaire plus élevée et donc augmente le niveau de séismicité. Ces deux études, qui ont aussi des implications pour l'orientation des puits horizontaux, ont été effectués parmi un simulateur poro-élastique développé pendant la thèse. Dans une étude suivante, il est suggéré que des réservoirs de chemin de contrainte haute pourraient servir pour injecter du fluide, parce que les changements de contrainte totale stabiliseraient le réservoir malgré une pression fluide montante. En outre, le concept de préconditionnement de contrainte est introduit, comme quoi des opérateurs altèrent la contrainte d'un réservoir EGS pour que les stimulations à suivre ont une distribution fréquence-magnitude de séismes plus favorable. Ces concepts, qui constituent les

Abstract

premiers trois chapitres de la thèse, sont tous de formes de gestion de réservoir qui réduisent le risque associé à la séismicité induite. Suivant ceci, dans une étude numérique, l'idée de pré-conditionnement de contrainte est étendue pour qu'une stimulation EGS puisse être dirigée dans un sens particulier. Enfin, l'idée d'introduire un bond de contrainte par la production de fluide pour qu'une fracture hydraulique ne propage pas verticalement est évaluée au moyen d'une analyse d'échelle et des simulations numériques, avec des implications pour le stockage carbone.

Plus que les propositions individuelles, cette thèse soutient la mentalité que, quand approprié, des essais d'altérer l'état de contrainte devrait être faits pour les bénéfices des opérations futures.

Mots-clés : séismicité induite, gestion de contrainte, fracturation hydraulique, stimulation de réservoir, Systèmes Géothermiques Stimulés, préconditionnement de contrainte, production de réservoir , stockage carbone, injection de fluide

Samenvatting

Het is al lang geweten dat de ondergrondse spanningstoestand invloed heeft op enkele belangrijke processen. Bijvoorbeeld, de criticaliteit van de spanningstoestand wijst hoe groot spanningsveranderingen moeten zijn voordat een breuk begint te schuiven, de gemiddelde effectieve spanning heeft controle over compactie en permeabiliteit verlies in koolwaterstof reservoirs, differentiële spanning heeft een grote invloed op de frequentie-mate distributie van aardbevingen, waar de spanningstoestand verder invloed heeft op of de breuk seismisch of aseismich schuift, en de spanningstoestand beïnvloed de propagatie van een hydrofractuur, waarbij spanningssprongen capabel zijn de propagatie van een hydrofractuur te stoppen. Om zulke redenen, is het al lang herkend dat de spanningstoestand een belangrijke parameter is voor ondergrondse industriële operaties zoals olie- en gaswinning, Enhanced Geothermal Systems (EGS's), koolzuuropslag, en hydrofracturering.

Alhoewel blijft de spanningstoestand normaliter niet constant tijdens veel van deze operaties. Dalende effectieve spanningen hebben geleid tot geïnduceerde seismiciteit tijdens injectie, vloeistof productie heeft geleid tot totaalspanningveranderingen die tot geïnduceerde seismiciteit, zelfs waar de poriewaterdrukte is verminderd, temperatuur-geïnduceerde spanningveranderingen hebben geleid tot shear stimulatie, en veranderingen in totaalspanning zijn verantwoordelijk voor zogenoemde "frac-hits", waarbij hydrofracturen propageren in de richting van geproduceerde gebieden. Deze voorbeelden laten de vermogen van een operator zien om de spanningstoestand te veranderen, toch zijn pogingen om de stresstoestand te veranderen voor toekomstige operaties maar een paar keer voorgesteld.

In deze thesis is het idee van het veranderen van de spanningstoestand uitgebreid door een serie van studies. Het wordt getoond dat, omdat productie geïnduceerde seismiciteit veroorzaakt wordt door totaalspanningveranderingen verbonden met de gradiënt van poriewaterdrukte, een hydrofractuur die de nodige gradiënt van poriewaterdrukte verminderd ook de resulterende seismiciteit zal verminderen. Daarentegen, compactie die tot permeabiliteitverlies leidt als gevolg ook tot hogere poriewaterdrukte gradiënten en seismiciteit zal leiden. Beide van deze studies, die ook gevolgen voor de oriëntatie van horizontale putten hebben, worden door een poroelastisch reservoir simulator onderzocht die onderworpen werd tijd de thesis. Volgend op deze studies, wordt het gesuggereerd dat reservoirs met een hoog spanningspad aantrekkelijke doelwitten voor injectie zijn, omdat totalspanningverandingen tot stabiliteit leiden ondanks een toenemende poriewaterdrukte. Verder, het concept van het preconditioneren van de spanningstoestand wordt geïntroduceerd, met het idee dat de spanningstoestand kan worden veranderd, zodat kleinere aardbevingen geïnduceerd worden tijdens het stimu-

Abstract

leren van een EGS-reservoir. Deze concepten, die de eerste drie hoofdstukken van de thesis samenstellen, zijn allemaal vormen van reservoirmanagement die de risico van geïnduceerde seismiciteit verminderen. Volgend op deze studies, wordt het idee van het preconditioneren van de spanningstoestand uitgebreid, zodat EGS-stimulaties gericht en daardoor makkelijker verbonden kunnen worden. Ten laatste wordt er onderzocht of geïnduceerde sprongen in spanning het stoppen van het propageren van een hydrofractuur kunnen veroorzaken door het uitvoeren van een maatanalyse en numerieke simulaties, met gevolgen voor koolzuuropslag. Meer dan de voorstelling op zich, promoteert deze thesis een manier van denken waarbij pogingen gemaakt worden om de spanningstoestand te veranderen ten gunste van toekomstige operaties.

Trefwoorden: Geïnduceerde seismiciteit, hydrofracturen, reservoir stimulation, Enhanced Geothermal Systems, spanningstoestand, spanningspreconditioneren, olie- en gaswinning, koolzuuropslag, brakwater en koolzuur injectie

Contents

Contents

List of Figures

List of Tables

Introduction

The successful industrial exploitation of the Earth's upper crust has been prevalent in advanced human societies for many thousands of years. This is unlikely to change, as not only do many of these practices, while evolved, still continue to this day, but fledging applications, such as CO_2 geosequestration and Enhanced Geothermal Systems (EGSs) are becoming increasingly more relevant. While there are many facets to these industrial activities, one fairly denominator is the importance of the stress state in the subsurface.

Indeed, the state of stress exhibits a major influence on some of significant issues facing many subsurface industrial activities. One of the most obvious examples is induced seismicity, a problem shared to various degrees by the geothermal energy production, CO_2 geosequestration, fluid extraction, mining, waste water disposal, hydraulic fracturing, and hydropower industries where it has, in some cases, incited strong reactions from the public and even led to failed operations. Of course, the stress state is not just relevant in terms of induced seismicity, but also exhibits influence on, among others, production-induced compaction and permeability loss, hydraulic fracturing and shear stimulation treatments.

The influence of the stress state and the ability of operators to manipulate it is the core of this thesis, and many of the issues mentioned above will be addressed in these terms. Note that much of the terminology used here and throughout the thesis is defined in the Appendix for the event that the reader is unfamiliar with some of the language used.

0.1   General background and thesis objectives

This thesis is based on a number of core concepts, related to the state of stress in the subsurface, which have relevance for a variety of subsurface industrial activities; the focus here being on long-term fluid extraction and injection, EGS stimulation, and hydraulic fracturing. Specifically, in-situ stress and stress changes have been previously shown to exhibit strong control over a variety of important elements associated with industries that deal with the subsurface. For example:

- The criticallity of the stress on a fault indicates the magnitude of stress changes required before slip can be expected. The crust can generally be assumed to be in a state of

1

failure equilibrium, with intraplate areas only seeming to be seismically quiet due to low strain rates (e.g., Harrison *et al.* (1954); Brudy *et al.* (1997); Townend and Zoback (2000); Zoback and Townend (2001); Zoback *et al.* (2002)).

- The mean effective stress (i.e., the average of the three principal stresses minus pore pressure) is generally thought to control compaction and specifically permeability loss associated with compaction. Compaction-induced permeability loss is generally seen to greatly accelerate when differential stress (i.e., the difference between the maximum and minimum principal stresses) is large (e.g., David *et al.* (1994); Zhu and Wong (1996); Boutéca *et al.* (2000); Chan and Zoback (2002); Schutjens *et al.* (2004); Fortin *et al.* (2005); Baxevanis *et al.* (2006)).

- Differential stress has a strong control on the size-distribution of earthquake catalogues (e.g., Amitrano (2003); Schorlemmer *et al.* (2005); Narteau *et al.* (2009); Gulia and Wiemer (2010); Goebel *et al.* (2013); Spada *et al.* (2013); El-Isa and Eaton (2014); Scholz (2015); Wu *et al.* (2018); Petruccelli *et al.* (2019a,b)).

- The effective normal stress on a fault plane has influence on the affinity of that fault to slip seismically or aseismically, where aseismic fault slip is stable with no earthquake nucleation (e.g., Scholz (1998)).

- The in-situ stress of a rock formation has an important influence on hydraulic frac-ture propagation (e.g., Simonson *et al.* (1978); Nolte and Smith (1981); Warpinski *et al.* (1982a,b); Warpinski and Teufel (1989); Jeffrey and Bunger (2009); Adachi *et al.* (2010); Jin and Zoback (2019)).

Given the relevance of many of these examples for the previously mentioned industrial opera-tions, this shows the importance of assessing the stress field before commencing an operation. However, frequently it cannot be assumed that this stress state will remain constant through-out the life of a given reservoir as it has already been shown that operators can and do influence the stress, albeit usually unintentionally:

- A decreasing effective normal stress in reservoirs during injection has led to fault slip (e.g., Häring *et al.* (2008); Rutqvist *et al.* (2016b)).

- Anisotropic total stress changes occurring inside and outside of a production reservoir have led to production-induced seismicity; stress changes in the opposite direction are predicted during injection (Segall, 1989).

- In high stress path reservoirs the total stress changes significantly in response to pore pressure changes. As a result, in these types of reservoirs in normal faulting stress regimes, stress changes induced by decreases in pore pressure can lead to seismicity within the pore pressure-depleted zone of the reservoir (e.g., Teufel *et al.* (1991); Segall and Fitzgerald (1998); Chan and Zoback (2002); Zoback and Zinke (2002)).

- Changes in temperature through fluid injection have led to changes in total stress and in some cases shear failure; temperature changes propagate more slowly than changes in pressure (Rutqvist *et al.*, 2016b; Vilarrasa, 2016; Parisio *et al.*, 2019).

- Changes in total stress have led to so-called "frac-hits", where hydraulic fractures propagate towards previously depleted zones (e.g., (Jin and Zoback, 2019)).

This begs the question as to whether operators can intentionally manipulate the stress field with their operations to aid them in achieving future goals and avoid failed operations. This has previously been done in two industrial operations settings:

- Operators have performed prior injection to alter the stress field such that future hydraulic fractures will be oriented differently to those prior to injection; other extensions to this idea have also been developed (Shuck, 1977; Bouteca *et al.*, 1983; Warpinski and Branagan, 1989; Elbel and Mack, 1993; Minner *et al.*, 2002; Fisher *et al.*, 2004; Vermylen and Zoback, 2011).

- Microseismic depletion delineation - a depletion-altered stress state results in microseismicity upon reinjection, with the change in differential stress affecting the frequency-magnitude distribution of the induced microseismicity. This approach allows operators to distinguish effectively fractured stages (Dohmen *et al.*, 2013, 2014; Norbeck and Horne, 2015; Dohmen *et al.*, 2017).

Further, it has been suggested that fluid production induced stress jumps, where stress jumps are defined as sudden changes in confining stress, could be used to ensure hydraulic fracture containment (van Eekelen, 1982). Similarly, this kind of stress management is the focus of this thesis. Indeed, it will be shown how production-induced stress changes can be, to a degree, managed such that the risks of induced seismicity and large permeability losses are reduced. It will be suggested that high stress path reservoirs in normal faulting stress regimes should be attractive targets for large-scale injection due to increased pore pressure leading to a more stable stress state. Additionally, it will be suggested that the stress state can be preconditioned prior to stimulation in EGS wells such that differential stress is lower upon stimulation, leading to a decreased chance of inducing a large seismic event when stimulation does finally occur. Further this idea of stress preconditioning, it will be suggested that the poroelastic stress changes associated with a stimulation treatment in an EGS well could be used to guide the stimulation in a second well. Finally, it will be suggested that potential carbon storage reservoirs can be hydraulically fractured in certain circumstances based on a scaling analysis of various hydraulic fracture propagation regimes.

0.2   Organization of thesis

The thesis is divided into five core chapters and a discussion/conclusion chapter:

Introduction

The first chapter is focused on mitigating depletion-induced seismicity. It is thought that depletion-induced seismicity occurring outside of the reservoir is caused by poroelastic stress changes associated with the reduced pore pressure (Segall, 1989). Insight into this phenomenon can be gained by looking at the two primary governing equations used to model poroelasticity in reservoirs: the equation of momentum balance and the continuity equation for mass balance. From the momentum balance equation, it is clear that the gradient of pore pressure is directly related to the stresses that are induced. From the continuity equation for mass balance (or, more precisely, Darcy's Law in the convection term of the continuity equation) it is clear that the gradient of pore pressure is directly related to the permeability. Therefore, in this chapter, because it increases the near-wellbore permeability, reservoir stimulation is proposed as a technique to mitigate induced seismicity. This investigation is performed numerically. Further results include implications for wellbore orientation and a discussion on the relative significance of pore pressure and stress changes at various distances.

The second chapter is based on the same principle. This time, however, it will be determined whether compaction-induced permeability loss can be large enough to significantly alter the resulting pore pressure gradient and cause an increase in stressing/seismicity rate while in the elastic domain. The effect of inelastic compaction will also be investigated. As inelastic compaction depends strongly on differential stress and production-induced stress changes from a horizontal well are anisotropic, the idea that wellbore orientation can have a significant influence on compaction will also be explored.

The third chapter is based on the idea that poro- and thermo-elastic stress changes are anisotropic, especially in laterally-extensive reservoirs. There will be two investigations. First, the idea of injection stabilizing certain types of reservoirs due to anisotropic total stress changes will be probed. In essence, the premise is that, because it is possible to destabilize certain types of reservoirs by decreasing the pore pressure, it might also be possible, counterintuitively, to stabilize certain types of reservoirs by increasing the pore pressure. The second investigation will concern the idea of "preconditioning" the stress field prior to a shear stimulation treatment of an EGS reservoir. Using a long period of time, this thesis will explore the idea of cooling the reservoir such that the differential stress of the reservoir is decreased. Given that there is a relationship between earthquake magnitude distribution and differential stress, this may result in a lowered chance of a large magnitude earthquake when the reservoir is finally stimulated.

The fourth chapter will continue with the idea of preconditioning the stress field. This time it will be investigated whether or not the poroelastic stress changes associated with the high pore pressures used to stimulate an EGS reservoir in shear can be used to guide the stimulation treatment of a second, nearby well. All three primary stress regimes will be investigated.

The fifth chapter will investigate the effect of a stress jump on a Planar 3D hydraulic fracture. A scaling analysis will be performed for four primary propagation regimes determined by whether or not the fracture is toughness or viscosity dominated and whether or not leak-off is

4

a dominant mechanism. The aim will be to predict the breakthrough of the hydraulic fracture through a dimensionless quantity applicable to a wide variety of cases, such that operators can quickly gain an idea of the predicted breakthrough without the use of a simulator. These results will then be used to discuss implications for the hydraulic fracturing of depleted hydrocarbon reservoirs for use in carbon storage.

Following these core chapters, a chapter is taken to discuss the findings in general. Here, a small selection of other ways that stress might be managed are also presented. A description of the reservoir simulator developed during this thesis and used in many of the chapters is given in the Appendix along with an introduction to many of the core concepts employed throughout the thesis.

1 Reservoir stimulation to counter depletion-induced seismicity

The results of this chapter are published in:

Journal paper:

Fryer, B., Siddiqi, G., and Laloui, L. (2018). Reservoir stimulation's effect on depletion induced seismicity. *Journal of Geophysical Research: Solid Earth*, **123**, 7806-7823.
https://doi.org/10.1029/2018JB016009

Contribution of candidate: Initial idea, development of code, analysis of results, writing of manuscript.

1.1 Chapter Summary

Depletion-induced seismicity can pose a problem in some fluid-producing subsurface reservoirs, in some cases requiring production rate control in order to limit the seismicity. This study investigates the use of reservoir stimulation to reduce the depletion-induced seismicity rate. Depletion-induced stress and pore pressure changes are evaluated in a shale caprock, sandstone reservoir, and shale underburden system which contains a horizontal well, all modelled in plane strain conditions. The seismicity rate is then predicted based on an existing seismicity model and is found to be dependent on the direction the well is drilled in with respect to the principal stresses. The case where the reservoir has first been stimulated is compared to the case where stimulation has not been performed (using the same production rates) for normal, reverse, and strike-slip faulting stress regimes. Seismicity is reduced in the case of reservoir stimulation for both reverse and strike-slip faulting stress regimes. The seismicity rate is only slightly reduced for the normal faulting stress regime. The findings are only relevant to earthquakes occurring outside of the reduced pore pressure zone. Stimulation also increases the distance that changes in pore pressure dominate over poroelastic stress changes in the reservoir. Further, it is found that the optimal orientation of a horizontal well, in terms of induced seismicity, is parallel to the minimum principal stress in normal faulting stress regimes and parallel to the maximum principal stress in reverse faulting stress regimes. The orientation of a horizontal well determines where the seismicity is located in a strike-slip faulting stress regime.

1.2 Introduction

During the last few years, induced seismicity due to fluid injection into subsurface reservoirs has become a major cause for concern despite its long-term record of observation (Ellsworth, 2013), with injection-induced earthquakes reaching moment magnitudes as large as 5.8 (Chen *et al.*, 2017). Whilst the primary focus has been on induced seismicity caused by changes in pore pressure (e.g., Layland-Bachmann *et al.*, 2012; Zhang *et al.*, 2013), poroelastic stresses are also thought to be a significant contributor in multiple cases of induced seismicity in both injection (see e.g. Barbour *et al.*, 2016; Chen *et al.*, 2017; Deng *et al.*, 2016; Goebel *et al.*, 2017a) and production scenarios (Segall, 1985, 1989). This has lead to poroelastic stresses being recognized as an important cause of induced seismicity and research has been performed on how to best account for these stresses such that induced seismicity is minimized (e.g., Chang and Segall, 2016a,b, 2017; Postma and Jansen, 2018; Segall and Lu, 2015).

Certainly, fluid extraction from subsurface reservoirs has long been known to be capable of inducing seismicity (Pratt and Johnson, 1926; Suckale, 2009, 2010). Indeed, there are a number of specific examples of depletion-induced seismicity. The first reported case of depletion-induced seismicity occurred in Goose Creek, Texas, where oil and gas production lead to normal faulting on the flanks of the producing reservoir, causing a disturbance to nearby inhabitants (Pratt and Johnson, 1926; Yerkes and Castle, 1970, 1976). The Wilmington oil field in the United States also exhibited reverse faulting at shallow depths above the reservoir during the primary production phase (Yerkes and Castle, 1976). Gas production from the Gazli gas field is thought to have possibly induced reverse faulting underneath the producing reservoir; the three largest induced events had a magnitude 7.0 in what was previously a seismically quiet region, injuring over one hundred people and resulting in one death (Simpson and Leith, 1985). However, it is difficult to conclusively determine whether or not this event was related to the nearby gas production (Suckale, 2010). The center of the Buena Vista Hills oil field showed signs of asiesmic reverse faulting at the surface as a result of oil production, leading to significant pipeline and casing damage (Koch, 1933; Yerkes and Castle, 1970, 1976). Hundreds of small to medium-sized earthquakes are thought to have been induced by very small poroelastic stress changes (no larger than 0.2 MPa) by production from the Lacq gas field in southwestern France (Segall *et al.*, 1994), with most of the earthquakes occurring above the reservoir in this reverse faulting environment (Bardainne *et al.*, 2008). Gas production from a reservoir near Rocky Mountain House, Alberta induced reverse faulting (M ≤ 3.4) below the producing reservoir (Wetmiller, 1986). In fact, seismicity has been induced throughout the Western Canada Basin (Baranova *et al.*, 1999). Low magnitude reverse faulting ($M_w < 1.0$) occurred in Clinton County, Kentucky above and below a shallow producing oil reservoir (Rutledge *et al.*, 1998). These specific cases all can be explained by the model proposed by Segall (1989), which showed that poroelastic stresses induced by fluid extraction cause normal faulting on the flanks of reservoirs and reverse faulting above and below the reservoir. The poroelasticity model has also been used to show that the reverse faulting shocks which occurred underneath the Coalinga oilfield in California were probably not induced due to the relatively small stress

changes fluid production was predicted to have induced near the earthquake hypocenters (Segall, 1985). Additionally, it has been shown that normal faulting can also be induced within the reservoir if the stress path (i.e., the ratio of the change in horizontal stress magnitudes to the change in pore pressure) is high enough (Chan and Zoback, 2002; Segall and Fitzgerald, 1998; Zoback and Zinke, 2002). Examples of this type of seismicity include the Valhall and Ekofisk oilfields (Zoback and Zinke, 2002), where normal faulting has been seen within the reservoir, and the normal faulting within the Groningen gas field (Dempsey and Suckale, 2017). It has also suggested that normal faulting occurring within the reservoir in the War-Wink gas field in West Texas may be explained by a high stress path (Zoback and Zinke, 2002). Previously, Doser *et al.* (1991) found that the poroelasticity model presented by Segall (1989) was unable to explain the seismicity of the field. The specific case of depletion-induced seismicity related to a high stress path will not be further investigated here.

In the fully coupled theory of poroelasticity, pore pressure changes result in changes in total stress and changes in total stress result in pore pressure changes (see Biot, 1941; Rice and Cleary, 1976; Wang, 2000). Specifically, it is the gradient of pore pressure that acts as an internal force in the equation of conservation of momentum and ultimately produces the deformation and poroelastic stress changes in the rock (Chang and Segall, 2017). This implies that, if operators of gas, oil, geothermal, wasterwater-disposal, or CO_2-sequestration wells were able to influence the gradient of pore pressure in the reservoir, they might also be able to influence the poroelastic stresses that are induced by their operations. Seeing how these stresses induce the seismicity as previously mentioned, it is probable that influencing the pore pressure gradient would also help them influence the seismicity rate. Hydraulic fracturing and acidization treatments are two forms of well and reservoir stimulation that could be used to improve the inflow performance of the near-well region such that a smaller pore pressure gradient is required to produce the same amount of fluid (Dake, 1978; Economides and Nolte, 2000).

Therefore, this work shows how reservoir stimulation may reduce induced changes in total stress and thereby reduce the induced seismicity during given production scenarios, an extension of the idea that subsidence depends on diffusivity (Segall, 1985). The analysis is performed for normal, reverse, and strike-slip faulting stress regimes with production from a horizontal well by assigning initial stresses based the notion of a critically-stressed crust (see Brudy *et al.*, 1997; Townend and Zoback, 2000; Zoback and Townend, 2001; Zoback *et al.*, 2002) and the idea that it is the frictional strength of pre-existing faults that limits differential stress; meaning that, for example, in a normal faulting environment with the vertical stress determined by the overburden, the minimum horizontal stress of a given stratum will be limited by the coefficient of friction of the faults that are likely to be present within that stratum (see Brudy *et al.*, 1997; Zoback and Harjes, 1997; Zoback and Healy, 1992). Therefore, the relatively low coefficients of friction seen in clay-rich rocks (Ewy *et al.*, 2003), will result in the shales being able to support less differential stress. A sequentially coupled poroelastic flow simulator based on the continuity equation for mass balance (Lake, 1989), the conservation of momentum, and the linear theory of poroelasticity (Biot, 1941; Chang and Segall, 2016a;

Rice and Cleary, 1976; Wang, 2000) is used to predict production-induced pressure and stress changes. Hydraulic fractures are modelled using relevant parameters from various hydraulic fracture treatments to produce an effective permeability near the well. The pressure and stress changes induced by reservoir pressure drawdown are then used as inputs for a seismicity model based on Dieterich (1994). In this way, the pore pressure changes, stress changes, and seismicity induced by production from the stimulated reservoir can be compared to the original, non-stimulated case. Specifically, the analysis of the effect of stimulation on induced pore pressure and stress changes that occur during production will provide insight into why stimulation is a production management tool with the potential to reduce induced seismicity in production reservoirs.

1.3 Methods

1.3.1 Coupled poroelastic flow model

Pore pressure and stress perturbations caused by fluid production are modelled with a poroelastic reservoir simulator which sequentially couples a finite volume flow model to a finite element linear elastic mechanical model. A 2D plane strain setup will be used. This is appropriate for the modelling of a horizontal well (Cheng, 1998). Although the simulation is 2D, it will still be possible to calculate 3D stress changes (Cheng, 1998).

Flow model

Flow is governed by the balance equation for conservation of mass of a single phase, or the continuity equation (Lake, 1989), in combination with Darcy's Law,

$$\frac{\partial (\phi \rho)}{\partial t} - \nabla \cdot \left(\frac{k}{\mu} \rho \left(\nabla P - \nabla \left(\rho g z \right) \right) \right) = q. \tag{1.1}$$

Here, ρ represents the fluid density, which is compressible, μ the fluid dynamic viscosity, P the pore pressure, ϕ the reservoir porosity, k the permeability, g the acceleration due to gravity, z the depth, and q the mass source terms which are dictated by well injection and production mass rates.

Because of its non-linear nature, the equation will be solved numerically. To do this, Equation 1.1 is discretized in a residual finite volume in space and fully implicit finite difference in time framework (Aziz and Settari, 2002) in order to solve for an update to the primary variable, pressure. Note that the fluid properties at the interfaces (except in the gravity term) are upstreamed. All model boundaries have no flow, Neumann boundary conditions, except the top which has a constant pressure, Dirichlet boundary condition.

Mechanical model

The conservation of momentum is written as

$$\nabla \cdot \sigma' + \nabla (\alpha P) = -f, \tag{1.2}$$

neglecting inertial terms, where σ' is the effective stress, α is the Biot coefficient, P represents the pore pressure whose gradient acts as an internal force, and f represents the body forces. Compression and contraction will be taken as positive. This is then combined with the linear theory of poroelasticity (Biot, 1941; Chang and Segall, 2016a; Rice and Cleary, 1976; Wang, 2000),

$$S_{ij} - \alpha P \delta_{ij} = \frac{E}{(1+\nu)} \epsilon_{ij} + \frac{E\nu}{(1+\nu)(1-2\nu)} \epsilon_{kk} \delta_{ij}, \tag{1.3}$$

where S is the total stress, E the drained Young's Modulus, ν the drained Poisson's Ratio, ϵ the strain, and δ_{ij} the Kronecker delta. The equations are then discretized in a finite element framework with linear basis functions and quadrilateral elements situated such that the nodes are located at the corners of the finite volume cells from the flow model. The poroelastic properties E, ν, and K_s, the solid bulk modulus, are defined for the system, allowing for the calculation of α (Detournay and Cheng, 1993) via the calculation of a drained bulk modulus. All boundary conditions have a fixed perpendicular displacement, Dirichlet boundary condition except the surface, which is free.

Coupling

Here, the poroelastic coupling is performed using the definition of Lagrangian porosity from Coussy (2007),

$$\phi = -\epsilon_{kk} \alpha + \frac{P(\alpha - \phi_0)}{K_s} + \phi_0. \tag{1.4}$$

Here, ϕ is the current porosity, ϵ_{kk} is the volumetric strain, positive in contraction, and ϕ_0 is the reference porosity at a reference pore pressure and volumetric strain. The volumetric strain is a sum of the axial strains. The pore pressures found after the convergence of the flow model (Equation 1.1) are applied as internal forces in the mechanical model (Equations 1.2 and 1.3). The mechanical model then finds the new volumetric strain based on these pressures. This volumetric strain is then applied back in the flow model, changing the porosity. This means

the fluid density (and therefore pressure) has to be adjusted such that mass is conserved. In this way the flow and mechanical model are iterated during each time step until convergence (determined by change in pressure) before moving on to the next time step.

1.3.2 Seismicity Model

The seismicity model is an adaptation based on an original formulation by Dieterich (1994) (Segall and Lu, 2015). In this formulation, the Coulomb stress, τ, is defined as,

$$\tau = \tau_s - \mu_f (S_n - P),$$
(1.5)

where the shear stress on the fault plane is given by τ_s, the normal total stress on an optimally oriented fault in a given stress regime (negative in tension) by S_n, and the static coefficient of friction by μ_f. A variable R is then defined as the ratio of the current rate of seismicity to the background level and obeys the following relationship,

$$\frac{dR}{dt} = \frac{R}{t_a} \left(\frac{\dot{\tau}}{\dot{\tau}_0} - R \right).$$
(1.6)

Here, $\dot{\tau}$ represents the stressing rate, $\dot{\tau}_0$ is the background stressing rate, and t_a is the characteristic decay time which is taken as 50 years, matching other authors (Segall and Lu, 2015). This seismicity model uses the stress and pore pressure updates coming from the poroelastic simulator to find a new stressing rate at the end of each time step. This is then used to iteratively solve for the new seismicity rate in an implicit finite difference manner by setting Equation 1.6 into a residual formulation,

$$r^\omega = \frac{R^\omega - R^n}{\Delta t} - \frac{R^\omega}{t_a} \left(\frac{\dot{\tau}^n}{\dot{\tau}_0} - R^\omega \right) = -\frac{\partial r}{\partial R} |^\omega \Delta R^{\omega+1}.$$
(1.7)

Here, r represents the value of the residual, n represents the previous time step, ω represents the current iteration, Δt is the time step size, and the update to the primary variable, R, is given by ΔR. Note that $\dot{\tau}^n$ is the average stressing rate over the time step. The minimum value for R is assigned to be 0.01. The seismicity rates produced by this model are used to estimate how seismicity responds to different production scenarios. Certainly, it can be deduced from Equation 1.5 that increases in pore pressure, increases in the maximum principal stress, and decreases in the least principal stress will all increase the Coulomb stress. Further, from Equation 1.6 it is apparent that increases in the Coulomb stress will cause a higher seismicity rate. In this way it is possible to have an intuition for the effect a given set of pressure and

stress changes will have on seismicity rate. Note that all lithologies present in the model will use this seismicity model; however, broadly speaking, each lithology's unique coefficient of friction and initial stress profile will govern how significant a change in pore pressure or stress will be in terms of induced seismicity.

1.4   Problem Setup

Production through a horizontal well in a plane strain case in a 378 meter thick, water-saturated sandstone reservoir with a shale cap rock and underlying shale layer is considered; see Figure 1.1. The thickness of the reservoir was chosen to match the range of the effective reservoir thickness seen at the Lacq gas field (Segall *et al.*, 1994). The producing reservoir being enclosed in the vertical direction by two shales is justified as this is similar to real examples of petroleum reservoirs (e.g., Coalinga (Segall, 1985)). In fact, in many practical applications the rocks surrounding the producing reservoir in oil and gas applications have very low perme-abilities (Segall, 1992). Production in this case occurs through a horizontal well as this type of well has been frequently used since the 1990's (Nurmi *et al.*, 1995; Zhang and Dusseault, 1994). A 2D plane strain setup is appropriate to model these kinds of conditions and allows for the calculation of stress changes in all three principal directions (Cheng, 1998). Example normal, reverse, and strike-slip faulting stress regimes are considered. In each case, the well is drilled parallel to the minimum principal stress based on an argumentation regarding fracture development (Hubbert and Willis, 1957), except in the reverse faulting case where the well is drilled parallel to the intermediate principal stress; see Table 1.1. The initial pore pressure and vertical stress are found through standard hydrostatic and lithostatic gradients respectively. Depending on the stress regime, either the initial maximum or initial minimum principal stress is then found using the vertical stress, pore pressure, and the assumption that the crust is critically stressed (see Brudy *et al.*, 1997; Townend and Zoback, 2000; Zoback and Townend, 2001; Zoback *et al.*, 2002) with the frictional strength of pre-existing faults limiting the differential stress supported by the crust (see Brudy *et al.*, 1997; Zoback and Harjes, 1997; Zoback and Healy, 1992). In the strike-slip faulting stress regime, it is first assumed that the minimum principal total stress is equivalent to 0.8 times the initial vertical total stress (Zoback, 2007). Production from the reservoir, whether it is stimulated or not, will occur over a period of 10 years from a 750-meter section of a horizontal well, a typical lateral section length of a horizontal well (Joshi, 1991), and with exactly the same production rate in all cases (beginning at 2e5 $\frac{kg}{year \cdot m}$, or approximately 2500 $\frac{bbl}{day}$ for this well). The production rate will remain constant during a plateau period of three years before declining at a rate of 6% per year, not dissimilar to the production decline behaviour that is seen in some oil fields (Höök *et al.*, 2009), Figure 1.2a. All test cases begin with an undisturbed pressure and stress field at the reservoir scale. The seismicity that might be incurred due to the process of hydraulic fracturing itself is not included in this analysis because hydraulic fracturing is not expected to induce seismicity at lateral distances larger than about 400-1000 meters (Rubinstein *et al.*, 2018; Westwood *et al.*, 2017), and the seismicity in the reservoir being evaluated here is occurring

Table 1.1 – *Principal stress orientations.* In each case the well is drilled in the y-direction; however, the orientations of the principal stresses change depending on the stress regime.

Regime	S_1	S_2	S_3
Normal Faulting	S_z	S_x	S_y
Reverse Faulting	S_x	S_y	S_z
Strike-Slip Faulting	S_x	S_z	S_y
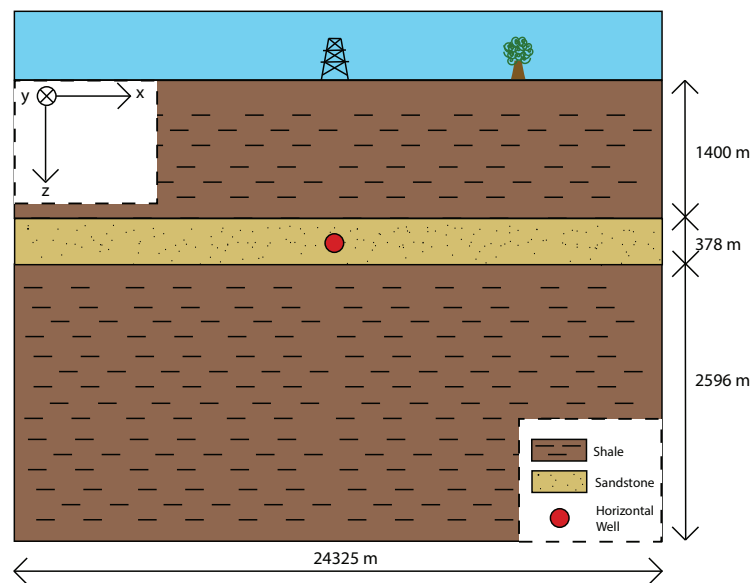
Figure 1.1 – Problem overview, vertically exaggerated

at least 1500 meters from the well. Also, although there are some exceptions, the seismicity occurring due to hydraulic fracturing only lasts a few days after the stimulation treatment (Lei *et al.*, 2017; Rubinstein *et al.*, 2018), whereas the analysis here is occurring over ten years. A full list of parameters used to perform the simulations can be found in Table 1.2. Note that, although different parameters will change the quantitative results, the qualitative effects that stimulation has on depletion-induced seismicity generally remain the same.

1.4.1   Modelling Reservoir Stimulation

In order to model a stimulated permeability field resulting from a hydraulic fracture treatment, parameters for a typical treatment were used to predict the size and effect of the resulting fracture. The height of the hydraulic fracture was estimated based on Flewelling *et al.* (2013), who used fracture mechanics models to estimate the height of a simple planar fracture such

Table 1.2 – *Model parameters*

Name	Variable	Value	Units
Model Width	L_x	24325	m
Cap rock height	$L_{z,c}$	1400	m
Reservoir height	$L_{z,r}$	378	m
Underlying shale height	$L_{z,us}$	2596	m
Grid cells, elements x	N_x	139	-
Grid cells, elements z	N_z	81	-
Production time	t_{prod}	10	years
Plateau flow rate	q_{flow}	2e5	$\frac{\text{kg}}{\text{year·m}}$
Fluid reference density	ρ_0	1000	$\frac{\text{kg}}{\text{m}^3}$
Fluid compressibility[ι]	c_f	5e-10	$\frac{1}{\text{Pa}}$
Fluid dynamic viscosity	μ	0.001	Pa·sec
Permeability shale[Γ]	k	1e-19	m^2
Permeability sandstone[β]	k	1e-15	m^2
Drained Young's Modulus shale[χ]	E	5e9	Pa
Drained Young's Modulus sandstone[β]	E	18e9	Pa
Drained Poisson's Ratio shale[χ]	ν	0.25	-
Drained Poisson's Ratio sandstone	ν	0.25	-
Grain bulk modulus shale[Θ]	K_s	6e9	Pa
Grain bulk modulus sandstone[β]	K_s	36e9	Pa
Initial porosity shale[Γ]	ϕ_0	0.23	-
Initial porosity sandstone[β]	ϕ_0	0.25	-
Coefficient of friction shale[Γ]	μ_f	0.35	-
Coefficient of friction sandstone[θ]	μ_f	0.6	-
Background stressing rate[θ]	$\dot{\tau}_0$	0.001	$\frac{\text{MPa}}{\text{year}}$
Characteristic decay time[θ]	t_a	50	years

[ι] Compressibility of water based on Osif (1988)

[Γ] Taken from Opalinus Clay (OPA) Shale (Orellana *et al.*, 2018)

[θ] Typical value (Segall and Lu, 2015)

[χ] Typical OPA Shale values, neglecting anisotropy (Favero *et al.*, 2018)

[β] In range of typical sandstone values (Detournay and Cheng, 1993)

[Θ] Typical for clay minerals (Vanorio *et al.*, 2003)

that,

$$H = \left[\frac{3\Omega V E}{\pi a_r P_n \left(1 - v^2\right)} \right]^{\frac{1}{3}}. \tag{1.8}$$

Here, H is the fracture height, V the volume of the fracture, a_r the fracture aspect ratio, which will be taken as 1.36, a reasonable value according to Smith *et al.* (2001), P_n the net pressure which is the difference between the fluid pressure in the fracture and the least principal stress, and Ω is a shape parameter which is given by $\Omega \cong \sqrt{1 + 1.464 a_r^{1.65}}$ (Anderson, 2005). Typically, the value of $\frac{E}{P_n}$ is around 10^3 at the borehole (e.g., Fisher *et al.*, 2002; Warpinski *et al.*, 1990). However, recognizing that this value may vary along the fracture, Flewelling *et al.* (2013) use a range between 6,000 and 30,000. Here, we will take a value of 22,000. The volume of the fracture can be calculated using the volume of the fluid injected and the leakoff, taken here as 20%, a reasonable value for conventional hydraulic fracturing (Shen *et al.*, 2011). The volume of fluid injected per stage will be taken as 2,338 m^3, which, based on a stage length of 100 m across a 750 m well, falls within the range of amount of fluid used to hydraulically fracture an average well in the Eagle Ford Shale (Nicot and Scanlon, 2012). Based on these values and consistent with field observations reported by Flewelling *et al.* (2013), the fracture height is approximately 385 m, assuming a sufficiently thick homogeneous reservoir rock. Based on the assumed aspect ratio, the fracture width is 525 m. Note that it is assumed that the fracture will remain in the sandstone reservoir and not propagate into the overlying and underlying shale layers. This is because, due to their lower coefficients of friction (Ewy *et al.*, 2003), shales are able to support less differential stress. As the vertical stress is determined by the overburden, this means that the minimum principal stress is predicted to be higher in shales than in sandstones in normal faulting environments (Zoback, 2007) based on the notion of a critically stressed crust, discussed previously. A hydraulic fracture needs to overcome the minimum principal stress in order to propagate, so it can be assumed that the higher minimum principal stress in the shale will prevent fracture propagation (Zoback, 2007). This is supported by experiments done by Warpinski *et al.* (1982a), who showed that differences in the minimum principal stress are the primary control on fracture propagation through multiple layers. It is also assumed that the hydraulic fracture in the strike-slip faulting stress regime will be contained within the sandstone reservoir. As will be discussed below, the hydraulic fracture in the reverse faulting stress regime does not propagate vertically.

Stimulation treatments performed in the Rotliegendes sandstone of Central Europe in Enhanced Geothermal Systems have inferred apertures up to 10 mm (Zimmermann *et al.*, 2015). Although these stimulation treatments are being performed at significantly greater depths than would be typical of hydrocarbon production, they do give an indication of a typical aperture size and indicate that a more conservative aperture of 2 mm is reasonable. Next, in order to calculate an effective permeability of the reservoir blocks containing the fracture, the

effective permeability of fractured media, given as (Roman *et al.*, 2012),

$$k = \frac{a^3}{12L_0},$$
(1.9)

is used, even though the smooth plate assumption inherent in this model is thought to overestimate the fracture permeability (Kluge *et al.*, 2017). Here, a is the fracture aperture and L_0 is the length of the porous media sample in the direction perpendicular to the fracture plane. Assuming that only one fracture forms per hydraulic fracturing stage, this length is then equivalent to the stage length, which is 100 m in this case. This results in an effective permeability of approximately 6.67×10^{-12} m^2 for all cells containing the fracture (Figure 1.2b and d). This is then the permeability for both the x- and z-directions in the model.

Note that in a reverse faulting case, the least principal stress is oriented vertically, so the fracture is expected to grow normal to the vertical direction. Although the fracture height will be the same, this height will actually be oriented in the horizontal direction. Further, the L_0 used in Equation 1.9 will now simply be the height of the reservoir grid block. The fracture will be modelled to not affect the vertical permeability and will be contained, in the z-direction, within one block, modelled with an effective permeability of 1.23×10^{-11} m^2, calculated from Equation 1.9, Figure 1.2c.

Although this is a simple way to model a stimulation treatment, it is sufficient to investigate the effect of a general stimulation treatment on the induced seismicity seen during subsequent fluid production.

1.5   Results & Interpretation

1.5.1   Normal Faulting Stress Regime ($S_z > S_x > S_y$)

A hypothetical well has been drilled parallel to the minimum principal stress in a normal faulting stress regime, which in this case is in the y direction. As this is a normal faulting stress regime, focus will be placed on the model's results at the flanks of the reservoir, between 1.5 and 4 kilometers from the well. Beyond 6 kilometers from the well, pore pressure and stress changes become constant due to the cumulation of the applied forces resulting from the pore pressure gradients nearer the well, indicating that the model is sufficiently wide to avoid boundary affects influencing the results. The flanks of the reservoir and surrounding rock are the most likely place for induced seismicity to occur in this stress regime (Segall, 1989). Indeed the reason for this can be seen in Figure 1.3c, where the negative (i.e. less compressive) total stress changes and pore pressure changes for the system are shown for the case where no stimulation has been performed. All stress magnitudes are taken at the same depth as the well. Note that although the stress changes are negative, the resultant stresses are all still
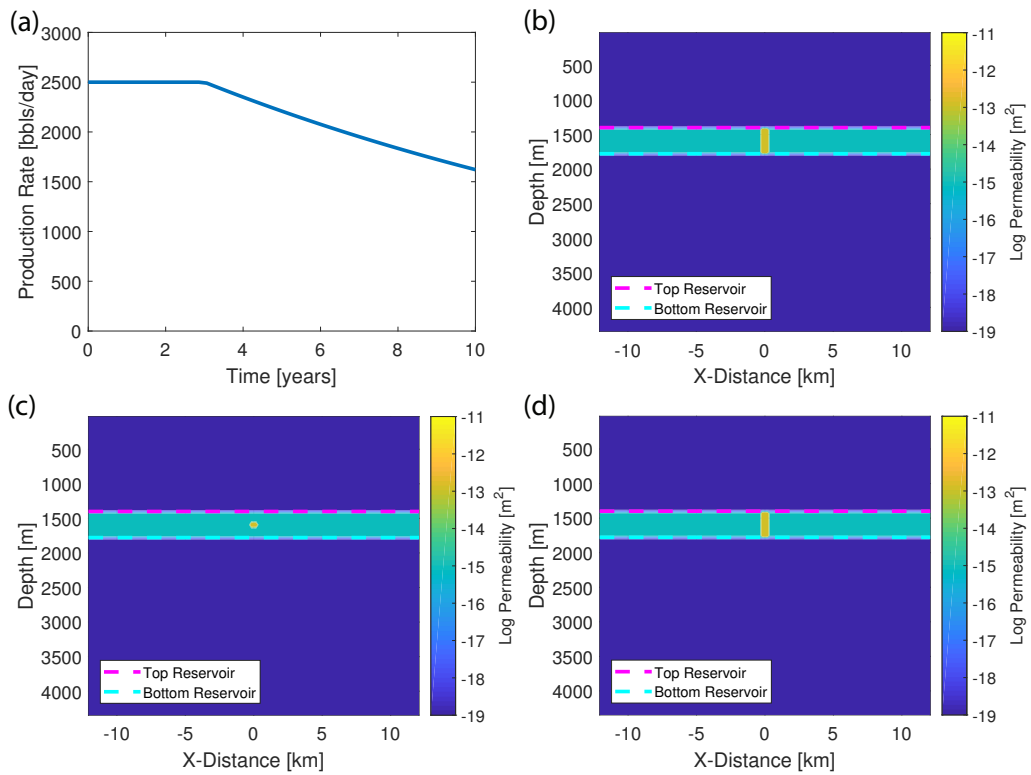
Figure 1.2 – (a) The production rate throughout the simulation. The stimulated permeability fields for the (b) normal, (c) reverse, and (d) strike-slip faulting stress regimes. The simulated hydraulic fracture always propagates in a plane perpendicular to the minimum principal stress. The fracture is therefore normal to the y-direction in the normal and strike-slip faulting stress regime cases and normal to the z-direction in the reverse faulting case.

compressive (positive) overall. This is because the largest stress changes are less than 10 MPa, which is significantly smaller than the initial stresses at that depth. At locations on the flanks of the reservoir which are within the reservoir but far away from the well (beginning around 2km from the well), tensile changes are induced in S_y, which is the least principal stress. The maximum principal stress, S_z, experiences the least amount of tensile change. The decrease of the least principal stress destabilizes any potential optimally oriented faults in the reservoir, while the tension induced in the maximum principal stress is relatively insignificant due to the small magnitude of the stress change. There is also, however, a decrease in pore pressure which helps to stabilize the reservoir. Overall, at large distances, the stress changes dominate and the reservoir is expected to destabilize as can be seen in Figure 1.3a. Poroelastic stress changes dominating over pore pressure changes and inducing seismicity at large distances also agrees with the findings of other authors (e.g., Chang and Segall, 2016a,b; Goebel *et al.*, 2017a; Segall and Lu, 2015).

The Coulomb stress changes that occur in the stimulated and non-stimulated cases can be seen in Figure 1.3d. Stimulation has the effect of reducing the pore pressure (after the first 185 *m* from the well - closer to the well pore pressure is actually higher in the stimulated case) and induces lower (more tensile) stresses than in the non-stimulated case. A lower pore pressure and a more tensile maximum principal stress (represented by the changes to S_z) are expected to reduce the seismicity; however, the changes to S_z are relatively small and the least principal stress, S_y, also becomes more tensile. Ultimately, as can be seen in Figure 1.3b, the seismicity is reduced due to large reductions in pore pressure far from the well, but the changes to S_y serve to mitigate this reduction in seismicity and the seismicity rate is only moderately reduced.

1.5.2 Reverse Faulting Stress Regime ($S_x > S_y > S_z$)

In a reverse faulting stress regime, with the well drilled parallel to the intermediate principal stress, the low pore pressures and decrease in S_x (the maximum principal stress) in the reservoir imply that the Coulomb stress and the seismicity in the reservoir are reduced. As can be seen in Figure 1.4c, however, above and below the reservoir S_x is increased. Poroelastic effects also mean that the pore pressure is increased at these locations. These two effects combine with a decrease in S_z, the least principal total stress, to cause Coulomb stress increases above and below the reservoir, resulting in an increase in seismicity, as seen in Figure 1.4a and predicted by (Segall, 1989).

As can be seen in Figure 1.4d, stimulation has the effect of reducing the Coulomb stress changes occurring above and below the reservoir. The higher diffusivity near the well reduces the tension induced in S_z as well as the compression induced in S_x above and below the reservoir. Further, it results in a reduction in the induced poroelastic pore pressure increase at these locations. All of these changes reduce the Coulomb stress above and below the reservoir and therefore also the seismicity rate, which can be seen in the comparison made in Figure 1.4b for selected locations above and below the reservoir. At each location the seismicity is reduced
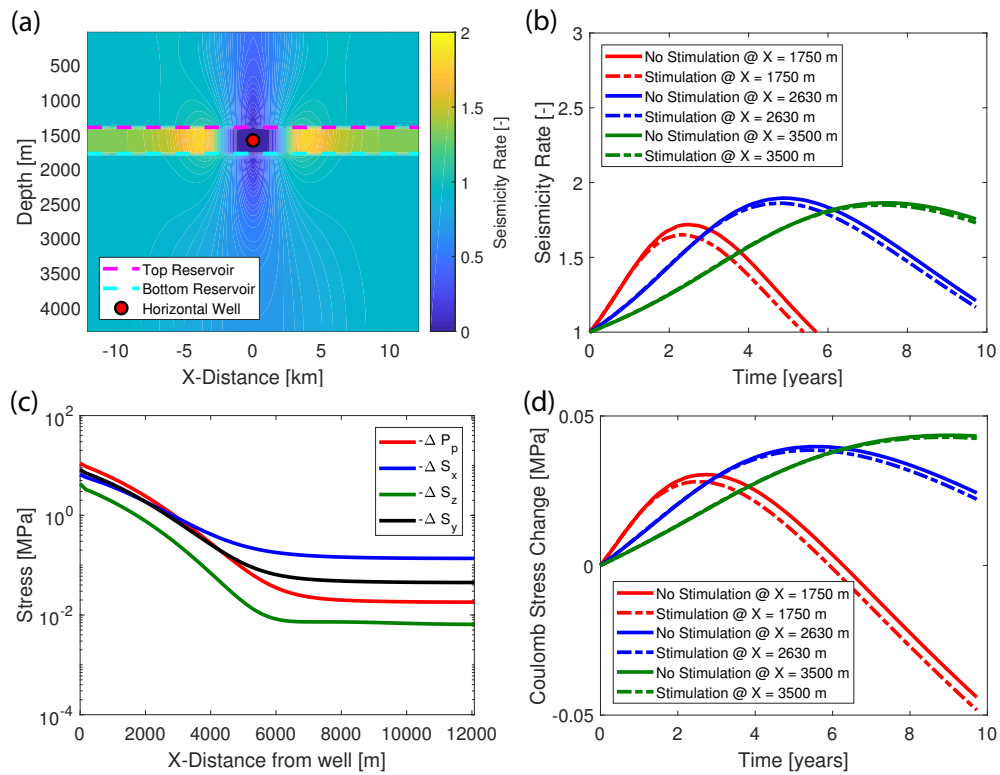
Figure 1.3 – Results at the end of simulation (t = 10 years); (a) The seismicity rate relative to the background seismicity rate in a normal faulting stress regime without stimulation. Seismicity is generally concentrated at the flanks of the reservoir as predicted by Segall (1989). (b) The seismicity rate at various locations at the same depth as the well with and without stimulation. Note that based on (a) these are the most seismically active areas in the simulation. (c) The reductions in pore pressure and the decreases in total stress due to production from the well in the case where no stimulation has occurred. Data are reported only for the locations at the same depth as the well. (d) The Coulomb stress changes for the stimulated and non-stimulated cases at various locations at the same depth as the well.
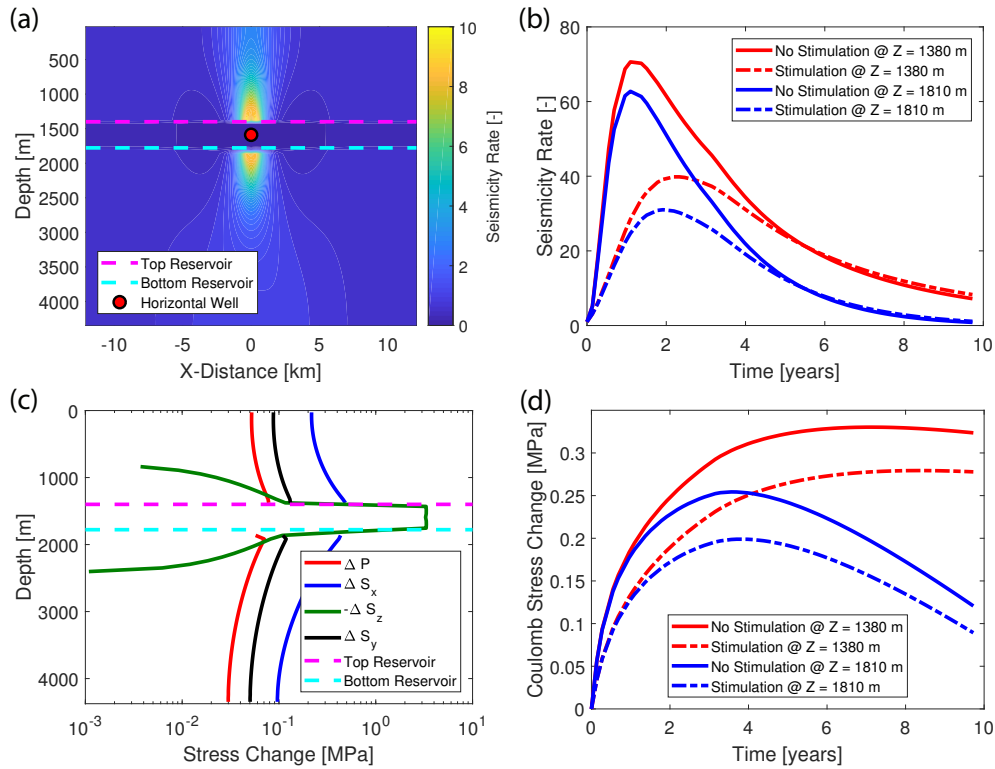
Figure 1.4 – Results at the end of simulation (t = 10 years); (a) The seismicity rate occurring for a reverse faulting environment which has not undergone stimulation. Seismicity is concentrated above and below the producing reservoir as predicted by Segall (1989). (b) A comparison between a stimulated and non-stimulated reservoir's seismicity rate. Two locations are shown, directly above the reservoir (Depth = 1380 *m*) and directly below the reservoir (Depth = 1810 *m*), in-line with the producing well. Note that based on (a) these are the most seismically active areas in the simulation. (c) The changes in stress and pore pressure that occur due to production from a non-stimulated reservoir. Stresses and pressures are taken in-line with the well in the vertical direction. The negative change in S_z is plotted because tension is induced at all relevant depths in this direction. (d) The Coulomb stress changes in the stimulated and non-stimulated cases. The comparison is made vertically, in-line with the producing well.

for the case that the reservoir was stimulated.

1.5.3 Strike-Slip Faulting Stress Regime ($S_x > S_z > S_y$)

In the case that a well is drilled in a strike-slip faulting stress regime (with S_y being the least principal stress), the production-related reduction in S_x occurring in the reservoir along with the production-related reduction in pore pressure, again mean that there is a reduction in seismicity occurring within the reservoir during production. Above and below the reservoir, however, the horizontal stresses increase, especially S_x, and, due to poroelastic effects, pore pressure also increases at these locations. The pore pressure and S_x increase lead to higher Coulomb stresses, which leads to a seismicity rate increase as seen in Figure 1.5a. The seismicity is less than in the reverse faulting stress regime case because the minimum stress, S_y, actually increases in this stress regime whereas in the reverse faulting stress regime the minimum stress, S_z, decreases due to production.

As seen in Figure 1.5b, in the case the reservoir is stimulated before production begins, subsequent depletion-induced seismicity is reduced. Two locations are evaluated in Figure 1.5b, just above and just below the reservoir. In both locations, the seismicity is reduced by a significant amount. This occurs because less Coulomb stress changes are induced in the case that the reservoir has been stimulated, as seen in Figure 1.5d. This is especially due to the reduction in the amount of compression in S_x that is occurring, which can be seen in Figure 1.5d, and also due to the lessening of the pore pressure increase, although this effect is of lesser importance than the change to S_x. The least principal stress, S_y, also experiences less compression due to the stimulation treatment (which is an undesired effect in terms of induced seismicity); however, the changes to S_x are again more significant.

1.5.4 Optimal Well Orientations

Based on the differences in horizontal stress changes seen in Figures 1.3c, 1.4c, and 1.5c, it is intuitive that the seismicity levels are likely to depend on the direction that a horizontal well is drilled in. In this section, the results for the non-stimulated case will be rerun with the wells drilled perpendicular to their original orientations. Because this would change how a hydraulic fracture would propagate, only the non-stimulated cases will be considered.

Normal Faulting Stress Regime

If the well were to be drilled in the direction of the intermediate principal stress instead of the least principal stress in a normal faulting stress regime, S_x would represent the changes to the least principal stress in Figure 1.3c. Seismicity on the flanks of the reservoir would be higher due to the even higher Coulomb stress (Figure 1.6a), because changes to S_x are larger than changes to S_y in the areas that experience seismicity. This agrees with the results of Altmann *et al.* (2014), who showed that radial stress changes are generally larger than tangential ones in
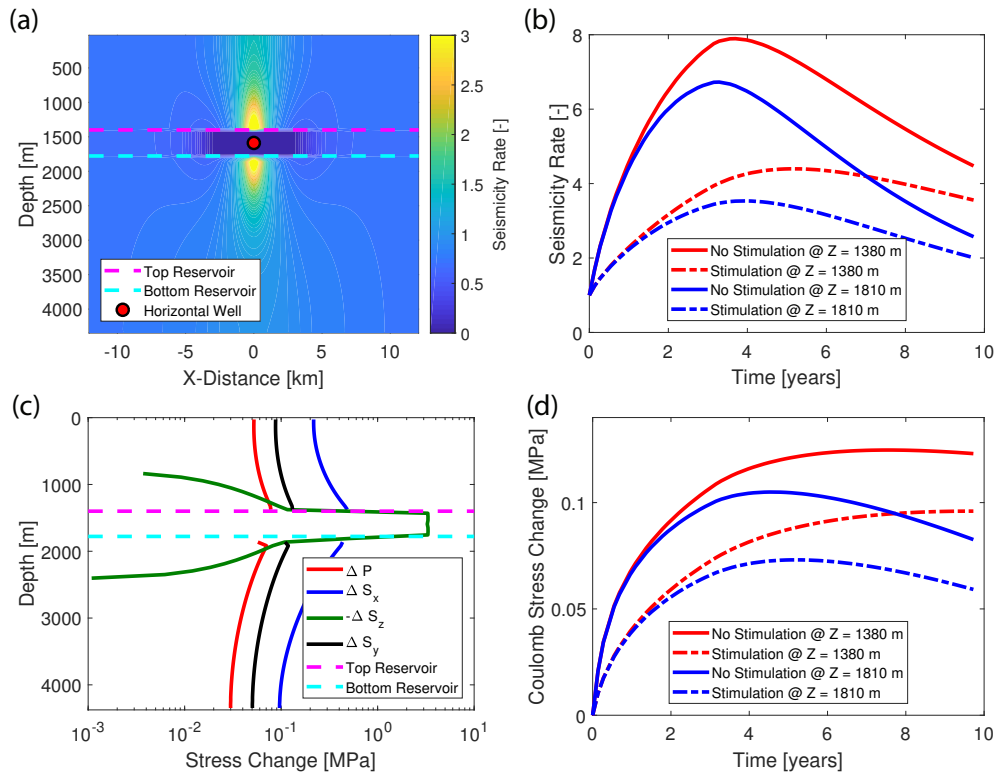
Figure 1.5 – Results at the end of simulation (t = 10 years); (a) Seismicity rate occurring in a strike-slip faulting environment where the reservoir has not undergone stimulation. Seismicity is concentrated above and below the producing reservoir. (b) A comparison between a stimulated and non-stimulated reservoir's seismicity rate. Two locations are shown, directly above the reservoir (Depth = 1380 m) and directly below the reservoir (Depth = 1810 m), in-line with the producing well. Note that based on (a) these are the most seismically active areas in the simulation. (c) The changes in stress and pore pressure that occur due to production from a non-stimulated reservoir. Stresses and pressures are taken in-line with the well in the vertical direction. The negative change in S_z is plotted because tension is induced at all relevant depths in this direction. (d) The Coulomb stress changes between the stimulated and non-stimulated cases. The comparison is made vertically, in-line with the producing well.
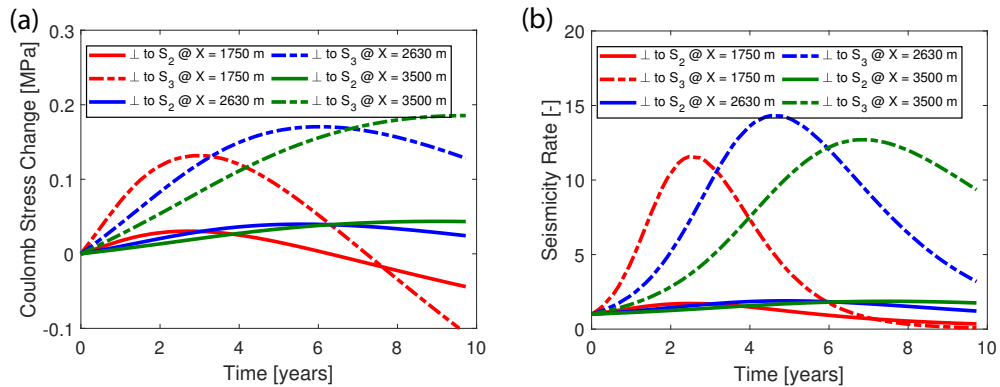
Figure 1.6 – The effect of changing the direction that the horizontal well is drilled in in a normal faulting stress regime with no stimulation on the (a) Coulomb stress changes and (b) the seismicity rate. The legend indicates the orientation of the horizontal well with respect to the principal stresses. All values are taken at the same depth as the well at a specified horizontal distance from the well.

production scenarios. Further, this implies that, if the goal is to minimize induced seismicity, in a normal faulting stress regime, horizontal wells should be drilled parallel to the least principal stress to minimize the induced Coulomb stress resulting from fluid production on optimally-oriented faults at the flanks of the reservoir. This is confirmed in Figure 1.6b.

Reverse Faulting Stress Regime

The seismicity in a reverse faulting stress regime depends on the direction that the horizontal well is drilled in. If the well were to be drilled parallel to the maximum principal stress, seismicity would likely be reduced above and below the reservoir. The reason for this can be seen in Figure 1.4c where compressive changes to S_x are larger than those to S_y. This means that drilling the well such that it is parallel to the maximum principal stress reduces the compression induced in the maximum principal stress, resulting in a smaller increase in the Coulomb stress, as seen in Figure 1.7a. Therefore, in terms of induced seismicity, it is beneficial to drill horizontal wells parallel to the maximum principal stress in a reverse faulting stress regime, as shown in Figure 1.7b. Regardless of well orientation in this stress regime, seismicity is not expected in the reservoir because in these locations more tension is induced in S_x and S_y than in the least principal stress, S_z, and pore pressure is reduced.

Strike-Slip Faulting Stress Regime

The results for strike-slip faulting stress regimes also depend on the direction that the horizontal well is drilled in. If the well were to be drilled parallel to the maximum principal stress as opposed to the least principal stress, the seismicity would be focused on the flanks of the reservoir, as shown in Figure 1.8. The reason for this can be seen in Figure 1.3c (which shows
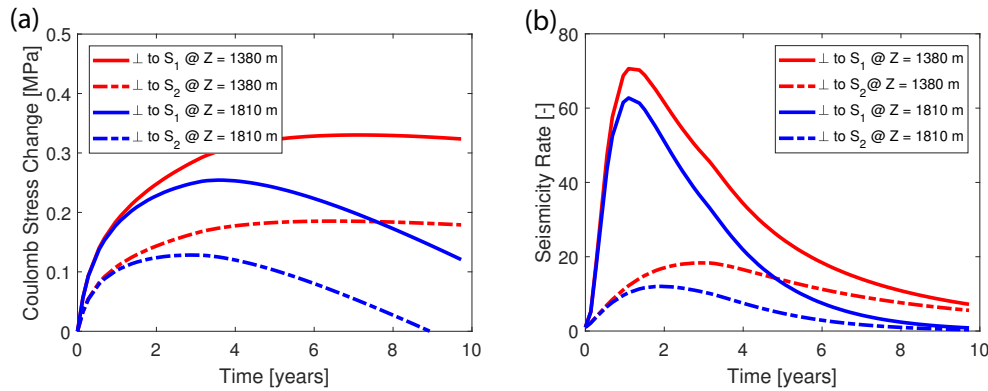
Figure 1.7 – The effect of changing the direction that the horizontal well is drilled in in a reverse faulting stress regime with no stimulation on the (a) Coulomb stress changes and (b) the seismicity rate. For both images two locations are shown, directly above the reservoir (Depth = 1380 m) and directly below the reservoir (Depth = 1810 m), in-line with the producing well. The legend indicates the orientation of the horizontal well with respect to the principal stresses.

stress changes in the reservoir as opposed to above and below it as in Figure 1.5c) where tensile changes to S_x (in this case the least principal stress) are larger than the tensile changes to S_y (in this case the maximum principal stress) at the flanks of the reservoir, meaning that the Coulomb stress will increase at these locations. Seismicity would not occur above and below the reservoir, based on the stress changes occurring above and below the reservoir in Figure 1.5c, because in these locations the compressive changes to S_x are larger than those to S_y.

1.6 Discussion and Conclusions

In a normal faulting stress regime, fluid production causes a reduction in the minimum principal stress and pore pressure at the flanks of the reservoir and a slight reduction in the vertical stress. The reduction in the minimum principal stress is what leads to seismicity at these locations. Drilling the horizontal well in a different orientation than parallel to the least principal stress, which is horizontal, is predicted to increase the induced seismicity. Indeed, it has been previously shown that an anisotropic stress field can have an effect on how seismicity develops (Schoenball *et al.*, 2010). Wellbores in horizontal wells drilled in the direction of the least principal stress are also more stable than those drilled in the direction of the secondary principal stress (Zoback, 2007). In the case that the reservoir is stimulated before production, the pore pressure distribution begins at a higher value near the well. It also has a much lower pore pressure gradient near the well, resulting in less induced tension at these locations. However, after a certain distance (in this simulation, 185 m away from the well), the pore pressure is actually lower in the stimulated case. This results in increased mechanical stability in these areas. That said, pore pressure also has a steeper gradient far
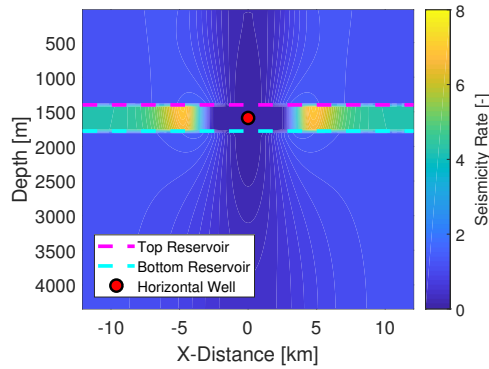
Figure 1.8 – The seismicity occurring in a strike-slip faulting environment which has not undergone stimulation when the well is drilled parallel to the maximum principal stress. Note where the seismicity is located in this figure when compared to Figure 1.5a. The results shown are for the end of simulation (t = 10 years).

from the well which results in more induced tension in S_y, an effect which would normally be destabilizing for optimally oriented faults. However, as the stimulation's effect on production-induced pore pressure changes is greater than its effect on production-induced changes in S_y, the stimulation has the effect of making these areas more stable. Although a small effect, the tension induced in S_z at the flank of the reservoir is also increased due to stimulation, somewhat stabilizing the area. Overall the stimulation has the effect of slightly reducing the induced seismicity caused by fluid production.

Further, because the effect of the fracture's presence is larger on the pore pressure distribution than on the stress changes over most of the reservoir, stimulation effectively increases the distance that pore pressure changes dominate over stress changes in terms of induced seismicity. In this numerical experiment, when compared to the non-stimulated case, pore pressure changes were larger than changes to S_x some 34 m farther away from the well in the case that the reservoir was stimulated. In this case this change is small, but this value is dependent on the simulation parameters. Qualitatively, the increase in distance that pore pressure changes are larger than stress changes can be predicted using the analytical solutions for pore pressure and stress due to fluid injection/production in an isotropic body of Rudnicki (1986), where the similarity variable, ξ, is

$$\xi = \frac{r_d}{\sqrt{ct}}. \tag{1.10}$$

Here, r_d is the radial distance from the point source, t is time, and c is the hydraulic diffusivity,

27

given by,

$$c = \frac{k}{\mu} \frac{(\lambda_u - \lambda)(\lambda + 2G)}{\alpha^2 (\lambda_u + 2G)}. \tag{1.11}$$

Here, μ is the fluid dynamic viscosity, k is the permeability of the isotropic medium, λ_u and λ are the undrained and drained Lamé parameters, respectively, and G is the shear modulus. Then, from Rudnicki (1986), the ratio of the pore pressure change to the stress change in the direction of a principal stress, in this case taking S_x as an example, is given by,

$$\frac{P}{S_x} = \frac{\mu c \alpha (\lambda_u + 2G) \operatorname{erfc}\left(\frac{1}{2}\xi\right)}{k(\lambda_u - \lambda) G \left[2\operatorname{erfc}\left(\frac{1}{2}\xi\right) + 4g\xi^{-2}\right]}, \tag{1.12}$$

where g is

$$g = \operatorname{erf}\left(\frac{1}{2}\xi\right) - \frac{\xi}{\sqrt{\pi}} e^{-\frac{1}{4}\xi^2}. \tag{1.13}$$

Based on Equation 1.12, it is clear that the ratio of pore pressure changes to changes in S_x is dependent on ξ. Therefore, based on Equations 1.10 and 1.11, the location where these two sets of changes are equal (i.e. where the ratio is equal to 1) will change as permeability changes. Specifically, the location where the pore pressure change is equivalent to a change in a principal stress increases with the square root of permeability, as illustrated in Figure 1.9. It should be noted, however, that the results of Rudnicki (1986) are for a point source of fluid mass in an isotropic and homogeneous medium, meaning they are not valid for predicting the increase in distance that pore pressure changes are larger than stress changes due to a hydraulic stimulation. That said, they do imply generally that increasing the permeability of a reservoir will increase this distance.

In a reverse faulting stress regime, the seismicity is primarily seen above and below the reservoir during production. This is because, in these locations, the maximum principal stress, S_x, increases and the least principal stress, S_z, decreases. Additionally, pore pressure increases at these locations due to poroelastic effects. All of these changes have an adverse influence on the Coulomb stress and therefore the seismicity rate. In the case where the reservoir has been stimulated, the smaller resultant pore pressure gradients result in all three of these changes being lessened. This then reduces the amount of seismicity expected. The optimal orientation of horizontal wells drilled in this stress regime, in terms of induced seismicity, is found to be parallel to the maximum principal stress, which is horizontal. This is also the optimal direction
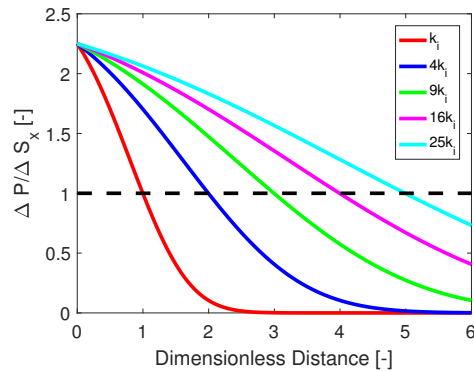
Figure 1.9 – The ratio of changes in pore pressure to changes in horizontal stress for various permeabilities. The parameters are taken from the sandstone in Table 1.2, where k_i is equal to the sandstone permeability, and a dimensionless distance is defined as the distance required for the stress changes to be larger than pore pressure changes in the case where the permeability is equal to k_i. Note that the distance required for the ratio of pressure and stress changes to equal one increases with the square of permeability.

of a horizontal well in this stress regime for borehole stability (Zoback, 2007).

Finally, in a strike-slip faulting stress regime with a horizontal well drilled parallel to the least principal stress, seismicity is seen above and below the reservoir during production but to a lesser extent than in the reverse faulting case. Here, the maximum principal stress, S_x, is increased and the pore pressure is also increased due to poroelastic effects, both decreasing stability. However, the least principal stress, S_y, is also increased which acts to stabilize these areas. Seismicity still occurs, however, as the changes in S_x are much larger. Stimulating the reservoir acts to reduce all of these changes in pressure and stress, and ultimately reduces the amount of induced seismicity. Drilling the well parallel to the maximum principal stress changes the location of the induced seismicity to the flanks of the reservoir. Drilling a horizontal well in the direction of the maximum principal stress in a strike-slip faulting regime is favourable in terms of well bore stability (Zoback, 2007).

The reduction of seismicity in fluid-producing reservoirs with stimulation, while demonstrated for a permeability field resulting from a hydraulic fracturing treatment, could be expected to be seen as a result of acidization treatments as well. This is because these type of treatments all act to increase the permeability (and therefore transmissibility) of the region around the well, allowing the same amount of fluid to be produced with a smaller drawdown. This reduces the changes in poroelastic stresses and pressure occurring above and below the reservoir. Stimulation also allows the reduction in pore pressure to propagate farther more quickly within the reservoir, stabilizing areas far from the well but still within the reservoir. While it is true that this results in higher pore pressure gradients far from the well (inducing more poroelastic stress changes which act to destabilize faults in a normal faulting stress regime), it also increases the distance that pore pressure changes dominate over poroelastic stress changes.

Conversely, depletion-induced compaction is likely to reduce the permeability of producing reservoirs over long periods of time (Schutjens *et al.*, 2004). This will presumably result in higher pore pressure gradients required to maintain the same production rate, which suggests that an increase in Coulomb stress and therefore seismicity rate will result, but this should be investigated. Further, the results imply that, generally speaking, in the case that equivalent flow rates are used to produce two reservoirs which are identical in all aspects bar their permeabilities, the reservoir with the lowest permeability should be expected to experience more seismicity, agreeing with the results related to subsidence in Segall (1985).

These results depend strongly on the stress regime. The stimulation treatment affects each of the principal stresses uniquely, and, therefore, the stimulation's effect on the induced seismicity will also differ in each of the different possible stress regimes depending on the orientation of the well. Indeed, stimulation is most effective at reducing seismicity in reverse and strike-slip faulting stress regimes and has only a moderate effect in a normal faulting stress regime. These results are also dependent on the parameters used during the simulation. Although, qualitatively speaking, the effects of the stimulation will be the same, certain cases may experience larger seismicity rate reductions than others. Indeed, the results still hold for faults which are not optimally oriented in the current stress field in the sense that a slightly sub-optimally-oriented normal fault on the flanks of the reservoir would still benefit from reservoir stimulation. Similarly, the presence of a fault could be expected to affect the local stress field. While this may affect the quantitative results, the qualitative results are expected to hold. Further, it should be noted that the seismicity model used does not provide insight into the size of the earthquakes induced.

The seismicity modelled here was induced with small Coulomb stress changes (on the order of 0.1 MPa or even less in the normal faulting stress regime case), but this is in agreement with what is seen in real life production scenarios. For example, 0.2 MPa stress changes were seen to be enough to induce felt seismicity in the Lacq gas field, France (Segall *et al.*, 1994), and 0.02 MPa stress changes induced microseismicity in the Seventy-Six oil field, Clinton County (Rutledge *et al.*, 1998). In some cases, even a stress change of 0.01 MPa may be sufficient to induce seismicity (Hardebeck *et al.*, 1998; Reasenberg and Simpson, 1992). Indeed, it is generally thought that a stress change of 0.1 MPa is enough to induce an earthquake under the correct circumstances (Stein, 1999).

Cases where small stress changes result in induced seismicity support the assumption of a critically-stressed crust used here. It is thought that most of the crust is critically stressed, even intraplate areas which do not often experience seismicity (Townend and Zoback, 2000; Zoback, 2007). However, intraplate earthquakes' infrequent occurrence may even make them more hazardous as these areas may not be prepared for seismicity. Intraplate areas are seismically relatively quiet only because of low strain rates (Zoback, 2007; Zoback *et al.*, 2002), and many intraplate areas do experience significant seismicity over long periods of time, including events with a large ($M_w \geq 7$) magnitude (Talwani, 2014; Zoback and Gorelick, 2012). In fact, the deadliest earthquake in human history was an intraplate earthquake (Talwani, 2014). Due

to the low stressing rates seen in intraplate areas, even small stress changes may significantly increase the chance of seismicity (Parsons, 2005). This helps explain why seismicity can be induced by fluid production in areas that were previously not associated with seismicity, such as in the Gazli gas field (Simpson and Leith, 1985), Goose Creek (Yerkes and Castle, 1976), the Lacq gas field (Segall *et al.*, 1994), and the Western Canada Sedimentary Basin (Baranova *et al.*, 1999), including Rocky Mountain House (Wetmiller, 1986). Further, most intraplate areas are characterised by either reverse or strike-slip faulting stress regimes (Zoback *et al.*, 1989) and many (approximately 40%) of the world's largest oil fields are found in tectonic settings which are characterised by reverse and strike-slip faulting (Mann *et al.*, 2001). This makes the results presented here especially relevant, as stimulation was shown to have the largest induced seismicity-reducing effect in these two stress regimes.

It is important to recognize that these results do not necessarily mean that reservoir stimulation will result in lower seismicity rates if the reservoir is then produced at a higher rate than it would have been without the stimulation treatment, as all simulations used the same producing mass flow rate. In effect, the simulations ran are equivalent to stimulating a reservoir for the sole purpose of reducing the seismicity and not in order to increase the production rate. Additionally, it is important to note that the act of hydraulically fracturing itself has been known to induce seismicity (e.g. Atkinson *et al.*, 2015; Clarke *et al.*, 2014; Deng *et al.*, 2016; Wang *et al.*, 2017), although the seismicity associated with hydraulic fracturing is usually seen to return to a low level shortly (on the order of days - much shorter than the typical production life of a conventional well) after the hydraulic fracturing treatment (Lei *et al.*, 2017; Rubinstein *et al.*, 2018). Further, the disposal of waste water either used to perform hydraulic fracturing treatments or co-produced with the hydrocarbons after stimulation treatments has also been seen to cause induced seismicity (e.g. Chen *et al.*, 2017; Horton, 2012; Keranen *et al.*, 2013). These are serious concerns that should be carefully considered before proceeding with a hydraulic fracturing treatment. Instead, this paper qualitatively highlights the positive impact a stimulated permeability field could have on depletion-induced seismicity occurring in and around the production reservoir.

These results could have implications for production wells in reservoirs experiencing depletion-induced seismicity. However, for large oil fields, multi-well simulations should be performed as these fields are typically produced with many wells as opposed to the one well example shown here. Finally, the manipulation of the pore pressure gradient to influence the induced poroelastic stresses and thereby reduce the seismicity is also something that might be achievable in other ways, such as through manipulating the fluid viscosity in injection scenarios.

2 Reservoir compaction's effect on depletion-induced seismicity

The results of this chapter are published in:

Journal paper:

Contribution of candidate: Initial idea, development of code, analysis of results, writing of manuscript.

2.1 Chapter Summary

Producing fluid out of subsurface reservoirs causes stress changes that can lead to induced seismicity. In the fully coupled theory of poroelasticity, these stress changes are caused by the gradient of pore pressure which acts as an internal force in the momentum balance equation. This implies that, if a larger pore pressure gradient is required to produce the fluid, larger stresses will be induced, likely leading to a higher seismicity rate.

Based on Darcy's Law, the gradient of pore pressure required to achieve a certain fluid production rate is inversely proportional to the permeability. The lower the permeability, the larger the pore pressure gradient required. Consequently, the permeability reductions that are seen due to compaction during fluid production may be significant in terms of induced seismicity because this will increase the pore pressure gradient required to produce a certain amount of fluid.

Therefore, using a poroelastic flow model and an existing seismicity model, it is shown that compaction-induced permeability loss has the effect of increasing the stress changes associated with the production of a certain amount of fluid and thereby indirectly increases the seismicity rate, even when the compaction remains in the near-elastic range. In the event that compaction begins occurring inelastically, the permeability decreases and seismicity rate increase are much more drastic. Finally, it is shown that the optimal orientation for a horizontal well, if inelastic compaction near the wellbore is to be avoided, is parallel to S_{Hmax}. These results have implications for reservoir management in fluid producing reservoirs.

2.2 Introduction

Scientists have been aware of the possible earthquake-inducing effect fluid injection at depth can have since induced events at the Rocky Mountain Arsenal (Healy *et al.*, 1968) and Rangely (Raleigh *et al.*, 1976). There has been an increased level of interest over the last few years due to significantly-sized (up to M_w 5.8 (Chen *et al.*, 2017)) earthquakes in the United States due to wastewater disposal (e.g., Horton (2012); Ellsworth (2013); Keranen *et al.* (2013, 2014); Rubinstein *et al.* (2014); Sumy *et al.* (2014); McNamara *et al.* (2015); Yeck *et al.* (2016); Chen *et al.* (2017); Goebel *et al.* (2017b); Rubinstein *et al.* (2018)). Although pore pressure increase is thought to be the primary triggering mechanism of these earthquakes (Keranen *et al.*, 2014), in some instances poroelastic stresses are thought to play a major role (e.g., Barbour *et al.* (2016); Deng *et al.* (2016); Chen *et al.* (2017); Goebel *et al.* (2017b)) and the attempted management and mitigation of these poroelastic stresses has been investigated (e.g., Segall and Lu (2015); Chang and Segall (2016a,b, 2017); Postma and Jansen (2018)). In fact, poroelastic stresses leading to earthquakes is not limited to injection scenarios, and a number of instances of induced seismicity in production scenarios have been reported.

For example, in the United States the first reported case of depletion-induced seismicity occurred at Goose Creek, Texas, as oil and gas production caused the edges of the reservoir to experience normal faulting (Pratt and Johnson, 1926; Yerkes and Castle, 1970, 1976). Additionally, further instances have been reported in the country, such as the reverse faulting which occurred above an oil-producing reservoir at the Wilmington oil field (Yerkes and Castle, 1976), or the reverse faulting which the Buena Vista Hills oil field experienced near the surface, resulting in damage (Yerkes and Castle, 1970, 1976; Koch, 1933). Additionally, reverse faulting occurred below a shallow producing oil reservoir in Clinton County, Kentucky (Rutledge *et al.*, 1998). Normal faulting also appears to have been induced within the reservoir at the War-Wink gas field in Texas (Zoback and Zinke, 2002).

In the previously aseismic region of northern Germany, a M_w 4.4 earthquake was induced near three major gas fields near Rotenburg in 2004 (Dahm *et al.*, 2007). The normal faulting earthquake was at approximately the same depth as the gas producing intervals, occurring at the edges. Although possibly the most noteworthy, this event does not represent the entirety of depletion-induced seismicity in Germany. In 2012, a magnitude 2.9 earthquake was felt by locals near the Völkersen gas field, some of whom reported damage; here normal faulting occurred on the edge of the gas-producing reservoir, in a region normally deviod of seismic activity (Bischoff *et al.*, 2013). More recently, in 2016, a M_L 3.1 earthquake was registered in Völkersen; again at approximately the same depth as the gas production, but this time within the gas field itself (Bischoff *et al.*, 2016). Another M_L 3.1 earthquake was felt by locals near the Emstek gas field in 2014 in a region that was previously seismically quiet (Bischoff *et al.*, 2015). This instance of normal faulting occurred in the east of the gasfield at a depth slightly below the producing horizon (although the depth of the gas reservoir lies within the uncertainty of the depth of the epicenter) (Bischoff *et al.*, 2015). In 2014, gas production near Syke, Germany also induced seismicity, this time of local magnitude 3.2, in what was previously a seismically quiet

region (Bischoff *et al.*, 2014). Although there was difficulty in determining the epicenter and focal mechanism precisely, it seems that this was another case of normal faulting occurring on the edges of a gas-producing reservoir (Bischoff *et al.*, 2014). Although there was poor seismic coverage at the time of the event, Dahm *et al.* (2007) also suggest that the 1977 M_L 4 earthquake at Soltau was induced by gas production. This earthquake was a strike-slip earthquake located adjacent to and probably slightly below producing gas fields (Leydecker *et al.*, 1980; Dahm *et al.*, 2007).

Similarly, in the Netherlands, gas production has also famously led to induced seismicity (Buijze *et al.*, 2017). Generally, these are cases of normal faulting occurring within production reservoirs; for example, most earthquakes in the Groningen gas field (Dost *et al.*, 2012) and the 1991 earthquake in the Eleveld gas field M_L 2.7 (Begeleidingscommissie Onderzoek Aardbevingen, 1993) had normal faulting mechanisms. However, there are exceptions, such as the 1986 Assen M_L 2.8 and the 1987 Hooghalen M_L 2.5 earthquakes, which occurred outside and above the Eleveld gas field (Begeleidingscommissie Onderzoek Aardbevingen, 1993), the (sometimes debated) 1997 reverse faulting occurring at Roswinkel M_L 3.4 (Dost and Haak, 2007), and the four largest earthquakes occurring at the Bergermeer gas field in 1994 and 2001, $M_L \leq 3.5$, which also had reverse faulting mechanisms (KNMI, 1994; Haak *et al.*, 2001). Other events with less certain focal mechanisms include the 2012 Huizinge earthquake, M_w 3.6, which occurred inside the Groningen gas field (Dost and Kraaijpoel, 2013).

In France, reverse faulting has been induced by gas production from the Lacq gas field (Segall, 1992; Segall *et al.*, 1994). Most of the earthquakes here were induced above the producing reservoir (Bardainne *et al.*, 2008).

In the North Sea, depletion of the Ekofisk and Valhall reservoirs has led to microseismicity primarily in and above the reservoirs (Teufel *et al.*, 1991; Rutledge *et al.*, 1994; Zoback and Zinke, 2002). Shear failure associated with the Ekofisk is thought to be associated with issues such as casing failures and gas leak through the cap rock (Zoback and Zinke, 2002).

Instances of depletion-induced seismicity are not limited to the oil and gas industry, however. The 2011 M_w 5.1 earthquake near Lorca, Spain, which killed nine people, was linked to groundwater production (González *et al.*, 2012). The earthquake occurred below the producing reservoir with a reverse and strike-slip faulting mechanism in an area which experienced a positive Coulomb stress change on the order of 0.01 MPa due to reservoir depletion (González *et al.*, 2012). Aquifer-depletion induced seismicity in the High Valley of the Aterno River, Italy; here normal faulting ($M = 3.9$) at the margin of an aquifer was induced by a destabilization of a few tenths of a MegaPascal due to a decreasing water level (Bella *et al.*, 1998).

There are further examples of depletion-induced seismicity, such as oil and gas production from the Natih and Shuaiba formations in Oman, which induced microseismicity (Sze *et al.*, 2005). Kuwait also experienced production-induced seismicity, with a magnitude 4.7 earthquake. This time seismicity was induced by high production rates associated with three-quarters of the field's wells either being set alight or left gushing by Iraqi forces during the

first Gulf War (Bou-Rabee and Nur, 2002). Two examples of reverse faulting below a production reservoir include the Gazli gas field, Uzbekistan (Simpson and Leith, 1985), and Rocky Mountain House, Alberta (Wetmiller, 1986). Indeed, the Western Canada Basin in general has exhibited induced seismicity (Baranova *et al.*, 1999). Hydrocarbon production in North America also led to seismicity in the Chaveroo Oil Field, New Mexico (Rutledge *et al.*, 1990). Other instances include faulting occurring in a seismically-quiet region over 3 km below gas-producing layers in the vicinity of Caviaga, Italy (Caloi *et al.*, 1956), faulting due to groundwater production in Houston, Texas (Holzer *et al.*, 1983), a M 4.7 earthquake above the large Starogroznenskoe Oilfield in Russia (Kouznetsov *et al.*, 1994), water extraction in Crimea (Shtengeolov, 1980), and quite a few other cases as described by Suckale (2009).

This volume of reports is significant when it is considered that depletion-induced seismicity is likely systematically under-reported: many producing fields are not equipped with seismic arrays, many producing fields are located in sparsely populated areas, and there is generally limited motivation for oil companies to report induced seismicity.

With the exception of possibly the Bergermeer and Soltau earthquakes (KNMI, 1994; Haak *et al.*, 2001; Dahm *et al.*, 2007), all of the earthquakes listed above with known focal mechanisms and focal depths can be explained by one of two mechanisms.

The first mechanism was described by Segall (1989) using many of the cases listed above in his development of a model which was able to explain depletion-induced seismicity (Segall, 1985, 1989; Segall and Fitzgerald, 1998). In this model, fluid production increases horizontal compression above and below the reservoir and decreases horizontal compression at the margins of the reservoir. These changes result in reverse faulting above and below the reservoir and normal faulting at the margins.

The second mechanism involves normal faulting earthquakes resulting from a high stress path within the producing reservoir (Teufel *et al.*, 1991; Chan and Zoback, 2002; Zoback and Zinke, 2002). These earthquakes have normal faulting focal mechanisms and occur within or very near the producing reservoir as decreases in pore pressure result in large changes in horizontal stress, promoting faulting in normal faulting stress regimes (Zoback and Zinke, 2002). Examples of these types of earthquakes include those in the Groningen gas field (Dost *et al.*, 2012), the Eleveld gas field (Begeleidingscommissie Onderzoek Aardbevingen, 1993), the Valhall and Ekofisk oil reservoirs (Teufel *et al.*, 1991; Rutledge *et al.*, 1994; Zoback and Zinke, 2002), the 2016 gas production-induced earthquake in Völkersen (Bischoff *et al.*, 2016), and potentially those in the War-Wink gas field (Zoback and Zinke, 2002). These stress path earthquakes will not be discussed further here.

Returning to the model proposed by Segall (1989), the poroelastic stresses induced by depletion are capable of inducing seismicity and dominate over pore pressure changes at large distances (Segall and Lu, 2015; Chang and Segall, 2016a,b; Deng *et al.*, 2016; Goebel *et al.*, 2017b). In addition, the induced poroelastic stresses couple with pore pressure changes to induce compaction, resulting in porosity and often times permeability loss in highly porous

rock (David *et al.*, 1994; Zhu and Wong, 1996, 1997; Boutéca *et al.*, 2000; Hettema *et al.*, 2000; Schutjens *et al.*, 2000; Chan and Zoback, 2002; Schutjens *et al.*, 2004; Baxevanis *et al.*, 2006). Potential compaction-induced permeability loss is significant in that it might reduce the inflow performance of nearby wells. However, it may also have implications for induced seismicity. Segall (1985) found that lower values of hydraulic diffusivity (which is directly proportional to permeability) may cause larger amounts of localized subsidence. This can be explained by considering that the gradient of pore pressure acts to induce poroelastic stress changes. These poroelastic stress changes are what induce seismicity in fluid-production scenarios. However, permeability exhibits a strong control over the pore pressure gradient required to produce an amount of fluid. Therefore, it is possible that the permeability-reducing effect of depletion-induced compaction will indirectly lead to higher levels of induced seismicity.

This study will specifically investigate the effect compaction-induced permeability loss can have on depletion-induced seismicity. The aim of this study is not to quantitatively predict the amount of seismicity increase that would occur for a given permeability decrease nor to link any instances of depletion-induced seismicity to depletion-induced permeability loss. Rather, the aim is to show how depletion-induced permeability loss as a mechanism could increase the stress changes induced by production and thereby qualitatively increase the amount of induced seismicity. This analysis will be carried out for normal, reverse, and strike-slip faulting stress regimes by first predicting pore pressure and stress changes due to production with a sequentially coupled poroelastic finite volume flow and finite element mechanical simulator. In the case that compaction-induced permeability loss will be included, the permeability loss model presented by Schutjens *et al.* (2004) will be used, assuming that the reservoir remains in the near-elastic domain during the simulation (an assumption which is then verified). According to Schutjens *et al.* (2004), the near-elastic domain is where elastic theory accurately describes rock deformation and where most deformation is reversible; this is as opposed to the in-elastic domain where deformation is not reversible and where permeability loss is more significant. Differential stress is generally the primarily determining factor of the type of deformation. Note that Schutjens *et al.* (2004) also includes the failure domain, where the rock is predicted to fail. The seismicity rate will be modelled using Segall and Lu (2015)'s adapted version of Dieterich (1994)'s seismicity model. In this way, the effect that compaction-induced permeability loss has on depletion-induced seismicity can be investigated. Further, the results will provide insight into the optimal horizontal well orientation in each stress regime such that it is less likely that the compaction leaves the near-elastic domain as described by Schutjens *et al.* (2004).

2.3 Methods

2.3.1 Coupled poroelastic flow model

The 2-D plane strain poroelastic flow model computes pressure and stress perturbations due to fluid production from a poroelastic medium and is based on a finite volume flow model

which is sequentially coupled to a finite element mechanical model. The coupling is two-way and the model is plane strain.

Flow model   The flow model is based on mass balance for a single phase,

$$\frac{\partial (\phi \rho)}{\partial t} - \nabla \cdot \left(\frac{k}{\mu} \rho \left(\nabla P - \nabla (\rho g z) \right) \right) = q, \tag{2.1}$$

where ϕ is the porosity, k the permeability, μ the dynamic fluid viscosity, ρ the fluid viscosity, g the acceleration due to gravity, z the depth, and q the fluid mass source terms. The flow model is solved in a finite volume in space, implicit finite difference in time framework (Aziz and Settari, 2002). No-flow boundary conditions will be used at all edges, except the surface which has a constant pressure boundary condition.

Mechanical model   The mechanical model is based on the conservation of momentum,

$$\nabla \cdot \sigma^{'} + \nabla (\alpha P) = -f, \tag{2.2}$$

where $\sigma^{'}$ is effective stress, α is Biot's coefficient, and f represents the body forces. The sign convention is such that extension and tension are negative. The conservation of momentum is combined with the linear theory of poroelasticity (Biot, 1941; Rice and Cleary, 1976; Wang, 2000),

$$S_{ij} - \alpha P \delta_{ij} = \frac{E}{(1+v)} \epsilon_{ij} + \frac{Ev}{(1+v)(1-2v)} \epsilon_{kk} \delta_{ij}, \tag{2.3}$$

where S is the total stress, E is the drained Young's Modulus, v is the drained Poisson's ratio, ϵ is the strain, and δ_{ij} is the Kronecker delta. Equations 2.2 and 2.3 will be discretized and solved in a finite element framework. Fixed-displacement boundary conditions will be used at all edges, except at the surface which is free.

Compaction model In order to model the effect of compaction on the reservoir porosity, the relationship presented by Schutjens *et al.* (2004),

$$\Delta\phi = \phi - \phi_0 = \frac{\frac{\Delta V_p}{V_{b0}}\left(\alpha - \phi_0\right)}{\alpha + \frac{\Delta V_p}{V_{b0}}}, \tag{2.4}$$

is used. Here, ϕ_0 is the initial porosity and $\frac{\Delta V_p}{V_{b0}}$ is equivalent to the negative volumetric strain. This change in porosity also acts as the coupling between the mechanical model and the flow model. The mechanical model responds to pressure gradients by predicting strains; these strains are then fed back to the flow model to produce porosity changes. When porosity changes, the fluid density must be adjusted to conserve fluid mass. As the fluid density is dependent on pressure, this results in a change in pressure. Further, compaction, through the increase of mean effective stress, is assumed to cause a reduction in the normalized permeability equivalent to $0.009\frac{1}{MPa}$, found for sandstones with porosities larger than 15% (Schutjens *et al.*, 2004). Permeability changes in the shales present in the model are not considered.

Seismicity model It will be assumed that potential seismicity will occur on faults which are optimally oriented for slip. The seismicity model used to predict the reservoir's and surrounding rocks' response to pore pressure and stress perturbations is based on Dieterich (1994) and was adapted by Segall and Lu (2015), such that the Coulomb stress, τ, is defined as,

$$\tau = \tau_s - \mu_f\left(S_n - P\right). \tag{2.5}$$

Here, τ_s is the shear stress acting on the fault, μ_f the static coefficient of friction, and S_n the normal total stress acting on the fault. The ratio of the current seismicity rate to the background seismicity rate, R, then follows the relationship,

$$\frac{dR}{dt} = \frac{R}{t_a}\left(\frac{\dot{\tau}}{\dot{\tau}_0} - R\right), \tag{2.6}$$

where t_a is the characteristic decay time, $\dot{\tau}$ the stressing rate, and $\dot{\tau}_0$ is the background stressing rate. At each time step, Equation 2.6 is solved for a new value of R using an implicit finite difference framework. The resulting value for R provides an indication of how the seismicity rate in a given location responds to the stress and pore pressure changes. For example, an R value of ten implies that the seismicity rate has increased by an order of magnitude. A
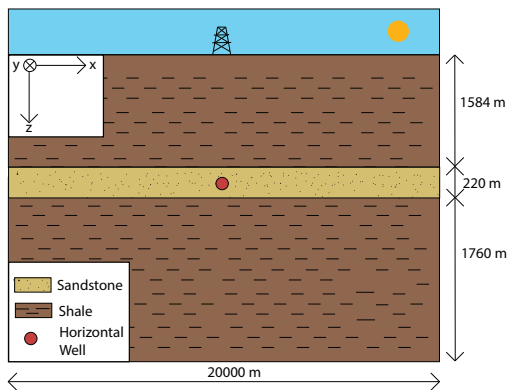
Figure 2.1 – 2-D plane strain problem set-up

minimum value of 0.01 is set for R. Note that this model does not predict magnitude nor does it account for source-to-source interactions.

2.3.2 Problem Set-Up

A sandstone reservoir, overlain by a shale cap rock and underlain by another shale, is penetrated by a horizontal well and is evaluated as in Figure 2.1. A permeable reservoir bounded above and below by relatively impermeable layers is typical, for example, of petroleum systems (Segall, 1992). For the base evaluation, the wells are oriented such that they are parallel to the minimum principal horizontal stress, S_{hmin}; however, wells drilled perpendicular to this direction, in the direction of S_{Hmax}, will be evaluated in Section 2.4.3. The 2-D plane strain simulator described previously is appropriate to model horizontal wells and will allow for an analysis of the development of the stresses in all three principal directions (Cheng, 1998).

During the simulation, the assumption of a linear elastic reservoir response is evaluated by ensuring that the reservoir will always be in a state of pressure and stress such that it remains in the near-elastic domain (Schutjens *et al.*, 2004). The reservoir is produced through a 750-meter section of horizontal well at an initial rate of 2000 $\frac{bbl}{day}$, or approximately $1.6e5\frac{kg}{year \cdot m}$. After a three-year plateau period, the rate will then decline by 6 % per year. Other parameters used during the study can be found in Table 2.1.

In order to initialize the stresses found in-situ, a differential stress of 10 MPa was assumed. This was used, in combination with the assumption that the vertical stress can be found with the lithostatic gradient, to initialize the stresses in the normal and reverse faulting stress regimes. In the strike-slip faulting stress regime, the minimum principal stress was first assumed to be 5 MPa less than the vertical stress. The initial stresses in the reservoir have implications for compaction, as will be discussed in later sections.

The same simulation is run both for the case where compaction-induced permeability loss is considered and where it is not considered. In this way, the differences in the pressure and

Table 2.1 – Summary of the parameters used during the study

Name	Variable	Value
Width	-	20000 m
Cap rock height	-	1584 m
Reservoir height	-	220 m
Underburden height	-	1760 m
Fluid compressibility[ι]	-	5e-10 $\frac{1}{\text{Pa}}$
Fluid viscosity	μ	1 mPa sec
Shale permeability[Γ]	k_{sh}	1e-19 m^2
Sandstone permeability[β]	k_{ss}	1e-15 m^2
Young's Modulus shale[χ]	E_{sh}	5e9 Pa
Young's Modulus sandstone[β]	E_{ss}	18e9 Pa
Poisson's ratio shale[χ]	ν_{sh}	0.25
Poisson's ratio sandstone	ν_{ss}	0.25
Grain bulk modulus shale[Θ]	K_{sh}	6e9 Pa
Grain bulk modulus sandstone	K_{ss}	36e9 Pa
Initial porosity shale[Γ]	$\phi_{0,sh}$	0.23
Initial porosity sandstone[β]	$\phi_{0,ss}$	0.25
Shale friction coefficient[Γ]	$\mu_{f,sh}$	0.35
Sandstone friction coefficient[θ]	$\mu_{f,ss}$	0.6
Background stressing rate[θ]	$\dot{\tau}_0$	1000 $\frac{\text{Pa}}{\text{year}}$
Characteristic decay time[θ]	-	50 years

[ι] Compressibility of water based on (Osif, 1988)
[Γ] Values from Opalinus Clay (OPA) Shale (Orellana *et al.*, 2018)
[θ] From Segall and Lu (2015)
[χ] Typical for OPA (Favero *et al.*, 2018)
[β] Reasonable sandstone values (Detournay and Cheng, 1993)
[Θ] Clay minerals (Vanorio *et al.*, 2003)

stress changes induced by production, as well as the seismicity rates, are readily evaluated.

2.4 Results

During production, the pore pressure within the reservoir decreases and the stress changes within the reservoir are all tensile, with the stress changes in the horizontal directions both being larger than those in the vertical direction, in agreement with Segall and Fitzgerald (1998).

Above and below the reservoir, compressive stress changes occur in the horizontal directions, with the stress changes perpendicular to the direction of the well being larger than those parallel to it. Pore pressure slightly increases in these locations due to poroelastic effects. Tensile stress changes are induced in the vertical direction but these stress changes are smaller in magnitude than those occurring in the horizontal directions.
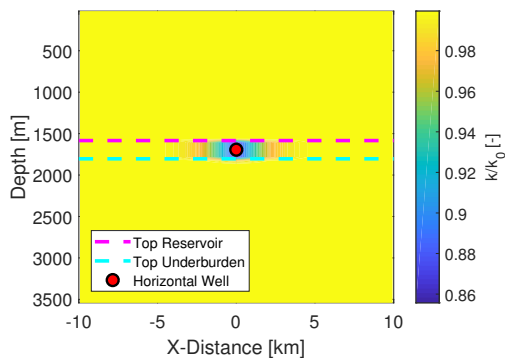
Figure 2.2 – Permeability reduction in a reverse faulting stress regime. Note that the permeability reduction in each stress regime is identical because the mean stress changes, which control permeability loss, are the same in each stress regime.

2.4.1 Compaction's Effect

The permeability loss during production can be seen for a reverse faulting stress regime in Figure 2.2. The permeability loss is concentrated around the wellbore where the largest mean effective stress changes have occurred. This is also representative of the permeability loss in the other stress regimes.

Normal Faulting Stress Regime ($S_z > S_x > S_y$)   In a normal faulting stress regime, production from a horizontal well results in a negative Coulomb stressing rate near the well (due to a decrease in pore pressure and the fact that the stress path in this particular case is low enough, ≈ 0.44, such that this area is stable (Zoback and Zinke, 2002)) and above and below the well (due to an increase in the least principal stress, which is horizontal). At the edges of the reservoir and far from the well, however, the induced stress changes have a more significant impact than the pore pressure changes (Segall and Lu, 2015; Chang and Segall, 2016a,b; Goebel *et al.*, 2017b). This results in an increase in Coulomb stressing rate (Figure 2.3a) and ultimately seismicity rate (Figure 2.3b) in these regions, in agreement with previous models (Segall, 1989).

In the case that the permeability decreases due to compaction during production, a higher pore pressure gradient is required near the wellbore to produce the fluid and the pore pressure perturbation travels more slowly to the edges of the reservoir. This results in a higher pore pressure at the edges of the reservoir, resulting in a higher Coulomb stressing rate (Figure 2.3c). This effect is mitigated by the fact that less tension is induced in the x and y-directions, an effect which reduces the Coulomb stressing rate because S_y is the minimum principal stress. Above and below the reservoir, the stress changes are larger due to the higher pore pressure gradient required to produce the fluid. As these stresses were stabilizing in this stress regime, the seismicity model still predicts that these areas will not experience induced seismicity. Ultimately, this permeability loss moderately increases the resulting seismicity rate in areas that were already at risk (Figure 2.3d).
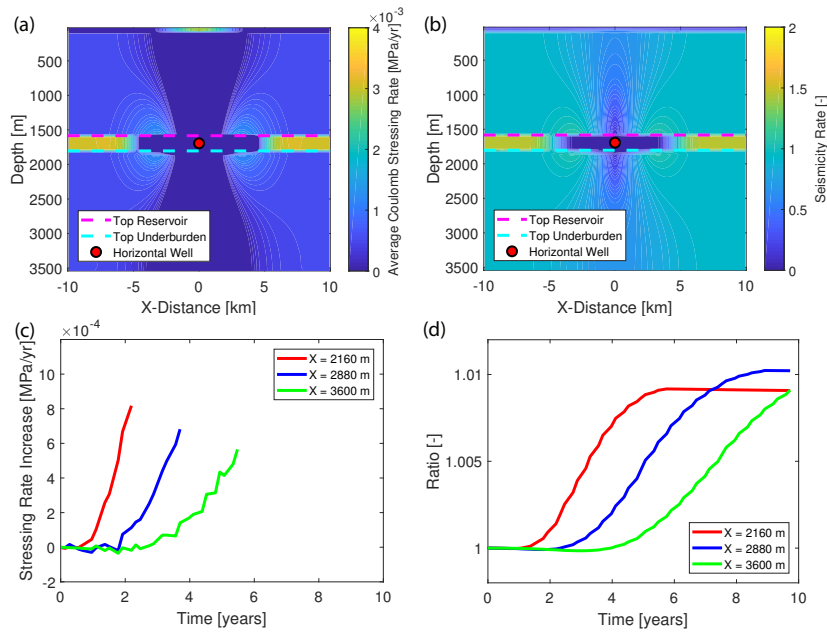
Figure 2.3 – Normal faulting stress regime a) average Coulomb stressing rate over 10 years due to fluid production without considering the permeability loss due to compaction. b) the predicted seismicity rate after 10 years without considering the permeability loss due to compaction. c) the difference in Coulomb stressing rate when permeability loss is considered. Locations are at the same depth as the well. A value above zero represents the amount stressing rate has increased between the case when permeability loss is considered and when it is not. The entirety of Coulomb stressing rate change is not plotted because after a given amount of time the Coulomb stressing rate in the original case (with no permeability loss) becomes negative, due to the decrease in pore pressure. Therefore, only times with positive original Coulomb stressing rate are plotted. d) the ratio of the cumulative seismicity rate between the case where permeability loss is considered and when it is not at three locations at the same depth as the well. A ratio higher than one means that the seismicity rate has increased.
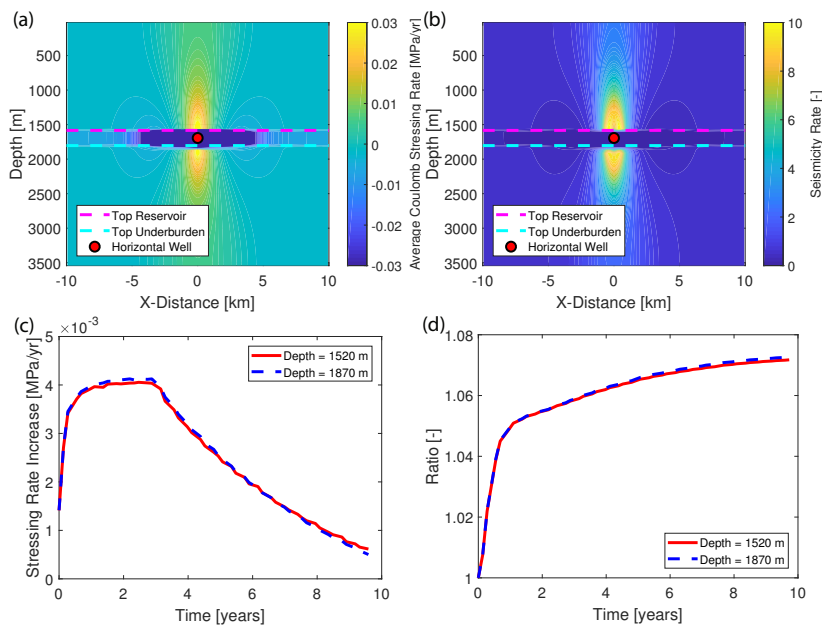
Figure 2.4 – Reverse faulting stress regime a) average Coulomb stressing rate over 10 years due to fluid production without considering the permeability loss due to compaction. b) the predicted seismicity rate after 10 years without considering the permeability loss due to compaction. c) the difference in Coulomb stressing rate when permeability loss is considered at two locations vertically in-line with the well. A value above zero represents the amount stressing rate has increased between the case when permeability loss is considered and when it is not. d) the ratio of the cumulative seismicity rate between the case where permeability loss is considered and when it is not at two locations vertically in-line with the well. A ratio higher than one means that the seismicity rate has increased.

Reverse Faulting Stress Regime ($S_x > S_y > S_z$)   Production from a horizontal well in a reverse faulting stress regime results in a negative Coulomb stressing rate throughout the reservoir (Figure 2.4a). This is due to decreases in pore pressure and the maximum principal stress. Above and below the reservoir, the maximum principal stress increases. This, combined with a decrease in the vertical stress and a slight increase in pore pressure due to poroelastic effects, results in an increase in Coulomb stressing rate (Figure 2.4a) and ultimately seismicity rate in these locations in this stress regime (Figure 2.4b).

When compaction-induced permeability loss is considered, however, the pressure gradients required to move fluid into the wellbore are larger. These larger pore pressure gradients result in larger total stress changes being induced, leading to a larger Coulomb stressing rate (Figure 2.4c), and ultimately a larger seismicity rate (Figure 2.4d) in the already seismically prone regions above and below the reservoir.

Strike-slip Faulting Stress Regime ($S_x > S_z > S_y$)   In a strike-slip faulting stress regime, the decrease in pore pressure acts to stabilize the reservoir. Within the reservoir, the tensile
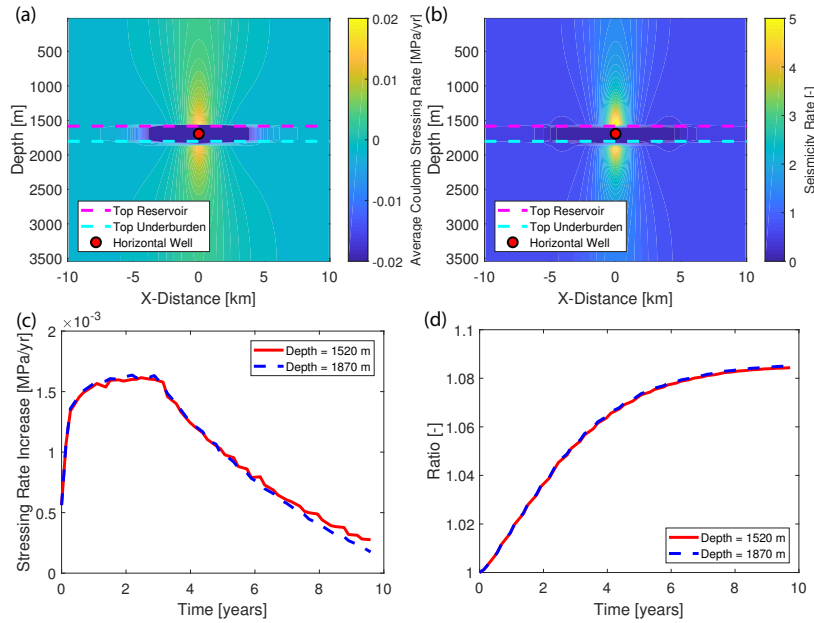
Figure 2.5 – Strike-slip faulting stress regime a) average Coulomb stressing over 10 years due to fluid production without considering the permeability loss due to compaction. b) the predicted seismicity rate after 10 years without considering the permeability loss due to compaction. c) the difference in Coulomb stressing rate when permeability loss is considered at two locations vertically in-line with the well. A value above zero represents the amount stressing rate has increased between the case when permeability loss is considered and when it is not. d) the ratio of the cumulative seismicity rate between the case where permeability loss is considered and when it is not at two locations vertically in-line with the well. A ratio higher than one means that the seismicity rate has increased.

changes to S_x are larger than those to S_y far from the well, meaning that the stress changes also result in a decreased Coulomb stressing rate as long as the well is drilled parallel to S_{hmin}. Above and below the reservoir, the compressive changes to S_x are larger than those to S_y, meaning that Coulomb stressing rate is increased in the case that the well has been drilled parallel to S_{hmin} (Figure 2.5a), resulting in an increase in seismicity rate (Figure 2.5b).

By considering compaction-induced permeability loss the stress changes occurring above and below the reservoir are increased. This results in a larger Coulomb stressing rate (Figure 2.5c) and ultimately seismicity rate in these locations (Figure 2.5d).

2.4.2 Inelastic Compaction

The previous sections have shown how even the permeability loss associated with near-elastic compaction is significant enough to influence induced seismicity rates. Here, the strike-slip faulting stress regime example will be repeated, this time initializing stresses using the concept of a critically-stressed crust (Brudy *et al.*, 1997; Townend and Zoback, 2000; Zoback

and Townend, 2001; Zoback *et al.*, 2002), meaning that the frictional strength of supposed optimally oriented, pre-existing faults limit the differential stress (Zoback and Healy, 1992; Brudy *et al.*, 1997; Zoback and Harjes, 1997), after assuming that the vertical stress can be found using the lithostatic gradient. The minimum principal total stress was assumed to be 0.8 times the vertical total stress (Zoback, 2007). This results in a stress state in the reservoir which is initially on the border between near-elastic and inelastic compaction (Figure 2.6a). Therefore, when production begins, the reservoir will begin compacting inelastically, allowing for a comparison between the case where the compaction occurs near-elastically and the case where the compaction occurs inelastically. The permeability loss in the inelastic domain is modelled as ten times larger than the permeability loss that would have been seen in the near-elastic domain, up until a maximum permeability loss of 90%, or one order of magnitude, agreeing with laboratory data on inelastic compaction-induced permeability loss (David *et al.*, 1994; Zhu and Wong, 1996; Boutéca *et al.*, 2000; Chan and Zoback, 2002; Fortin *et al.*, 2005; Baxevanis *et al.*, 2006). Note that the poroelastic mechanical model is still employed, meaning that strains in the reservoir will be underestimated (Pijnenburg *et al.*, 2018) and the results will represent a conservative estimate of the effect of inelastic compaction on strains, although stress changes may be overestimated. In this case the loading path is one directional, as the reservoir will not be unloading, meaning there is no need for plasticity.

The permeability loss in this simulation for both the near-elastic and inelastic case can be seen in Figure 2.6b. Note that due to the large permeability loss in the inelastic case, large drawdowns are needed to maintain the same flow rate as in the near-elastic case. Due to this large drawdown, the flow rate can not be maintained for the full period of ten years. As comparing the two simulations at differing flow rates would make a fair comparison difficult, both simulations were run using the same poroelastic flow model and were stopped after approximately 1.5 years.

In Figure 2.6c the difference in stressing rate between the near-elastic and inelastic compaction cases is shown. It can be seen that, in the case that the permeability loss is inelastic, the Coulomb stressing rate is over double the stressing rate associated with near-elastic compaction shown in Figure 2.5. This increase in stressing rate is then responsible for an increase in seismicity rate by over a factor of two as shown in Figure 2.6d. Although not shown, similar results can also be obtained for inelastic permeability loss in a reverse faulting stress regime.

2.4.3 Well Orientation

As shown in Figure 2.6a, differential stress has implications for the type of compaction experienced by a production reservoir. As the stress changes occurring due to fluid production are not isotropic, the direction that the well is drilled in will have implications for the differential stress throughout the reservoir/caprock/underburden system and will ultimately effect the type of compaction experienced by the reservoir. Because the stress changes occurring near the wellbore are the largest in magnitude, it is especially important to understand in
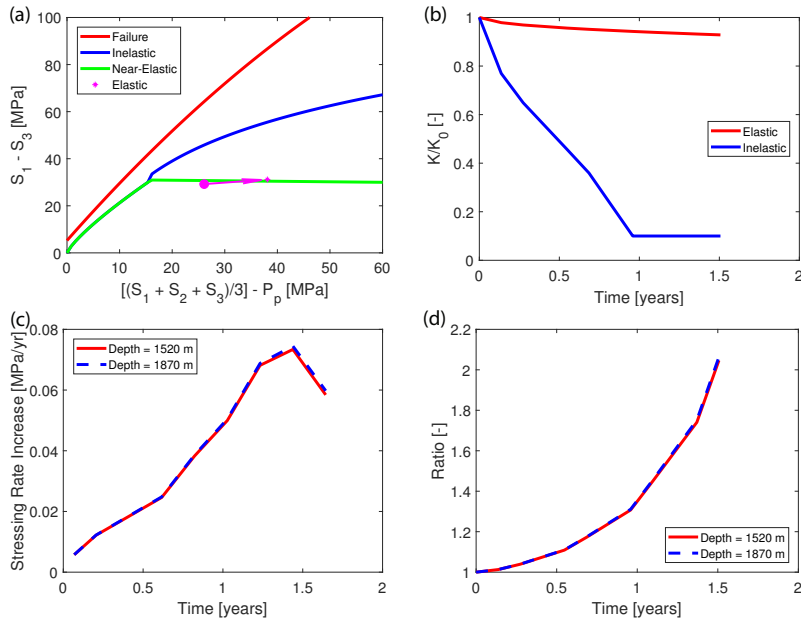
Figure 2.6 – A comparison of the effects of inelastic and near-elastic permeability loss for a strike-slip faulting case. (a) An example of the change in differential and mean effective stresses occurring during 10 years of production with near-elastic permeability loss only. The point represents the initial stress state and the star represents the stress state after 10 years of production. The bounding lines are based on Schutjens *et al.* (2004). Below the green bounding line the compaction is near-elastic. Then, up to the blue line the compaction is inelastic. Above the blue line is the failure domain. It can be seen that compaction passes into the inelastic domain during production. Therefore, the simulation is rerun considering inelastic permeability loss. The rerun simulations consider a period of 1.5 years. (b) The permeability loss near the wellbore depending on whether or not near-elastic or inelastic permeability loss is considered. (c) The increase in Coulomb stressing rate when inelastic permeability loss is considered (as opposed to just near-elastic permeability loss). The two locations used are vertically in-line with the producing well. A value above zero represents the amount stressing rate has increased between the case when inelastic permeability loss is considered and when it is not. It can be seen that inelastic permeability loss results in a Coulomb stressing rate which is significantly higher than the Coulomb stressing rate in the near-elastic case. (d) The ratio of the cumulative seismicity rate for the two types of permeability loss at two locations vertically in-line with the producing well. It can be seen that inelastic permeability loss results in a seismicity rate which is twice as high.

which direction the largest stress changes are occurring in this area. To do this, to begin with, Equation 2.3 can be written out for S_{xx} and S_{yy} as

$$S_{xx} = \alpha P + \frac{E}{(1+\nu)(1-2\nu)}\left[(1-\nu)\epsilon_{xx} + \nu\epsilon_{zz}\right] \tag{2.7}$$

and

$$S_{yy} = \alpha P + \frac{E}{(1+\nu)(1-2\nu)}\left[\nu\epsilon_{xx} + \nu\epsilon_{zz}\right]. \tag{2.8}$$

The difference between the two total stresses is therefore

$$S_{xx} - S_{yy} = \frac{E}{(1+\nu)(1-2\nu)}(1-2\nu)\epsilon_{xx}. \tag{2.9}$$

Because Young's modulus is positive and Poisson's ratio generally has a value between 0 and 0.5 (Gercek, 2007), changes to S_{xx} will be more tensile than those to S_{yy} when ϵ_{xx} is negative and less tensile when ϵ_{xx} is positive. From Figure 2.7a it can be clearly seen that ϵ_{xx} is positive near the well and negative far from the well during fluid production. This implies changes to S_{xx} will be less tensile near a producing horizontal well and more tensile far from a horizontal well than changes to S_{yy}.

Because the largest mean effective stress changes occur near the well, the area closest to the well is the most likely to experience compaction, especially inelastic compaction, through mechanisms such as grain sliding and rotation, intragranular cracks, shear band formation, and cement breakage (Zhu and Wong, 1996; Schutjens *et al.*, 2004). The onset of inelastic compaction is dependent on differential stress (Zhu and Wong, 1997; Schutjens *et al.*, 2004; Baxevanis *et al.*, 2006). The fact that production will induce total stress changes which are less tensile in S_{xx} than in S_{yy} near the wellbore therefore has implications for optimal wellbore orientation if inelastic compaction is to be avoided.

In a normal faulting stress regime, S_{hmin} is the minimum principal stress. A reduction in the minimum stress results in an increase in differential stress. Higher differential stresses lead to more inelastic compaction (Zhu and Wong, 1997; Schutjens *et al.*, 2004; Baxevanis *et al.*, 2006). For this reason, a horizontal well should be ideally drilled in the direction that reduces S_{hmin} by the least amount if inelastic compaction near the well is to be avoided. Based on the above analysis, this means horizontal wells should be drilled parallel to S_{Hmax} (S_2) in a normal faulting stress regime. Indeed, this can be seen to be the case in Figure 2.7b, where the

initial normal faulting stress regime case from Section 2.4.1 is compared to the case where the well is drilled parallel to S_{Hmax}.

S_{Hmax} is the maximum principal stress in a reverse faulting stress regime. A decrease in the maximum principal stress decreases the differential stress. As mentioned, to avoid inelastic compaction it is preferable to keep the differential stress low. Therefore, if the goal is to minimize inelastic compaction near the well, horizontal wells in reverse faulting stress regimes should be drilled parallel to S_{Hmax} (S_1) such that S_{Hmax} is reduced more than it would have been with any other orientation of horizontal well. Note that, because there is more tension induced in the horizontal directions than in the vertical direction during production from a horizontal well, the differential stress is expected to decrease regardless of the well orientation during production. This can be seen in Figure 2.7c, where the initial reverse faulting stress regime case from Section 2.4.1 is compared to the case where the well is drilled parallel to S_{Hmax}.

Finally, in a strike-slip faulting stress regime, S_{Hmax} is the maximum principal stress and S_{hmin} is the minimum principal stress. In order to keep the differential stress from increasing such that inelastic compaction can be avoided, a horizontal well should be drilled parallel to S_{Hmax}, as can be seen in Figure 2.7d, where the initial strike-slip faulting stress regime case from Section 2.4.1 is compared to the case where the well is drilled parallel to S_{Hmax}.

2.5 Discussion

The results qualitatively show that compaction associated with depletion has the indirect effect of increasing the induced poroelastic stresses in areas which are likely to experience induced seismicity, even when that compaction remains near-elastic. This is caused by the decrease in permeability in areas experiencing large effective stress increases, such as near the well, which result in larger required pore pressure gradients which cause larger induced stress changes and therefore induced seismic activity. This shows the possible positive impact pressure management, whether that be through fluid injection or other means, could have on fields experiencing large pressure drops. In fact, limiting pressure drawdown has been shown to limit the permeability and productivity loss associated with compaction (Raghavan and Chin, 2002).

The results were shown here for horizontal wells. In reality, many fluid production wells are vertical. Qualitatively, however, it is likely that permeability loss around vertical wells is also capable of resulting in increased seismicity rates. The results regarding well orientation and inelastic compaction are not directly applicable to vertical wells. However, the stress changes due to production from a vertical well will not be isotropic at any given location away from the wellbore (e.g., Segall and Lu (2015)). Therefore, it is possible that inelastic permeability loss may be more likely to occur along an axis in the direction of S_{hmin}. This is because changes in stress at a given location are larger in the radial direction than in the tangential direction. A larger reduction in S_{hmin} relative to S_{Hmax} will result in larger differential stresses for normal
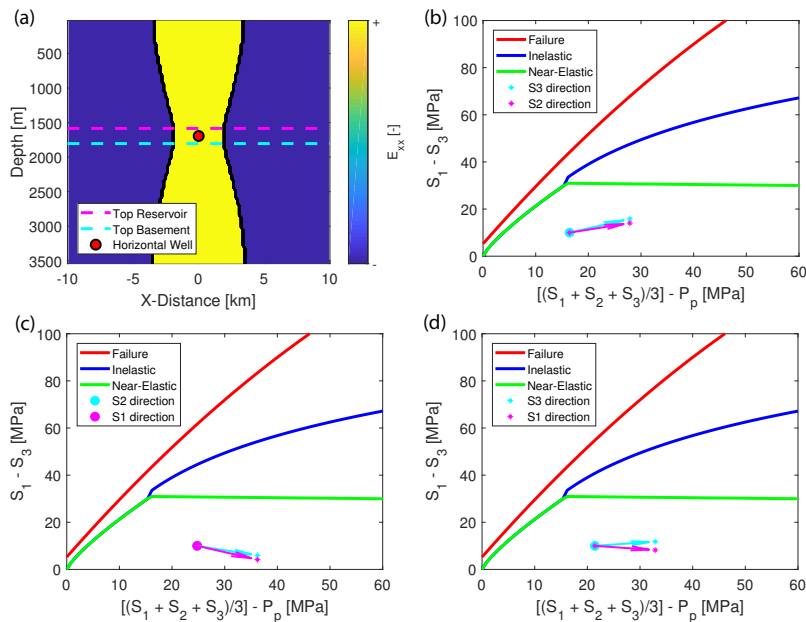
Figure 2.7 – a) Areas where ϵ_{xx} is positive marked in yellow and negative marked in blue. A positive ϵ_{xx} means that tensile changes to S_{xx} will be smaller than those to S_{yy}. b-d) Differential stress versus mean effective stress next to the horizontal well for a normal (b), reverse (c), and strike-slip (d) faulting stress regime. The points represent the initial stress state and the stars represent the stress state after 10 years of production. The bounding lines are based on Schutjens *et al.* (2004). Below the green bounding line the compaction is near-elastic. Then, up to the blue line the compaction is inelastic. Above the blue line is the failure domain. It can be seen in each case that drilling parallel to S_{Hmax} results in less differential stress in this area.

and strike-slip faulting stress regimes. Note that in a normal faulting stress regime in both directions there will be an increase in differential stress but this reduction will be larger in the direction of S_{hmin}. As shown above, larger differential stresses are expected to lead to inelastic compaction. For reverse faulting stress regimes, the differential stress is expected to reduce in all directions.

There is thought to be no correlation between static stress changes less than 0.01 MPa and increased seismicity (Beeler and Lockner, 2003). However, although the Coulomb stress differences caused by compaction-induced permeability loss are small, even during near-elastic compaction in this numerical experiment the differences (compared to when no permeability loss is considered) are larger than the 0.01 MPa stress changes which have been shown to strongly correlate with the timing of stick-slip events (Stein, 1999), suggesting that the stress differences caused by compaction-induced permeability loss are significant enough to lead to an increase in induced seismicity. In depletion-induced seismicity, for example, Coulomb stress changes on the order of 0.01 MPa were enough to trigger a M_w 5.1 earthquake near Lorca, Spain (González *et al.*, 2012). Further, in Clinton County, Kentucky, a 0.02 MPa stress change induced microseismicity in the Seventy-Six oil field (Rutledge *et al.*, 1998). Although Coulomb stress changes are not a perfect predictor of seismicity (Beeler and Lockner, 2003), they do give the indication, at least qualitatively, that the permeability loss associated with depletion is capable of indirectly inducing seismicity.

Additionally, earthquakes being triggered by small changes in Coulomb stress are further evidence of a critically-stressed crust. Even intraplate areas, which can frequently be aseismic, are thought to be critically stressed (Townend and Zoback, 2000). A critically-stressed crust not only has implications for intraplate and induced seismicity, but also compaction. The vertical stress can generally be assumed to be fixed by the overburden (Zoback, 2007). This then means that the coefficient of friction and the presumed hydrostatic pore pressure can be used in combination with the Mohr-Coulomb failure criteria of an optimally oriented fault to determine the maximum principal stress in a reverse faulting stress regime and the minimum principal stress in a normal faulting stress regime. The result of this is that, at a given depth, the reverse faulting stress regime will be predicted to be supporting more differential stress. As many authors have found that differential stress is an important determining factor in the onset of inelastic compaction (e.g., Delage *et al.* (1996); Zhu and Wong (1997); Hettema *et al.* (2000); Chan and Zoback (2002); Schutjens *et al.* (2004); Baxevanis *et al.* (2006)), this implies that rocks in reverse faulting stress regimes are more likely to begin compacting inelastically than those in normal faulting stress regimes at a given depth.

Usually, induced seismicity is discussed for intraplate regions. This is generally because induced seismicity is easier to distinguish from natural seismicity in these regions than in interplate regions. This is in part due to the fact that the smaller stressing rates in these regions mean less events are needed to detect the effect of industrial activities (Beeler and Lockner, 2003). Additionally, intraplate regions are generally less prepared for the effects of induced seismicity as seismicity in these regions is generally not commonplace, meaning any

anthropogenic earthquakes are likely to gain significant attention.

In this context, the Coulomb stressing rates caused by depletion seen in some of the stress regimes modelled here are not small. In fact, the Coulomb stressing rate seen in the reverse faulting stress regime case (in the first year approximately 0.1 MPa/yr and on average over 0.03 MPa/yr, Figure 2.4c) is on the order of magnitude of the stress rates seen in the most active sections of the San Andreas fault (Smith-Konter and Sandwell, 2009). This shows how even intraplate areas can experience induced seismicity despite being previously seismically quiet. Also, the increase in stressing rate seen when near-elastic compaction-induced permeability loss is included (in this experiment up to 4e-3 MPa/yr) is itself on the order of the smallest stressing rates seen along the San Andreas Fault System (Smith-Konter and Sandwell, 2009), despite the permeability loss remaining entirely in the near-elastic range during the simulations. In fact, this permeability loss effect represents a stressing rate increase which is over an order of magnitude larger than typical stressing rates in intraplate regions, which are generally less than 1e-4 MPa/yr (Calais *et al.*, 2016), meaning that compaction-induced permeability loss's effect on stressing rate is large enough (Parsons, 2005) to have significant induced seismicity implications. Additionally, inelastic compaction-induced permeability loss has been shown here to be capable of inducing stress changes of over 0.1 MPa/yr, meaning this mechanism is capable of doubling the stressing rate associated with production, highlighting the importance of understanding how the reservoir rock compacts and how applied production strategies affect the nearby pore pressures and stresses.

These results fit well with the combination of notions that lower permeabilities necessitate larger pore pressure gradients to produce fluids and larger pore pressure gradients induce larger stress changes. Indeed, there is certainly evidence of larger poroelastic stress changes being induced for higher pore pressure gradients both numerically (Chang and Segall, 2017) and in the field (Holzer *et al.*, 1983; Rutledge *et al.*, 1998; Bou-Rabee and Nur, 2002), when one considers that loading rate is directly proportional to depletion rate, which is generally proportional to production rate (Lahaie and Grasso, 1999). This is further supported by the observation that subsidence depends on diffusivity (Segall, 1985).

Fields that would be likely to benefit from pressure management in terms of induced seismicity are fields which experience significant permeability loss due to an increase in mean effective stress, especially in fields located in reverse and strike-slip faulting stress regimes. However, it should be noted that an increase in water saturation, which would be associated with water injection for pressure maintenance, may actually increase subsidence in certain cases due to capillary effects, as demonstrated for hydrocarbon production-induced subsidence (Delage *et al.*, 1996; Simoni *et al.*, 1999; Menin *et al.*, 2008; Santagiuliana *et al.*, 2015). It has also been shown to be capable of contributing to subsidence by decreasing the reservoir rock strength (Chin and Nagel, 2004). Additionally, compaction is not necessarily an occurrence that only has negative consequences as, while reservoir compaction generally decreases the permeability and, as shown, can increase the chance of inducing seismicity, it can also help to drive the production of pore fluids through compaction drive (Dake, 1978; Schutjens *et al.*,

2000).

As previously shown, in certain stress regimes, seismicity can be induced above and below the producing reservoir. In this model, this means that this seismicity is occurring in shales. Although shales can exhibit seismic slip, they are generally aseismic in nature (Ikari *et al.*, 2009). In reality, however, other lithologies which are likely to slip seismically may be present in these locations. Although the different parameters associated with these lithologies may change the results slightly, the key finding about the indirect increase in seismicity due to permeability reduction still holds.

During the first part of this numerical experiment, permeability changes were modelled based on the assumption that the reservoir remained in the near-elastic domain, meaning the permeability changes near the well were quite small ($\approx 15\%$). However, in reality, with continued production, it is probable that the reservoir would begin to deform inelastically, especially in deeper reservoirs. In this case, the permeability loss would likely be more extreme (potentially more than an order of magnitude) (David *et al.*, 1994; Zhu and Wong, 1996; Boutéca *et al.*, 2000; Chan and Zoback, 2002; Fortin *et al.*, 2005; Baxevanis *et al.*, 2006), and induced stress changes at the edges of, above, and below the reservoir would be more significant, resulting in higher seismicity rates. This was shown to be the case in Section 2.4.2. Therefore, generally, it is desirable to avoid inelastic compaction as it can not only lead to large permeability loss in highly porous sandstones (Zhu and Wong, 1996, 1997; Boutéca *et al.*, 2000; Fortin *et al.*, 2005; Baxevanis *et al.*, 2006), but also the formation of flow barriers in the form of shear bands (Zhu and Wong, 1996), surface subsidence (Schutjens *et al.*, 2000), possible casing damage (Schutjens *et al.*, 2000), and sand production (Baxevanis *et al.*, 2006; Hettema *et al.*, 2006). Certainly, when a critical pressure is reached, the onset of grain crushing and pore collapse may cause severe permeability loss (Brace, 1978; David *et al.*, 1994) and subsidence (Hettema *et al.*, 2002) in porous rocks. Indeed, subsidence is generally more severe in younger, high porosity, poorly cemented rocks (Hettema *et al.*, 2002). Conversely, in some cases, inelastic compaction may actually result in less permeability reduction (David *et al.*, 1994) or even entail permeability enhancement in low porosity rocks (Zhu and Wong, 1996; Boutéca *et al.*, 2000) and high porosity chalks (Teufel *et al.*, 1991), so care should be taken to evaluate each reservoir thoroughly when compaction effects are being considered. An example of this type of permeability increase has been seen in the Lacq gas field, Southwestern France, where depletion caused the reservoir permeability to increase to 20 times its original value (Rolando *et al.*, 1997).

Many authors agree that elastic compaction-induced permeability reduction is based on mean effective stress (Zhu and Wong, 1996, 1997; Schutjens *et al.*, 2004; Fortin *et al.*, 2005; Baxevanis *et al.*, 2006), albeit not always agreeing that this relationship is linear. Whether or not this compaction is elastic or not, however, is also dependent on differential stress (Delage *et al.*, 1996; Zhu and Wong, 1997; Hettema *et al.*, 2000; Chan and Zoback, 2002; Schutjens *et al.*, 2004; Baxevanis *et al.*, 2006). The mean effective stress changes in the reservoir will not be influenced by the direction of the horizontal well, but the differential stress will be. This

means that, if the goal is to avoid inelastic deformation, the orientation that horizontal wells are drilled in is significant. Specifically, because induced poroelastic stress changes near the wellbore are less tensile perpendicular to the direction of the horizontal well than parallel to the direction of the horizontal well, wells should be drilled parallel to the maximum horizontal stress in order to avoid inelastic compaction. It should be noted that this is perpendicular to the direction horizontal wells are generally drilled in for hydraulic fracturing, based on the principles outlined by Hubbert and Willis (1957), and, while also optimal in terms of wellbore stability for reverse and strike-slip faulting stress regimes, this well orientation is the least stable orientation of a horizontal well in a normal faulting stress regime (Zoback, 2007). Further, this does not mean that these well directions are optimal in terms of induced seismicity, just that they help to prevent depletion-induced compaction from becoming inelastic.

Although this work shows how compaction-induced permeability loss could lead to higher rates of induced seismicity, it does not necessarily imply that compaction-induced permeability loss is the link connecting subsidence and induced seismicity nor that the onset of permeability loss associated with compaction is required for induced seismicity. Instead, the stress changes caused by compaction-induced permeability loss show that it is a potential, but not prerequisite, mechanism for increasing the induced stress changes that lead to induced seismicity. These results will have implications for producing reservoirs which are likely to experience induced seismicity, especially those which have already shown the first signs of compaction.

2.6 Conclusions

Depletion-induced compaction results in permeability loss that is not only detrimental to the inflow performance of producing wells, it also leads to larger total stress changes caused by fluid production, which, in turn, lead to a larger chance of failure on faults which are well-positioned for slip. This previously unconsidered effect of depletion-induced compaction is therefore another aspect that can be considered while making pressure management decisions for fluid-producing reservoirs. Additionally, these results have implications for the optimal orientation of horizontal producing wells, suggesting that they should be drilled parallel to S_{Hmax} to reduce the chance of inelastic compaction occurring in the vicinity of the wellbore, a mechanism which has been shown here to be capable of further worsening induced seismicity should it not be avoided.

The results here also highlight the need for depletion-induced seismicity prediction models to account for permeability loss associated with compaction, especially when this permeability loss is inelastic. Additional insight could also be obtained with a model capable of accurately considering inelastic strains.

3 High stress path reservoirs and temperature-induced stress preconditioning

The results of this chapter are published in:

Journal paper:

Fryer, B., Siddiqi, G., and Laloui, L. (2020). Injection-induced seismicity: Strategies for reducing risk using high stress path reservoirs and temperature-induced stress preconditioning. *Geophysical Journal International*, **220**, 1436-1446 https://doi.org/10.1093/gji/ggz490.

Contribution of candidate: Initial idea, development of theory, analysis of results, writing of manuscript.

3.1 Chapter Summary

It is suggested that fluid injection in normal faulting stress regimes can stabilize a reservoir if the stress path is high enough. This stabilization is not seen when the reservoir is significantly cooled as a result of injection. Further, a new strategy is suggested for stimulating reservoirs in shear with a reduced chance of inducing a large magnitude seismic event. The version of this methodology presented here is applicable for reverse faulting stress regimes and involves an initial stress preconditioning stage where the reservoir is cooled and the pressure increase is limited. This process reduces the horizontal total stress and thereby also the differential stress. Next, the reservoir is stimulated with a rapid increase in pore pressure, resulting in shear failure at a lower differential stress than was initially present in the reservoir. Due to the connection seen between the Gutenberg-Richter b-value and differential stress, it is suggested that reservoirs stimulated in this fashion will exhibit higher b-values and thereby also have a reduced chance of hosting a large magnitude event. It is suggested that adaptations of this methodology are applicable to both normal and strike-slip faulting stress regimes.

3.2 Introduction

Induced seismicity has become a relevant topic in many different industries in recent years, especially in fluid injection operations Foulger *et al.* (2018). Indeed, injection operations such as Carbon Capture and Store (CCS) (e.g., Zoback and Gorelick (2012)), wastewater injection (e.g., Ellsworth (2013)), hydraulic fracturing (e.g., Skoumal *et al.* (2018)), and Enhanced Geothermal System (EGS) stimulation are all liable to induce seismicity. Induced seismicity can be of serious public concern and is capable of leading to a failed project purely due to societal pressure.

Induced seismicity in particular has proven to be a significant issue for EGS, for example. Hydraulic stimulation famously induced felt seismicity in the city of Basel, Switzerland in late 2006 Häring *et al.* (2008). This proved to be a major setback to Swiss geothermal ambitions. More recently, a magnitude 5.4 earthquake was induced in Pohang, South Korea Grigoli *et al.* (2018); Kim *et al.* (2018), to the surprise of many who did not expect such a large magnitude earthquake due to such a small amount of injected fluid. It is likely that the Pohang event, like the Basel seismicity before it, will have significant implications for the EGS industry. It is therefore essential that methodologies are developed that mitigate the seismic risk associated with EGS and geothermal in general. The same can also be said for wastewater injection and especially CCS, which, given its fledgeling nature, would also suffer heavily as an industry from a large induced earthquake.

The primary mechanism thought to be responsible for induced seismicity in these injection-based industries is an increase of pore pressure associated with injection (e.g., Ellsworth (2013)). Other mechanisms, such as poroelastic stressing (e.g., Chen *et al.* (2017)), temperature effects (e.g., Rutqvist *et al.* (2016b)), and pore fluid pressure oscillations (e.g., Noël *et al.* (2019b)) are also capable of inducing seismicity, however.

Rather counter-intuitively, earthquakes have also been induced in fluid production scenarios where pore pressure has decreased Suckale (2009). These earthquakes generally occur outside of the reservoir and are due to the poroelastic stressing associated with the production of fluid Segall (1989). There are exceptions to this general rule, as earthquakes have also been induced within the producing reservoir, despite the decrease in pore pressure. Examples include the Groningen gas field Dost *et al.* (2012), the Eleveld gas field Begeleidingscommissie Onderzoek Aardbevingen (1993), the Valhall and Ekofisk oil reservoirs Teufel *et al.* (1991); Rutledge *et al.* (1994); Zoback and Zinke (2002), and the War-Wink gas field Zoback and Zinke (2002). These earthquakes are a result of a high stress path in a normal faulting stress regime Teufel *et al.* (1991); Segall and Fitzgerald (1998); Chan and Zoback (2002); Zoback and Zinke (2002). The term stress path here corresponds to the ratio of change in horizontal total stress to the change in pore pressure. As pore pressure decreases, horizontal total stress decreases as a result of poroelasticity (the vertical total stress remains fairly constant in laterally extensive reservoirs). In a normal faulting stress regime, the minimum principal stress is horizontal. As such, this reduction of horizontal total stress results in an increase in differential stress. In the event

that the horizontal total stress change is larger than 0.67 times the pore pressure changes, optimally-oriented normal faults will be destabilized despite the decreasing pore pressure for a standard coefficient of friction Chan and Zoback (2002).

An interesting implication of these high stress path production-induced earthquakes is that, in these cases, pore pressure increases should increase stability. For this reason, high stress path reservoirs may be attractive for injection operations. Therefore, this semi-analytical investigation will concern fluid injection into high stress path reservoirs. Of course, in certain cases such as geothermal reservoirs and CO_2 sequestration, changes of temperature are also significant and will be included here in a following section.

Conversely, in certain situations fault/fracture shear is unavoidable and some level of seismicity will be induced. Indeed, the mechanism by which stimulation occurs in many EGS stimulations is essentially the same as that in induced earthquakes, shear failure. Recently there has been an increased focus on soft stimulation (e.g., Hofmann *et al.* (2018)), whereby an effort is made to encourage the shear failure required for reservoir stimulation and avoid the shear failure associated with large magnitude induced seismicity. In this sense, a stimulation technique which lends itself to the induction of small seismic events and not large ones would represent a major step forward for the EGS industry.

In the Northwest Geysers EGS Demonstration Project, shear stimulation was performed via the combined effects of temperature-induced total stress changes and pore pressure increases Rutqvist *et al.* (2016b). Specifically, a large period of time (approximately one year) was taken to allow for a significant temperature drop in the near-wellbore region whilst limiting the pressure increase in the reservoir Rutqvist *et al.* (2016b). As mentioned in Rutqvist *et al.* (2016b); Vilarrasa (2016) and further discussed in the following sections, the total stress changes associated with fluid-injection induced temperature changes can be anisotropic. This is especially true when injection occurs from a horizontal well and even more so when the reservoir is laterally extensive. Due to this anisotropy, it is suggested here that it is possible to design a stimulation treatment that begins with a long period of injection-induced temperature change with the goal of reducing the differential stress in the reservoir, preconditioning the stress. During this stress-preconditioning phase, as in the above-mentioned Northwest Geysers EGS Demonstration Project, the pore pressure increase is limited such that shear failure is avoided. Then, after this period of temperature change, a short period of high-rate injection occurs with the goal of increasing the pore pressure. This second phase induces shear failure on the optimally-oriented faults/fractures in the reservoir. Importantly, the shear failure that occurs on faults/fractures when following this methodology occurs on shear planes that are supporting less differential stress than they would have been had the reservoir been stimulated without the first phase of temperature change.

The advantage of maintaining a low differential stress comes from the connection seen between differential stress and the Gutenberg-Richter *b*-value Amitrano (2003); Schorlemmer *et al.* (2005); Narteau *et al.* (2009); Gulia and Wiemer (2010); Goebel *et al.* (2013); Spada *et al.*

(2013); El-Isa and Eaton (2014); Scholz (2015); Wu *et al.* (2018). This correlation is well accepted, albeit poorly constrained Gischig *et al.* (2014); El-Isa and Eaton (2014). In fact, the dependence of *b*-value on state of stress has long been known Scholz (1968). Further evidence of this relationship can be seen in induced seismicity data sets (e.g., Pearson (1981); Häring *et al.* (2008); Goertz-Allmann *et al.* (2011); Layland-Bachmann *et al.* (2012); Goertz-Allmann and Wiemer (2013); Kwiatek *et al.* (2014); Dohmen *et al.* (2017)). This connection implies that, by maintaining a low differential stress, a high *b*-value will be seen during stimulation. A high *b*-value results in more low magnitude seismic events and relatively few large magnitude events that might pose a nuisance to the public, or even cause damage. In this way, EGS reservoir stimulation can still be performed, inducing shear failure on pre-existing planes of weakness, with a lower risk of inducing large events. In this work the potential of this strategy will also be investigated.

This work will be divided into three parts. First, in Section 3.3.1, the possibility of using high stress path reservoirs for isothermal fluid injection such that the risk of induced seismicity is reduced will be evaluated. Next, in Section 3.3.2, a similar investigation will be carried out except this time including the temperature effects that would be associated with injection into a geothermal reservoir. Finally, in Section 3.4, the possibility of preconditioning the stress field of a reservoir by first cooling it will be investigated with the goal of inducing shear failure at a relatively low differential stress, such that the risk of a large seismic event is reduced. These investigations will be carried out using poroelastic and thermoelastic solutions for laterally extensive reservoirs. In Section 3.4, the general relationship between differential stress and Gutenberg-Richter *b*-value will also be incorporated.

3.3 Injection Into High Stress Path Reservoirs

3.3.1 Isothermal Injection

As an initial evaluation of the seismic risk associated with injection into high stress path reservoirs, a semi-analytical approach is taken for a normal faulting stress regime. An example depth of 4000 m is taken, a reasonable depth for deep geothermal for example. At this depth, using standard lithostatic and hydrostatic gradients, the vertical total stress, S_v, and pore pressure, P_p, can be expected to be 92 MPa and 40 MPa respectively. Next, using a standard coefficient of friction, μ, of 0.6 and the notion of critically stressed crust Brudy *et al.* (1997); Townend and Zoback (2000); Zoback and Townend (2001); Zoback *et al.* (2002), the minimum principal total stress (S_{hmin} in this case) can be calculated. This is done through the use of the Coulomb failure condition (e.g., Zoback (2007)),

$$\frac{(S_1 - P_p)}{(S_3 - P_p)} = \frac{(S_v - P_p)}{(S_{hmin} - P_p)} = \left(\sqrt{\mu^2 + 1} + \mu\right)^2. \tag{3.1}$$

Here S_1 and S_3 designate the maximum and minimum principal total stresses, respectively Note that it is assumed here that Terzaghi's effective stress governs shear failure Mandl (2000). Based on this equation, S_{hmin} can be found to be 56.7 MPa and the ratio of the effective stresses is 3.12. This value represents a frictional stability limit; values higher than this predict failure on optimally-oriented shear planes. Next, assuming an isotropic, porous, elastic reservoir, that is thin relative to its lateral extensiveness, the change in horizontal total stress due to a pore pressure change can be found using Segall and Fitzgerald (1998); Chan and Zoback (2002); Zoback (2007),

$$\frac{\Delta S_{hmin}}{\Delta P_p} = \alpha \frac{1-2\nu}{1-\nu} = A, \tag{3.2}$$

where α is the Biot coefficient and ν is Poisson's ratio. A is the stress path. The vertical total stress in this case can be assumed to remain unchanged during injection due to the assumption that the reservoir is thin relative to its lateral extensiveness. This implies that the horizontal strains are negligible and reults in zero vertical total stress change as described by Segall and Fitzgerald (1998). Note that this is nearly always the case for sedimentary reservoirs such as those which are commonly exploited in the oil and gas industry (e.g., Segall and Fitzgerald (1998); Zoback (2007)) and which are likley to be targeted for large-scale injection (e.g., Rutqvist (2012)). In the event that the Biot coefficient is large and Poisson's ratio is small, the stress path (i.e. the ratio between the change in S_{hmin} and pore pressure) will be large. Examples of such reservoirs have previously been investigated in terms of production-induced seismicity Teufel *et al.* (1991); Segall and Fitzgerald (1998); Chan and Zoback (2002); Zoback and Zinke (2002); Dempsey and Suckale (2017). In production scenarios with a coefficient of friction of 0.6, normal faulting is expected for stress paths above 0.67 Chan and Zoback (2002). In this example, the Biot coefficient will be assumed to be one and Poisson's ratio will be taken as 0.15. This yields a stress path of 0.82 and would correspond to a high stress path reservoir similar to such reservoirs as Alwyn, Valhall Flank, and Eldfisk amongst others Chan and Zoback (2002).

In this case, as the crust is assumed to be critically stressed, one might expect fluid injection to immediately lead to induced seismicity. However, with such a large stress path, the reservoir will actually stabilize as pore pressure increases. To illustrate this, a reservoir pressure increase of 10 MPa will be assumed. Based on Equation 3.2, this yields an increase of S_{hmin} of 8.2 MPa. Then, the Coulomb failure criteria can be re-evaluated. Using Equation 3.1, the ratio between the effective stresses, which was initially 3.12, has now decreased to 2.81. This stabilization is illustrated in Figure 3.1a. In Figure 3.1b, this result is compared to the case that Poisson's ratio is 0.33 and the resulting stress path is only 0.51. In this case, the change to S_{hmin} is only expected to be 5.1 MPa during the pore pressure increase. Using Equation 3.1, the resulting effective stress ratio for this case is found to be 3.59, a destabilization.
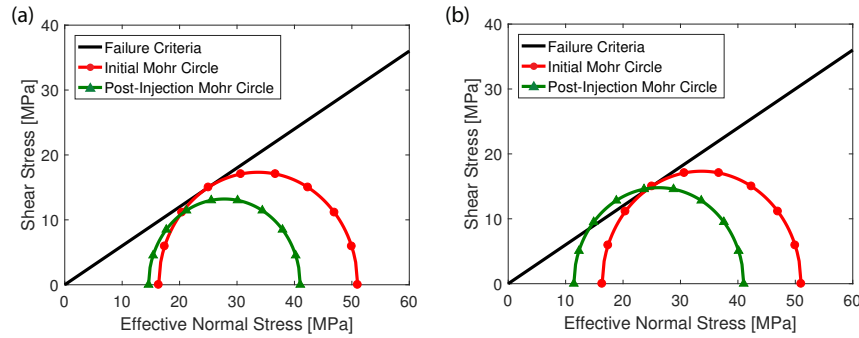
Figure 3.1 – The result of isothermal fluid injection in a critically stressed crust in a normal faulting stress regime when (a) the stress path is high (0.82), resulting in stabilization despite the increasing pore pressure, and when (b) the stress path is low (0.51), resulting in destabilization. Note how in both cases the minimum principal effective stress, which is horizontal, is reduced less than the maximum principal effective stress, which is vertical. This is due to the horizontal total stress increases associated with poroelasticity.

It has been previously pointed out that isothermal injection in a normal faulting stress regime can actually increase stability Vilarrasa (2016); Lavrov (2016); however, through the above examples it is clear that this is only true for large stress path reservoirs or reservoirs containing faults characterized by low coefficients of friction. This point will be further addressed in Section 3.5.2. Of course, this approach does not consider the thermal effects that would be associated with injection into a geothermal reservoir. However, these results do indicate the potential important influence that a reservoir's stress path may have on seismic risk.

3.3.2 Thermally-Coupled Solution

Equation 3.2 can be extended to thermo-elasticity using the solution provided by Cheng (2016),

$$\Delta S_{hmin} = \frac{1-2\nu}{1-\nu}\left(\alpha \Delta P_p + \alpha_d \Delta T\right),$$ (3.3)

where α_d is the drained thermoelastic effective stress coefficient and ΔT is the change in temperature throughout the reservoir. As in Equation 3.2, the vertical total stress can be assumed to remain unchanged due to temperature changes within in the reservoir based on the assumption of a laterally extensive reservoir Segall and Fitzgerald (1998); Cheng (2016). A reasonable value for α_d in a sandstone can be calculated using a volumetric expansion coefficient, β_d, of $4e^{-5}\ \frac{1}{^0C}$ Fjær *et al.* (2008) and a drained Bulk Modulus of $6.6e^9\ Pa$ Hart and Wang (1995), resulting in a drained thermoelastic effective stress coefficient of 0.26 $\frac{MPa}{^0C}$. Assuming, as before, a Biot coefficient of one and a Poisson's ratio of 0.15, the change in S_{hmin} is calculated for a pore pressure increase of 10 MPa and a temperature drop of 5 ^0C. It is
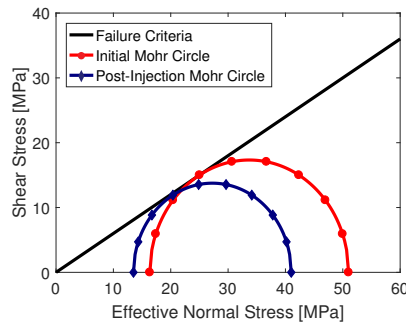
Figure 3.2 – The result of cold fluid injection in a critically-stressed crust in a normal faulting stress regime with a high stress path (0.82). The decrease in temperature (5 ^0C decrease) results in a larger differential stress and a stress state which is closer to failure than in the isothermal case, Figure 3.1a. Larger temperature drops would result in predicted failure on optimally-oriented shear planes in the reservoir.

assumed that the temperature drop is uniform throughout the reservoir. This would be a first-order approximation because in reality temperature would be lowest near the injection well and increase away from it. Based on these assumptions, S_{hmin} increases by 7.15 MPa, with poroelastic total stress changes accounting for an 8.22 MPa increase in S_{hmin} and thermoelastic total stress changes accounting for a 1.07 MPa decrease in S_{hmin}. For this very modest temperature decrease the effective stress ratio is 3.04, stabilized compared to the initial conditions but less stable compared to the isothermal case. For more significant temperature changes optimally-oriented faults could be brought to failure, implying that even high stress path reservoirs can not be completely protected from shear failure if significant cooling occurs during injection. In order to promote stability in a normal faulting stress regime, the change to S_{hmin} found via Equation 3.3 still has to result in a large enough stress path, as defined by Equation 3.2 for the isothermal case.

3.4 Preconditioned Shear Stimulation

Here, the learnings from Section 3.3 will be used to suggest that the stress field in a reservoir in a reverse faulting stress regime can be preconditioned before stimulation using induced temperature changes. This is predicted to result in a lower differential stress, which is expected to reduce the risk of large induced seismic events when stimulation does finally occur. The manner in which this preconditioning methodology occurs is qualitatively outlined in Figure 3.3. Initially, it is assumed that the reservoir is critically stressed and small increases in pore pressure would be enough to stimulate the reservoir, as has seen to be the case for many EGS reservoirs which were stimulated in shear Evans *et al.* (2012); Rutqvist *et al.* (2016b). Then, as in Rutqvist *et al.* (2016b), the reservoir is slowly cooled over an extended period of time while pore pressure increase is limited. This results in a less critically-stressed state and a smaller differential stress. Finally the reservoir is stimulated with a rapid increase in pore pressure which results in shear failure and only a slight increase in differential stress. By following this
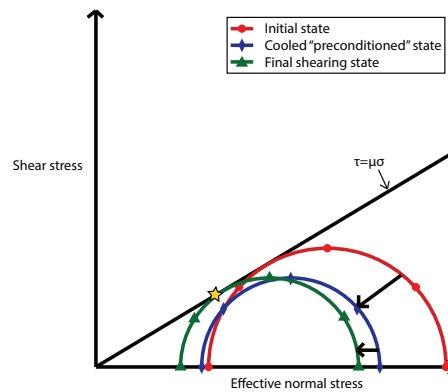
Figure 3.3 – A qualitative schematic of the stress preconditioning process for a reverse faulting stress regime. The changes in total stress are exaggerated for clarity. Initially (red), the reservoir is critically stressed with a relatively large differential stress. The reservoir is preconditioned (blue) using low temperature injection over a long period of time. This reduces the horizontal total stress resulting in a lower differential stress. The pore pressure increase is limited such that this phase does not induce shear failure. Finally (green), shear failure is induced by rapid fluid injection. The differential stress is slightly increased during this phase due to poroelastic effects. Overall, however, the differential stress at failure using this methodology is less than the differential stress in the initial state.

methodology, therefore, the reservoir is stimulated at a reduced differential stress.

3.4.1 Gutenberg-Richter b-Value

Seismicity tends to follow a power law relationship known as the Gutenberg-Richter Law Gutenberg and Richter (1944),

$$\log N = a - b M_w, \tag{3.4}$$

where N represents the cumulative number of earthquakes, a is the activity, M_w is the moment magnitude of a given event, and the b-value gives an indication of how many large events there are relative to small events. Higher b-values indicate proportionally more small events and low b-values indicate proportionally more large events. The b-value has been seen to be inversely correlated to the differential stress Amitrano (2003); Schorlemmer $et\ al.$ (2005); Spada $et\ al.$ (2013); Scholz (2015), although accurately determining the exact correlation is difficult Gischig $et\ al.$ (2014). Here, a linear relationship between b-value and differential stress will be used, as in Layland-Bachmann $et\ al.$ (2012) in their simulation of the induced seismicity at the

EGS in Basel, Switzerland, such that,

$$\frac{db}{d\sigma_D} = -0.021 \frac{1}{MPa}.$$

(3.5)

Here, σ_D represents the differential stress in MPa. The initial state of the reservoir will be assumed to correspond to a b-value of 1. In order to crudely predict the number of large magnitude events that each case is expected to produce, Equation 3.4 will be used in combination with a fixed activity (the same for all cases) and each case's b-value. The activity will be based on an assumed 10,000 events above a magnitude of completeness, $M_w = 0$.

3.4.2 Example Reverse Faulting Scenario

To illustrate how the preconditioning would work, an example case is presented. The reservoir is assumed to be in a reverse faulting stress regime at 4000 m depth. The reservoir is initially critically stressed, with a differential stress of 108 MPa and an effective stress ratio of 3.12, Figure 3.4. This differential stress is reasonable for a compressive regime at this depth (e.g., Zoback and Harjes (1997)). Reasonable values for Poisson's ratio (0.2), grain bulk modulus (36 GPa), and the drained bulk modulus (10 GPa) are chosen, resulting in a Biot coefficient of 0.72 and an isothermal stress path of 0.54. The thermal volumetric expansion coefficient is taken as $4e^{-5} \frac{1}{{}^0C}$. The coefficient of friction is taken as 0.6.

During the preconditioning phase, the reservoir undergoes a temperature decrease of 30 ${}^0C$ and a pressure increase of 2 MPa, reasonable for one year of injection based on the temperature and pressure changes modelled for the Northwest Geysers EGS Demonstration Project by Rutqvist *et al.* (2016b). This results in a differential stress of 100 MPa and an effective stress ratio of 3.04 (Figure 3.4). The reduced effective stress ratio means that the reservoir is less critically stressed than it was initially and shear failure is not predicted to have occurred.

Next, the reservoir is stimulated by increasing pore pressure up to the point of shear failure (corresponding to an effective stress ratio of 3.12). To accomplish this the pressure is increased by approximately 1.4 MPa. Temperature is assumed to remain constant during this phase due to the relatively short time scale of stimulation. The increase in pressure results in an increase in horizontal total stress of 0.75 MPa, meaning the differential stress at shear failure is approximately 101 MPa, Figure 3.4.

Due to the relationship between b-value and differential stress, Equation 3.5, the different phases of this methodology correspond to different expected b-values. The initial state of differential stress is assumed to correspond to a b-value of 1. The subsequent cooling reduces the differential stress and therefore increases the expected b-value by 0.17. Then, the slight change of S_{Hmax} during the stimulation phase results in a modest decrease of the predicted
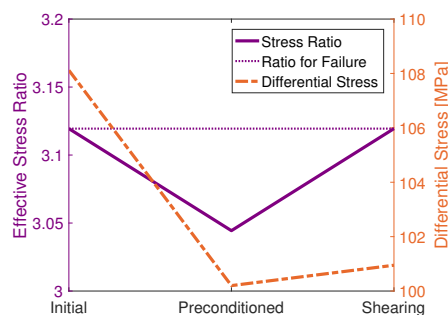
Figure 3.4 – The effective stress ratio (purple) and the differential stress (orange) at the three stages of the proposed methodology for a reverse faulting stress regime. The effective stress ratio which corresponds to shear failure (3.12) is designated by a dotted purple line. Initially, the reservoir is near shear failure due to the assumed critically-stressed nature of the reservoir. Due to the temperature-induced stress preconditioning, the differential stress is reduced because the horizontal total stress is reduced while the total vertical total stress remains constant. Next, the pressure is rapidly increased to induce shear failure. The differential stress increases only slightly during this time due to poroelastic effects. The result of the entire process is that shear failure is induced at a lower differential stress than was originally present.

b-value by 0.02. Ultimately, the entire process has resulted in an expected b-value which is 0.15 higher than the expected b-value would have been, had the preconditioning not been employed and the reservoir been stimulated in its initial state, Figure 3.5.

Based on the change in b-value and a fixed activity, the expected number of events larger than M_w 3 can be calculated. This is done by solving Equation 3.4 for N, similar to approaches by other authors (e.g., Wiemer (2000)). Had the reservoir been stimulated in its initial state, 10 events larger than M_w 3 would have been expected. Using the preconditioning methodology, however, only 3.5 events larger than this magnitude are expected. In this way, the preconditioning has reduced the chance of a large magnitude event while still allowing for the reservoir to be stimulated. Note that the assumption of a fixed activity is discussed in Section 3.5.

3.5 Discussion

3.5.1 Limitations and assumptions of approach

The poro- and thermo-elastic solutions used here assume no lateral strain, or lateral extensiveness of the reservoir. A laterally extensive reservoir is one with a limited height, presumably bound by an impermeable layer both above and below it. The setup is common for sedimentary reservoirs and can be frequently seen, for example, in many petroleum systems. It was also representative of the situation in the Northwest Geysers EGS Demonstration Project Rutqvist *et al.* (2016b). This reservoir was stimulated in shear, making it a relevant example of the type of reservoir that might be targeted for the shear stimulation preconditioning presented in
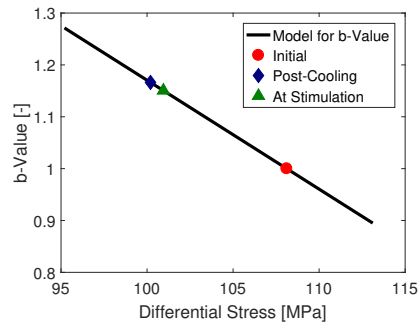
Figure 3.5 – The assumed linear relationship between differential stress and *b*-value (black). The three phases present in the example are plotted as points along the model line. Note the increase in predicted *b*-value occurring as a result of the decreased differential stress associated with cooling.

Section 3.4. The applicability of this assumption to other reservoirs stimulated in shear, such as a reservoir comprised of crystalline rock as is common in the EGS industry, is probably less valid. Additionally, these types of reservoirs frequently have their porosity and permeability dominated by permeable fault/fracture zones. Indeed, these types of rocks may otherwise exhibit little matrix porosity/permeability. Indeed, these types of reservoirs may otherwise exhibit little matrix porosity/permeability. In these cases, the effects of preconditioning would need to be evaluated using more rigorous numerical techniques (e.g., Jeanne *et al.* (2017)). It should be noted that, even if the assumption of lateral extensiveness does not hold for a given reservoir, the poro/thermo-elastic total stress changes associated with production/injection from a well are still anisotropic (e.g., Jeanne *et al.* (2017)), so this methodology would not necessarily be ineffective in either the presented - or an adapted - form.

Further, the models used here assume uniform pressure and temperature changes occurring throughout the reservoir. This is generally not the case over short time periods in low permeability reservoirs saturated by liquids. It is especially not the case for temperature changes, which have a tendancy to be focused near the wellbore (e.g., Rutqvist *et al.* (2016b)). For this reason, it is possible that the temperature-induced total stress changes responsible for the stress preconditioning in Section 3.4 would be focused near the wellbore and only have limited influence on the far-field induced seismicity where large magnitude events frequently occur Layland-Bachmann *et al.* (2012). It should be noted that this is thought to be due to the shearing of non-optimal planes near the wellbore resulting in high *b*-values in this area; a result of the high pore pressure near the wellbore Goertz-Allmann and Wiemer (2013). That said, the cooling zone, with approximately 30 ^0C of cooling or more, shown by Rutqvist *et al.* (2016b) for a period of 270 days, already had a diameter of a few hundred meters, not so dissimilar in size to the seismic cloud which occurred at Basel, for example Häring *et al.* (2008). Certainly, it is important that the preconditioning phase lasts long enough to affect a large area around the wellbore, ideally affecting the entire volume that is to be stimulated.

It was assumed in this analysis that pore pressure changes were contained within the reservoir.

In terms of injection-induced seismicity, this is a large simplification as seismicity is commonly seen below the injection horizon and is frequently attributed to pore pressure increases (e.g., Ellsworth (2013)). In this sense, injection into high stress path reservoirs has only been shown here to stabilize locations within the reservoir. For this reason, no claim can be made here as to the effect of the reservoir's stress path on seismicity occurring outside of the reservoir, such as is commonly the case in wastewater disposal induced seismicity in the United States.

The methodology used to predict the change in the number of large magnitude events in Section 3.4 is crude, although similar methodologies for predicting the number of large events have been employed previously (e.g., Wiemer (2000)). One major difference between this example scenario and most other field analyses is that the activity, a, is assumed to remain constant between the two cases here and is not based on monitoring data. The activity remaining constant implies that the same number of total events occur in each instance. It is unclear if this would really be the case with two different differential stresses even if the reservoir were to otherwise be the same. However, it is likely that the reduced differential stress would still lead to less large magnitude seismicity. Indeed, it has been shown that earthquakes tend to grow larger in high-stress environments Schorlemmer *et al.* (2005); Narteau *et al.* (2009); Gulia and Wiemer (2010).

The dependence of b-value on differential stress used here represents a moderate value for the induced seismicity in Basel Layland-Bachmann *et al.* (2012); Gischig *et al.* (2014), indicating that the strength of the dependency used here is not unreasonable. However, it is possible that the b-value has either a stronger or weaker dependence in many other cases. A weaker dependence would represent a less efficient preconditioning treatment and would therefore not reduce the risk of a large earthquake as much as in the example given here.

3.5.2 Avoiding seismicity within the reservoir

The isothermal results from Section 3.3.1 have implications for injection scenarios where the temperature of the in-situ fluid and injected fluid do not greatly differ. In fact, the results predict stabilization during injection in high stress path reservoirs in normal faulting stress regimes due to the reduction of shear stress on the fault associated with the increase in the horizontal total stress which brings the reservoir to a more isotropic stress state. More precisely, isothermal injection will lead to stability in normal faulting stress regimes if

$$A \geq \frac{S_v - S_{hmin}}{S_v - P_p} \tag{3.6}$$

is satisfied. This particular result has implications for isothermal injection in scenarios such as certain instances of waste water injection, waterflooding, and potentially certain instances of CO_2 geosequestration. One implication of Equation 3.6 is that, in injection scenarios,

less critically-stressed reservoirs stabilize even with relatively low stress paths, potentially indicating that injection can be safely performed in reservoirs with low stress paths as long as the reservoirs are not critically-stressed initially. It is generally assumed, however, that the crust is critically stressed Brudy *et al.* (1997); Townend and Zoback (2000); Zoback and Townend (2001); Zoback *et al.* (2002). Although this has also been seen to be the case in most EGS's in crystalline rock and even many reservoirs in sedimentary rock, for example (e.g., Evans *et al.* (2012); Zoback (2007)), there has also been evidence of some reservoirs which are less critically stressed, requiring Coulomb stress changes, a measure of the criticallity of a fault (e.g., Stein (1999)), of up to 5 MPa, or more, before responding seismically (e.g., Evans *et al.* (2012); Dempsey and Suckale (2017); Riffault *et al.* (2018)).

Conversely, if Equation 3.6 is satisfied for a fluid-producing reservoir in a normal faulting stress regime, the effective stress ratio can be expected to increase, leading to a less stable stress state (unless the two terms are exactly equal). In the case that the crust can be assumed to be critically stressed, Equation 3.6 can be simplified to yield,

$$A \geq 1 - \frac{1}{\left(\sqrt{\mu^2 + 1} + \mu\right)^2}.$$

(3.7)

One implication of Equation 3.7 is that injection into reservoirs containing faults characterized by low coefficients of friction in normal faulting stress regimes is more likely to result in fault stabilization than the case where the faults have high coefficients of friction, Figure 3.6.

In production scenarios, if Equation 3.7 is satisfied, not only will production result in a higher effective stress ratio, the destabilization of optimally-oriented faults within the reservoir can be expected, with an onset delay depending on how critically-stressed the reservoir was initially. Note that in the case that the coefficient of friction is equal to 0.6, Equation 3.7 is satisfied for values of A larger than 0.68 which is in agreement with the results of Chan and Zoback (2002). In a similar fashion to injection scenarios, Equation 3.7 suggests that production-induced seismicity is more likely to be induced within the reservoir in normal faulting stress regimes when the coefficients of friction that characterize the faults in the reservoir are low, Figure 3.6. The derivation of Equations 3.6 and 3.7 can be found in Appendix A.1.

Notably, even if the reservoir is being stabilized during injection due to poroelastic stress changes, this is not necessarily the case outside of the reservoir, and, in certain instances, the stability of bounding layers can be of great importance. For example, in CO_2 sequestration, the thermal and poroelastic total stress changes that are occurring in the caprock are also of significance as they may have implications for the stability of the caprock Vilarrasa *et al.* (2014); Vilarrasa (2016). Indeed, in the same way that total stress changes associated with fluid production can induce seismicity above, below, and on the flanks of a producing reservoir Segall (1989), so too can the total stress changes associated with fluid injection. The difference
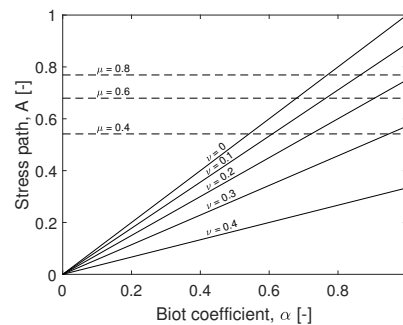
Figure 3.6 – The parameter space, extended from Chan and Zoback, 2002 for various coefficients of friction, in which isothermal injection would promote stability in a critically-stressed, laterally-extensive reservoir in a normal faulting stress regime. Stability is promoted for a given combination of Poisson's ratio and Biot coefficient when the resulting stress path is above the dotted line corresponding to the coefficient of friction which characterizes the faults in the reservoir. This implies that reservoirs with low Poisson's ratios and high Biot coefficients are more likely to remain stable during injection in normal faulting stress regimes. Further, low coefficients of friction are also preferable in terms of promoting stability during injection; however, in production scenarios it should be noted that the opposite is true, such that faults with low coefficients of friction are more readily destabilized by a decreasing pore pressure in normal faulting regimes.

being that fluid injection would induce horizontal tension above and below the reservoir and compression in the flanks, opposite to the changes caused by production. For this reason, it can be expected that isothermal poroelastic stressing due to fluid injection is capable of inducing normal faulting above and below the reservoir and reverse faulting on the flanks, even with limited or no pore pressure increases in these locations. Whether or not isothermal poroelastic stressing is capable of inducing strike-slip faulting outside of the reservoir is less clear; however, it is likely that this is indeed the case Lavrov (2016). Away from the injecting well, total stress changes are anisotropic, being larger in the radial direction Rudnicki (1986). For this reason, it is possible that strike-slip faulting can be induced on the flanks of the reservoir primarily in the direction of S_{Hmax} and above and below the reservoir primarily in the direction of S_{hmin}. Further study is necessary to confirm this, however. In the case that the injection procedure can not be considered isothermal, these general trends will still hold unless the total stress changes induced by temperature effects are negative (i.e., correspond to reservoir cooling) and larger in magnitude than the poroelastic total stress changes. Additionally, it is also possible for hydraulic conduits such as permeable faults and fractures to lead to pore pressure increases in the layers above and below the reservoir. This can lead to induced seismicity in the geologic basement, such as has been seen to be the case in the United States due to wastewater injection Zhang *et al.* (2013). Due to the possibility of inducing earthquakes outside of the reservoir, it is preferable to inject into reservoirs bounded by impermeable aseismic shales.

It is likely that, in most of the relevant types of operations, the injected fluid will either be the

Table 3.1 – Preferable operating conditions of high stress path, laterally-extensive geothermal reservoirs in normal and reverse faulting stress regimes in terms of fault stability within the reservoir.

Stress regime	Operating temperature	Operating pressure
Normal	Close to in-situ	Above in-situ
Reverse	Below in-situ	Below in-situ

same temperature or cooler than the in-situ fluid. This may lead to the cooling of the reservoir over time. This cooling will result in a reduction of the horizontal total stresses in the reservoir, which has implications for the stability of faults within the reservoir. Based on these results, it can be concluded that, in terms of avoiding induced seismicity in a circulating geothermal doublet system for laterally-extensive reservoirs with high stress paths, it is preferable to:

- Operate high stress path reservoirs in normal faulting stress regime environments at pressures above the in-situ pressure

- Minimize temperature decrease in reservoirs in normal faulting stress regime environments

- Operate reservoirs in reverse faulting stress regime environments at a pressure below the in-situ pressure, or as low a pressure as reasonably possible

- Operate reservoirs in reverse faulting stress regime environments at a temperature below the in-situ temperature

These preferable operating conditions are summarized in Table 3.1. Note that these preferable operating conditions are only in terms of induced seismicity within the reservoir. It is likely that other considerations, such as the possible rate of heat extraction, do not align with these recommendations.

The reason it is preferable to operate high stress path reservoirs in a normal faulting stress regime at pressures above the in-situ pressure is that the total stress changes incurred by injection are compressive and act to stabilize normal faults in the reservoir by increasing the minimum principal total stress, which is horizontal. This makes high stress path reservoirs in normal faulting stress regimes attractive because the possibility of elevated injection pressures allows for more pressure support and ultimately higher circulation rates. It is preferable to minimize temperature reduction in high stress path reservoirs in a normal faulting stress regime because temperature decrease reduces the minimum principal total stress, resulting in a destabilization of normal faults in the reservoir.

The reason it is preferable to operate reservoirs in a reverse faulting stress regime at pressures below the in-situ pressure is that, not only would a high pore pressure reduce the effective

principal stresses, but the total stress changes that would be incurred by a pore pressure increase would result in a higher horizontal total stress, further destabilizing faults in the reservoir. It is preferable to allow temperature reduction in high stress path reservoirs in a reverse faulting stress regime because temperature decrease reduces the maximum principal total stress, resulting in a stabilization of reverse faults in the reservoir.

The simple example in Section 3.3.2 demonstrates the significant influence temperature changes can have on the stability of faults and fractures, Figure 3.2.

3.5.3 Temperature-induced stress preconditioning

The temperature-induced stress preconditioning presented in Section 3.4 is based on the connection seen between b-value and differential stress Amitrano (2003); Schorlemmer *et al.* (2005); Narteau *et al.* (2009); Gulia and Wiemer (2010); Goebel *et al.* (2013); Spada *et al.* (2013); El-Isa and Eaton (2014); Scholz (2015); Wu *et al.* (2018). By reducing the differential stress in the reservoir, this methodology raises the expected b-value of any induced seismicity, thereby reducing the risk of a large seismic event. Indeed, seismic events are predicted to have a smaller chance of growing to larger sizes when the medium exhibits a low differential stress level Goebel *et al.* (2013); Norbeck and Horne (2018). In fact, a lower normal stress, which is another result of this approach, increases the critical nucleation length required for seismic instability (e.g., Scholz (1998)), implying that the approach described here may also promote stable slip. Additionally, a lower normal stress results in larger dilatancy during shear motion and therefore a larger increase in permeability Cornet (2019). Further, the connection seen between b-value and differential stress implies that less critically-stressed reservoirs and reservoirs with shear planes characterized by lower coefficients of friction are more likely to exhibit high b-values and a lower risk of large seismic events when stimulated in shear. Rather counter-intuitively, it may be the case that less critically-stressed reservoirs are attractive targets for shear stimulation for this reason. It should also be expected that reservoirs stimulated in shear in reverse faulting stress regimes would exhibit lower b-values than those in strike-slip faulting stress regimes, which in turn would exhibit lower b-values than those in normal faulting stress regimes. This is supported by field data collected from natural earthquakes Schorlemmer *et al.* (2005); Gulia and Wiemer (2010); El-Isa and Eaton (2014); Wu *et al.* (2018) and suggests that shear stimulations performed in normal faulting stress regimes may generally have a lower risk of inducing a large earthquake than those in reverse or strike-slip faulting stress regimes.

Reservoir engineering operations have previously been shown to be capable of intentionally preconditioning the stress field, altering the differential stress, and ultimatley resulting in a change in the frequency-magnitude distribtion of seismic events induced at a later stage Dohmen *et al.* (2017); Eaton (2018). Temperature changes in a reservoir have also previously been shown to be capable of changing the differential stress Vilarrasa (2016); Zimmerman (2017); Voake *et al.* (2017). Further, the ability of temperature changes to influence frequency-

magnitude distributions fit with the observation of Kwiatek *et al.* (2015), in a predominantly normal faulting setting, that the larger seismic events tended to occur close to the injection wells, an area which would have experienced the largest temperature changes. In a normal faulting stress regime, cooling is expected to increase the differential stress by reducing S_{hmin}. The large events occurring near the well then fit with the model based on the relationship between differential stress and b-value.

In fact, in many ways the approach outlined here shares many similarities with the reservoir engineering operation of Microseismic Depletion Delineation (MDD) as described by Dohmen *et al.* (2013, 2014); Norbeck and Horne (2015); Dohmen *et al.* (2017); Eaton (2018). These similarities are especially evident when viewed graphically as in Figure 3.3. In MDD, the stress field is also preconditioned, but through production. As in the strategy proposed here, this production also results in a decreased horizontal total stress; however, MDD is typically applied to normal faulting stress regimes, so this total stress decrease results in an increase in differential stress. After production, fluid is injected, quickly raising the pore pressure within fractures and other potential shear planes. The pore pressure in the matrix remains fairly constant during this injection due to the short time scale of the injection; this means that the decreases in the horizontal total stress largely remain during this injection. Due to the elevated pore pressure, optimally-oriented shear planes slip. Regions that have experienced the total stress changes due to production tend to exhibit lower b-values due to an elevated differential stress. The strategy proposed here is quite similar, except temperature changes, and not production, are proposed to reduce the horizontal total stress, and, because the strategy proposed here is for reverse and not normal faulting stress regimes, the b-value is expected to increase due to the preconditioning.

The temperature-induced stress preconditioning presented in Section 3.4 is also similar in terms of procedure to that of the Northwest Geysers EGS Demonstration Project. There, as here, a large period of time, approximately one year, was taken to slowly cool the reservoir while minimizing the pore pressure changes Rutqvist *et al.* (2016b). However, in the Northwest Geysers EGS Demonstration Project these temperature changes, in combination with limited pressure changes (≤ 2 MPa), were used to induce shear failure, with the temperature changes responsible for significant changes in total stress. In the methodology presented here, the temperature changes result in a lower differential stress which results in a stabilization of optimally-oriented shear planes in the reservoir. After this initial stabilization phase, shear failure is then induced on these optimally-oriented planes by rapidly increasing the pore pressure, resulting in shear failure at a relatively low differential stress. The time scale of the pore pressure increase in the reservoir for this second phase is much shorter than that needed to induce the temperature changes during the first phase. The reason the predicted results for this methodology were not seen for the Northwest Geysers EGS Demonstration Project is that this project was not in a reverse faulting stress regime, the stress regime for which this particular variation of temperature-induced stress preconditioning is suggested.

Regarding other stress regimes, the same methodology would be expected to work in a normal

faulting stress regime using an initial period of warming instead of cooling. This would result in an increase of S_{hmin} and therefore a decrease in the differential stress, allowing for induced shear failure at a relatively low differential stress. Obviously this is likely to be more difficult to implement in geothermal reservoirs which exhibit high in-situ temperatures. Normal and reverse faulting stress regimes lend themselves to this kind of preconditioning due to the limited changes to the vertical total stress which occur during fluid injection/production. As the vertical stress is the maximum principal stress in a normal faulting stress regime and the minimum principal stress in a reverse faulting stress regime, this means that pressure and temperature changes in these stress regimes only affect one of either the maximum or minimum principal total stresses, resulting in a change in the differential stress. Strike-slip faulting stress regimes are slightly more difficult, because both the maximum and minimum principal total stresses are affected by pressure and temperature changes, limiting the change in differential stress (e.g., Eaton (2018)). However, in the case of a horizontal well, induced total stresses due to pore pressure and temperature changes are anisotropic with the largest total stress changes occurring in the direction of the wellbore Vilarrasa (2016). Based on this anisotropy and the principals outlined above, it may also be possible to design similar earthquake-risk reducing procedures for strike-slip faulting stress regimes by drilling horizontal wells parallel to S_{hmin} and using an initial period of heating. Note that temperature-induced preconditioning in a strike-slip stress regime would also be possible with cooling if the well is drilled parallel to S_{Hmax} and the reservoir is not critically stressed initially. In fact, in this case the cooling preconditioning phase will lead to shear stimulation at a certain point, similar to what was seen in the Northwest Geysers EGS Demonstration Project Rutqvist *et al.* (2016b). In this way, the reservoir can be stimulated while reducing the differential stress, Figure 3.7a. This also implies that drilling the well in the opposite direction would result in an increased differential stress during stimulation with cool fluids, Figure 3.7b. Unfortunately, shear stimulations in EGS reservoirs frequently either propagate in the direction of S_{Hmax} (e.g., Häring *et al.* (2008)) or in the direction of strike of optimally-oriented shear planes (e.g., Evans *et al.* (2005b)), meaning that drilling a horizontal well parallel to S_{Hmax} is at best suboptimal. If the well is therefore drilled parallel to S_{hmin} in a strike-slip faulting stress regime, cooling should be minimized.

All versions of this methodology require the reservoir to be initially at least somewhat permeable. Any reservoir that requires shear stimulation in order to be sufficiently productive is unlikely to be highly permeable. Due to critically-stressed shear planes in the subsurface, such as the ones frequently targeted for EGS stimulation, the bulk permeability in the upper crust is thought to generally have permeabilities on the order of at least 10^{-17} m^2 (approximtely 0.01 mD) Zoback and Townend (2001). In the EGS industry, this has been supported by pre-production tests, which have shown similar, and also significantly larger, effective permeabilities Evans *et al.* (2005a); Ladner and Häring (2009). For example, taking the pre-stimulation transmissivity at Soult-sous-Forêts of 0.7 $\frac{L}{sec \cdot MPa}$ Evans *et al.* (2005a), for a 2 MPa perturbation in pore pressure it should be possible to inject over 44 million kilograms of water in one year. The total represents about 4-5% of what was injected at the Northwestern Geysers
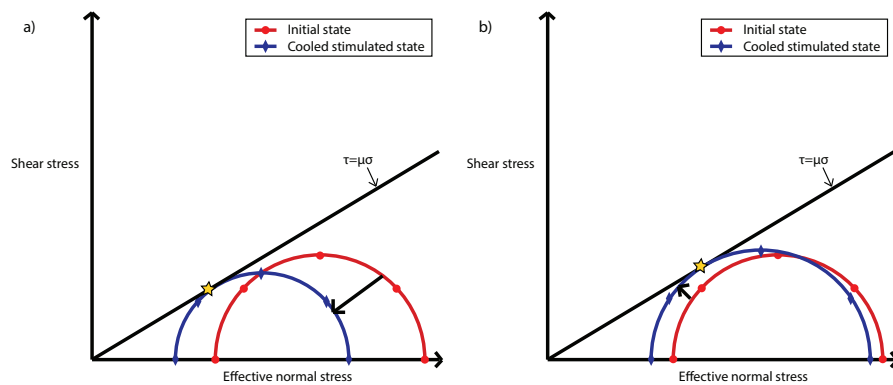
Figure 3.7 – A qualitative schematic of the cooling-induced stimulation for a strike-slip faulting stress regime from a horizontal well. The changes in stress are exaggerated for clarity. Initially (red), the reservoir is not critically stressed. The reservoir is cooled until failure (blue). Cooling induces a larger total stress change in the direction of the well. a) When the well is drilled parallel to S_{Hmax}, the differential stress is reduced because S_{Hmax} is reduced more than S_{hmin}. b) When the well is drilled parallel to S_{hmin}, the differential stress is increased because S_{hmin} is reduced more than S_{Hmax}. In both cases, shear failure still occurs due to the decreasing of both stresses. The b-value of the induced seismicity in case (a) is expected to be higher than the b-value of the induced seismicity in case (b) due to the differences in differential stress resulting from the cooling from different orientation wells. It is likely that more cooling needs to be induced before shear failure occurs in case (a) than in case (b).

EGS Demonstration Project over the course of one year where large ($> 40^0 C$) changes occurred many hundreds of meters away from the well Rutqvist *et al.* (2016b)). It is therefore likely that this strategy is readily applicable in locations with permeability similar to that seen at the Northwestern Geysers EGS Demonstration (on the order of 10^{-14} m^2 Rutqvist *et al.* (2016b)), but it is unclear if this strategy would be applicable in cases where the permeability is closer to that of Soultz-sous-Forêts (on the order of 10^{-16} m^2 Evans *et al.* (2005a)). Indeed, it is possible that low permeabilities will represent a serious challenge for the implementation of this methodology in many cases, and this is one of the major reasons that such long pre-stimulation times are thought to be necessary to precondition the stress in the reservoir. This methodology may not be practically viable in cases of extremely low permeability.

This methodology may not, in itself, be sufficient to adequately reduce the risk of large induced seismic events during EGS stimulation. It does open the door for further research into other forms of stress preconditioning, however. Methodologies which precondition the stress field without inducing large temperature changes would be especially interesting for the geothermal industry, for example. It may be possible to use the methodology outlined here in combination with "soft stimulation" approaches to design shear stimulation treatments with acceptably low risks of large seismic events. Alternatively, the use of multi-stage or multi-well stimulation may allow for more efficient temperature preconditioning, something that might also be attainable by beginning the preconditioning phase with a short period of high pressure injection to stimulate the near wellbore region. Certain variations of this methodology might, upon further

development, even have applications for shallow natural seismicity on known faults.

3.6 Conclusion

It has been suggested here that high stress path reservoirs in normal faulting stress regimes become more stable during pore pressure increases and therefore are attractive targets for fluid injection. However, these reservoirs too can be destabilized if significant cooling takes place during injection. Further, a new methodology has been proposed to stimulate reverse faulting reservoirs in shear with a reduced risk of an induced large magnitude event. The premise behind the methodology is the connection seen between differential stress and Gutenberg-Richter b-value, which implies that less large magnitude events will occur if the differential stress is low. As shown in previous field examples, cooling has a significant influence specifically on the horizontal total stresses, and significant cooling can be induced with limited pore pressure increase. Therefore, it is possible to precondition the stress field before stimulation by cooling the reservoir. After this initial phase of preconditioning, the reservoir can be stimulated in shear by increasing the pore pressure. The result is a reservoir stimulated in shear at a relatively low differential stress, implying that less large magnitude events will be induced. The proposed preconditioning methodology is suitable for laboratory- and meso-scale testing and is also applicable to normal and strike-slip faulting stress regimes with adaptations.

4 EGS doublet preconditioning

The results of this chapter are submitted for publication as:

Journal paper:

Fryer, B., Ma, X., Siddiqi, G., and Laloui, L. *Under Review.* Critically-stressed reservoir stimulation direction via stress preconditioning in horizontal EGS doublets. *Geothermics.*

Conference paper:

Fryer, B., Ma, X., Siddiqi, G., and Laloui, L. *Under Review.* Stress preconditioning for critically-stressed EGS reservoir stimulation in reverse faulting stress regimes. In: *Proceedings: World Geothermal Congress 2020.*

Contribution of candidate: Initial idea, development of code, analysis of results, writing of manuscripts.

4.1 Chapter Summary

In this work, it is suggested numerically that it is possible to direct shear stimulation treatments in critically-stressed reservoirs. This would aid in the creation of Enhanced Geothermal Systems by promoting hydraulic connectivity in doublet-well systems. In this case, the stimulation treatment is directed using only the poroelastic stress changes associated with a previous stimulation treatment to precondition the stress field. This methodology is shown for reverse, strike-slip, and normal faulting stress regimes.

4.2 Introduction

Low permeability and inter-well connectivity are common problems preventing Enhanced Geothermal Systems (EGS) from reaching their potential (Tester *et al.*, 2006; Ziagos *et al.*, 2013). Indeed, it has previously been pointed out that the optimal distribution of permeable pathways is critical for the successful development of sufficient productivity for commercial EGS power generation (Robinson *et al.*, 1971; Ziagos *et al.*, 2013). For this reason, the ability to guide reservoir stimulation treatments such that specific areas of the reservoir can be targeted for stimulation would represent a significant development. A further advantage of this kind of stimulation targeting would be the ability to avoid the reactivation of large faults; either directly in the case that fault locations are known, or indirectly, in that only the most crucial parts of a reservoir are stimulated, thus moderating the risk that the stimulation treatment encounters large faults (e.g., Kim *et al.* (2018)). This should aid in the mitigation of induced seismicity. In fact, it is thought that the development of alternate stimulation concepts is integral to the mitigation of seismic risk from hydraulic stimulation (Häring *et al.*, 2008) and that the engineering of reservoir connectivity would represent a key development for EGS (Rybach, 2010).

Directed reservoir stimulation techniques have been investigated before. For example, in Soultz-sous-Forêts, Baria *et al.* (2004) showed the positive effect of the contemporaneous stimulation of two wells in the context of an EGS project in crystalline rock. Their focus was primarily on the effect that an elevated pore pressure would have on the stimulation of a second well. However, the idea of altering the stress field in order to benefit a stimulation treatment has also been suggested as long ago as 1977 when Shuck (1977) filed a patent which involved injecting fluid to alter the plane of the maximum principal stress for use in hydraulic fracturing. Bouteca *et al.* (1983) investigated, both numerically and experimentally, the possibility of using fluid injection to alter the stress state such that a hydraulic fracturing treatment would connect two wells. This idea has been expanded upon by, for example, Warpinski and Branagan (1989), who were able to show stress changes of over 2 MPa due to the opening of a hydraulic fracture in lenticular reservoirs with the intent of reorienting potential hydraulic fractures such that they would intersect natural ones. Warpinski and Branagan (1989) estimated that larger pre-stimulation treatments would be able to induce stress changes of over 4 MPa, which, in this case, was a stress change large enough swap the directions of the principal horizontal stresses. Warpinski and Branagan (1989) primarily considered their results relevant for single-well systems. Certainly, the effect of stress shadowing due to fracture opening has been widely discussed (e.g., Fisher *et al.* (2004); Vermylen and Zoback (2011)). Other relevant works include the effects of poroelastic stress changes due to production on refracturing (Elbel and Mack, 1993), the work by Minner *et al.* (2002), which showed that injection and production can result in poroelastic stress changes that can dramatically alter fracture geometry on infill wells, and Berchenko and Detournay (1997); Gao *et al.* (2019) who used models to analyze the deviation of hydraulic fractures associated with poroelastic stress changes resulting from production and injection.

Although there have been numerous examples of EGS in sedimentary rocks (e.g., Evans *et al.* (2012)), the focus here will be on EGS in crystalline rocks, which are deeper and therefore tend to offer higher temperatures. Various configurations exist for EGS wells (e.g., Chen and Jiang (2015)), but the standard EGS setup employs a doublet well configuration (e.g., Jupe *et al.* (1992); Dorbath *et al.* (2009); Kim *et al.* (2018)) whereby fluid is circulated between an injection and a production well, which can either be vertical or directional in nature. Crystalline rock and high temperatures do pose new challenges for directional drilling, but improvements are being made (Tester *et al.*, 2006). Certainly, a number of EGS wells have been drilled directionally (e.g., Tester *et al.* (2006); Kwiatek *et al.* (2008); Dorbath *et al.* (2009); Kwiatek *et al.* (2014); Kim *et al.* (2018); Norbeck *et al.* (2018); Kwiatek *et al.* (2019)) and horizontally drilling in hard, high temperature rock is possible (albeit potentially cost inhibitive) (Shiozawa and McClure, 2014). In fact, recent publications are beginning to consider the multi-stage stimulation of horizontal wells for EGS (e.g., Meier *et al.* (2015); Kumar and Ghassemi (2019)). It has even been suggested that the multi-stage horizontal well stimulation employed in the oil and gas industry should act as a model for the EGS industry (Ziagos *et al.*, 2013).

Typically, for EGS in crystalline rock, the reservoirs are primarily thought to be stimulated in shear (Evans *et al.*, 2005a; Zang *et al.*, 2014). Coulomb faulting theory is a typical way to assess shear failure potential. From Coulomb faulting theory, it is clear that an increase in pore pressure reduces the effective stress on a shear plane and brings the shear plane closer to failure. Indeed, in many instances of shear stimulation in crystalline rock, it is thought that the increase in pore pressure was the dominant contributor to the induced shear (Pearson, 1981; Pine and Batchelor, 1984; Jupe *et al.*, 1992; Deichmann and Giardini, 2009). From Coulomb faulting theory it is clear that it is possible to stimulate EGS reservoirs with injection pressures below the minimum principal stress. This is a fundamental difference between EGS stimulation and hydraulic fracturing operations. However, changes in total stress can also cause shear failure. For example, poroelastic stress changes have been shown to be significant in induced seismicity, where they have at times played an important role in fluid production (e.g., Segall (1989)), injection (e.g., Chen *et al.* (2017)), and hydraulic fracturing (e.g., Deng *et al.* (2016)) operation-induced seismicity. Poroelastic stressing differs from changes in pore pressure in that it does not necessarily lead to isotropic changes in effective stress. An increase or decrease in pore pressure will not directly lead to a change in the differential stress; however, importantly, the resulting poroleastic changes to total stress can be, and frequently are, anisotropic. This induced anisotropy allows poroelastic stress changes to have a significant influence on a shear plane's potential for failure, even when small in magnitude, as these changes are capable of either increasing or decreasing differential stress.

In this work, the stimulation of an EGS doublet well system will be investigated. Specifically, an investigation will be made into the possibility of guiding the stimulation from one well to another, as previously discussed by Baria *et al.* (2004). Unlike in Baria *et al.* (2004), however, this work will consider poroelastic stress changes, which have been shown to be relevant in EGS stimulations (Jacquey *et al.*, 2018), as well as address the three main stress regimes in generic scenarios. This investigation will be carried out by first stimulating one of the

doublet wells according to normal stimulation procedure. The stress changes associated with this first stimulation treatment will then encourage stimulation in a certain direction, allowing the stimulation treatment of the second well to be guided toward the stimulated region surrounding the first well. In this way the stress field is "preconditioned" before the stimulation of the second well. The advantage of this methodology is that it (1) helps ensure connectivity between the two doublet wells and (2) reduces the stimulation of less useful rock mass, which decreases the chance of accidentally inducing a large magnitude event on a nearby fault. This investigation will be performed with a poroelastic reservoir simulator where the permeability enhancement is based on the results of field studies. Even if, as mentioned above, further technological advancement may be necessary to allow horizontal EGS wells to be readily and cost-effectively drilled, here the investigation will concern the stimulation of horizontal EGS doublet wells drilled in critically-stressed crystalline rock. This investigation will also have implications for directionally-drilled wells; however, in these cases the results would depend on the inclination of the wells.

4.3 Methodology

In order to model the pressure and stress changes resulting from either fluid production or injection, a sequentially coupled 2-D plane strain poroelastic reservoir simulator is employed. Although the model is 2-D plane strain, it will be appropriate for modelling 3-D stress changes due to fluid production and injection activities from horizontal wells (Cheng, 1998). A bulk approach will be employed, meaning that fractures will not be explicitly modelled. This approach was taken because the fractured rock mass bulk behaviour is the focus and scale of the paper.

4.3.1 Flow Model

The combination of the conservation of mass of a single phase and Darcy's Law,

$$\frac{\partial(\phi\rho)}{\partial t} - \nabla \cdot \left(\frac{k}{\mu} \rho \left(\nabla P - \nabla \left(\rho g z \right) \right) \right) = q, \tag{4.1}$$

is used as the foundation of the flow model. Here ϕ is the porosity, ρ the fluid density, k the permeability, μ the fluid's dynamic viscosity, P the pore pressure, g the acceleration due to gravity, z the depth, and q the mass source terms. A fully implicit finite difference in time, finite volume in space framework (Aziz and Settari, 2002) is used to discretize the equation, which is then solved for the primary variable of pressure.

4.3.2 Mechanical Model

The mechanical model is based on the conservation of momentum,

$$\nabla \cdot \sigma^{'} + \nabla \left(\alpha P \right) = -f, \tag{4.2}$$

where $\sigma^{'}$ is the effective stress, α the Biot coefficient, and f represents the body forces. The sign convention is such that tension and extension are negative. This equation is then combined with the linear theory of poroelasticity (Biot, 1941; Rice and Cleary, 1976; Wang, 2000),

$$S_{ij} - \alpha P \delta_{ij} = \frac{E}{(1+\nu)} \epsilon_{ij} + \frac{E\nu}{(1+\nu)(1-2\nu)} \epsilon_{kk} \delta_{ij}, \tag{4.3}$$

in a finite element framework such that the stresses and strains associated with fluid production and injection can be solved for. Here, the total stress is represented by S, the Kronecker delta by δ_{ij}, the drained Young's Modulus by E, the drained Poisson's ratio by ν, and the strain by ϵ.

4.4 Problem Setup

The horizontal wells in this investigation will penetrate granitic basement rock, all at 4500 m depth, a similar depth to the EGS program of Soultz, France (Dorbath *et al.*, 2009). The granitic basement rock will be assumed to extend up to 2500 m depth, not unlike Basel EGS, Switzerland (Ladner and Häring, 2009). The overburden, however, will not be modelled and will be instead replaced with a constant applied stress based on a reasonable lithostatic gradient. The model boundaries are chosen such that the wells are far enough away to limit their effect on the simulations. As shown in Figure 4.1, the entire set-up will be modelled in 2-D plane strain, an appropriate approach to model horizontal wells (Cheng, 1998). The investigation of the effects of preconditioning will be investigated for reverse, strike-slip, and normal stress regimes. In each case, all three wells will be drilled parallel to S_{hmin}. Note that there are conflicting results regarding the orientation of reservoir creation during the stimulation of crystalline rock, with some operations indicating nearly parallel to S_{Hmax} (Häring *et al.*, 2008; Kwiatek *et al.*, 2019) and others indicating an offset such that reservoir creation occurs in the direction of strike of optimally oriented shear planes (Evans *et al.*, 2005a; Kim *et al.*, 2017, 2018) with it at times being difficult to determine exactly what happened in each case. It is further likely that the created reservoir geometry depends on the pre-existing discontinuities (Häring *et al.*, 2008). For this reason and given observational inconsistencies, it is difficult to determine the optimum orientation of the wells with respect to the stress field.
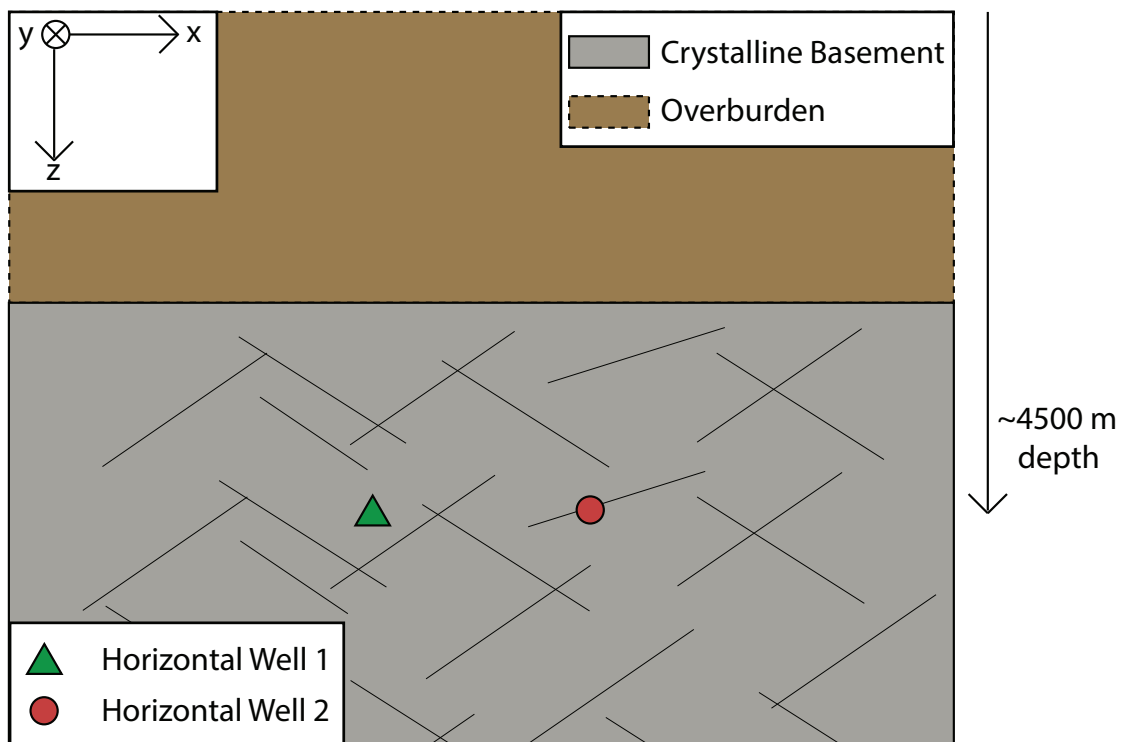
Figure 4.1 – Schematic of the problem setup for reverse and strike-slip faulting stress regimes. This represents a side view of two horizontal wells. The plane is normal to the orientation of the wells. The overburden is not modelled. Not to scale.

The initial pore pressure and vertical stress are calculated using typical hydrostatic and litho-static gradients, respectively. The assumption that the crust is critically stressed (Brudy *et al.*, 1997; Townend and Zoback, 2000; Zoback and Townend, 2001; Zoback *et al.*, 2002) is then used alongside the notion that the frictional strength of pre-existing faults is what limits the differential stress in the crust (Zoback and Healy, 1992; Brudy *et al.*, 1997; Zoback and Harjes, 1997). This allows for the direct calculation of the minimum principal stress in the normal faulting stress regime and the maximum principal stress in the reverse faulting stress regime. For example, in a normal faulting stress regime, the minimum possible horizontal stress that could be present on a supposed optimally-oriented fault can be calculated using the vertical stress, the pore pressure, and the assumed coefficient of friction. This process is repeated at all depths to calculate the initial minimum principal stress everywhere in the model. In the strike-slip faulting stress regime, the maximum principal stress is calculated using this methodology after the minimum principal stress is assumed to be 0.8 times the vertical stress. The coefficient of friction will be assumed to 0.6, although there have been indications that the coefficient of friction in granitic rock may be higher (e.g., Blanpied *et al.* (1995)). It will be assumed that the frictional coefficient remains constant during stimulation, in agreement with laboratory studies (e.g., Ishibashi *et al.* (2018)).

A reasonable value of the intact Young's Modulus for granite is 36 GPa (Villeneuve *et al.*, 2018). However, the rock is assumed to be fractured, meaning that, depending on the density of fractures, it may not be possible to use the intact Young's Modulus to describe the bulk behaviour (Villeneuve *et al.*, 2018). Using a moderate fracture density and geological strength index, the rock mass Young's Modulus was taken as 50 % of the intact Young's Modulus based on findings by Villeneuve *et al.* (2018). This results in an equivalent Young's Modulus of 18 GPa. The Biot coefficient of this fractured granite is taken as 0.76, similar to that found by (Evans *et al.*, 2003) for a fractured granite. The Poisson's ratio of the granite rock will be taken as 0.15, a relatively low value for granite due to its fractured nature (Walsh, 1965). A summary of the parameters used can be found in Table 4.1.

In order to avoid the compounding effects of thermal strains and to more clearly illustrate the effects of the stress preconditioning, the production and stimulation phases will be assumed to be isothermal (i.e., the reservoir will be assumed to be stimulated with water at reservoir temperature). This is obviously not a realistic scenario for a typical geothermal stimulation, and the probable effects of the thermal strains will be discussed in a later section.

4.4.1 Initial Bulk Permeability

Granite fractures can be assumed to have a high permeability (on the order of 10^{-12} m^2 (Ishibashi *et al.*, 2018)) compared to granitic matrix, which generally has a permeability on the order of 10^{-21} to 10^{-20} m^2 (Morrow *et al.*, 1986). For this reason, the matrix permeability will be assumed to be negligible compared to the fracture permeability, meaning that flow will be principally in the fractures, equivlanent to the level B distinction suggested by Cornet (2016),

Table 4.1 – *Model parameters*

Variable	Value	Unit
Fluid reference density, ρ_f	1000	$\frac{kg}{m^3}$
Fluid compressibility, c_f	$5e-10$	$\frac{1}{Pa}$
Fluid dynamic viscosity, μ	0.001	$Pa \cdot sec$
Granite drained Young Modulus, E_g	$18e9$	Pa
Granite drained Poisson's Ratio, ν_g	0.15	–
Granite initial bulk porosity, ϕ_g	0.02	–
Granite Biot coefficient, $\alpha_{s,g}$	0.76	–
Coefficient of friction, μ_f	0.6	–
Cell size, horizontal	43.1	m
Cell size, vertical	49.4	m

where flow is dominated by flow through reactivated fractures. In highly fractured and faulted crystalline rocks, the permeability of critically-stressed faults is much higher than that of faults which are poorly oriented for failure in the modern-day stress field (Barton *et al.*, 1995). Evans *et al.* (2012) found in a study of European case histories, that all crystalline rock masses investigated were critically stressed. Therefore, the optimally-oriented faults and fractures in the granite investigated here will be assumed to be initially at least somewhat permeable, even if they need further shear stimulation to become economically productive. This is supported by, for example, the pre-stimulation tests performed in granite in the Soultz HDR site and the Basel 1 enhanced geothermal system which yielded effective permeabilities of $3 \cdot 10^{-16}$ m^2 and 10^{-17} m^2 respectively (Evans *et al.*, 2005a; Häring *et al.*, 2008; Ladner and Häring, 2009). These tests also agree with the findings of Zoback and Townend (2001), who found that bulk permeability in the upper crust is high (10^{-17} m^2 to 10^{-16} m^2) due to critically-stressed faults. For this reason a starting value of 10^{-17} m^2 is used for bulk permeability, a value on the low end of bulk permeabilities seen in the field as mentioned above. The actual initial value of the permeability seen in the simulation will be lower than this value due its dependence on pressure and stress addressed in Section 4.4.2.

4.4.2 Shear Stimulation

Although stimulation in Enhanced Geothermal Systems may well be mixed mode between the creation of new fractures and the shearing of old fractures and faults (McClure and Horne, 2014; Norbeck *et al.*, 2018) (especially with injection pressures above the minimum principal stress), it is thought that shear failure is the dominant and most promising mechanism of reservoir creation in hard rock formations in EGS stimulation (Evans *et al.*, 2005a; Ziagos *et al.*, 2013; Zang *et al.*, 2014). Indeed, it has been previously shown in laboratory (e.g., Chen *et al.* (2000); Ishibashi *et al.* (2018)) and field (e.g., Jupe *et al.* (1992); Evans *et al.* (2005a); Ladner and Häring (2009); Guglielmi *et al.* (2015)) studies of granitic rock that fracture permeability increases with shear displacement. In this study specifically, it will be assumed that the

fractures and faults optimally oriented for shear in the prevailing stress field will be the planes upon which shear failure occurs, as seen, for example at Soultz (Evans *et al.*, 2005a).

Shear stimulation of granitic reservoirs results in a permeability increase that can vary depending on the site, even varying within in the same well (Evans *et al.*, 2005b). For example, permeability was increased by three orders of magnitude at the Fjällbacka Hot Dry Rocks Project, Sweden following stimulation (Jupe *et al.*, 1992), but Soultz, France only saw an increase in tranmissivity of a factor of fifteen when the effect of the stimulation is evaluated over the entire wellbore (Evans *et al.*, 2005b). Here, stimulation will be assumed to ultimately result in a permeability increase of a factor of 200, similar to the results of stimulation at Basel (Ladner and Häring, 2009) and the 1993 stimulation of a 550 m section of hole at Soultz (Evans *et al.*, 2005b).

The permeability used in the numerical model will be based on the notion of a changing aperture width with effective normal stress and a stepwise change in permeability occuring after a failure condition is reached (Miller and Nur, 2000; Miller, 2015). As in Miller (2015), permeability is assumed to take the form

$$k = k_0 e^{\frac{-\bar{\sigma}_n}{\sigma^*}}, \tag{4.4}$$

where k_0 is the initial permeability defined in Section 4.4.1, $\bar{\sigma}_n$ is the effective normal stress acting on the assumed shear plane, and σ^* is a normalizing constant taken as 100 MPa. Again following the model used by Miller (2015), the failure planes (with one assumed orientation for each reservoir block) will follow a normal distribution with a mean orientation corresponding to the optimal orientation in the given stress regime and a standard deviation of 0.02 radians. Note that this model implies, based on the assumed critically-stressed nature of the reservoir, that minuscule changes in stress or pore pressure could result in shear failure if a given cell is optimally oriented. In fact, however, it will be assumed that all cells require a Coulomb stress increase of 0.1 MPa before failure in addition to any stress increase required due to a non-optimal orientation. A 0.1 MPa Coulomb stress increase is a reasonable valuable for the initiation of slip (Stein, 1999). Coulomb stress, τ, is defined as

$$\tau = \tau_s - \mu_f (S_n - P), \tag{4.5}$$

where τ_s and S_n are the shear stress and normal stress on a potential shear plane (for calculations of Coulomb stress this plane is assumed to be optimally oriented in the prevailing stress regime) and μ_f is the static coefficient of friction. Generally, the Coulomb stress will increase when the maximum principal total stress increases, the minimum principal total stress decreases, or the pore pressure increases.
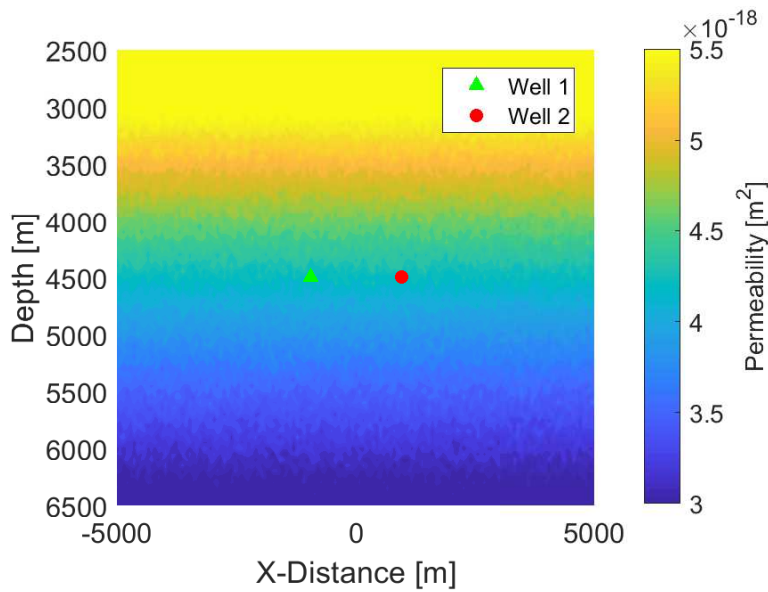
Figure 4.2 – The initial permeability field used in the reverse faulting case. The heterogeneity is due to the randomness associated with the permeability model.

If the Coulomb failure criteria for a given cell is reached, a stepwise change in permeability will occur (Miller and Nur, 2000; Miller, 2015) such that k_0 in Equation 4.4 will be replaced by k_0'; where k_0' is defined as

$$k_0' = x k_0. \tag{4.6}$$

Here, x is a multiplication factor taken to be equal to 200 based on the reviewed stimulation treatments mentioned above. This methodology for modelling permeability enhancement due to shear stimulation implies that permeability enhancement largely remains after high pressure is stopped. This is representative, for example, of the shear stimulation at the Soultz HDR site (Evans *et al.*, 2005a). Note that porosity is kept constant throughout the simulation, reflecting, for example, the methodologies of Miller and Nur (2000) and Baisch *et al.* (2010). This means that the coupling between the mechanical model and the flow model is entirely contained in the change of permeability. An example of the permeability field, Figure 4.2, is shown for the reverse faulting case. Although the permeability fields of each run will vary slightly due to the randomness associated with the permeability model, this variation is limited and the results are repeatable.

Table 4.2 – *Principal stress orientations.* The wells are drilled in the y-direction; however, the orientations of the principal stresses change depending on the stress regime. Note that S_x is S_{Hmax} and S_y is S_{hmin} in each case.

Regime	S_1	S_2	S_3
Normal Faulting	S_z	S_x	S_y
Reverse Faulting	S_x	S_y	S_z
Strike-Slip Faulting	S_x	S_z	S_y

4.5 Results

This section will be subdivided into three subsections, one subsection for each stress regime, Table 4.2. Beginning with a reverse faulting stress regime, two wells will be stimulated with the goal of connecting the stimulated regions of each well to create a doublet system. In the reverse faulting case, the comparison will be made between the case where the first well is flownback after its stimulation and the case where this first well is not flownback after stimulation and instead the second well is stimulated immediately. For the remaining stress regimes, however, the flowback case will not be presented and instead the effect of the first stimulation treatment on the second will be shown by comparing the average propagation lengths of the stimulated region outside of the two wells and inside the two wells.

4.5.1 Reverse Faulting

In a reverse faulting stress regime, the maximum principal stress is horizontal and the minimum principal stress is vertical. Therefore, increases in the total horizontal stress (specifically the maximum horizontal stress, S_{Hmax}) and decreases in the total vertical stress will generally result in an increase in Coulomb stress.

In this case, the two wells will be located at a depth of 4500m and separated by 1884m, with the midpoint between the two wells having and X-Distance coordinate of 0m, Figure 4.2. The stimulation treatment procedure is begun by first stimulating the left-most of the two wells with an injection rate of 0.014 $\frac{kg}{msec}$, which corresponds to 7.0 $\frac{kg}{sec}$ for a 500 m long well length section, over a period of three days. This stimulation treatment would be similar to, but slightly smaller than, the 2000 stimulation of GPK2 at Soultz-sous-Forêts, for example (Dorbath *et al.*, 2009). The permeability increases and Coulomb stress changes associated with this stimulation treatment are shown in Figure 4.3.

Next, the first well is flown back with a rate of 2.33 $\frac{kg}{sec}$ over a period of 9 days, resulting in the entire fluid mass that was injected with the stimulation treatment being reproduced. Note that it is probably unlikely that the entire injected mass would be reproduced in reality; however, the purpose here is simply to illustrate the effect of flowback on the far-field poroelastic stresses. The permeability above and below the previously stimulated region increases slightly during this flow back period, Figure 4.4a. This is due to production inducing increased
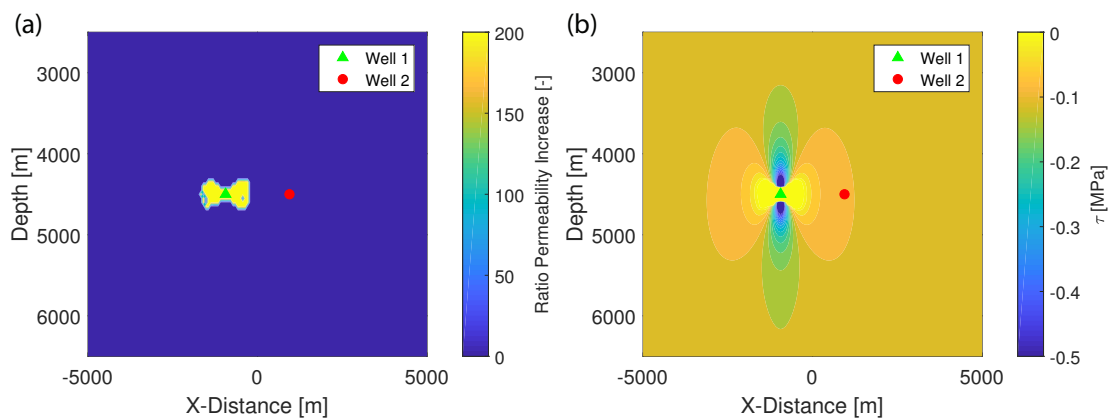
Figure 4.3 – The result of the stimulation of well 1 in the reverse faulting stress regime case. (a) The permeability enhancement associated with the stimulation treatment (t=3 days). (b) The Coulomb stress changes resulting from the stimulation treatment (t=3 days).

total horizontal stresses and decreased total vertical stresses in this region. The Coulomb stress changes associated with this flowback period, Figure 4.4b, show the result of these stress changes with increases above and below the previously stimulated region. This type of increased Coulomb stress and shear failure occurring above production zones is analogous to the reverse faulting sometimes seen during hydrocarbon production (e.g., Segall (1989)). Figure 4.4b also indicates that the Coulomb stress in-between the two wells has decreased since flowback began, when compared to Figure 4.3b.

At this stage, the second well is stimulated using the same stimulation treatment that was used in the first well. The Coulomb stress changes, Figure 4.4c, and permeability field enhancements, Figure 4.4d, indicate that the two stimulated zones were not connected in this case, being still separated by 362m of unstimulated rock mass.

If, instead of flowing back the well, the well is simply shut-in and the second stimulation begun immediately after the termination of the first, the Coulomb stress changes associated with the first stimulation will largely remain during the second stimulation. As these Coulomb stress changes are encouraging failure and are larger closer to the first well, they may potentially cause the stimulation treatment of the second well to be directed towards the stimulated zone of the first well.

To test this procedure, the first well is stimulated as before with an injection rate of 7.0 $\frac{kg}{sec}$ over three days. Following this, the second well is stimulated immediately after the first stimulation treatment with no flowback period. The stimulation treatment again consists of an injection rate of 7.0 $\frac{kg}{sec}$ over three days. In this way, the Coulomb stress changes associated with the first stimulation treatment remain and help to ensure connection between the two wells' stimulated regions.

At the midpoint between the two wells, the Coulomb stress just before the second stimulation
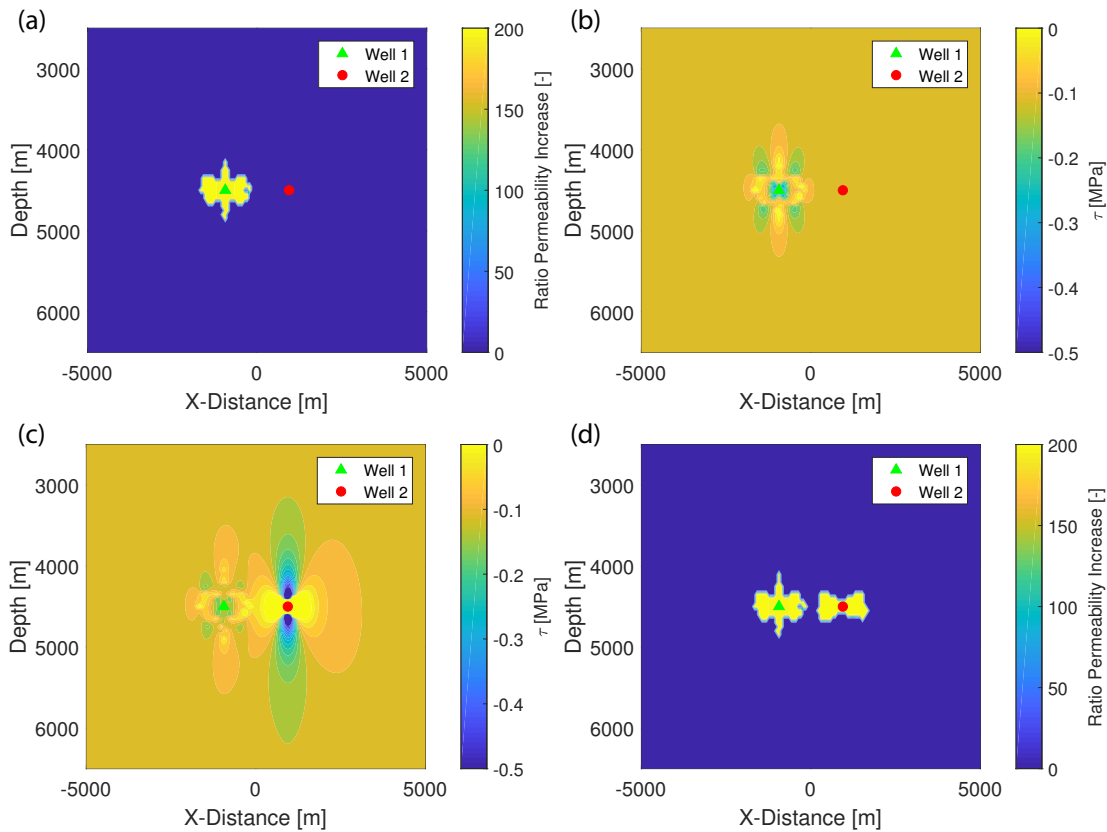
Figure 4.4 – For the reverse faulting stress regime case, the result of flowing back the first well before stimulating the second well. (a) The permeability enhancement at a time immediately after the flowback period (t=12 days), note the enhancement that has occurred above the initially stimulated region. (b) The Coulomb stress at a time immediately after the flowback period of the first well (t=12 days). The Coulomb stresses in-between the two wells has been reduced since the initial stimulation treatment, when compared to Figure 4.3b. (c) The Coulomb stresses after the stimulation of the second well (t=15 days). (d) The permeability enhancement at the end of the entire procedure (t=15 days). The two wells are not connected with a separation of the two stimulated zones of 362m.
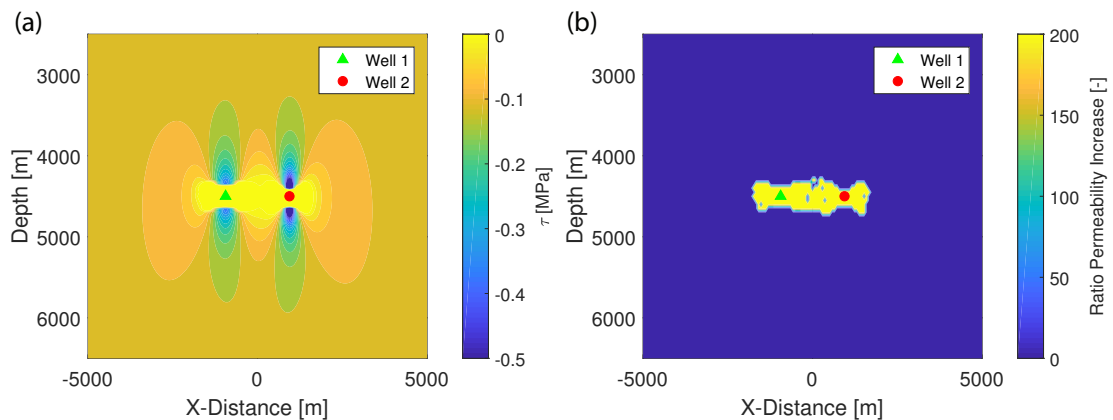
Figure 4.5 – For the reverse faulting stress regime case, the result of not flowing back the first well before beginning the stimulation treatment of the second well. (a) The Coulomb stresses after the stimulation of the second well (t=6 days). (b) The permeability enhancement at the end of the entire procedure (t=6 days). The stimulated zone of each well extends and average 761m away from the other doublet well and 942m towards it.

had increased by 0.056 MPa, Figure 4.3b. However, at the location of equivalent distance from well 2 but in the opposite direction (a depth of 4500m and an X-distance of 1884m), the Coulomb stress just before the second stimulation has only increased by 0.0056 MPa. These differences in Coulomb stress change are what ultimately cause the stimulation of well 2 to be directed towards the stimulated region of well 1 as opposed to propagating equal distances in both directions. In fact, the stimulation treatments of both wells, on average, propagate 761 m away from the other doublet well and 942 m towards it, Figure 4.5b, meaning that the stimulated zones extend over 20% farther in-between the two wells than they do on the outside of the two wells. Note that the average stimulation length of each well here is shorter than, for example, the seismicity cloud resulting from stimulation at Soutlz-sous-Forêts (Evans *et al.*, 2005a).

Unlike the results shown by Baria *et al.* (2004), the direction of the stimulation treatment here is accomplished entirely by changes in stress, not pore pressure. At an X-Distance of 0 (the center point between the two wells - 942m from each well), the pore pressure change after the stimulation of the first well is zero. The change in the S_{Hmax}, however, is 0.045 MPa, and results in over half of the Coulomb stress change required for failure.

For the remaining two stress regimes, a flowback case will not be shown. Instead, the average distances of propagation will be used to demonstrate the degree to which the stimulation treatment was effectively directed.

4.5.2 Strike-Slip Faulting

In a strike-slip faulting stress regime, the maximum and minimum principal stresses are both horizontal. The stress changes induced by injection through a horizontal well will be anisotropic. For example, during the stimulation of the first well, Figure 4.6a and b, the horizontal stress perpendicular to the first well will be experience greater compressive changes than the horizontal stress parallel to it at large distances. Assuming the well is drilled parallel to the minimum principal stress, this means that the maximum principal stress will increase (becoming more compressive) more than the minimum principal stress, resulting in an increase in differential stress and Coulomb stress. These Coulomb stress changes will be more pronounced near the stimulated region of the first well, meaning that the stimulation treatment of the second well will be more likely to propagate towards the first well than in the other direction. In this case, the two wells will be located at a depth of 4500m and separated by 1450m, with the midpoint between the two wells having and X-Distance coordinate of 0m.

The stimulation treatment procedure is begun by first stimulating the left-most of the two wells with a stimulation rate of 0.0247 $\frac{kg}{msec}$, which corresponds to 12.37 $\frac{kg}{sec}$ for a 500 m long well length section, over a period of three days, Figure 4.6a. This stimulation treatment would be similar to, but slightly smaller than, the 2000 stimulation of GPK2 at Soultz-sous-Forêts, for example (Dorbath *et al.*, 2009). Next, injection into the first well is stopped and the second well is stimulated with exactly the same stimulation treatment. The first well does not undergo a flowback period before the stimulation of the second well.

At the midpoint between the two wells, the Coulomb stress just before the second stimulation has increased by 0.042 MPa, Figure 4.6b. However, at the location of equivalent distance from well 2 but in the opposite direction (a depth of 4500m and an X-distance of 1450m), the Coulomb stress just before the second stimulation has only increased by 0.004 MPa. These differences in Coulomb stress change are what ultimately cause the stimulation of well 2 to be directed towards the stimulated region of well 1 as opposed to propagating equal distances in both directions. In fact, the stimulation treatments of both wells, on average, propagate 543 m away from the other doublet well and 725 m towards it, Figure 4.6d, meaning that the stimulated zones extend over 30% farther in-between the two wells than they do on the outside of the two wells.

This change in Coulomb stress that guides the stimulation treatment of the second well towards the first well is caused by changes in total stress, not changes in pore pressure. At the midpoint of the two wells, the change in the maximum horizontal stress just before the second stimulation is 0.145 MPa whereas the change in the pore pressure is 4e-7 MPa.

4.5.3 Normal Faulting

In a normal faulting scenario, the vertical stress is the maximum principal stress. In the case that two doublet wells are drilled horizontally in a direction parallel to the minimum principal
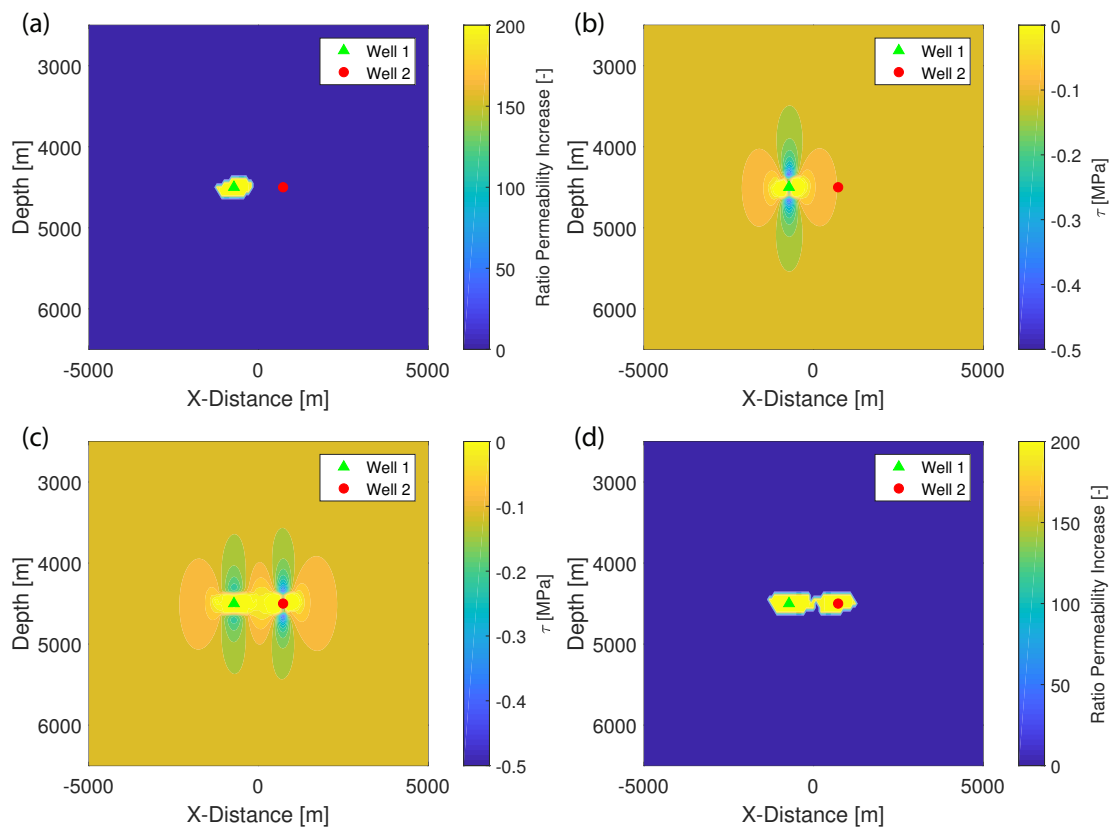
Figure 4.6 – The result of the stimulation treatment in a strike-slip faulting stress regime. (a) The permeability enhancement associated with the stimulation treatment of the first well (t=3 days). (b) The Coulomb stress changes resulting from the stimulation treatment of the first well (t=3 days). (c) The Coulomb stresses after the stimulation of the second well (t=6 days). (d) The permeability enhancement at the end of the entire procedure (t=6 days). The stimulated zone of each well extends and average 543m away from the other doublet and 725m towards it.

stress, the injection-induced poroelastic stress changes caused by the stimulation of the first well will be expected increase the total vertical stress primarily in locations above and below the stimulated well. This implies that the poroelastic stress changes will primarily encourage shear failure in locations which are vertically in-line with the well and not those horizontally in-line. For this reason, the wells are aligned vertically with a separation of 1000m at depths of 3500m and 4500m.

The stimulation treatment procedure is begun by first stimulating the shallower of the two wells with a stimulation rate of 0.0125 $\frac{kg}{msec}$, which corresponds to 6.25 $\frac{kg}{sec}$ for a 500 m long well length section, over a period of three days, Figure 4.7a. This stimulation treatment would be similar to, but slightly smaller than, the 2000 stimulation of GPK2 at Soultz-sous-Forêts, for example (Dorbath *et al.*, 2009). Next, injection into the first well is stopped and the second well is stimulated with exactly the same stimulation treatment. The first well does not undergo any flowback period before the stimulation of the second well.

At the midpoint between the two wells (a depth of 4000m and an X-distance of 0m), the Coulomb stress just before the second stimulation has increased by 0.047 MPa, Figure 4.7b. However, at the location of equivalent distance from well 2 but in the opposite direction (a depth of 5000m and an X-distance of 0m), the Coulomb stress just before the second stimulation has only increased by 0.002 MPa. These differences in Coulomb stress change are what ultimately cause the stimulation of well 2 to be directed towards the stimulated region of well 1 as opposed to propagating equal distances in both directions. In fact, the stimulation treatments of both wells, on average, propagate 400 m away from the other doublet well and 500 m towards it, Figure 4.7d, meaning that the stimulated zones extend 25% farther in-between the two wells than they do on the outside of the two wells.

This change in Coulomb stress that guides the stimulation treatment of the second well towards the first well is caused by changes in total stress, not changes in pore pressure. At the midpoint of the two wells, the change in the vertical stress just before the second stimulation is 0.159 MPa whereas the change in the pore pressure is 1.65e-5 MPa.

4.6 Discussion

4.6.1 Assumptions

Isothermal Simulations

The influence of temperature has not been considered in the analyses although temperature-induced stresses may play a significant role during EGS stimulation (e.g., Ghassemi and Tao (2016)). This was primarily done to simplify the analyses and more clearly illustrate the effects of stress preconditioning. In case-specific applications of this methodology, temperature effects should be considered. In fact, it may even be possible to design a stimulation procedure such that temperature-change induced stresses further precondition the stress field in a
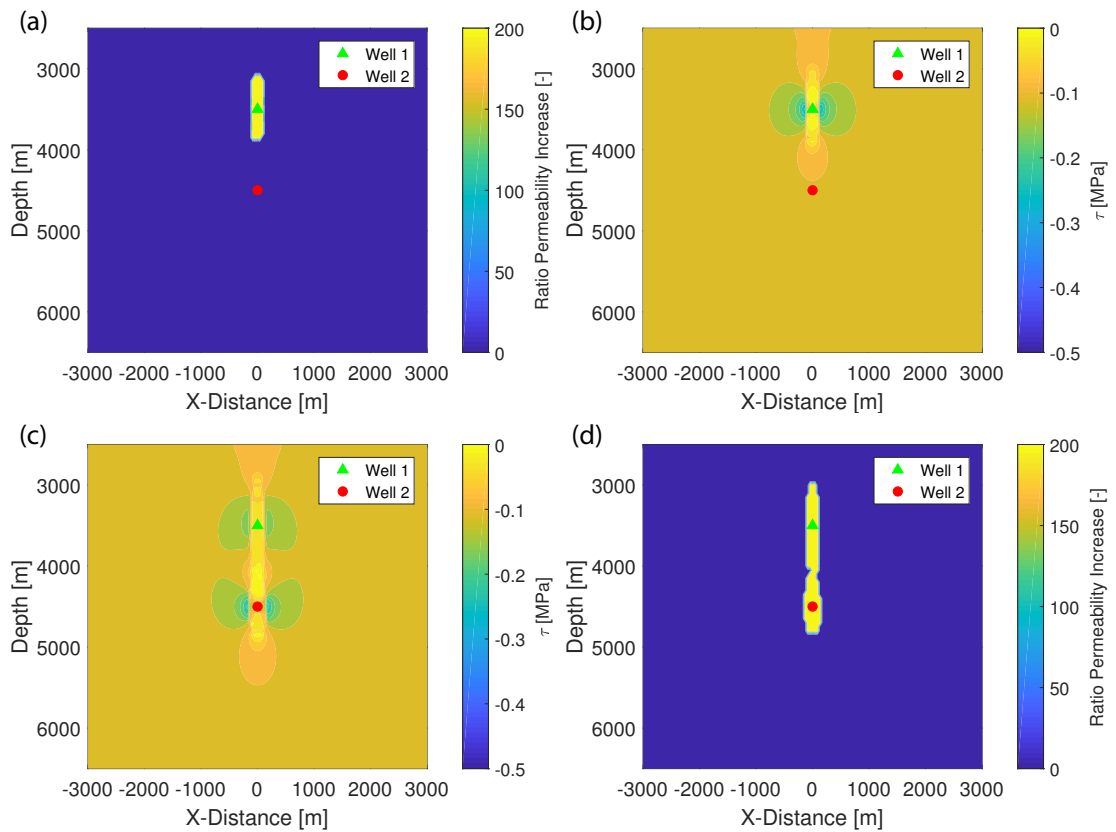
Figure 4.7 – The result of the stimulation treatment in a normal faulting stress regime. (a) The permeability enhancement associated with the stimulation treatment of the first well (t=3 days). (b) The Coulomb stress changes resulting from the stimulation treatment of the first well (t=3 days). (c) The Coulomb stresses after the stimulation of the second well (t=6 days). (d) The permeability enhancement at the end of the entire procedure (t=6 days). The stimulated zone of each well extends and average 400m away from the other doublet and 500m towards it.

beneficial manner.

To evaluate the influence of the temperature-change induced stresses such that their neglection can be justified, the flow model was extended to include the conservation of energy,

$$\frac{\partial H_m}{\partial t} + \nabla \cdot \Gamma + \nabla \cdot f_t = q_T, \tag{4.7}$$

where H_m is the enthalpy of the entire medium, Γ is the heat conduction, f_T is the convection, and q_T represents the source terms. The equation is discretized and solved fully implicitly with the mass conservation equation, yielding both pressure and temperature. Equilibrium is assumed between the fluid and rock temperature in each cell. To simplify the analysis, the fluid density and viscosity are assumed to remain constant with change in temperature. In the mechanical model, the thermal strain, ϵ_T,

$$\epsilon_T = \alpha_T \Delta T, \tag{4.8}$$

is added to the mechanical strains before the computation of stress changes. Here, α_T is the coefficient of linear thermal expansion and T is the temperature. A surface temperature of 30 ^0C and a thermal gradient of 0.035 $\frac{^0C}{m}$ are assumed. The thermal conductivity of the water and granite are assumed to be 0.67 and 2.5 $\frac{W}{mK}$ respectively. The heat capacity of the water and granite are assumed to be 4183 and 950 $\frac{J}{kgK}$ respectively. The coefficient of linear expansion of granite is taken as $40 \cdot 10^{-6}$ $\frac{1}{^0C}$, and the fluid enters the reservoir at a temperature of 47 ^0C.

Using this updated model, the reverse faulting case was rerun up to the point just before the second stimulation. At the midpoint between the two wells, the difference in change in Coulomb stress in this case and in the case presented previously where temperature effects were not considered is 0.0002 MPa. Considering that the Coulomb stress change due only to poroelastic effects was 0.056 MPa, this justifies not including stress changes due to temperature in the model. These Coulomb stress changes are small due to the small temperature changes of the system. The small temperature changes are due to the relatively small injection volumes (approximately 1620 m^3 over 500 m of wellbore over 3 days). In order to keep the model as simple as possible and better illustrate the effects of poroelastic stress changes, the effect of temperature is therefore not included in the model.

Stress Criticality

In the simulations presented here, the reservoir was assumed to be critically stressed based on findings by Evans *et al.* (2012). In reality, however, knowledge of the in situ stress state is very important for reservoir stimulation activities, and the state of stress should ideally be

investigated in each case before the start of operations. If the crust is less critically stressed than in the presented cases, larger pore pressure changes will be needed to stimulate the reservoir as shear failure would become more pore-pressure dominated. The poroelastic stresses that guide the second stimulation treatment will make up less of the required changes for failure. For instance, in this case it was assumed that a Coulomb stress change of 0.1 MPa is required to induce shear failure. The Coulomb stress change induced by the preconditioning at the mid-point between the wells was approximately 0.05 MPa, meaning that it made up half of the required stress change. However, if the required Coulomb stress change was instead 0.5 MPa, this preconditioning stress would only make up ten percent of this value and it would presumably play a smaller role in directing the second stimulation treatment. Conversely, this would mean larger pore pressure changes would have been needed to stimulate the first well. This would result in larger induced poroelastic stress changes.

Stress Redistribution

The model used here does not include stress redistribution associated with shear failure occurring during stimulation. Previous studies (e.g., Catalli *et al.* (2013)) have shown that stress redistribution associated with shear failure during hydraulic stimulation can have a significant impact on future events. Indeed, stimulation treatments of granitic rock have been shown to be capable of altering the stress field through aseismic slip occurring within the stimulated zone (e.g., Cornet and Julien (1989); Schoenball *et al.* (2014)). Although these stress changes have been shown to be large (on the order of ten MegaPascals), they are thought to be largely confined to the stimulated region (Schoenball *et al.*, 2014). It is less clear how to rigorously account for the stress changes associated with this type of slip for regions outside of the stimulated zone. However, it is possible to come up with a far-field estimate, if, for example, the Coulomb stress changes occurring near the location of the second well can be calculated assuming the energy release equivalent to a dynamic earthquake of M_w 3.0 occurring at the wellbore of the first well. This amount of energy release due to aseismic slip is approximately equal to that which occurred at the Le Mayet de Montagne granitic test site (Cornet, 2016). An M_w 3.0 earthquake corresponds to a fault length of approximately 330 m according to typical earthquake scaling laws (Stein and Wysession, 2003). King *et al.* (1994) found unclear correlations between aftershocks and Coulomb stress changes after distances of about 3 fault lengths, which is less than the separation between the two wells in each of the three cases presented. Given that correlation between stress changes and aftershocks was seen for positive Coulomb stress changes of the order of 0.01 MPa (King *et al.*, 1994), the stress changes associated with aseismic slip in the reservoir at the location of the second well are most likely not significantly larger than the poroelastic stress changes induced by the treatment itself (0.05 MPa at the midpoint of the two doublet wells in the reverse faulting case where the well separation is the largest). Therefore, although it would be unreasonable to claim that stress changes associated with slip in the stimulated zone of the first well are negligible for the stimulation of the second well, it can be concluded that the poroelastic stress changes are significant in their own right. For this reason, the poroelastic stress changes shown

here may still be significant enough to direct a given stimulation treatment. However, in order to better evaluate the possibility of directing a stimulation treatment, the effect of the stress redistribution associated with the events occurring during the first stimulation treatment on the far-field stresses should be investigated. Regardless of whether this stress preconditioning methodology is employed or not, stress redistribution associated with shear failure in the stimulated region of the first well is likely to occur.

Use of an Elastic Model

The mechanical model used here is also entirely elastic. It is probable that a more rigorous approach would alter the magnitude of the stress changes found. For example, Pijnenburg *et al.* (2018) recently showed that the use of an elastic simulator during the modelling of fluid production in a sandstone likely under-predicts strains and over-predicts total stress changes in the case that the deformation is inelastic. Essentially, the use of a linear elastic simulator here corresponds to the assumption that the non-linear responses of the system remain localized such that the mechanical behaviour of the rock mass as a whole can be well represented by such a linear elastic model (Cornet, 2016). The plane strain assumption is a suitable one for horizontal wells (Cheng, 1998).

Further, certain parameters are likely to change throughout the stimulation procedure. For example, the relatively low Poisson's ratio chosen due to the fractured nature of the rock is likely to increase as shear failure occurs (Walsh, 1965). This would have implications for the magnitude of the changes to each component of the stress tensor. It is also probable in reality that many of the poroelastic parameters used here vary with effective stress (e.g., Walsh (1965); Bernabé (1986)). This variation was not accounted for in the analyses performed here.

4.6.2   Implications

Variations on this approach could be imagined. For example, stimulating both wells at the same time would allow for both wells to benefit from advantageous stress changes. However, each well would experience less preconditioning Coulomb stress changes than the second well experienced during these simulations. This is due to the fact that the pore pressures will not yet have reached their post-stimulation values. Additionally, this approach would require sufficient pumping power to stimulate two wells at once. Another possibility would be to use the poroelastic and thermoelastic stress changes associated with an existing doublet-well system to direct the stimulation treatment of a third well. This would presumably incur larger stress changes than those used here and would allow for the more efficient direction of the stimulation of the third well.

It should be noted that one possible drawback to not flowing back the wells is the possibility of inducing a large seismic event. Frequently these large magnitude events occur after stimulation activities have been stopped (e.g., (Häring *et al.*, 2008; Kim *et al.*, 2018)), and it has even

been suggested that flowing the wells back could help prevent seismicity (McClure, 2015). Despite this, the methodology proposed here is designed to use the built up poroelastic stresses due to the increased pore pressure associated with injection to facilitate the stimulation of another well. As shown in Section 4.5.1, flowing the well back makes this process significantly less effective.

The successful implementation of this methodology would yield a number of advantages. Engineers would have higher confidence in connecting two wells separated by a given distance when using this methodology as opposed to the case where the wells are flown back before the next stimulation. Alternatively, wells could be separated by a larger distance, reducing the risk of short-circuiting and increasing the contact time of the circulating fluid with the reservoir. Additionally, because this methodology encourages the second stimulation treatment to advance towards the first well, it seems less likely that this stimulation treatment will stimulate a large fault as the total stimulated reservoir volume is reduced for a given well separation distance. Further, it can be imaged that this type of technique could be implemented in combination with other similar techniques, such as fluid production, to provide reservoir engineering solutions for large-scale reservoir creation. Of course, the ability to influence the direction of a stimulation treatment does not mean that operators have total control over how the stimulation treatment propagates, simply that the stimulation treatment is guided such that it is more likely to advance in a certain direction.

4.6.3 Future Outlook

These results potentially have implications for hydraulic fracturing. Although not directly applicable, it has been shown that poroelastic stress changes during injection are able to alter the stress field and affect a shear stimulation. Mode I fracturing depends on the pore pressure overcoming the minimum principal stress. It can therefore be imagined that both injection and production are capable of altering the minimum stress such that mode I fracture propagation is either attracted to or repelled from a particular region of a reservoir. In fact, it has already been shown that hydraulic fracture propagation is affected by pre-existing injection and production wells (e.g., Berchenko and Detournay (1997); Gao *et al.* (2019)). Further investigations should be performed on how to purposefully use these stress changes to help direct hydraulic fracturing treatments.

The numerical results found here indicate that a shear stimulation treatment can be directed in a critically-stressed crust. Following this, experiment work should be carried out to try to achieve these results in a real experimental rock laboratory. Should those experiments be successful, other methodologies for directing stimulation treatments should be investigated, especially ones capable of directing stimulation treatments in less critically-stressed reservoirs.

4.7 Conclusion

In this work, shear stimulation treatments in critically-stressed fractured granitic rock from horizontal wells have been directed via the stress changes associated with a previous stimulation to preconditioning the stress field for the next stimulation. These stress changes increase the Coulomb stress primarily in the region between the two wells which results in the stimulation treatment of the second well preferentially propagating towards the first. These results have implications for reservoir engineering applications in EGS reservoirs. Further research should be performed to both confirm the results in meso-scale field demonstrations and develop methodologies for directing stimulation treatments in less critically-stressed reservoirs.

5 The propagation of a planar-3D hydraulic fracture across a stress jump

The results of this chapter are being prepared for a potential journal publication.

Contribution of candidate: co-development of scaling analysis, applications to CCS, performed simulations, analysis of results, writing of text.

Contributions not by candidate (B. Lecampion & H. Zia): co-development of scaling analysis (including teaching the candidate how to perform a scaling analysis), development of PyFrac simulator, initial idea to perform scaling analysis, set-up/installation of PyFrac, general guidance.

5.1 Chapter Summary

In analyzing the problem of the propagation of a planar 3D hydraulic fracture across a stress jump, a scaling analysis was performed indicating that the breakthrough of the hydraulic fracture depends on a dimensionless parameter, G_σ, which is specific to the regime of propagation of the hydraulic fracture. By performing numerical simulations with PyFrac, a planar 3D hydraulic fracture simulator (Zia and Lecampion, 2019), this dependence of breakthrough on G_σ was demonstrated for the viscosity-storage, toughness-storage, viscosity-leak-off, and toughness-leak-off regimes. It was found that below certain values of G_σ a hydraulic fracture is not contained. Further, it was found that asymptotic breakthrough, when achieved, is inversely proportional to that regime's G_σ. The results for the viscosity-storage regime were compared against experimental results from Garagash *et al.* (2008). Additionally, the scaling behaviour of fracture half-length, fracture width, and pressure in each regime were compared against known solutions for radial and, where applicable, Perkins-Kern-Nordgren scalings. In the storage regimes, it was found that the behaviours of fracture half length and fracture width match well with radial scalings initially, before, in the viscosity-dominated regime, conforming to Perkins-Kern-Nordgren scalings at late time, after breakthrough. In the leak-off regimes, less satisfactory results were achieved due largely to the difficulties in achieving leak-off dominated propagation with the simulator. The results were interpreted and applied to suggest that depleted hydrocarbon reservoirs can be hydraulically fractured and employed for carbon storage.

5.2 Introduction

The propagation of hydraulic fractures has been a popular subject of research since at least the 1950's (Khristianovic and Zheltov, 1955; Hubbert and Willis, 1957). A variety of models exist to model the propagation of hydraulic fractures with varying degrees of complexity and fidelity. For example, the Khristianovic-Geertsma de Klerk (KGD) model (Khristianovic and Zheltov, 1955; Geertsma and de Klerk, 1969) assumes a large fracture height and is therefore not appropriate for long, contained hydraulic fractures. Another example includes the Perkins-Kern-Nordgren (PKN) model (Perkins and Kern, 1961; Nordgren, 1972), applicable to fractures which are vertically contained and propagate horizontally, with one-dimensional flow. This type of model is not able to handle layered reservoirs nor does it account for toughness. Similarly, the radial, or penny-shaped, model is also more suitable for homogeneous reservoirs. A large improvement came to the PKN-type model with the advent of a Pseudo-3D model (P3D) (Simonson *et al.*, 1978). A P3D model is able to account for different confining stresses in various layers, but only accounts for homogeneous reservoir properties and struggles with uncontained fracture growth. Note that while P3D models account for toughness while determining vertical propagation, they do not account for it while determining lateral propagation. P3D models also tend to either over- or under-estimate height growth depending on the nature of the propagation (Bunger and Lecampion, 2017). Planar 3D models (PL3D) (e.g., Siebrits and Peirce (2002); Peirce and Detournay (2008); Zia and Lecampion (2019)) are more accurate than PKN or P3D models but are also computationally more expensive. The PL3D model is better suited to handle uncontained fracture growth and layered reservoirs. A more detailed discussion of the differences between the various models can be found in Adachi *et al.* (2007).

It has been found that certain dimensionless groups control the propagation of a hydraulic fracture (Detournay, 2004). Essentially, if the energy dissipated by viscous flow is small compared to the energy dissipated by the creation of new fracture area, the fracture is said to be propagating in the toughness-dominated regime. In the opposite case, the fracture is said to be propagating in the viscosity-dominated regime. Further, the fracture is said to be either in the leak-off or storage domain depending on the significance of the leak-off (e.g., Detournay *et al.* (2007)). The combination of these two classifications results in four principal asymptotic regimes, with semi analytical and numerical solutions being provided for each (e.g., Detournay (2004); Bunger *et al.* (2005); Detournay *et al.* (2007); Peirce and Detournay (2008); Hu and Garagash (2010); Garagash *et al.* (2011); Moukhtari *et al.* (2019)): the storage-viscosity, or M, asymptote, the storage-toughness, or K, asymptote, the leak-off-viscosity, or $\tilde{M}$, asymptote, and the leak-off-toughness, or $\tilde{K}$, asymptote. Additionally, analytical asymptotic frameworks have been developed where two physical processes might be dominating at the same time (Mitchell *et al.*, 2007). All of these types of analyses allow for insight into what governs the propagation of a hydraulic fracture and can even potentially offer operators a ready-made solution for making predictions about a given hydraulic fracture in the field. Indeed, most hydraulic fracture are thought to propagate in the viscosity-dominated regime (Detournay *et al.*, 2007), making this solution particularly applicable.

There have also been similar analyses performed for specific cases of hydraulic fractures, such as those that propagate through a stress jump (e.g., Wu *et al.* (2008); Adachi *et al.* (2010)). Indeed, it has been suggested that stress jumps promote fracture containment (Harrison *et al.*, 1954; Simonson *et al.*, 1978; Nolte and Smith, 1981; Warpinski *et al.*, 1982a,b; El Rabaa, 1984; Warpinski and Teufel, 1989; Jeffrey and Bunger, 2009), and there have been numerous examples of stress contrasts causing the termination of hydraulic fractures (van Eekelen, 1982; Warpinski and Teufel, 1989; Sone and Zoback, 2014). Indeed, some authors have suggested the artificial creation of a stress contrast induced through production to help ensure the containment of a hydraulic fracture (van Eekelen, 1982).

Stress jumps can either be naturally occurring or induced by operators. The notion of a critically-stressed crust (Harrison *et al.*, 1954; Brudy *et al.*, 1997; Townend and Zoback, 2000; Zoback and Townend, 2001; Zoback *et al.*, 2002) predicts that layers in the subsurface with a higher coefficient of friction will be able to support larger differential stress. In a normal faulting stress regime, for example, the vertical stress is generally given by the lithostatic gradient (Zoback, 2007), implying that larger minimum principal stresses will occur in layers with a lower coefficient of friction. Differences in coefficients of friction between layers can therefore lead to stress jumps (e.g., van Eekelen (1982); Alberty and McLean (2001); Gunzburger and Cornet (2007); Sone and Zoback (2014)). Additionally, stress jumps can be induced (van Eekelen, 1982; Alberty and McLean, 2001). This is most commonly seen during depletion scenarios, where poroelasticity is responsible for a decreasing total horizontal stress as pore pressure is reduced (e.g., Segall and Fitzgerald (1998); Chan and Zoback (2002); Zoback (2007)); however, in principal, similar results can be achieved through pore pressure increases and thermoelasticity (e.g., Segall and Fitzgerald (1998); Cheng (2016)).

Previous investigations into the effect of a stress jump on the propagation of a hydraulic fracture have included both experimental and numerical analyses on the propagation of a planar 3D hydraulic fracture, where it was found that fracture growth strongly favors propagation into zones with a lower confining stress (Wu *et al.*, 2008), a finding supported by other numerical studies (Peirce and Detournay, 2008; Peirce, 2016). Further, Adachi *et al.* (2010) performed a scaling analysis on the pseudo-3D model of a hydraulic fracture and were able to determine explicitly when breakthrough takes place as well as under which conditions breakthrough becomes unstable, resulting in a runaway hydraulic fracture. These results were in contrast to Palmer and Carroll (1983) whose parametric analysis indicated that fracture height growth through a stress contrast was independent of toughness in the case of large stress contrasts. Additionally, Garagash *et al.* (2008) matched the result of their scaling analyses to a plane strain experiment in a viscosity-dominated case with no fluid leak-off. Experimental testing has also found not only that stress contrasts can contain a fracture, but that these contrasts are more effective in softer material and in thicker reservoirs reservoirs (El Rabaa, 1984).

The goal of this investigation is to better understand how a fracture breaks through a stress barrier in viscosity and toughness-dominated conditions with the planar 3-D model for a propagating hydraulic fracture. The effect of leak-off will also be investigated. By understand-
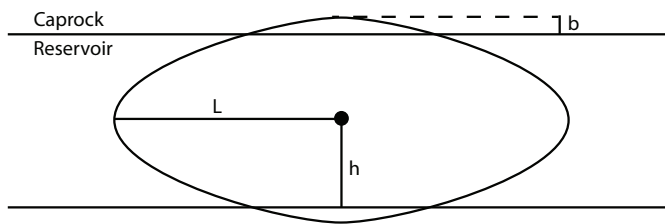
Figure 5.1 – A cross-sectional view of the reservoir-caprock system. The injection well, a point source marked by a black dot, is located in the middle of the reservoir, equidistant from two bounding interfaces, such that the problem has a horizontal line of symmetry. The half height of the reservoir is shown as h. The fracture outline is shown, with it's half length designated as L and breakthrough, b. The fracture encounters a compressive confining stress jump when leaving the reservoir and entering the caprock.

ing which dimensionless parameter(s) control breakthrough, it will be possible to provide first-order estimates and engineering charts to operators such that breakthrough can be predicted without the use of a hydraulic fracturing simulator or interpretations of pressure records, which are difficult to use to predict fracture propagation (Lecampion *et al.*, 2017). Comparisons using the numerical tool PyFrac (Zia and Lecampion, 2019), a planar 3D hydraulic fracturing simulator, will be made to other analyses, both analytical and experimental in nature. The assumption of a critically-stressed crust will then be used to discuss the global relevance of stress jumps for the possibility of hydraulic fracturing in potential carbon storage reservoirs.

5.3 Methodology

In order to evaluate the effect of a stress jump on hydraulic fracture propagation in a PL3D geometry, a scaling analysis will be compared to simulations using the open source hydraulic fracture propagation simulator PyFrac (Zia and Lecampion, 2019). While more complete descriptions can be found in Detournay (2016); Lecampion *et al.* (2018); Zia and Lecampion (2019), the governing equations will be briefly restated and described here for completeness. The dimensionless groups associated with these governing equations will then be provided for the various regimes.

5.3.1 Governing Equations

Before introducing the governing equations, it is helpful to introduce the setup of the problem, Figure 5.1. In this image, the geometry of the planar 3-D fracture is shown with the half height of the reservoir, the half length of the fracture, and the breakthrough of the fracture all illustrated.

Elasticity

The momentum balance without inertial terms relates the fracture width, w, to the net pressure, p, such that (Zia and Lecampion (2019) and references therein),

$$p = p_f - \sigma_0(x, y) - \Delta\sigma(x, y) = -\frac{E'}{8\pi} \int_{A_p(t)} \frac{w\left(x_1', x_3', t\right) d A_p\left(x_1', x_3'\right)}{\left[\left(x_1' - x_1\right)^2 + \left(x_3' - x_3\right)^2\right]^{\frac{3}{2}}}. \tag{5.1}$$

Here, p_f is the fluid pressure, σ_0 is the confining total stress, $\Delta\sigma$ is a stress jump, t is time, E' is the plane strain Young's modulus, and A_p is the area of a planar fracture in a homogeneous isotropic material. Note that terms are generally negligible for hydraulic fractures (Zia and Lecampion, 2017).

The stress intensity factor is assumed to be equal to the material toughness once the fracture has initiated and, near the tip, is estimated by (e.g., Lecampion *et al.* (2017)),

$$w \sim \sqrt{\frac{32}{\pi}} \frac{K_I}{E'} \sqrt{R - r}, \tag{5.2}$$

where K_I is the stress intensity factor, R is the radius of the fracture, and r is the radial coordinate. The equation can be simplified by stating that $K' = \sqrt{\frac{32}{\pi}} K_I$. Note that while the radius of the fracture, R, is used here initially, after the fracture reaches the reservoir-caprock interface, reference will be made to the fracture half length, L.

Fluid flow

The continuity equation for mass balance for a slightly compressible fluid obeying the lubrication approximation,

$$\frac{\delta w}{\delta t} + \frac{1}{r} \frac{\delta}{\delta r}\left(rq\right) + \frac{C'}{\sqrt{t - t_0(r)}} = Q, \tag{5.3}$$

ensures that the mass of fluid is conserved via a volume balance. Here, $C' = 2Cl$ where Cl is the Carter's leak-off coefficient, q is the fluid flux within the fracture, and Q is a point source injection term of constant rate. The lubrication approximation applied to the momentum

balance of the fluid results in Poiseuille's law,

$$q = -\frac{w^3}{\mu'}\frac{\delta p_f}{\delta r},$$

(5.4)

where $\mu' = 12\mu$, with μ being the fluid viscosity.

Boundary Conditions

It is assumed there is no fluid lag, a reasonable assumption for most practical applications (Detournay, 2016). Further, the injection rate is held constant at a value, Q_0, and the hydraulic fracture is assumed to be propagating in quasi-static equilibrium, meaning that the stress intensity factor along the fracture front is never larger than the rock's toughness.

5.3.2 Dimensionless formulation

Scaling

The governing equations can be scaled by introducing characteristic parameters for fracture length, L_*, fracture aperture, W_*, net pressure, P_*, and flow rate, Q_*, such that,

$$\gamma = \frac{r}{L_*}, \quad \Omega = \frac{w}{W_*}, \quad \Pi = \frac{p}{P_*}, \quad \Psi = \frac{q}{Q_*}.$$

(5.5)

These characteristic quantities are then introduced into the governing equations yielding the following dimensionless groups (Peirce and Detournay, 2008),

$$G_e = \frac{W_* E'}{P_* L_*}, \quad G_m = \frac{Q_* \mu'}{P_* W_*^3}, \quad G_v = \frac{Q_* t}{W_* L_*^2}, \quad G_q = \frac{Q_0}{Q_*}$$

(5.6)

$$G_K = \frac{K'\sqrt{L_*}}{E' W_*}, \quad G_\sigma = \frac{\Delta\sigma}{P_*}, \quad G_C = \frac{C' L_*^2}{Q_* \sqrt{t}}.$$

(5.7)

These dimensionless groups are ultimately what control the problem. Setting any of these dimensionless groups to one indicates that that quantity is on the order of one. For example, setting G_v to one implies that the volume of fluid injected into the hydraulic fracture is on the order of the volume of hydraulic fracture, guaranteeing that the length scale, L_* is representative of the fracture half length (Peirce and Detournay, 2008).

M **scaling: Viscosity dominated, no leak-off**

In the case that the problem is controlled by viscosity and storage, the fracture is propagating in the M regime and a unique set of scalings govern the solution (see Detournay (2004); Detournay *et al.* (2007); Mitchell *et al.* (2007); Garagash *et al.* (2008); Peirce and Detournay (2008); Hu and Garagash (2010) for details of viscosity-dominated fractures). In this case, G_e, G_v, G_m, and G_q can all be set to one, yielding,

$$P_* = \left(\frac{\mu' E'^2}{t} \right)^{\frac{1}{3}}, \quad L_* = \left(\frac{Q_*^{\frac{3}{4}} E'^{\frac{1}{4}} t}{\mu'^{\frac{1}{4}}} \right)^{\frac{4}{9}}, \quad W_* = \left(\frac{Q_*^3 \mu'^2 t}{E'^2} \right)^{\frac{1}{9}}, \tag{5.8}$$

which are valid prior to breakthrough while the fracture is propagating radially. Indeed, these scalings are the same as those found for a radial hydraulic fracture in the M regime (Detournay, 2004; Detournay *et al.*, 2007; Lecampion *et al.*, 2017).

K **scaling: Toughness dominated, no leak-off**

In the case that the problem is controlled by toughness and storage, the fracture is propagating in the K regime and a unique set of scalings govern the solution (see Detournay (2004); Bunger *et al.* (2005); Mitchell *et al.* (2007); Peirce and Detournay (2008); Hu and Garagash (2010); Moukhtari *et al.* (2019) for details of toughness-dominated fractures). In this case, G_e, G_v, G_K, and G_q can all be set to one, which yields,

$$P_* = \left(\frac{K'^6}{Q_0 E' t} \right)^{\frac{1}{5}}, \quad L_* = \left(\frac{Q_0 E' t}{K'} \right)^{\frac{2}{5}}, \quad W_* = \left(\frac{K'^4 Q_0 t}{E'^4} \right)^{\frac{1}{5}}, \tag{5.9}$$

which are valid prior to breakthrough while the fracture is propagating radially. Indeed, these scalings are the same as those found for a radial hydraulic fracture in the K regime (Detournay, 2004; Detournay *et al.*, 2007; Peirce and Detournay, 2008; Lecampion *et al.*, 2017).

$\tilde{M}$ **scaling: Viscosity dominated with leak-off**

In the case that the problem is controlled by viscosity and leak-off, the fracture is propagating in the $\tilde{M}$ regime and a unique set of scalings govern the solution (see Peirce and Detournay (2008); Hu and Garagash (2010) for examples of scaling for viscosity-leak-off-dominated

fractures). In this case, G_e, G_C, G_m, and G_q can all be set to one, which yields,

$$P_* = \left(\frac{C'^2 E'^4 \mu'^{\frac{4}{3}}}{Q_*^{\frac{2}{3}} t} \right)^{\frac{3}{16}}, \quad L_* = \left(\frac{Q_*^2 t}{C'^2} \right)^{\frac{1}{4}}, \quad W_* = \left(\frac{Q_*^6 \mu'^4 t}{C'^2 E'^4} \right)^{\frac{1}{16}},$$

(5.10)

which are valid prior to breakthrough while the fracture is propagating radially. Indeed, these scalings are the same as those found for a radial hydraulic fracture in the $\tilde{M}$ regime (Peirce and Detournay, 2008).

$\tilde{K}$ scaling: Toughness dominated with leak-off

In the case that the problem is controlled by viscosity and leak-off, the fracture is propagating in the $\tilde{K}$ regime and a unique set of scalings govern the solution (see Peirce and Detournay (2008); Hu and Garagash (2010) for examples of scaling for toughness-leak-off-dominated fractures). In this case, G_e, G_C, G_K, and G_q can all be set to one, which yields,

$$P_* = \left(\frac{K'^8 C'^2}{Q_*^2 t} \right)^{\frac{1}{8}}, \quad L_* = \left(\frac{Q_*^2 t}{C'^2} \right)^{\frac{1}{4}}, \quad W_* = \left(\frac{K'^8 Q_*^2 t}{E'^8 C'^2} \right)^{\frac{1}{8}},$$

(5.11)

which are valid prior to breakthrough while the fracture is propagating radially. Indeed, these scalings are the same as those found for a radial hydraulic fracture in the $\tilde{K}$ regime (Peirce and Detournay, 2008).

5.3.3 Scaling Transition Times

The transition time from one regime to the next can be found by first taking the scalings found in the initial regime (i.e., the expressions found for P_*, L_*, and W_*) and then setting the value for G corresponding to the next regime equal to one and then solving for time. For example, if the problem begins in the storage, viscosity regime (M), and then transitions into the storage, toughness regime (K), the time of this transition can be found by taking the expression for L_* from Equation 5.8 and setting G_K equal to one. Given that both of these expressions contain L_*, this variable can be eliminated and time can be solved for, yielding (Lecampion *et al.*, 2017),

$$t_{MK} = \frac{Q_0^{\frac{3}{2}} \mu'^{\frac{5}{2}} E'^{\frac{13}{2}}}{K'^9}.$$

(5.12)

This value for time represents when toughness will begin playing a significant role in the fracture's propagation. Note that it actually takes a significantly longer amount of time before the fracture is propagating in the toughness regime (Lecampion *et al.*, 2017). The other three transitions times are,

$$t_{M\tilde{M}} = \frac{Q_0^{\frac{6}{7}}\mu'^{\frac{4}{7}}}{C'^{\frac{18}{7}}E'^{\frac{4}{7}}}, \quad t_{K\tilde{K}} = \frac{K'^{\frac{8}{3}}Q_0^{\frac{2}{3}}}{C'^{\frac{10}{3}}E'^{\frac{8}{3}}}, \quad t_{\tilde{M}\tilde{K}} = \frac{E'^{12}C'^2\mu'^4Q_0^2}{K'^{16}}.$$

(5.13)

Note that essentially only $t_{M\tilde{M}}$ and $t_{K\tilde{K}}$ are relevant here, because the transition time from viscosity- to toughness-dominated propagation is either zero or infinite when toughness and viscosity are set to zero, respectively, as will be the case the simulations presented here.

5.4 Results

5.4.1 Viscosity dominated, no leak-off

Breakthrough time

By setting the L_* found for this regime equal to h, the height between the injection well and the reservoir-caprock interface, it is possible to solve for the time until breakthrough, t_{bt_M},

$$t_{bt_M} = \left(\frac{h^9\mu'}{Q_0^3E'}\right)^{\frac{1}{4}},$$

(5.14)

because when the radius of the fracture equals the distance between the injection well and the reservoir-caprock interface the fracture begins attempting to breakthrough the caprock.

Stress jump intensity

A value of P_* at breakthrough can be found, P_{*bt}, through use of t_{bt_M} found in Equation 5.14. The stress jump intensity can then be found by inputting P_{*bt} into the definition for G_σ, yielding,

$$G_\sigma = \frac{\Delta\sigma}{P_*} = \left(\frac{\Delta\sigma^4 h^3}{Q_0\mu'E'^3}\right)^{\frac{1}{4}},$$

(5.15)

which serves to represent the intensity of a stress jump encountered in a viscosity-dominated
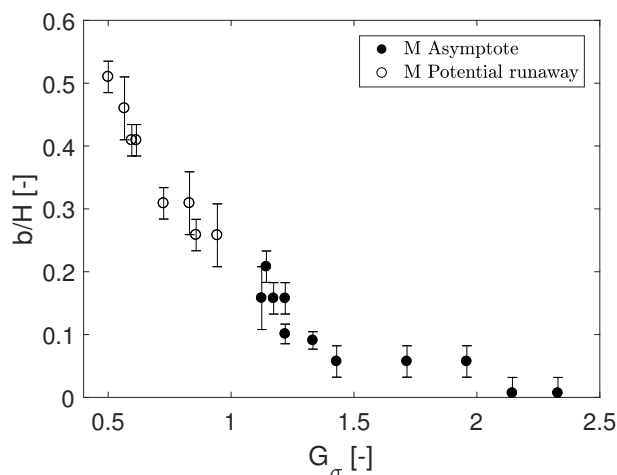
Figure 5.2 – Simulation results of breakthrough normalized by half of the reservoir height against G_σ in the M-scaling regime for a wide range of parameters. Note that the unfilled points potentially did not converge to an asymptotic value and may still propagate vertically as injection continues. The error bars represent the height of one cell.

propagation regime with no leak-off. Indeed, G_σ governs the magnitude of the breakthrough, as shown by the results of many different simulation runs in Figure 5.2. The results indicate that breakthrough is significantly reduced for large values of G_σ and are consistent enough to suggest that a value for breakthrough can be predicted when G_σ is known. The trial parameters used for each simulation are shown in the Appendix, Table A.1.

Note that these results agree with the experimental findings of El Rabaa (1984), where fracture breakthrough in the presence of a stress contrast was reduced in the event of large stress contrasts, softer rocks, thicker reservoirs, and low injection rates.

Asymptotic time scale

The scale for the transition time after breakthrough to the asymptotic solution of breakthrough, T_M, can be found by taking this regime's solution for P_*, setting $G_\sigma = 1$, then solving for time, such that,

$$T_M = \frac{E'^2\mu'}{\Delta\sigma^3}. \tag{5.16}$$

This result agrees with the finding of Garagash *et al.* (2008) found for the viscosity-dominated

113
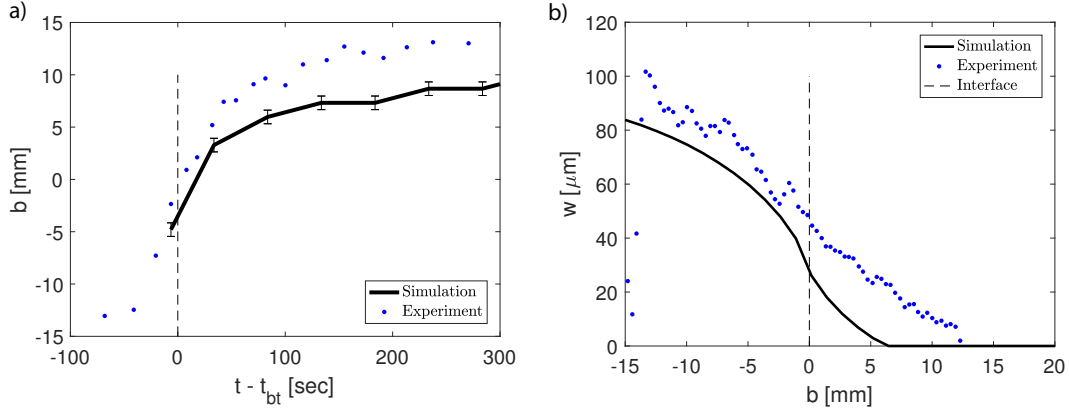
Figure 5.3 – A comparison of a PyFrac simulation (M1 in Table A.1) to the data presented in Garagash *et al.* (2008) with *M* scaling. (a) The breakthrough plotted as a function of time since breakthrough, where breakthrough occurred after 41 seconds in the numerical simulation. The error bars represent the height of one cell. (b) The width as a function of the vertical coordinate after 186.7 seconds. The interface marked is the interface where the stress jump occurs.

regime. Note that by normalizing T_M by t_{bt_M},

$$\frac{T_M}{t_{bt_M}} = \left(\frac{E'^3 Q_0 \mu'}{\Delta\sigma^4 h^3}\right)^{\frac{3}{4}} = \left(\frac{1}{G_\sigma}\right)^3, \tag{5.17}$$

we find that this transition time scales as $\frac{1}{G_\sigma^3}$. Physically, this means that, for larger values of G_σ, the hydraulic fracture is expected to reach the asymptotic value of breakthrough more quickly.

Comparison to Garagash et al., 2008

By comparing the experimental results presented by Garagash *et al.* (2008), to the simulation results from PyFrac, Figure 5.3, it is clear that the simulator is able to match the experimental results reasonably well. The match is not exact; however, considering the difficulties in keeping a constant injection rate during experiments and the difficulty in performing viscosity-dominated hydraulic fracture experiments (Bunger *et al.*, 2005), the match is acceptable. For example, the shape of the breakthrough curve matches fairly well with experimental results while being slightly smaller in magnitude, Figure 5.3a. Further, the width profile after 186.7 seconds of injection under-predicts the width above the interface while being a closer match within the reservoir, Figure 5.3b. Note that a series of verifications for PyFrac, including those with a stress jump, can be found in Zia and Lecampion (2019).
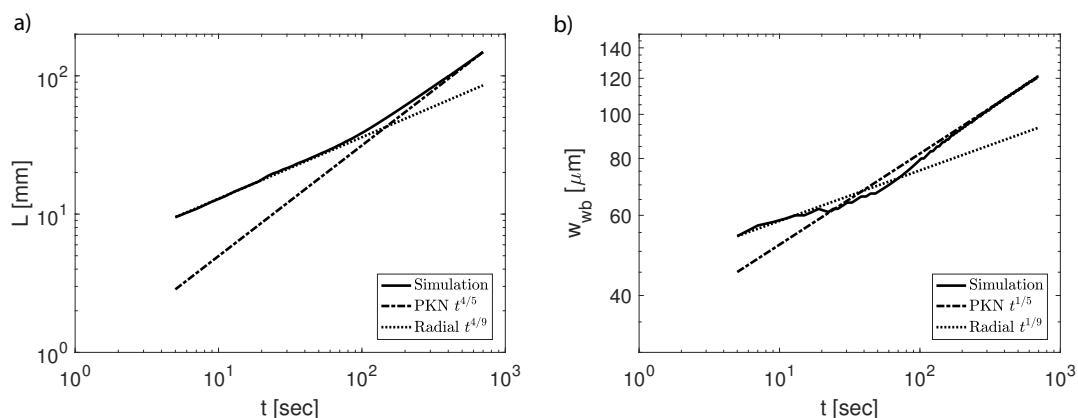
Figure 5.4 – From the simulation using the parameters of the Garagash *et al.* (2008) experiment (M1 in Table A.1) with *M* scaling, (a) the horizontal extent of the fracture as a function of time, log-log scale. The predicted horizontal extent based on both the PKN and radial scalings are also shown. (b) The width at the wellbore as a function of time, log-log scale. The predicted width based on both the PKN and radial scalings are also shown.

Further insight can be gained by comparing the results of the simulation to both PKN and radial scalings. For example, at early time, the half length of the fracture, L, scales with time as would a radial fracture (e.g., Detournay (2004); Detournay *et al.* (2007); Lecampion *et al.* (2017)); however, at late time the half length scales with time as a PKN fracture (Nordgren, 1972), Figure 5.4a. Similarly, the width of the fracture, w_{wb}, scales as a radial fracture at early time (e.g., Peirce (2015)) and as a PKN fracture at late time (Nordgren, 1972), Figure 5.4b. Similar results have been found by Zia and Lecampion (2019) for PL3D height-contained fractures using PyFrac.

Finally, a similar analysis can be performed for the wellbore pressure, P_{wb}, highlighting that the fracture does not scale as either a radial (e.g., Lecampion *et al.* (2017)) or PKN fracture (e.g., Zia and Lecampion (2017)), Figure 5.5.

5.4.2 Toughness dominated, no leak-off

Breakthrough time

By setting the L_* found for this regime equal to h, it is possible to solve for the time until breakthrough, t_{bt_K},

$$t_{bt_K} = \frac{h^{\frac{5}{2}} K'}{Q_0 E'}.$$

(5.18)
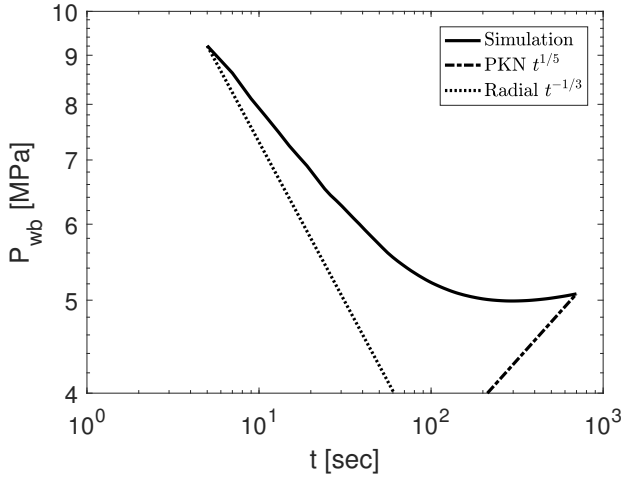
Figure 5.5 – From the simulation using the parameters of the Garagash *et al.* (2008) experiment (M1 in Table A.1) with *M* scaling, (a) the pressure at the wellbore as a function of time, log-log scale. The predicted pressure based on the radial and PKN scalings are shown.

Stress jump intensity

A value of P_* at breakthrough can be found, P_{*bt}, through use of t_{bt_K} found in Equation 5.18. The stress jump intensity can then be found by inputting P_{*bt} into the definition for G_σ, yielding,

$$G_\sigma = \frac{\Delta\sigma}{P_*} = \frac{\Delta\sigma\sqrt{h}}{K'}, \qquad (5.19)$$

which serves to represent the intensity of a stress jump encountered in a toughness-dominated propagation regime with no leak-off. Indeed, G_σ governs the magnitude of the breakthrough asymptote, Figure 5.6. The results indicate that breakthrough is significantly reduced for large values of G_σ and are consistent enough to suggest that a value for breakthrough can be predicted when G_σ is known. The trial parameters used for each simulation are shown in the Appendix, Table A.2.

Note that these results agree with the experimental findings of El Rabaa (1984), where fracture breakthrough in the presence of a stress contrast was reduced in the event of large stress contrasts, softer rocks, and thicker reservoirs.

Asymptotic time scale

The scale for the transition time after breakthrough to the asymptotic solution of breakthrough, T_K, can be found by taking this regime's solution for P_*, setting $G_\sigma = 1$, then solving for time,
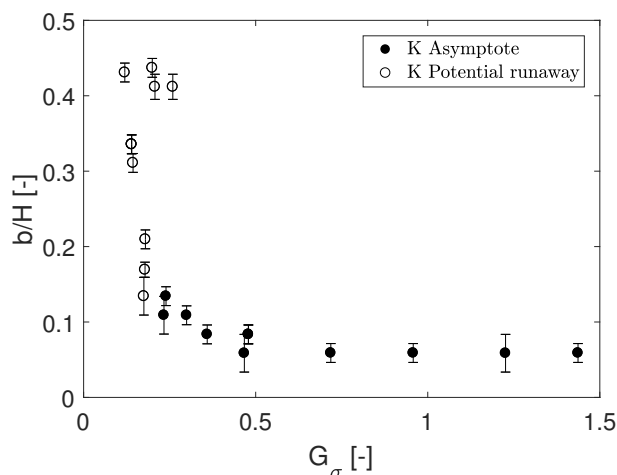
Figure 5.6 – Simulation results of breakthrough normalized by half of the reservoir height against G_σ in the K-scaling regime for a wide range of parameters. Note that the unfilled points potentially did not converge to an asymptotic value and may still propagate vertically as injection continues. The error bars represent the height of one cell.

such that,

$$T_K = \frac{K'^6}{E'Q_0\Delta\sigma^5}.$$ (5.20)

Note that by normalizing T_K by t_{bt_K},

$$\frac{T_K}{t_{bt_K}} = \frac{K'^5}{\Delta\sigma^5 h^{\frac{5}{2}}} = \left(\frac{1}{G_\sigma}\right)^5,$$ (5.21)

we find that this transition time scales as $\frac{1}{G_\sigma^5}$. Physically, this means that, for larger values of G_σ, the hydraulic fracture is expected to reach the asymptotic value of breakthrough more quickly. Notably, the dependency of T_K on G_σ is stronger than that of T_M. This is also true of T_K's dependency on $\Delta\sigma$, implying that stress jumps encountered while a hydraulic fracture is propagating in a toughness-dominated regime are more efficient at causing the hydraulic fracture to reach an asymptotic value of breakthrough than those encountered while the hydraulic fracture is propagating in the viscosity-dominated regime.

117
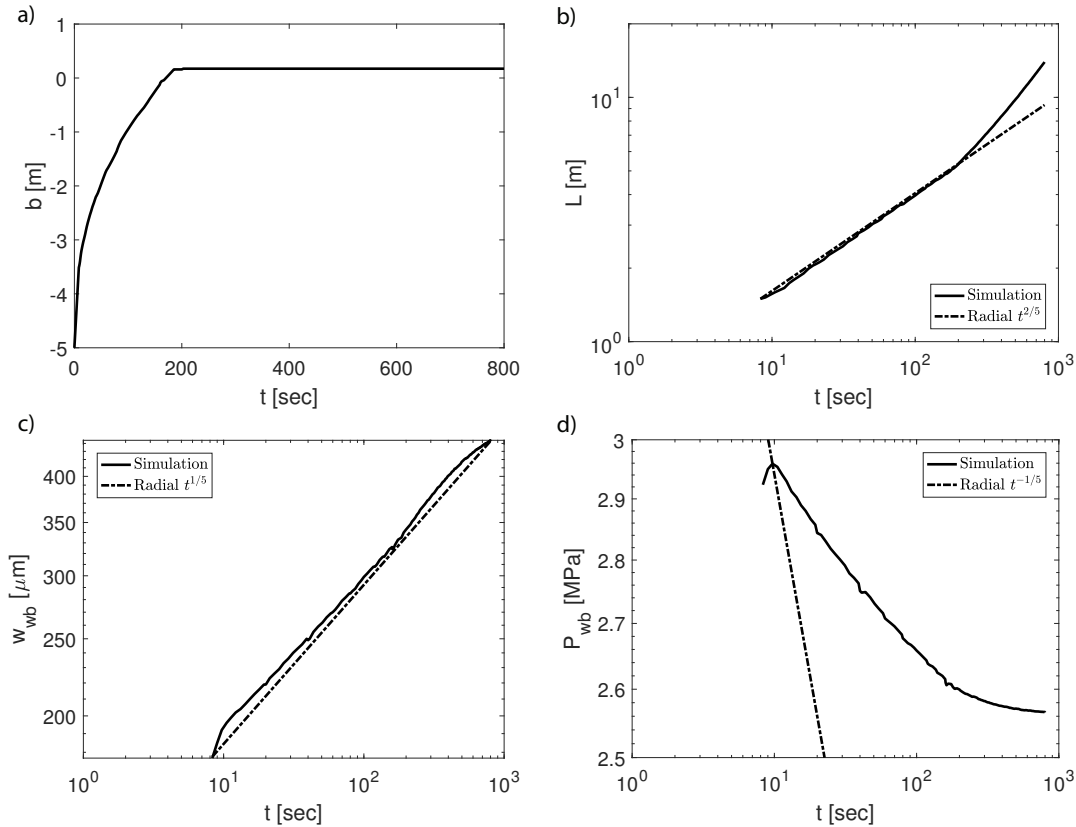
Figure 5.7 – Results of a toughness-dominated Pyfrac simulation (K21 in Table A.2). (a) The breakthrough as a function of time. Final breakthrough is equal to 173 mm. (b) The horizontal extent of the fracture as a function of time, log-log scale. The predicted horizontal extent based on radial scaling is shown. (c) The width at the wellbore as a function of time, log-log scale. The predicted width based on radial scaling is shown. (d) Wellbore pressure as a function of time, log-log scale. The pressure based on radial scaling is shown.

Simulation results

By taking the results of one trial, simulation K21 in Table A.2, it is possible to understand how key parameters are evolving over the course of the simulation. From Figure 5.7a it is clear that the breakthrough in this case evolves to an asymptotic value at large time. As was shown in Figure 5.6, the value of this asymptote depends on G_σ. Further, from Figure 5.7b it can be seen that, at large time, the length of the fracture does not conform to radial scaling (e.g., (Detournay, 2004; Detournay *et al.*, 2007; Lecampion *et al.*, 2017)). From Figure 5.7c it is evident that this type of fracture's width evolves as a function of time raised to the power of one-fifth, as would be appropriate for a radial fracture (e.g., Lecampion *et al.* (2017)). Finally, the pressure declines with time to a power which is less negative, Figure 5.7d, (i.e. a smaller magnitude power, closer to $t^{\frac{-1}{20}}$) than that of a radial fracture (e.g,. Lecampion *et al.* (2017)).

5.4.3 Viscosity dominated, with leak-off

Breakthrough time

By setting the L_* found for this regime equal to h, it is possible to solve for the time until breakthrough, $t_{bt\tilde{M}}$,

$$t_{bt\tilde{M}} = \frac{h^4 C'^2}{Q_*^2}. \tag{5.22}$$

Stress jump intensity

A value of P_* at breakthrough can be found, P_{*bt}, through use of $t_{bt\tilde{M}}$ found in Equation 5.22. The stress jump intensity can then be found by inputting P_{*bt} into the definition for G_σ, yielding,

$$G_\sigma = \left(\frac{\Delta\sigma^4 h^3}{Q_0 \mu' E'^3} \right)^{\frac{1}{4}}, \tag{5.23}$$

which serves to represent the intensity of a stress jump encountered in a viscosity-dominated propagation regime with leak-off. Note that this expression for G_σ does not depend on the leak-off coefficient and is exactly the same as that found for viscosity-dominated case without leak-off, Equation 5.15. New simulation cases were ran and plotted against those found for the viscosity-dominated regime without leak-off, Figure 5.8. The trial parameters used for each simulation are shown in the Appendix, Table A.3.

Asymptotic time scale

The scale for the transition time after breakthrough to the asymptotic solution of breakthrough, $T_{\tilde{M}}$, can be found by taking this regime's solution for P_*, setting $G_\sigma = 1$, then solving for time, such that,

$$T_{\tilde{M}} = \frac{C'^2 E'^4 \mu'^{\frac{4}{3}}}{\Delta\sigma^{\frac{16}{3}} Q_0^{\frac{2}{3}}}. \tag{5.24}$$
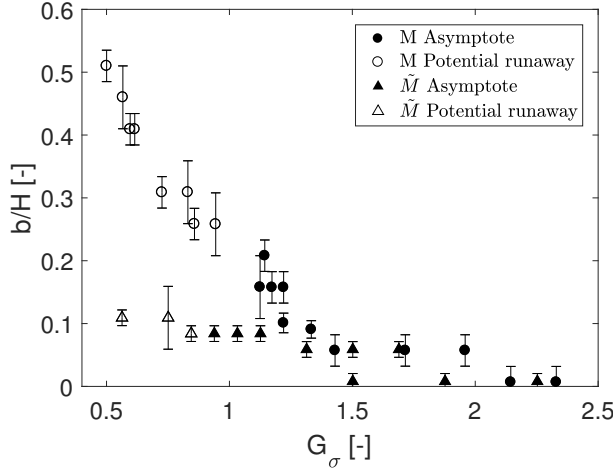
Figure 5.8 – Figure 5.2 with simulation results of breakthrough normalized by half of the reservoir height against G_σ in the $\tilde{M}$-scaling regime added. Note that the unfilled points potentially did not converge to an asymptotic value and may still propagate vertically as injection continues. The error bars represent the height of one cell.

Note that by normalizing $T_{\tilde{M}}$ by $t_{bt\tilde{M}}$,

$$\frac{T_{\tilde{M}}}{t_{bt\tilde{M}}} = \left(\frac{E'^{\frac{3}{4}} \mu'^{\frac{1}{4}} Q_0^{\frac{1}{4}}}{\Delta\sigma h^{\frac{3}{4}}} \right)^{\frac{16}{3}} = \left(\frac{1}{G_\sigma} \right)^{\frac{16}{3}}, \tag{5.25}$$

we find that this transition time scales as $\frac{1}{G_\sigma^{\frac{16}{3}}}$. Physically, this means that, for larger values of G_σ, the hydraulic fracture is expected to reach the asymptotic value of breakthrough more quickly. Note that while the value for G_σ is the same in the two viscosity-dominated regimes, the transition time has a larger dependence in the leak-off dominated case.

Simulation results

By taking the results of one trial, simulation $\tilde{M}5$ in Table A.3, it is possible to understand how key parameters are evolving over the course of the simulation. From Figure 5.9a it is clear that the breakthrough in this case evolves to an asymptotic value at large time. As was shown in Figure 5.8, the value of this asymptote depends on G_σ. Further, from Figure 5.9b it can be seen that the length of the fracture does not conform to radial scaling for the leak-off case. From Figure 5.9c it is evident that this type of fracture's width evolution does not conform to radial scaling. Finally, the pressure declines with time to a power which is less negative, Figure 5.9d than that of a radial fracture. The possible reasons for the mismatch between the simulation results and radial scaling power laws are addressed in the discussion, Section 5.5.1.
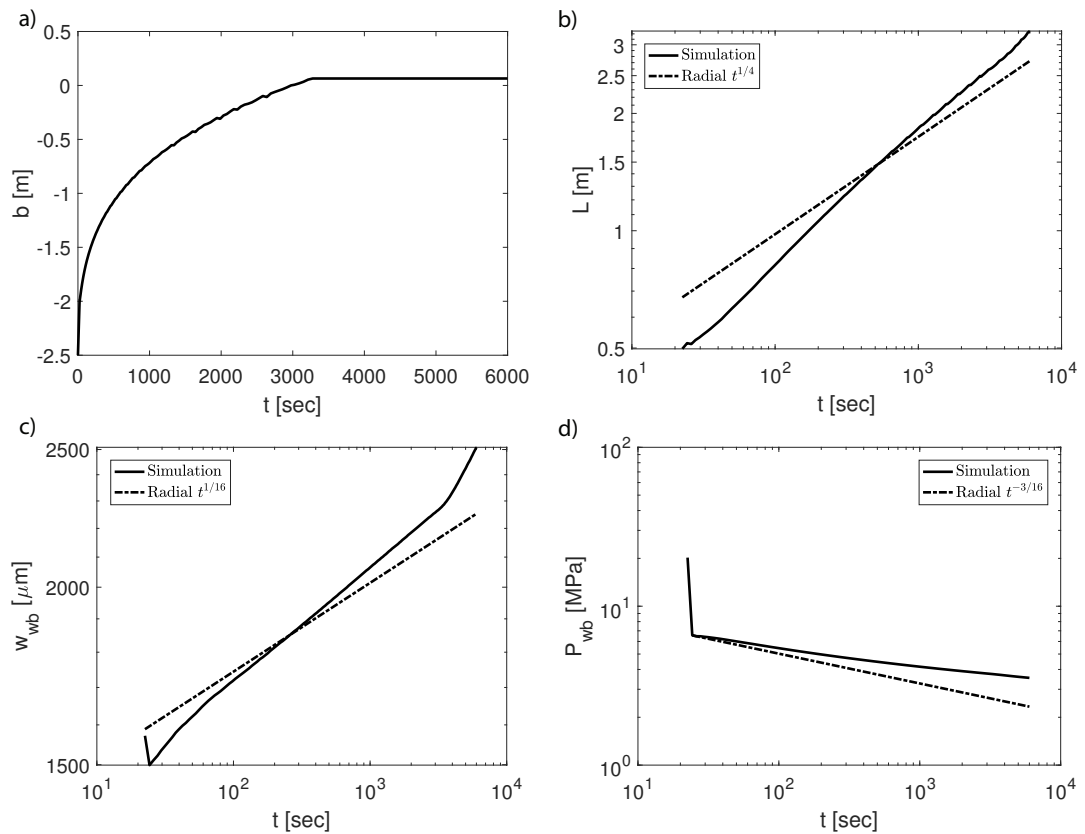
Figure 5.9 – Results of a toughness-dominated Pyfrac simulation ($\tilde{M}5$ in Table A.3). (a) The breakthrough as a function of time. Final breakthrough is equal to 147 mm. (b) The horizontal extent of the fracture as a function of time, log-log scale. The predicted horizontal extent based on radial scaling is shown. (c) The width at the wellbore as a function of time, log-log scale. The predicted width based on radial scaling is shown. (d) Wellbore pressure as a function of time, log-log scale. The pressure based on radial scaling is shown.

5.4.4 Toughness dominated, with leak-off

Breakthrough time

By setting the L_* found for this regime equal to h, it is possible to solve for the time until breakthrough, $t_{bt\tilde{K}}$,

$$t_{bt\tilde{K}} = \frac{h^4 C'^2}{Q_0^2}. \tag{5.26}$$

Stress jump intensity

A value of P_* at breakthrough can be found, P_{*bt}, through use of $t_{bt\tilde{K}}$ found in Equation 5.26. The stress jump intensity can then be found by inputting P_{*bt} into the definition for G_σ, yielding,

$$G_\sigma = \frac{\Delta\sigma\sqrt{h}}{K'}, \tag{5.27}$$

which serves to represent the intensity of a stress jump encountered in a toughness-dominated propagation regime with leak-off. Note that this expression for G_σ does not depend on the leak-off coefficient and is exactly the same as that found for toughness-dominated case without leak-off, Equation 5.19. New simulation cases were ran and plotted against those found for the toughness-dominated regime without leak-off, Figure 5.10. The trial parameters used for each simulation are shown in the Appendix, Table A.4.

Asymptotic time scale

The scale for the transition time after breakthrough to the asymptotic solution of breakthrough, $T_{\tilde{K}}$, can be found by taking this regime's solution for P_*, setting $G_\sigma = 1$, then solving for time, such that,

$$T_{\tilde{K}} = \frac{K'^8 C'^2}{\Delta\sigma^8 Q_0^2}. \tag{5.28}$$
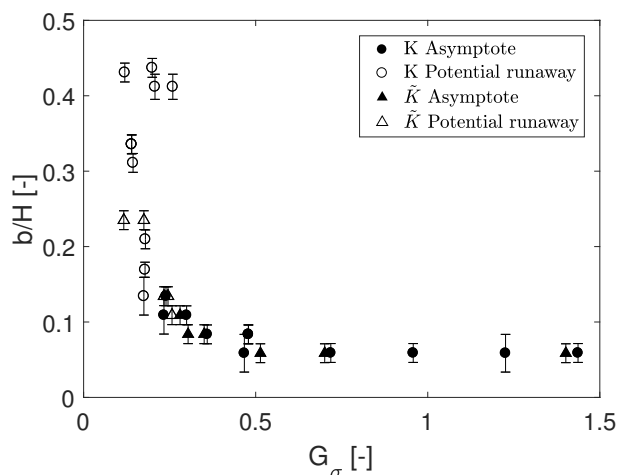
Figure 5.10 – Figure 5.6 with simulation results of breakthrough normalized by half of the reservoir height against G_σ in the $\tilde{K}$-scaling regime added. Note that the unfilled points potentially did not converge to an asymptotic value and may still propagate vertically as injection continues. The error bars represent the height of one cell.

Note that by normalizing $T_{\tilde{K}}$ by $t_{bt\tilde{K}}$,

$$\frac{T_{\tilde{K}}}{t_{bt\tilde{K}}} = \left(\frac{K'}{\Delta\sigma\sqrt{h}}\right)^8 = \left(\frac{1}{G_\sigma}\right)^8, \tag{5.29}$$

we find that this transition time scales as $\frac{1}{G_\sigma^8}$. Physically, this means that, for larger values of G_σ, the hydraulic fracture is expected to reach the asymptotic value of breakthrough more quickly. Note that while the value for G_σ is the same in the two toughness-dominated regimes, the transition time has a larger dependence in the leak-off dominated case.

Simulation results

By taking the results of one trial, simulation $\tilde{K}10$ in Table A.4, it is possible to understand how key parameters are evolving over the course of the simulation. From Figure 5.11a it is clear that the breakthrough in this case evolves to an asymptotic value at large time. As was shown in Figure 5.10, the value of this asymptote depends on G_σ. Further, from Figure 5.11b it can be seen that the length of the fracture does not conform to radial scaling for the leak-off case, except possibly initially. From Figure 5.11c, it is evident that this type of fracture's width does not conform to radial scaling. Finally, the pressure declines with time to a power which is less negative, Figure 5.11d, than that of a radial fracture. The possible reasons for the mismatch between the simulation results and radial scaling power laws are addressed in the discussion, Section 5.5.1.
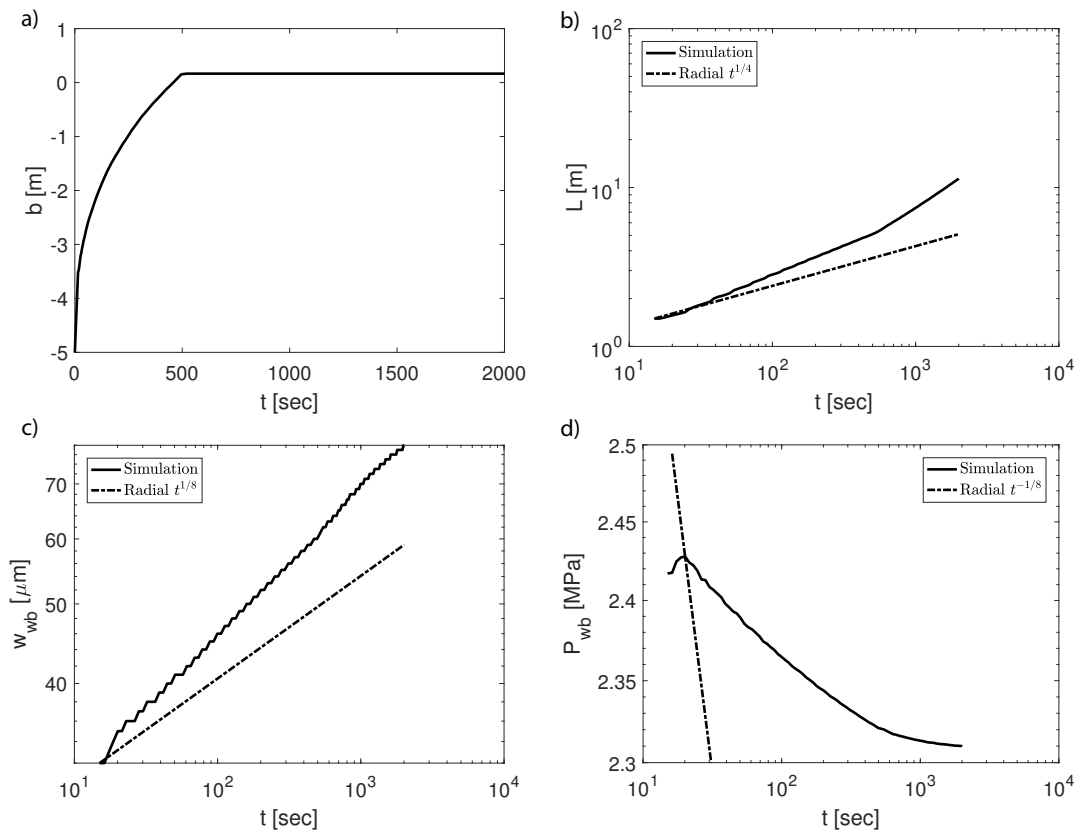
Figure 5.11 – Results of a toughness-dominated Pyfrac simulation ($\tilde{K}10$ in Table A.4). (a) The breakthrough as a function of time. Final breakthrough is equal to 293 mm. (b) The horizontal extent of the fracture as a function of time, log-log scale. The predicted horizontal extent based on radial scaling is shown. (c) The width at the wellbore as a function of time, log-log scale. The predicted width based on radial scaling is shown. (d) Wellbore pressure as a function of time, log-log scale. The pressure based on radial scaling is shown.

5.5 Discussion

It has been shown that breakthrough varies inversely with G_σ. Further, at low values of G_σ it is possible that the hydraulic fracture will be uncontained, with the stress jump only serving to slow the propagation in the vertical direction and not halt it. Note therefore that the asymptotic values for breakthrough shown in Figures 5.2, 5.6, 5.8, and 5.10 are not really asymptotic values in the case that the fracture is running away, designated by the unfilled circles. The trend of increasing breakthrough for decreasing values of G_σ in these cases is instead a result of the time of simulation being fairly constant (fixed by when the fracture leaves the domain or a set time). Therefore, these breakthrough values are a reflection of the speed of vertical propagation and not asymptotic breakthrough as in the cases at high values of G_σ where the fracture is contained. For this reason, the value of breakthrough is of significance for high values of G_σ where the fractures are contained but not at low values of G_σ where the fractures are not contained. These data points simply serve to show that the fracture was not contained at these low values of G_σ. Physically, G_σ can be thought of as a measure of how large the net pressure is in the reservoir in comparison to the stress jump that it must overcome. Therefore, cases with G_σ larger than one are always contained, as in this case the confining pressure in the caprock will not be overcome.

The transition times to asymptotic breakthrough, T_M and T_K, that were found previously, show that a stress jump in a toughness-dominated regime is more efficient at causing a hydraulic fracture to reach an asymptotic value of breakthrough than those encountered while the hydraulic fracture is propagating in the viscosity-dominated regime. This is due to T_K having a stronger dependence on $\Delta\sigma$ than T_M. Indeed, in most cases, a hydraulic fracture will reach a breakthrough asymptote much more quickly in a toughness-dominated regime than in a viscosity-dominated one. This can be seen by taking standard field parameters, $E' = 33\ GPa$, $K' = 5e5\ Pa\sqrt{m}$, $\mu' = 0.12\ Pa \cdot sec$, $Q_0 = 0.3\ \frac{m^3}{sec}$, and $\Delta\sigma = 1\ MPa$, and solving for the ratio $\frac{T_M}{T_K}$, which yields a value of $8e7$. These transition times also provide some intuition as to why hydraulic fractures with large values of G_σ are unable to breakthrough. If G_σ is greater than one in any of the regimes, the transition time to asymptotic breakthrough is smaller than the breakthrough time, implying that the fracture will immediately be at an asymptotic breakthrough as soon as it reaches the reservoir-caprock interface.

5.5.1 Discussion of scales

Storage domain

In the two storage regimes, M and K, the half-length of the fractures evolves initially with a radial scaling, Figures 5.4a and 5.7b. However, at late time, after breakthrough, this scaling changes, increasing in both cases. After breakthrough, the fracture is either entirely contained, as in Figure 5.7b, or simply inhibited, as in Figure 5.4a. Either way, since the volumetric injection rate is constant and the vertical propagation reduced, the scaling of the speed of propagation in the horizontal direction increases. In the M scaling case, the length then

evolves with a PKN scaling.

Characteristic width, Figures 5.4b and 5.7c, evolves with radial scaling in both of the storage regimes initially. After breakthrough in the M scaling case, however, the characteristic width begins to follow PKN scaling. Radial scaling is maintained throughout in the K scaling case.

The scaling of characteristic pressure, here the wellbore pressure, however, does not match radial scaling in either case, Figures 5.5 and 5.7d. In both cases, both before and at short time after breakthrough, the pressure decreases as in radial scaling; however, this decrease does not match the radial scaling power law. In the M scaling case, the pressure does begin to increase at late time. Similarly, in PKN scaling, pressure is expected to increase; however, again, these two power laws do not match in Figure 5.5. While it is possible that the continued fracture growth in the vertical direction, albeit reduced, could explain the mismatch between the M scaling and PKN scaling at late time, it is unclear why the early time wellbore pressure does not match the radial scaling in both the M and K scaling examples.

Leak-off domain

The leak-off scalings presented in Figures 5.9 and 5.11 did not match well with the predicted scaling presented in Equations 5.10 and 5.11, even before breakthrough. The likely reason for this is that the fractures were not truly propagating in the leak-off regime. Indeed, many of the scalings presented in Figures 5.9 and 5.11 match more closely to the storage scalings.

Note that the calculated transition time between the K and $\tilde{K}$, $t_{K\tilde{K}}$, in Figure 5.11 is calculated to be 0.9 seconds, which is significantly lower than the breakthrough time, which is closer to 500 seconds. However, clearly this transition time needs to be reduced further. Unfortunately, high leak-offs are very taxing for the numerical simulator and lead to very long run times, if not non-convergence. This further implies that the results presented for breakthrough's dependence on G_σ in Figures 5.8 and 5.10 may need to be re-evaluated.

5.5.2 The effect of leak-off

As shown in Sections 5.4.3 and 5.4.4, the value of G_σ is not expected to change for either viscosity or toughness dominated fractures when leak-off becomes significant. This is reflected in Figures 5.9 and 5.11. This is further supported by a previous finding that leak-off has no effect on the amount of breakthrough when a fracture encounters a stress jump (Adachi *et al.*, 2010). Leak-off does have an effect on the time of breakthrough and the time to transition to an asymptotic value of breakthrough, however. Essentially, leak-off affects the time it takes for a fracture to reach an asymptotic value of breakthrough but does not affect the value of that asymptote. Further simulations in the leak-off dominated domains are required before it is possible to conclude on the effect of leak-off on the breakthrough of a PL3D hydraulic fracture through a stress boundary due to the difficulties encountered in ensuring that a fracture is propagating in a leak-off dominated regime.

5.5.3 Implications for CCS

The results of this study have some interesting implications for large scale fluid injection, in particular for Carbon Capture and Storage, CCS or simply carbon storage. According to the Intergovernmental Panel on Climate Change (IPCC), large scale CO_2 sequestration for a coal-fired power plant is defined as at least 800,000 tons of CO_2 per year (IPCC, 2014). Part of the difficulty with CCS is that, for it to have a significant global impact, it must be implemented on a massive scale (e.g., Zoback and Gorelick (2012)), requiring large numbers (i.e., 1000's) of sites capable of accepting large volumes of CO_2 at large rates. Therefore, one of the many problems that faces CCS is the availability of deep basal aquifers in the vicinity from large CO_2 sources that are capable of accepting high rates of CO_2 injection.

It is clear from this study that positive stress jumps are capable of inhibiting fracture propagation, and that, in the case of a sufficient positive stress jump, a hydraulic fracture is predicted to reach a penetration asymptote in the overlying layer and then propagate exclusively in the horizontal direction. Hydraulically fracturing the near-wellbore region can greatly increase the injectivity of a well and, if the fracture remains contained in the reservoir with limited penetration into the caprock, could represent a method of greatly increasing the number of reservoirs capable of the kinds of injection rates necessitated by large-scale CCS injection while posing a limited risk to the reservoir seal. In fact, it has previously been noted that fractures propagating a small distance into sufficiently large caprocks do not pose risk to storage (Verdon *et al.*, 2013).

Of course, in order for a hydraulic fracture to be contained, a stress jump has to be present. One possible source of this stress jump could be reservoir depletion associated with hydrocarbon production (e.g., van Eekelen (1982); Alberty and McLean (2001)). As pore pressure decreases over the course of a field's life, poroelasticity predicts that the total stress within that reservoir will decrease. In the case of a horizontally-extensive reservoir, typical of hydrocarbon reservoirs (Segall and Fitzgerald, 1998; Zoback, 2007), it can be assumed that the vertical total stress remains constant and the horizontal total stress changes depending on the stress path of the reservoir by (Segall and Fitzgerald, 1998; Chan and Zoback, 2002),

$$\frac{\Delta S_{hmin}}{\Delta P_p} = \alpha \frac{1-2\nu}{1-\nu} = A. \tag{5.30}$$

Here, A is the stress path, a parameter which is defined by the properties of the reservoir and which governs the total horizontal stress changes associated with production-induced pore pressure changes, α is Biot's coefficient, and ν is Poisson's ratio. In fact, the horizontal total stress of the hydraulically-isolated bounding layers is also expected to increase (e.g., Segall (1989)), further enlarging any resulting stress jump, but this effect will be ignored here.

If an operator were to pick a penetration into the caprock which they deem to be acceptable,
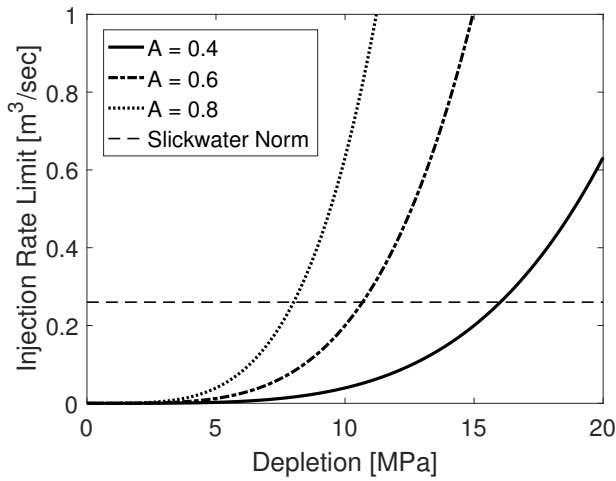
Figure 5.12 – Given certain injection parameters for a hydraulic fracturing treatment, the depletion required such that a desired injection rate can be achieved. The depletion required varies depending on the stress path of the reservoir. The fracture is assumed to be viscosity-dominated. A typical slickwater fracturing injection rate is given as reference. This analysis is not valid for reverse faulting stress regimes.

such that the caprock's height is significantly larger than the penetration of the fracture, a value for G_σ could be read from Figure 5.2 or 5.6, depending on the assumed propagation regime. In this example, a value for G_σ of 2.0 will be used, corresponding to a breakthrough equivalent to 10% of the reservoir height for a viscosity-dominated fracture. The fracture will be assumed to be viscosity-dominated, common for typical hydraulic fractures (Detournay *et al.*, 2007). Further, Young's modulus will be taken as 18 GPa, Poisson's ratio as 0.2, the reservoir height as 20 m, and the viscosity of the fracture fluid as 0.01 Pa sec. At this stage, the amount of pore pressure depletion in a given reservoir required such that a given pump rate can be safely achieved can be found for various reservoir stress paths, Figure 5.12.

Based on Figure 5.12 it is clear that somewhere between 5 and 15 MPa of depletion is necessary to create a sufficient stress jump. The required depletion (in terms of pressure) would be less in the case that the reservoir were thicker. Additionally, injection with a more viscous fluid would require more depletion. Note that this approach would only work in stress regimes where the minimum horizontal stress was also the minimum principal stress, i.e. normal and strike-slip faulting stress regimes. It could similarly be assumed that the fracture will be toughness-dominated, with $K1C$ assumed to be $1e6\ Pa\sqrt{m}$. In this case, G_σ is independent of injection rate, and the depletion required for a given reservoir can be calculated, Figure 5.13, assuming that operators will not perform a hydraulic fracturing treatment where G_σ is greater than 0.5, based on Figure 5.6. Note that while injection associated with the hydraulic fracturing treatment can raise the pore pressure, generally the time scale of the hydraulic fracture is significantly shorter than the time required to significantly alter the matrix pressure (Lecampion *et al.*, 2018).
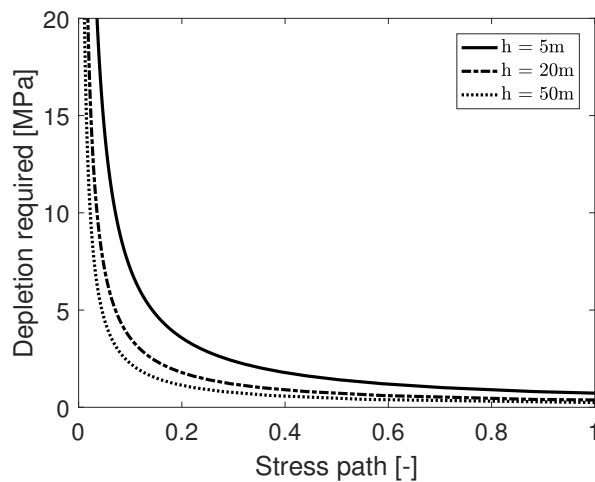
Figure 5.13 – The depletion required for various reservoir thicknesses such that the ensuing toughness-dominated hydraulic fracturing treatment has a G_σ value not exceeding 0.5. The resulting required depletion is based on the reservoir's stress path and an assumed $K1C$ of $1e6$ $Pa\sqrt{m}$. This analysis is not valid for reverse faulting stress regimes.

While the notion of hydraulically fracturing a potential CCS reservoir may seem brazen, as it undoubtedly is, this idea can be taken further. As hydraulic fractures in the presence of a sufficient stress jump are expected to reach a penetration asymptote and then propagate horizontally, a hydraulic fracture under these conditions with a constant injection rate is not expected to propagate any further vertically, after its initial penetration, even if injection is maintained continuously over the life of the reservoir. This implies that these reservoirs can be constantly operated under conditions which keep hydraulic fractures open. The advantage of this approach would be large gains in injectivity. It should be noted that this approach has been taken already, albeit probably unintentionally. Indeed, there have been numerous cases of long-term injection operating under conditions which initiate and maintain open hydraulic fractures (e.g., Healy *et al.* (1968); Eltvik *et al.* (1992); United States Environmental Protection Agency (1994); Bissell *et al.* (2011)).

Additionally, it is likely not necessary to exclusively employ depleted reservoirs for either of these approaches. Based on the notion of a critically-stressed crust (Harrison *et al.*, 1954; Brudy *et al.*, 1997; Townend and Zoback, 2000; Zoback and Townend, 2001; Zoback *et al.*, 2002), strata in normal faulting stress regimes with high coefficients of friction are expected to exhibit lower total horizontal stresses. As shales, typical caprocks, frequently have lower coefficients of frictions than sandstones (Kohli and Zoback, 2013; Ikari *et al.*, 2009; Saffer and Marone, 2003), this implies that shales overlying sandstones in normal faulting stress regimes may have larger total horizontal stresses and a positive stress jump will be present in-situ. These in-situ stress jumps have been predicted since the 1950's (Harrison *et al.*, 1954) and have since been seen in nature (van Eekelen, 1982; Alberty and McLean, 2001; Gunzburger and Cornet, 2007; Sone and Zoback, 2014). Based on the notion of a critically-stress crust,
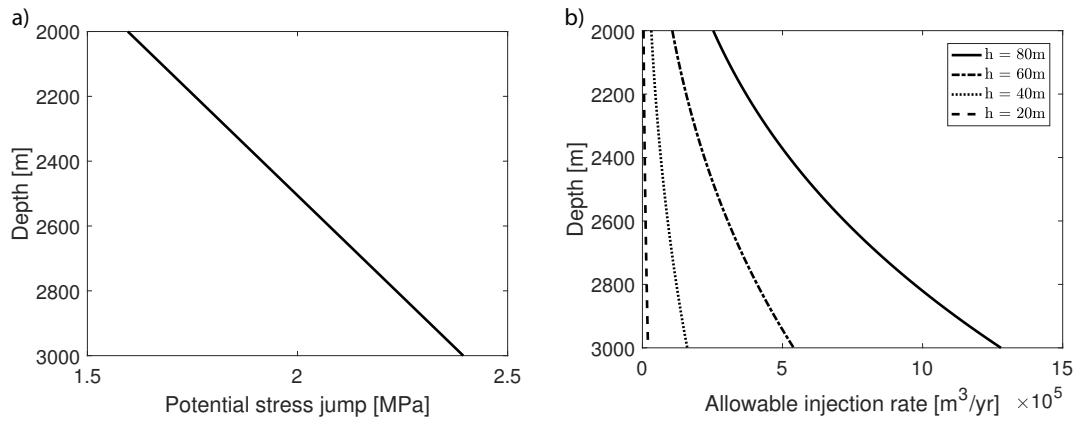
Figure 5.14 – For a normal faulting stress regime and a critically-stress crust, (a) the potential stress jump between a sandstone and shale versus the depth of their interface. (b) The allowable injection rate such that G_σ does not exceed 2.0.

an assumed coefficient of friction of 0.5 for a shale caprock, and a coefficient of friction of 0.6 for a sandstone reservoir, a stress jump profile can be created, where the potential stress jump at the interface between the caprock and reservoir is plotted versus the depth of that interface, Figure 5.14a. Based on this stress jump profile, an allowable G_σ value of 2.0, again from Figure 5.2 for a viscosity-dominated fracture, a Young's modulus of 18 GPa, a Poisson's ratio of 0.2, and a viscosity of the injected CO_2 of 0.01 Pa sec, the allowable injection rate versus the depth of the caprock-reservoir interface for various reservoir heights can be solved for, Figure 5.14b. Note that the larger the reservoir height, the larger the predicted breakthrough into the caprock as the value for G_σ was chosen based on a breakthrough height normalized with the reservoir height. A similar set of curves can be developed by picking the exact amount of allowable breakthrough and solving for the corresponding value of G_σ for each reservoir height.

Note that, while it is thought that most hydraulic fractures are viscosity-dominated (Detournay *et al.*, 2007), fractures become increasingly toughness dominated with increasing time. Therefore, given that the proposed scenario involves long-term injection it is probably more appropriate to use a toughness-dominated scaling. In this way, the minimum reservoir height for a given interface depth can be found for various values of $K1C$ such that G_σ does not exceed 0.5 for a toughness-dominated fracture, Figure 5.15. Note that in this case there is no dependence on injection rate. For this case, the coefficients of friction were again taken as 0.5 and 0.6 for shale and sandstone, respectively.

In these simple analyses the poroelastic stress increase associated with injection, which might be particularly relevant for the long term fracturing strategy, were neglected. These stress changes would be compressive and would act to reduce the stress jump. Also neglected, however, were the thermo-elastic stress changes associated with the injection of the cooler CO_2. These stress changes would be tensile in nature and would therefore act to increase
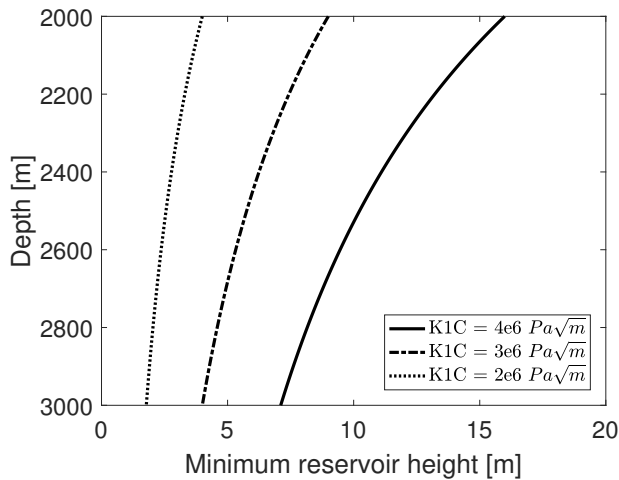
Figure 5.15 – Assuming a critically-stress crust and a normal faulting stress regime, the minimum reservoir height required such that a toughness-dominated hydraulic fracture will not exceed a G_σ value of 0.5.

the stress jump present between the caprock and reservoir. These effects are only relevant at very large times, but may be relevant in the case that a CO_2 storage reservoir is continuously fractured.

Note that, although these approaches would allow for a significantly increased injectivity, potentially allowing CCS to be implemented on a large enough global scale to make a significant dent in global emissions, this kind of massive injection would still result in an increase in pore pressure far from the well, as pointed out by other authors (e.g., Zoback and Gorelick (2012)). Indeed, it should be noted that the IPCC cut-off for "large-scale" CCS is higher than the kinds of waste water injection rates that have been seen to induce significant levels of induced seismicity (Ellsworth, 2013; IEAGHG, 2013; Keranen *et al.*, 2013) and so caution should be employed when considering such large-scale injection. Of course, these findings have implications for other areas of study such as hydraulic fractures in the petroleum industry and in the interpretation of geological sills.

5.6 Conclusion

Stress jumps are capable of halting the vertical propagation of a planar 3D hydraulic fracture, causing the total breakthrough to reach an asymptotic value which is based on a dimensionless parameter derived from scaling analyses, G_σ, readily determined from reservoir and operational parameters. This parameter can also be used to determine if the hydraulic fracture will runaway, being only hindered and not halted in the vertical direction. The specific form of G_σ depends on the whether the hydraulic fracture is propagating in the toughness- or viscosity-dominated regime, with leak-off only affecting the time that is required to arrive at an asymptotic value for breakthrough. The predictions from the scaling analyses are sup-

ported by numerical simulations, with more computing power potentially required to achieve a sufficient number of satisfactory leak-off dominated data points. These findings imply that the number of reservoirs suitable for carbon storage can be greatly increased through the contained hydraulic fracturing of depleted hydrocarbon reservoirs, or even virgin reservoirs in normal faulting stress regimes, where stress jumps are expected in-situ based on the notion of a critically-stressed crust.

6 Discussion and Conclusion

This thesis has been built on three fundamental ideas. Namely that:

1. The stress state has an important influence on certain subsurface industrial operations.

2. It has been previously shown that certain subsurface industrial operations are capable of influencing the stress state.

3. In certain cases operators have intentionally altered the stress state for their own benefit.

The combination of these facts has to led here to the notion that the stress state, at least in some cases, is something that can be managed by operators and is not simply an unchangeable parameter, for example, like a reservoir's depth or distance from a population center. Here this notion was built upon with the development of a series of novel ideas all of which attempt to manage the stress state in some capacity.

6.1 Key findings and summary

As the thesis was divided into distinct chapters, the key findings of each chapter will be summarized individually here.

The first chapter dealt with depletion-induced seismicity and the mitigating effect that reservoir stimulation can have on it. This chapter was based on the premise that the gradient of pore pressure is what determines the magnitudes of the stress changes occurring outside of the reservoir. Reservoir stimulation reduces the pore pressure gradient required to produce at a certain flow rate, thereby reducing the magnitudes of the stress changes induced. This essentially reduces the stressing rates that occur on nearby faults during production, reducing the rate of induced seismicity. As such, the key finding here is that hydraulic fracturing may be able to reduce production-induced seismicity. Also included in this chapter were a discussion of optimal wellbore orientation such that stressing rate is reduced and a discussion on the

distance from the wellbore after which poroelastic total stress changes dominate over pore pressure changes.

The second chapter also dealt with depletion-induced seismicity, but this time focusing on the effect that compaction-induced permeability loss has on the seismicity rate. Unsurprisingly, it was found that compaction-induced permeability loss increases the pore pressure gradient required to produce fluid at a certain flow rate, increasing the stressing rate occurring outside of the reservoir and with it the seismicity rate. This effect was seen to be heightened in the event that compaction began occurring inelastically. Whether or not compaction occurs inelastically is known to depend on differential stress. Therefore, it was possible to show here that wellbore orientation has a significant influence on whether near-wellbore compaction occurs inelastically, therefore again implying that wellbore orientation has an influence on depletion-induced seismicity.

The third chapter dealt with two ideas, both based on the anisotropy of total stress changes due to pore pressure and temperature changes in a reservoir. First, it has previously been shown that production from high-stress-path reservoirs in a normal faulting stress regime can lead to induced seismicity within the pore-pressure depleted zone of a reservoir due to changes in the horizontal total stress. It was therefore suggested here that high-stress-path reservoirs in normal faulting stress regimes should be attractive targets for large-scale injection, as these reservoirs can counter intuitively be expected to stabilize with increasing pore pressure. The cut-off criterion for determining whether a reservoir has a suitably high stress path was extended based on the notion of a critically-stressed crust. This has significant implications for large-scale injection such as might be employed for carbon storage. Second, it was suggested that the stress state of an EGS reservoir can be preconditioned in reverse faulting stress regimes by slowly injecting cold fluid, reducing the horizontal - and thereby the differential - stress. Then, when the reservoir is stimulated with high pore pressure, the lower differential stress is predicted to result in less large-magnitude events. This suggestion can be divided into two parts: the suggestion that a reservoir's stress can be preconditioned, reducing the risk of a large earthquake, and the suggestion that this preconditioning can be achieved by slowly injecting cold fluid. A discussion on how this might be possible in strike-slip and normal faulting stress regimes was also presented. This work has implications for push in EGS to have only small shearing events during stimulation and can be readily extended and adapted.

The fourth chapter again dealt with stress preconditioning. In this case, the stress changes associated with one stimulation treatment of an EGS well were used to guide the stimulation treatment of another EGS well. This was shown for normal, strike-slip, and reverse faulting stress regimes. This chapter provides further support to the idea that the stress of a reservoir can be preconditioned.

The fifth chapter investigated the effect of a stress jump on a Planar 3D hydraulic fracture. A scaling analysis was performed for four primary propagation regimes determined by whether

or not the fracture is toughness or viscosity dominated and whether or not leak-off is a dominant mechanism. The result was a dimensionless quantity that predicts the magnitude of hydraulic fracture breakthrough. The predictions of the scaling analysis were compared against numerical simulations for a wide range of parameters and found to be consistent. These results were then used to discuss the possibility of hydraulically fracturing depleted hydrocarbon reservoirs for use in carbon storage, implying that it may be possible to safely fracture depleted reservoirs such that large volumes of carbon can be easily injected.

6.2   Future outlook

There are almost certainly many more examples of how stress should be managed, or at least considered, in the planning of subsurface operations. While the management of stress was presented here primarily in a few particular contexts, this approach to stress should be applied in any operation in which stress is an important factor. Other operations not considered here, such as reservoir impoundment, mining, hydrogen and natural gas storage, and methane creation, may also be relevant. For example, in the case of gas storage there are generally both high and low pressure limits which limit the amount of gas that can be stored (Crotogino, 2016). Specifically regarding the upper limit, operators may ask themselves if this limit may change if the gas were injected at a different temperature such that it cools the surrounding rock. While the answer to this question is not answered in this thesis, the idea behind this thesis would be that this is now a question worth answering as the initial stress state is something that can be changed in certain cases.

The following subsections contain an number examples of how what we know about the stress field and our influence on it can be used to benefit other types of operations. These will be the immediate extensions of this thesis; however, other potential strategies can be readily proposed through the combination of the principles presented at the start of this chapter.

Temperature-induced stimulation's shut in potential

As previously mentioned, EGS stimulation treatments generally rely on high pore pressures to stimulate rock and this has been known to induce seismicity in certain cases. Other forms of stimulation exist for EGS reservoirs, however. For example, there have been numerous instances of acid stimulation in EGS reservoirs, although these reservoirs are primarily sedimentary in nature (Evans *et al.*, 2012). Further, the Northwest Geysers EGS Demonstration Project in California was actually stimulated via the injection of cold fluid (Rutqvist *et al.*, 2016b).

Both high pressure and low temperature stimulation treatments operate on the principal of inducing shear on well-oriented fracture planes as seen in Coulomb faulting theory. Unfortunately, this means that both treatments are capable of inducing shear failure on major faults, meaning they may potentially produce large-magnitude seismicity. One major difference

between the two forms of stimulation, however, is the speed of propagation of the temperature and pressure waves. Pore pressure changes propagate through a reservoir much more quickly than temperature changes. This can be seen by the difference in time scales required to stimulate reservoirs using high pore pressure (hours-days) and low temperature (months - years) injections. This also at least partially explains why producing fluid out of the well after the end of the stimulation treatment cannot guarantee the end of seismicity; the high pore pressure wave will continue to propagate and the low pore pressure wave will generally be unable to catch it meaning shear failure may still occur in the far-field.

Here, a shut-in technique is proposed which is predicted to quickly reduce the Coulomb stress in the reservoir after shut-in and result in a reduced risk of a large magnitude event post shut-in. The proposed methodology involves the reservoir being stimulated due to low temperature fluid injection. When the treatment is to be stopped and the well shut in, fluid is instead produced from the well at a high rate, resulting in a low pore pressure wave in the reservoir. As the pore pressure wave is predicted to travel faster than the temperature wave, the reduced pore pressure region will engulf the low temperature region, resulting in predicted stability according to Coulomb faulting theory.

The further development of temperature-induced stress preconditioning

The temperature preconditioning proposed in this thesis can be further expanded upon. Specifically, the focus of chapter 3 was on temperature preconditioning in reverse faulting stress regimes, while an idea was given of how a similar strategy might be applicable to strike-slip faulting stress regimes by making use of the anisotropy of stress changes from a horizontal well. This idea can be further expanded upon and ideally combined with the notion of multi-stage stimulation. As the stress changes in a strike-slip faulting stress regime will likely alter differential stress less than they would in either of the other two stress regimes, it may be necessary to make use of stimulated stages in a horizontal well to cause large temperature changes that would then affect the next stage. Essentially, beginning with one stimulated stage, the high permeability in this stage allows for large injection rates. These large injection rates more quickly result in large temperature and therefore stress changes. Then, a neighbouring stage can be stimulated with a significantly reduced differential stress as a result of these large stress changes.

The preconditioning of fault gouges to promote aseismic slip

It has previously been suggested that the repeated loading of a specimen may reduce the peak strength of that specimen, such that when shear failure occurs the amount of energy released is reduced (Cornet, 2019). What is essentially being suggested by this author is the preconditioning of the rock, by decreasing the shear modulus of the rock mass the kinetic energy that may be released through unstable slip is also reduced (Cornet 2019, personal communication). From rate and state friction, however, one would imagine that a reduced

shear modulus might actually promote seismic slip (Scholz, 1998). Indeed, mixed results have been achieved with cyclic stimulation up to this point (e.g., Zang *et al.* (2013); Noël *et al.* (2019b,a)). A potential avenue for future research might be to first understand from literature what the effect of altering either the matrix or fault properties is on seismicity, specifically in terms of seismic/aseismic behaviour, and then propose an approach for achieving this change prior to EGS stimulation.

Temperature-induced stress preconditioning to alter failure mode

The proposed investigation involves the suggestion that it may be possible to alter the stress state of a reservoir such that reservoirs that would normally have failed along a pre-existing, well-oriented crack instead fail primarily in mode I upon stimulation with high pore pressure. This would involve reducing the differential stress before stimulation. Again, the most probable approach would involve using temperature changes. Regarding the relevance of this suggestion, it may be beneficial in certain instances to fail in mode I as opposed to shear (or vice-versa), and it should be noted that there are instances of operators who would only consider "hard" stimulation in the case that differential stress is low (e.g., Veldkamp, H. and Boxem, T. (2015)).

6.3 Conclusion

A variety of engineering solutions to problems such as production-induced seismicity, induced seismicity related to EGS stimulation, induced seismicity related to large-scale fluid injection, connectivity in EGS reservoir stimulation, and hydraulic fracturing for carbon storage have been presented here. All of these solutions are in some way related to the management, or at the very least consideration, of the stress field and the changes that it will undergo during the proposed operation. Indeed, the underlying theme of this thesis has been that the stress state of a reservoir and the changes that that reservoir and its surroundings will undergo are not some unchangeable givens that operators simply have to accept. These stress fields are something that can be changed, or at the very least influenced, such that these operations are exposed to less risk. It is the opinion of the author that this line of thought should be continued and expanded to other applications, with a few possible avenues of research having been provided. Additionally, the solutions presented here are all numerical and/or semi-analytical. Before these proposed solutions can be applied in their respective domains, experiment and testing must surely be performed.

Bibliography

Adachi, J., Siebrits, E., Peirce, A., and Desroches, J. (2007). Computer simulation of hydraulic fractures. *International Journal of Rock Mechanics and Mining Sciences*, **44**, 739–757. https://doi.org/10.1016/j.ijrmms.2006.11.006.

Adachi, J., Detournay, E., and Peirce, A. (2010). Analysis of the classical pseudo-3d model for hydraulic fracture with equilibrium height growth across stress barriers. *International Journal of Rock Mechanics & Mining Sciences*, **47**, 625–639.

Alberty, M. and McLean, M. (2001). Fracture gradients in depleted reservoirs - drilling wells in late reservoir life. In *SPE/IADC Drilling Conference, 27 February-1 March, Amsterdam, Netherlands*.

Alt II, R. and Zoback, M. (2017). In situ stress and active faulting in Oklahoma. *Bulletin of Seismological Society of America*, **107**. https://doi.org/10.1785/0120160156.

Altmann, J., Müller, B., Müller, T., Heidbach, O., Tingay, M., and Weißhardt, A. (2014). Pore pressure stress coupling in 3D and consequences for reservoir stress states and fault reactivation. *Geothermics*, **52**, 195–205. https://dx.doi.org/10.1016/j.geothermics.2014.01.004.

Amitrano, D. (2003). Brittle-ductile transition and associated seismicity: Experimental and numerical studies and relationship with b value. *Journal of Geophysical Research*, **108**. https://dx.doi.org/10.1029/2001JB000680.

Anderson, T. (2005). *Fracture Mechanics Fundamentals and Applications*. Taylor & Francis Group, LLC.

Atkinson, G., Assatourians, K., Cheadle, B., and Greig, W. (2015). Ground motions from three recent earthquakes in Western Alberta and Northeastern British Columbia and their implications for induced-seismicity hazard in eastern regions. *Seismological Research Letters*, **86**, 1022–1031. https://doi.org/10.1785/0220140195.

Aziz, K. and Settari, A. (2002). *Petroleum Reservoir Simulation*. Blitzprint Ltd., Calgary, Alberta.

Baisch, S., Vörös, R., Rothert, E., Stang, H., and Jung, R. (2010). A numerical model for fluid injection induced seismicity at Soultz-sous-Forêts. *International Journal of Rock Mechanics & Mining Sciences*, **47**, 405–413. https://doi.org/10.1016/j.ijrmms.2009.10.001.

Bibliography

Baranova, V., Mustaqeem, A., and Bell, S. (1999). A model for induced seimsicity caused by hydrocarbon production in the Western Canada Sedimentary Basin. *Canadian Journal of Earth Sciences.* https://doi.org/10.1139/e98-080.

Barbour, A., Norbeck, J., and Rubinstein, J. (2016). The effects of varying injection rates in Osage County, Oklahoma, on the 2016 Mw 5.8 Pawnee earthquake. *Seismological Research Letters.* https://doi.org/10.1785/0220170003.

Bardainne, T., Dubos-Sallée, N., Sénéchal, G., Gaillot, P., and Perroud, H. (2008). Analysis of the induced seismicity of the Lacq gas field (Southwestern France) and model of deformation. *Geophysical Journal International.* https://doi.org/10.1111/j.1365-246X.2007.03705.x.

Barenblatt, G. (1996). *Scaling, self-similarity, and intermediate asymptotics.* Cambridge University Press.

Barenblatt, G. (2003). *Scaling.* Cambridge University Press.

Baria, R., Michelet, S., Baumgaertner, J., Dyer, B., Gerard, A., Nicholls, J., Hettkamp, T., Teza, D., Soma, N., Asanuma, H., Garnish, J., and Megel, T. (2004). Microseismic monitoring of the World's largest potential HDR reservoir. In *Twenty-Ninth Workshop on Geothermal Reservoir Engineering Stanford University, Stanford, California, January 26-28, 2004.*

Barton, C., Zoback, M., and Moos, D. (1995). Fluid flow along potentially active faults in crystalline rock. *Geology*, **23**, 683–686. https://doi.org/10.1130/0091-7613(1995)023<0683:FFAPAF>2.3.CO;2.

Baxevanis, T., Papamichos, E., Flornes, O., and Larsen, I. (2006). Compaction bands and induced permeability reduction in Tuffeau de Maastricht calcarenite. *Acta Geotechnica.* https://doi.org/10.1007/s11440-006-0011-y.

Beeler, N. and Lockner, D. (2003). Why earthquakes correlate weakly with the solid Earth tides: Effects of periodic stress on the rate and probability of earthquake occurrence. *Journal of Geophysical Research.* https://doi.org/10.1029/2001JB001518.

Begeleidingscommissie Onderzoek Aardbevingen (1993). Eindrapport multidisciplinair onderzoek naar de relatie tussen gaswinning en aardbevingen in Noord-Nederland.

Bella, F., Biagi, P. F., Caputo, M., Cozzi, E., Della Monica, G., Ermini, A., Plastino, W., and Sgrigna, V. (1998). Aquifer-induced seismicity in the Central Apennines (Italy). *Pure and Applied Geophysics.* https://doi.org/10.1007/s000240050191.

Berchenko, I. and Detournay, E. (1997). Deviation of hydraulic fractures through poroelastic stress changes induced by fluid injection and pumping. *International Journal of Rock Mechanics and Mining Sciences*, **34**, 1009–1019. https://doi.org/10.1016/S1365-1609(97)80010-X.

Bernabé, Y. (1986). The effective pressure law for permeability in Chelmsford Granite and Barre Granite. *International Journal of Rock Mechanics and Mining Sciences & Geomechanics Abstracts*, **23**, 267–275. https://doi.org/10.1016/0148-9062(86)90972-1.

Biot, M. (1941). General theory of three-dimensional consolidation. *Journal of Applied Physics*, **12**, 155–164.

Bischoff, M., C., B., Fritz, J., Gestermann, N., and Plenefisch, T. (2013). Untersuchungsergebnisse zum Erdbeben bei Völkersen (Landkreis Verden) am 22.11.2012. Technical report for the Landesamt für Bergbau, Energie, und Geologie and the Bundesanstalt für Geowissenschaften und Rohstoffe.

Bischoff, M., Ceranna, L., Fritz, J., Gestermann, N., and T., P. (2014). Untersuchungsergebnisse, zum Erdbeben bei Syke (Landkreis Diepholz) am 01.05.2014. Technical report for the Landesamt für Bergbau, Energie, und Geologie and the Bundesanstalt für Geowissenschaften und Rohstoffe.

Bischoff, M., Bönnemann, C., Ceranna, L., Fritz, J., Gestermann, N., Pasternak, M., and Plenefisch, T. (2015). Kurzbericht zum Erdbeben bei Emstek (Landkreis Cloppenburg) am 19.12.2014. Technical report for the Landesamt für Bergbau, Energie, und Geologie and the Bundesanstalt für Geowissenschaften und Rohstoffe.

Bischoff, M., Ceranna, L., Fritz, J., Gestermann, N., and Plenefisch, T. (2016). Kurzbericht zum Erdbeben bei Völkersen (Landkreis Verden) am 22. April 2016, M_L 3,1. Technical report for the Landesamt für Bergbau, Energie, und Geologie and the Bundesanstalt für Geowissenschaften und Rohstoffe.

Bissell, R., Vasco, D., Atbi, M., Hamdani, M., Okwelegbe, M., and Goldwater, M. (2011). A full field simulation of the In Salah gas production and CO_2 storage project using a coupled geo-mechanical and thermal fluid flow simulator. *Energy Procedia*, **4**, 3290–3297. https://doi.org/10.1016/j.egypro.2011.02.249.

Blanpied, M., Lockner, D., and Byerlee, J. (1995). Frictional slip of granite at hydrothermal conditions. *Journal of Geophysical Research*, **100**, 13045–13064. https://doi.org/10.1029/95JB00862.

Bommer, J., Oates, S., Cepeda, J., Lindholm, C., Bird, J., Torres, R., Marroquín, G., and Rivas, J. (2006). Control of hazard due to seismicity induced by a hot fractured rock geothermal project. *Engineering Geology*, **83**, 287–306. https://doi.org/10.1016/j.enggeo.2005.11.002.

Bou-Rabee, F. and Nur, A. (2002). The 1993 M4.7 Kuwait earthquake: Induced by the burning of the oil fields. *Kuwait Journal of Science & Engineering*, **29**, 155–163.

Bourne, S., Oates, S., van Elk, J., and Doornhof, D. (2014). A seismological model for earthquakes induced by fluid extraction from a subsurface reservoir. *Journal of Geophysical Research: Solid Earth*, **119**, 8991–9015. https://doi.org/10.1002/2014JB011663.

Bibliography

Bouteca, M., Lessi, J., and Sarda, J. (1983). Stress changes induced by fluid injection in a porous layer around a wellbore. In *24th U.S. Symposium on Rock Mechanics June 1983*.

Boutéca, M., Sarda, J., and & Vincké, O. (2000). Constitutive law for permeability evolution of sandstones during depletion. *2000 SPE International Symposium on Formation Damage Control*. https://doi.org/10.2118/58717-MS.

Brace, W. (1978). Volume changes during fracture and frictional sliding: A review. *Pure and Applied Geophysics*. https://doi.org/10.1007/BF00876527.

Brudy, M., Zoback, M., Fuchs, K., Rummel, F., and Baumgärtner, J. (1997). Estimation of the complete stress tensor to 8 km depth in the KTB scientific drill holes: Implications for crustal strength. *Journal of Geophysical Research*, **102**, 18453–18475. https://doi.org/10.1029/96JB02942.

Buijze, L., van den Bogert, P., Wassing, B., Orlic, B., and ten Veen, J. (2017). Fault reactivation mechanisms and dynmanic rupture modelling of depletion-induced seismic events in a Rotliegend gas reservoir. *Netherlands Journal of Geosciences*. https://doi.org/10.1017/njg.2017.27.

Bunger, A. and Lecampion, B. (2017). Four critical issues for successful hydraulic fracturing applications. In X.-T. Feng, editor, *Rock Mechanics and Engineering*, chapter 16. CRC Press/Balkema.

Bunger, A., Detournay, E., and Garagash, D. (2005). Toughness-dominated hydraulic fracture with leak-off. *International Journal of Fracture*, **134**, 175–190.

Calais, E., Camelbeeck, T., Stein, S., Liu, M., and Craig, T. J. (2016). A new paradigm for large earthquakes in stable continental plate interiors. *Geophysical Research Letters*. https://doi.org/10.1002/2016GL070815.

Caloi, P., De Panfilis, M., Di Filippo, D., Marcelli, L., and Spadea, M. C. (1956). Terremoti della Val Padana del 15-16 maggio 1951. *Annali di Geofisica*.

Cappa, F., Guglielmi, Y., Nussbaum, C., and Birkholzer, J. (2018). On the relationship between fault permeability increases, induced stress perturbation, and the growth of aseismic slip during fluid injection. *Geophysical Research Letters*, **45**. https://doi.org/10.1029/2018GL080233.

Carslaw, H. and Jaeger, J. (1959). *Conduction Of Heat In Solids*. Oxford University Press.

Castelletto, N., White, J., and Tchelepi, H. (2015). Accuracy and convergence properties of the fixed-stress iterative solution of two-way coupled poromechanics. *International Journal for Numerical and Analytical Methods in Geomechanics*, **39**, 1593–1618. https://dx.doi.org/10.1002/nag.2400.

142

Catalli, F., Meier, M., and Wiemer, S. (2013). The role of Coulomb stress changes for injection-induced seismicity: The Basel enhanced geothermal system. *Geophysical Research Letters*, **40**, 72–77. https://dx.doi.org/10.1029/2012GL054147.

Chan, A. and Zoback, M. (2002). Deformation analysis in reservoir space (DARS): A simple formalism for prediction of reservoir deformation with depletion. *SPE/ISRM Rock Mechanics Conference Proceedings, 20-23 October, 2002.* https://doi.org/10.2118/78174-MS.

Chang, K. and Segall, P. (2016a). Injection-induced seismicity on basement faults including poroelastic stressing. *Journal of Geophysical Research.* https://doi.org/10.1002/2015JB012561.

Chang, K. and Segall, P. (2016b). Seismicity on basement faults induced by simultaneous fluid injection-extraction. *Pure and Applied Geophysics.* https://doi.org/10.1007/s00024-016-1319-7.

Chang, K. and Segall, P. (2017). Reduction of injection-induced pore-pressure and stress in basement rocks due to basal sealing layers. *Pure and Applied Geophysics.* https://doi.org/10.1007/s00024-017-1567-1.

Chen, J. and Jiang, F. (2015). Designing multi-well layout for enhanced geothermal system to better exploit hot dry rock geothermal energy. *Renewable Energy*, **74**, 37–48. https://dx.doi.org/10.1016/j.renene.2014.07.056.

Chen, X., Nakata, N., Pennington, C., Haffener, J., Chang, J., He, X., Zhan, Z., Ni, S., and Walter, J. (2017). The Pawnee earthquake as a result of the interplay among injection, faults and foreshocks. *Scientific Reports.* https://doi.org/10.1038/s41598-017-04992-z.

Chen, Z., Narayan, S., Yang, Z., and Rahman, S. (2000). An experimental investigation of hydraulic behaviour of fractures and joints in granitic rock. *International Journal of Rock Mechanics & Mining Sciences*, **37**, 1061–1071. https://doi.org/10.1016/S1365-1609(00)00039-3.

Cheng, A. (1998). On generalized plane strain poroelasticity. *International Journal of Rock Mechanics and Mining Sciences*, **35**, 183–193. https://doi.org/10.1016/S0148-9062(97)00327-6.

Cheng, A. (2016). *Poroelasticity*. Springer Nature.

Chin, L. and Nagel, N. (2004). Modeling of subsidence and reservoir compaction under waterflood operations. *International Journal of Geomechanics.* https://doi.org/10.1061/(ASCE)1532-3641(2004)4:1(28).

Clarke, H., Eisner, L., Styles, P., and Turner, P. (2014). Felt seismicity associated with shale gas hydraulic fracturing: The first documented example in Europe. *Geophysical Research Letters*, **41**. https://doi.org/10.1002/2014GL062047.

Bibliography

Connor, C., Chapman, N., and Connor, L. (2009). *Volcanic and Tectonic Hazard Assessment for Nuclear Facilities*. Cambridge University Press.

Cornet, F. (2016). Seismic and aseismic motions generated by fluid injections. *Geomechanics for Energy and the Environment*, **5**, 42–54. httsp://dx.doi.org/10.1016/j.gete.2015.12.003.

Cornet, F. (2019). The engineering of safe hydraulic stimulations for EGS development in hot crystalline rock masses. *Geomechanics for Energy and the Environment*. https://doi.org/10.1016/j.gete.2019.100151.

Cornet, F. and Julien, P. (1989). Stress determination from hydraulic test data and focal mechanisms of induced seismicity. *International Journal of Rock Mechanics and Mining Sciences & Geomechanics Abstracts*, **26**, 235–248. https://doi.org/10.1016/0148-9062(89)91973-6.

Coussy, O. (2007). Revisiting the constitutive equations of unsaturated porous solids using a Lagrangian saturation concept. *International Journal for Numerical and Analytical Methods in Geomechanics*, **31**, 1675–1694. https://doi.org/10.1002/nag.613.

Crotogino, F. (2016). Large Scale Hydrogen Storage. In T. Letcher, editor, *Storing Energy*, chapter 20, pages 411–429. Elsevier.

Cueto-Felgueroso, L., Santillán, D., and Mosquera, J. (2017). Stick-slip dynamics of flow-induced seismicity on rate and state faults. *Geophysical Research Letters*, **44**, 4098–4106. https://doi.org/10.1002/2016GL072045.

Dahm, T., Krüger, F., Stammler, K., Klinge, K., Kind, R., Wylegalla, K., and Grasso, J. (2007). The 2004 M_w Rotenburg, Northern Germany, earthquake and its possible relationship with gas recovery. *Bulletin of Seismological Society of America*. https://doi.org/10.1785/0120050149.

Dake, L. (1978). *Fundamentals of Reservoir Engineering*. Elsevier Science, Amsterdam, The Netherlands.

David, C., Wong, T., Zhu, W., and Zhang, J. (1994). Laboratory measurement of compaction-induced permeability change in porous rocks: Implications for the generation and maintenance of pore pressure excess in the crust. *Pure and Applied Geophysics*. https://doi.org/10.1007/BF00874337.

Deichmann, N. and Giardini, D. (2009). Earthquakes induced by the stimulation of an Enhanced Geothermal System below Basel (Switzerland). *Seismological Research Letters*, **80**, 784–798. https://doi.org/10.1785/gssrl.80.5.784.

Delage, P., Schroeder, C., and Cui, Y. (1996). Subsidence and capillary effects in chalks. In *Proceedings Eurock 96, Turin*, pages 1291–1298.

Dempsey, D. and Suckale, J. (2017). Physics-based forecasting of induced seismicity at Groningen gas field, the Netherlands. *Geophysical Research Letters*, **44**, 7773–7782. https://doi.org/10.1002/2017GL073878.

Denbury Resources Inc. (2008). Denbury Resources Inc. 2008 Annual Report.

Deng, K., Liu, Y., and Harrington, R. (2016). Poroelastic stress triggering of the December 2013 Crooked Lake, Alberta, induced seismicity sequence. *Geophysical Research Letters*. https://doi.org/10.1002/2016GL070421.

Detournay, E. (2004). Propagation regimes of fluid-driven fractures in impermeable rocks. *International Journal of Geomechanics*, **4**, 35–45.

Detournay, E. (2016). Mechanics of hydraulic fractures. *Annual Review of Fluid Mechanics*, **48**, 311–339.

Detournay, E. and Cheng, A. (1993). Fundamentals of poroelasticity. In C. Fairhurst, editor, *Comprehensive Rock Engineering: Principles, Practice and Projects, Vol. II, Analysis and Design Method*, chapter 5, pages 113–171. Pergamon Press.

Detournay, E., Peirce, A., and Bunger, A. (2007). Viscosity-dominated hydraulic fractures. In *Proceedings: 1st Canada - U.S. Rock Mechanics Symposium, 27-31 May, Vancouver, Canada*. American Rock Mechanics Association.

Dieterich, J. (1994). A constitutive law for rate of earthquake production and its application to earthquake clustering. *Journal of Geophysical Research*. https://doi.org/10.1029/93JB02581.

Dohmen, T., Zhang, J., Li, C., Blangy, J., Simon, K., Valleau, D., Ewles, J., Morton, S., and Checkles, S. (2013). A new surveillance method for delineation of depletion using microseismic and its application to development of unconventional reservoirs. In *SPE Annual Technical Conference and Exhibition, 30 September-2 October, New Orleans, Louisiana, USA*. Society of Petroleum Engineers. https://doi.org/10.2118/166274-MS.

Dohmen, T., Blangy, J., and Zhang, J. (2014). Microseismic depletion delineation. *Interpretation*, **2**, SG1–SG13. https://dx.doi.org/10.1190/INT-2013-0164.1.

Dohmen, T., Zhang, J., Barker, L., and Blangy, J. (2017). Microseismic magnitudes and b-values for delineating hydraulic fracturing and depletion. *SPE Journal*, **22**. https://doi.org/10.2118/186096-PA.

Dorbath, L., Cuenot, N., Genter, A., and Frogneux, M. (2009). Seismic response of the fractured and faulted granite of Soultz-sous-Forêts (France) to 5 km deep massive water injections. *Geophysical Journal International*, **177**, 653–675. https://doi.org/10.1111/j.1365-246X.2009.04030.x.

Doser, D., Baker, M., and Mason, D. (1991). Seismicity in the War-Wink Gas Field, Delaware Basin, West Texas, and its relationship to petroleum production. *Bulletin of the Seismological Society of America*, **81**, 971–986. https://doi.org/10.1016/0148-9062(92)93679-E.

Dost, B. and Haak, H. W. (2007). Natural and induced seismicity. In T. E. Wong, D. A. J. Batjes, and J. de Jager, editors, *Geology of the Netherlands*, pages 223–239. Royal Netherlands Academy of Arts and Sciences.

Bibliography

Dost, B. and Kraaijpoel, D. (2013). The August 16, 2012 earthquake near Huizinge (Groningen). Koninklijk Nederlands Meteorologisch Instituut, De Bilt, The Netherlands.

Dost, B., Goutbeek, F., and van Eck, T. (2012). Monitoring induced seismicity in the north of the netherlands: status report 2010. Royal Netherlands Meteorological Institute, De Bilt, The Netherlands.

Eaton, D. (2018). *Passive Seismic Monitoring of Induced Seismicity (Fundamental Principles and Application to Energy Technologies).* Cambridge University Press.

Economides, M. and Nolte, K. (2000). *Reservoir Stimulation.* John Wiley & Sons Ltd.

El-Isa, Z. and Eaton, D. (2014). Spatiotemporal variations in the b-value of earthquake magnitude-frequency distributions: Classification and causes. *Tectonophysics*, **615**, 1–11. https://dx.doi.org/10.1016/j.tecto.2013.12.001.

El Rabaa, W. (1984). Hydraulic fracture propagation in the presence of stress variation. In *Proceedings: The 62nd Annual Technica[Conference and Exhibition of the Society of Petroleum Engineers held in Dallas, TX September 27-30, 1987.*

Elbel, J. and Mack, M. (1993). Refracturing: Observations and theories. In *SPE Production Operations Symposium, 21-23 March, Oklahoma City, Oklahoma.*

Ellsworth, B. (2013). Injection-induced earthquakes. *Science*, **341**. https://doi.org/10.1126/science.1225942.

Eltvik, P., Skoglunn, T., and Settari, A. (1992). Waterflooding-induced fracturing: Water injection above parting pressure at Valhall. In *Proceedings: SPE Annual Technical Conference and Exhibition, 4-7 October, Washington, D.C.*

Ernst, J. (2013). Denbury fined $662,500 for Mississippi blowout of CO_2 injected in high pressure enhanced oil recovery, So much carbon dioxide came out that it settled in hollows, suffocating deer and other animals. *Ernst v. EnCana Corporation.* https://www.ernstversusencana.ca/denbury-fined-662500-for-mississippi-blowout-of-co2-injected-in-high-pressure-enhanced-oil-recovery-so-much-carbon-dioxide-came-out-that-it-settled-in-hollows-suffocating-deer-and-other-animals/.

Evans, K. (2005). Permeability creation and damage due to massive fluid injections into granite at 3.5 km at Soultz 2. Critical stress and fracture strength. *Journal of Geophysical Research*, **110**. https://doi.org/10.1029/2004JB003169.

Evans, K., Dahlø, T., and Roti, J. (2003). Mechanisms of pore pressure-stress coupling which can adversely affect stress mesurements conducted in deep tunnels. *Pure and Applied Geophysics*, **160**, 1087–1102. https://doi.org/10.1007/PL00012562.

Evans, K., Moriya, H., Niitsuma, H., Jones, R., Phillips, W., Genter, A., Sausse, J., Jung, R., and Baria, R. (2005a). Microseismicity and permeability enhancement of hydrogeologic

structures during massive fluid injections into granite at 3 km depth at the Soultz HDR site. *Geophysical Journal International*, **160**, 388–412. https://doi.org/10.1111/j.1365-246X.2004.02474.x.

Evans, K., Genter, A., and Sausse, J. (2005b). Permeability creation and damage due to massive fluid injections into granite at 3.5 km at Soultz 1. Borehole observations. *Journal of Geophysical Research*, **110**. https://doi.org/10.1029/2004JB003168.

Evans, K., Zappone, A., Kraft, T., Deichmann, N., and Moia, F. (2012). A survey of the induced seismic responses to fluid injection in geothermal and CO_2 reservoirs in Europe. *Geothermics*, **41**, 30–54. https://doi.org/10.1016/j.geothermics.2011.08.002.

Ewy, R., Stankovich, R., and Bovberg, C. (2003). Mechanical behavior of some clays and shales from 200m to 3800m depth, Paper 570. In *39th U.S. Rock Mechanics Symposium/12th Panamerican Conference on Soil Mechanics and Geotechnical Engineering*, Cambridge, MA.

Favero, V., Ferrari, A., and Laloui, L. (2018). Anisotropic behaviour of Opalinus Clay through consolidated and drained triaxial testing in saturated conditions. *Rock Mechanics and Rock Engineering*. https://doi.org/10.1007/s00603-017-1398-5.

Fisher, M., Wright, C., Davidson, B., Goodwin, A., Fielder, E., Buckler, W., and Steinsberger, N. (2002). Integrating fracture-mapping technologies to optimize stimulations in the Barnett Shale. https://doi.org/10.2118/77441-MS.

Fisher, M., Heinze, J., Harris, C., Davidson, B., Wright, C., and Dunn, K. (2004). Optimizing horizontal completion techniques in the Barnett Shale using microseismic fracture mapping. In *SPE Annual Technical Conference and Exhibition, 26-29 September, Houston, Texas*.

Fjær, E., Holt, R., Horsrud, P., Raaen, A., and Risnes, R. (2008). *Petroleum Related Rock Mechanics*. Elsevier B.V., Amsterdam, The Netherlands.

Flewelling, S., Tymchak, M., and Warpinski, N. (2013). Hydraulic fracture height limits and fault interactions in tight oil and gas formations. *Geophysical Research Letters*, **40**, 3602–3606. https://doi.org/10.1002/grl.50707.

Fortin, J., Schubnel, A., and Guéguen, Y. (2005). Elastic wave velocities and permeability evolution during compaction of Bleurswiller sandstone. *International Journal of Rock Mechanics and Mining Sciences*. https://doi.org/10.1016/j.ijrmms.2005.05.002.

Foulger, G., Wilson, M., Gluyas, J., Julian, B., and Davies, R. (2018). Global review of human-induced earthquakes. *Earth-Science Reviews*, **178**, 438–514. https://dx.doi.org/10.1016/j.earscirev.2017.07.008.

Gao, Q., Cheng, Y., Han, S., Yan, C., and Jiang, L. (2019). Numerical modeling of hydraulic fracture propagation behaviors influenced by pre-existing injection and production wells. *Journal of Petroleum Science and Engineering*, **172**, 976–987. https://doi.org/10.1016/j.petrol.2018.09.005.

Bibliography

Garagash, D., Rohde, A., and Bunger, A. (2008). Leading edge of a hydraulic fracture crossing a stress boundary. In *Proceedings: 12th International Conference on Fracture At: Ottawa*.

Garagash, D., Detournay, E., and Adachi, J. (2011). Multiscale tip asymptotics in hydraulic fracture with leak-off. *Journal of Fluid Mechanics*, **669**, 260–297.

Geertsma, J. and de Klerk, F. (1969). A rapid method of predicting width and extent of hydraulically induced fractures. *Journal of Petroleum Technology*, **21**. https://doi.org/10.2118/2458-PA.

Geoscience Australia (2019). Gippsland Basin. *Australian Government*. https://www.ga.gov.au/scientific-topics/energy/province-sedimentary-basin-geology/petroleum/offshore-southern-australia/gippsland.

Gercek, H. (2007). Poisson's ratio values for rocks. *International Journal of Rock Mechanics and Mining Sciences*. https://doi.org/10.1016/j.ijrmms.2006.04.011.

Ghassemi, A. and Tao, Q. (2016). Thermo-poroelastic effects on reservoir seismicity and permeability change. *Geothermics*, **63**, 210–224. https://dx.doi.org/10.1016/j.geothermics.2016.02.006.

Gischig, V. and Wiemer, S. (2013). A stochastic model for induced seismicity based on nonlinear pressure diffusion and irreversible permeability enhancement. *Geophysical Journal International*, **194**, 1229–1249. https://dx.doi.org/10.1093/gji/ggt164.

Gischig, V., Wiemer, S., and Alcolea, A. (2014). Balancing reservoir creation and seismic hazard in enhanced geothermal systems. *Geophysical Journal International*, **198**, 1585–1598. https://dx.doi.org/10.1093/gji/ggu221.

Global-CCS-Institute (2017). Large-scale ccs facilities - definition. [Online; accessed 7-August-2017].

Goebel, T., Schorlemmer, D., Becker, T., Dresen, G., and Sammis, C. (2013). Acoustic emissions document stress changes over many seismic cycles in stick-slip experiments. *Geophysical Research Letters*, **40**, 2049–2054. https://doi.org/10.1002/grl.50507.

Goebel, T., Weingarten, M., Chen, X., Haffener, J., and Brodsky, E. (2017a). The 2016 Mw 5.1 Fairview, Oklahoma earthquakes: Evidence for long-range poroelastic triggering at >40 km from fluid disposal wells. *Earth and Planetary Science Letters*, **472**, 50–61. https://dx.doi.org/10.1016/j.epsl.2017.05.011.

Goebel, T., Weingarten, M., Chen, X., Haffener, J., and & Brodsky, E. (2017b). The 2016 Mw 5.1 Fairview, Oklahoma earthquakes: Evidence for long-range poroelastic triggering at > 40 km from fluid disposal wells. *Earth and Planetary Science Letters*. https://doi.org/10.1016/j.epsl.2017.05.011.

Goebel, T., Kwiatek, G., Becker, T., Brodsky, E., and Dresen, G. (2017c). What allows seismic events to grow big?: Insights from b-value and fault roughness analysis in laboratory stick-slip experiments. *Geology*. https://doi.org/10.1130/G39147.1.

Goertz-Allmann, B. and Wiemer, S. (2013). Geomechanical modeling of induced seismicity source parameters and implications for seismic hazard assessment. *Geophysics*, **78**, KS25––KS39. https://dx.doi.org/10.1190/GEO2012-0102.1.

Goertz-Allmann, B., Goertz, A., and Wiemer, S. (2011). Stress drop variations of induced earthquakes at the Basel geothermal site. *Geophysical Research Letters*, **38**. https://dx.doi.org/10.1029/2011GL047498.

Goertz-Allmann, B., Kühn, D., Oye, V., Bohloli, B., and Aker, E. (2014). Combining microseismic and geomechanical observations to interpret storage integrity at the In Salah CCS site. *Geophysical Journal International*, **198**, 447–461. https://doi.org/10.1093/gji/ggu010.

Goertz-Allmann, B., Gibbons, S., Oye, V., Bauer, R., and Will, R. (2017a). Characterization of induced seismicity patterns derived from internal structure in event clusters. *Journal of Geophysical Research - Solid Earth*, **122**, 3875–3894. https://doi.org/10.1002/2016JB013731.

Goertz-Allmann, B., Oye, V., Gibbons, S., and Bauer, R. (2017b). Geomechanical monitoring of CO_2 storage reservoirs with microseismicity. *Energy Procedia*, **114**, 3937–3947. https://doi.org/10.1016/j.egypro.2017.03.1525.

González, P., Tiampo, K., Palano, M., Cannavó, F., and Fernández, J. (2012). The 2011 Lorca earthquake slip distribution controlled by groundwater crustal unloading. *Nature Geoscience*. https://doi.org/10.1038/NGEO1610.

Grigoli, F., Cesca, S., Rinaldi, A., Manconi, A., López-Comino, J., Clinton, J., Westaway, R., Cauzzi, C., Dahm, T., and Wiemer, S. (2018). The November 2017 Mw 5.5 Pohang earthquake: A possible case of induced seismicity in South Korea. *Science*, **360**, 1003–1006. https://doi.org/10.1126/science.aat2010.

Guglielmi, Y., Cappa, F., Avouac, J., Henry, P., and Elsworth, D. (2015). Seismicity triggered by fluid injection-induced aseismic slip. *Science*, **348**, 1224–1226. https://doi.org/10.1126/science.aab0476.

Gulia, L. and Wiemer, S. (2010). The influence of tectnoic regimes on the earthquake size distribution: A case study for Italy. *Geophysical Research Letters*, **37**. https://doi.org/10.1029/2010GL043066.

Gunzburger, Y. and Cornet, F. (2007). Rheological characterization of a sedimentary formation from a stress profile inversion. *Geophysical Journal International*, **168**, 402–418. https://doi.org/10.1111/j.1365-246X.2006.03140.x.

Gutenberg, B. and Richter, C. (1944). Frequency of earthquakes in California. *Bulletin of the Seismological Society of America*, **34**, 185–188.

Bibliography

Haak, H. W., Dost, B., and Goutbeek, F. H. (2001). Seismische analyse van de aardbevingen bij Alkmaar op 9 en 10 september en Bergen aan Zee op 10 oktober 2001. Koninklijk Nederlands Meteorologisch Instituut, De Bilt, The Netherlands.

Hardebeck, J., Nazareth, J., and Hauksson, E. (1998). The static stress change triggering model: Constraints from two southern California aftershock sequences. *Journal of Geophysical Research*, **103**, 24427–24437. https://doi.org/10.1029/98JB00573.

Häring, M., Schanz, U., Ladner, F., and Dyer, B. (2008). Characterisation of the Basel 1 enhanced geothermal system. *Geothermics*, **37**, 469–495. https://doi.org/10.1016/j.geothermics.2008.06.002.

Harrison, E., Kieschnick, W., and McGuire, W. (1954). The mechanics of fracture induction and extension. *Petroleum Transactions*, **201**, 252–263.

Hart, D. and Wang, H. (1995). Laboratory measurements of a complete set of poroelastic moduli for Berea sandstone and Indiana sandstone. *Journal of Geophysical Research*, **100**, 17741–17751. https://doi.org/10.1029/95JB01242.

Healy, J., Rubey, W., Griggs, D., and Raleigh, C. (1968). The Denver earthquakes. *Science*. https://doi.org/10.1126/science.161.3848.1301.

Heidbach, O., Reinecker, J., Tingay, M., Müller, B., Sperner, B., Fuchs, K., and Wenzel, F. (2007). Plate boundary forces are not enough: Second- and third-order stress patterns highlighted in the World Stress Map database. *Tectonics*, **26**. https://doi.org/10.1029/2007TC002133.

Heidbach, O., Tingay, M., Barth, A., Reinecker, J., Kurfeß, and Müller, B. (2010). Global crustal stress pattern based on the World Stress Map database release 2008. *Tectonophysics*, **482**, 3–15. https://doi.org/10.1016/j.tecto.2009.07.023.

Heidbach, O., Rajabi, M., Cui, X., Fuchs, K., Müller, B., Reinecker, J., Reiter, K., Tingay, M., Wenzel, F., Xie, F., Ziegler, M., Zoback, M., and Zoback, M. (2018). The World Stress Map database release 2016: Crustal stress patterns across scales. *Tectonophysics*, **744**, 484–498. https://doi.org/10.1016/j.tecto.2018.07.007.

Helwany, S. (2007). *Applied Soil Mechanics with ABAQUS Applications.* John Wiley & Sons, Inc.

Hettema, M., Schutjens, P., Verboom, B., and Gussinklo, H. (2000). Production-induced compaction of a sandstone reservoir: The strong influence of stress path. *SPE Reservoir Evaluation & Engineering*. https://doi.org/10.2118/65410-PA.

Hettema, M., Papamichos, E., and Schutjens, P. (2002). Subsidence delay: Field observations and analysis. *Oil & Gas Science and Technology*. https://doi.org/10.2516/ogst:2002029.

Hettema, M., Andrews, J., Blaasmo, M., and Papamichos, E. (2006). The relative importance of drawdown and depletion in sanding wells: Predictive models compared with data from the Statfjord Field. In *SPE International Symposium and Exhibition on Formation Damage Control. Lafayette, L.A. 15–17 Feb 2006.*

Hofmann, H., Zimmermann, G., Zang, A., and Min, K. (2018). Cyclic soft stimulation (CSS): a new fluid injection protocol and traffic light system to mitigate seismic risks of hydraulic stimulation treatments. *Geothermal Energy*, **6**. https://doi.org/10.1186/s40517-018-0114-3.

Hofmann, H., Zimmermann, G., Farkas, M., Huenges, E., Zang, A., Leonhardt, M., Kwiatek, G., Martinez-Garzon, P., Bohnhoff, M., Min, K., Fokker, P., Westaway, R., Bethmann, F., Meier, P., Yoon, K., Choi, J., Lee, T., and Kim, K. (2019). First field application of cyclic soft stimulation at the Pohang Enhanced Geothermal System stie in Korea. *Geophysical Journal International*, **217**, 926–949. https://doi.org/10.1093/gji/ggz058.

Holzer, T., Gabrysch, R. K., and Verbeek, E. R. (1983). Faulting arrested by control of groundwater withdrawal in Houston, Texas. *Earthquake Information Bulletin*, **15**, 204–209.

Höök, M., Söderbergh, B., Jakobsson, K., and Aleklett, K. (2009). The evolution of giant oil field production behavior. *Natural Resources Research*, **18**, 39–56. https://doi.org/10.1007/s11053-009-9087-z.

Horton, S. (2012). Disposal of hydrofracking waste fluid by injection into subsurface aquifers triggers earthquake swarm in Central Arkansas with potential for damaging earthquake. *Seismological Research Letters*. https://doi.org/10.1785/gssrl.83.2.250.

Hu, J. and Garagash, D. (2010). Plane-strain propagation of a fluid-driven crack in a permeable rock with fracture toughness. *Journal of Engineering and Mechanics*, **136**, 1152–1166.

Hubbert, M. and Willis, D. (1957). Mechanics of hydraulic fracturing. *Petroleum Transactions, AIME*, **210**, 153–168.

IEAGHG (2013). Induced seismicity and its implications for CO_2 storage risk.

Ikari, M., Saffer, D., and Marone, C. (2009). Frictional and hydrologic properties of clay-rich fault gouge. *Journal of Geophysical Research*. https://doi.org/10.1029/2008JB006089.

Ikari, M., Marone, C., and Saffer, D. (2011). On the relation between fault strength and frictional stability. *Geology*, **39**, 83–86. https://doi.org/10.1130/G31416.1.

IPCC (2014). Climate Change 2014 Synthesis Report. Contribution of Working Groups I, II and III to the Fifth Assessment Report of the Intergovernmental Panel on Climate Change. page 151. IPCC, Geneva, Switzerland.

Ishibashi, T., Elsworth, D., Fang, Y., Riviere, J., Madara, B., Asanuma, H., Watanabe, N., and Marone, C. (2018). Friction-stability-permeability evolution of a fracture in granite. *Water Resources Research*.

Jacquey, A., Urpi, L., Cacace, M., Blöcher, G., Zimmermann, G., and Scheck-Wenderoth, M. (2018). Far field poroelastic response of geothermal reservoirs to hydraulic stimulation treatment: Theory and application at the Groß Schönebeck geothermal research facility. *International Journal of Rock Mechanics and Mining Sciences*, **110**, 316–327. https://doi.org/10.1016/j.ijrmms.2018.08.012.

Bibliography

Jeanne, P., Rutqvist, J., and Dobson, P. (2017). Influence of injection-induced cooling on deviatoric stress and shear reactivation of preexisting fractures in Enhanced Geothermal Systems. *Geothermics*, **70**, 367–375. https://dx.doi.org/10.1016/j.geothermics.2017.08.003.

Jeffrey, R. and Bunger, A. (2009). A detailed comparison of experimental and numerical data on hydraulic fracture height growth through stress contrasts. In *SPE Hydraulic Fracturing Technology Conference, 29-31 January, College Station, Texas, U.S.A.* https://doi.org/10.2118/106030-MS.

Jin, L. and Zoback, M. (2019). Depletion-induced poroelastic stress changes in naturally fractured unconventional reservoirs and implications for hydraulic fracture propagation. In *Proceedings: SPE Annual Technical Conference and Exhibition, 30 September - 2 October, Calgary, Alberta, Canada.*

Joshi, S. (1991). *Horizontal Well Technology.* PennWell Publishing Co.

Jupe, A., Green, A., and Wallroth, T. (1992). Induced microseismicity and reservoir growth at the Fjällbacka Hot Dry Rocks Project, Sweden. *International Journal of Rock Mechanics and Mining Sciences & Geomechanics Abstracts*, **29**, 343–354.

Karvounis, D. and Wiemer, S. (2015). Decision making software for forecasting induced seismicity and thermal energy revenues in enhanced geothermal systems. In *Proceedings World Geothermal Congress 2015*, Melbourne, Australia. International Geothermal Association.

Keranen, K., Savage, H., Abers, G., and Cochran, E. (2013). Potentially induced earthquakes in Oklahoma, USA: Links between wastewater injection and the 2011 Mw 5.7 earthquake sequence. *Geology*. https://doi.org/10.1130/G34045.1.

Keranen, K., Weingarten, M., Abers, G., Bekins, B., and Ge, S. (2014). Sharp increases in central Oklahoma seismicity since 2008 induced by massive wastewater injection. *Science*. https://doi.org/10.1126/science.1255802.

Khalili, N. and Valliappan, S. (1996). Unified theory of flow and deformation in double porous media. *European Journal of Mechanics Series A Solids*, **15**, 321–336.

Khristianovic, S. and Zheltov, Y. (1955). Formation of vertical fractures by means of highly viscous fluids. In *Proceeding 4th World Petroleum Congress.*

Kim, H., Xie, L., Min, K., Bae, S., and Stephansson, O. (2017). Integrated In Situ Stress Estimation By Hydraulic Fracturing, Borehole Observations, And Numerical Analysis At The EXP-1 Borehole In Pohang, Korea. *Rock Mechanics and Rock Engineering*, **50**, 3141–3155. https://doi.org/10.1007/s00603-017-1284-1.

Kim, K., Ree, J., Kim, Y., Kim, S., Kang, S., and Seo, W. (2018). Assessing whether the 2017 M_w 5.4 Pohang earthquake in South Korea was an induced event. *Science*, **360**, 1007–1009. https://doi.org/10.1126/science.aat6081.

King, G., Stein, R., and Lin, J. (1994). Static stress changes and the triggering of earthquakes. *Bulletin of the Seismological Society of America*, **84**, 935–953.

Király, E., Gischig, V., Karvounis, D., and Wiemer, S. (2014). Validating models to forecasting induced seismicity related to deep geothermal energy projects. In *Proceedings, Thirty-Ninth Workshop on Geothermal Reservoir Engineering*, Stanford, California. Stanford Geothermal Program, Curran Associates Inc.

Király, E., Zechar, D., Gischig, V., Wiemer, S., Karvounis, D., and Doetsch, J. (2016). Validating induced seismicity forecast models - Induced Seismicity Test Bench. *Journal of Geophysical Research: Solid Earth*, **121**, 6009–6029. https://doi.org/10.1002/2016JB013236.

Király, E., Gischig, V., Zechar, J., and Wiemer, S. (2017). Multi-component ensemble models to forecast induced seismicity. *Geophysical Journal International*. https://doi.org/10.1093/gji/ggx393.

Kluge, C., Milsch, H., and Blöcher, G. (2017). Permeability of displaced fractures. *Energy Procedia*, **125**, 88–97. https://doi.org/10.1016/j.egypro.2017.08.077.

KNMI (1994). Seismische analyse van de aardbeving bij Alkmaar op 21 september 1994. Koninklijk Nederlands Meteorologisch Instituut, De Bilt, The Netherlands.

Koch, T. W. (1933). Analysis and effects of current movements on an active fault in Buena Vista Hills oil field, Kern County, California. *Bulletin of the American Association of Petroleum Geologists*, **17**, 694–712.

Kohli, A. and Zoback, M. (2013). Frictional properties of shale reservoir rocks. *Journal of Geophysical Research: Solid Earth*, **118**, 5109–5125. https://doi.org/10.1002/jgrb.50346.

Kouznetsov, O., Sidorov, V., Katz, S., and Chilingarian, G. (1994). Interrelationships among seismic and short-term tectonic activity, oil and gas production, and gas migration to the surface. *Journal of Petroleum Science and Engineering*, **13**, 57–63. https://doi.org/10.1016/0920-4105(94)00058-C.

Kumar, D. and Ghassemi, A. (2019). Multistage hydraulic fracturing of EGS wells with application to FORGE. In *Proceedings, 44th Workshop on Geothermal Reservoir Engineering*, Stanford University, Stanford, California.

Kwiatek, G., Bohnoff, M., Dresen, G., Schulze, A., Schulte, T., Zimmermann, G., and Huenges, E. (2008). Microseismicity induced during fluid-injection: A case study from the geothermal site at Groß Schönebeck, North German Basin. *Acta Geophysica*, **58**, 995–1020. https://doi.org/10.2478/s11600-010-0032-7.

Kwiatek, G., Bulut, F., Bohnhoff, M., and Dresen, G. (2014). High-resolution analysis of seismicity induced at Berlín geothermal field, El Salvador. *Geothermics*, **52**, 98–111. https://dx.doi.org/10.1016/j.geothermics.2013.09.008.

Bibliography

Kwiatek, G., Martínez-Garzón, P., Dresen, G., Bohnhoff, M., Sone, H., and Hartline, C. (2015). Effects of long-term fluid injection on induced seismicity parameters and maximum magnitude in northwestern part of The Geysers geothermal field. *Journal of Geophysical Research: Solid Earth*, **120**, 7085–7101. https://dx.doi.org/10.1002/2015JB012362.

Kwiatek, G., Saarno, T., Ader, T., Bluemle, F., Bohnhoff, M., Chendorain, M., Dresen, G., Heikkinen, P., Kukkonen, I., Leary, P., Leonhardt, M., Malin, P., Martínez-Garzón, P., Passmore, K., Passmore, P., Valenzuela, S., and Wollin, C. (2019). Controlling fluid-induced seismicity during a 6.1-km-deep geothermal stimulation in Finland. *Science Advances*, **5**. https://dx.doi.org/10.1126/sciadv.aav7224.

Ladner, F. and Häring, M. (2009). Hydraulic characteristics of the Basel 1 Enhanced Geothermal System. *Geothermal Resources Council Transactions*, **33**, 199–204.

Lahaie, F. and Grasso, J. R. (1999). Loading rate impact on fracturing pattern: Lessons from hydrocarbon recovery, Lacq gas field, France. *Journal of Geophysical Research*, **104**, 17941–17954. https://doi.org/10.1029/1999JB900139.

Lake, L. (1989). *Enhanced Oil Recovery*. Prentice Hall.

Lavrov, A. (2016). Dynamics of stresses and fractures in reservoir and cap rock under production and injection. *Energy Procedia*, **86**, 381–390. https://doi.org/10.1016/j.egypro.2016.01.039.

Layland-Bachmann, C., Wiemer, S., Woessner, J., and Hainzl, S. (2011). Statistical analysis of the induced Basel 2006 earthquake sequence: introducing a probability-based monitoring approach for Enhanced Geothermal Systems. *Geophysical Journal International*, **186**, 793–807. https://doi.org/10.1111/j.1365-246X.2011.05068.x.

Layland-Bachmann, C., Wiemer, S., Goertz-Allmann, B., and Woessner, J. (2012). Influence of pore-pressure on the event-size distribution of induced earthquakes. *Geophysical Research Letters*, **39**. https://dx.doi.org/10.1029/2012GL051480.

Lecampion, B., Desroches, J., Jeffrey, R., and Bunger, A. (2017). Experimental versus theory for the initiation and propagation of radial hydraulic fractures in low-permeability materials. *Journal of Geophysical Research: Solid Earth*, **122**, 1329–1263.

Lecampion, B., Bunger, A., and Zhang, X. (2018). Numerical methods for hydraulic fracture propagation: A review of recent trends. *Journal of Natural Gas Science and Engineering*, **49**, 66–83.

Lei, X., Yu, G., Ma, S., Wen, X., and Wang, Q. (2008). Earthquakes induced by water injection at 3km depth within the Rongchang gas field, Chongqing, China. *Journal of Geophysical Research*, **113**. https://doi.org/10.1029/2008JB005604.

Lei, X., Huang, D., Su, J., Jiang, G., Wang, X., Wang, H., Guo, X., and Fu, H. (2017). Fautl reactivation and earthquakes with magnitudes of up to Mw 4.7 induced by shale-gas hydraulic

fracturing in Sichuan Basin, China. *Scientific Reports*, **7**. https://doi.org/10.1038/s41598-017-08557-y.

Leydecker, G., Steinwachs, M., Seidl, D., Kind, R., Klussmann, J., and Zerna, W. (1980). Das Erdbeben vom 2. Juni 1977 in der norddeutschen Tiefebene bei Soltau. *Geologisches Jahrbuch*.

Li, C. and Laloui, L. (2016). Coupled multiphase thermo-hydro-mechanical analysis of supercritical CO_2 injection: Benchmark for the In Salah surface uplift problem. *International Journal of Greenhouse Gas*, **51**, 394–408. https://dx.doi.org/10.1016/j.ijggc.2016.05.025.

Likhachev, E. (2003). Dependence of water viscosity on temperature and pressure. *Technical Physics*, **48**, 514–515. https://doi.org/10.1134/1.1568496.

Lockner, D. and Byerlee, J. (1986). Laboratory measurements of velocity-dependent frictional strength.

Mandl, G. (2000). *Faulting in Brittle Rocks*. Springer-Verlag.

Mann, P., Gahagan, L., and Gordon, M. (2001). Tectonic setting of the world's giant oil fields. *World Oil*, **222**.

Marone, C. and Saffer, D. (2007). Fault friction and the upper transition from seismic to aseismic faulting. In T. Dixon and J. Moore, editors, *The Seismogenic Zone of Subduction Thrust Faults*, chapter 12, pages 346–369. New York: Columbia University Press.

McClure, M. (2015). Generation of large postinjection-induced seismic events by backflow from dead-end faults and fractures. *Geophysical Research Letters*, **42**, 6647–6654. https://doi.org/10.1002/2015GL065028.

McClure, M. and Horne, R. (2014). An investigation of stimulation mechanisms in Enhanced Geothermal Systems. *International Journal of Rock Mechanics & Mining Sciences*, **72**, 242–260. https://doi.org/10.1016/j.ijrmms.2014.07.011.

McGarr, A. (1980). Some constraints on levels of shear stress in the crust from observations and theory. *Journal of Geophysical Research*, **85**, 6231–6238. https://doi.org/10.1029/JB085iB11p06231.

McNamara, D., Hayes, G., Benz, H., Williams, R., McMahon, N., Aster, R., Holland, A., Sickbert, T., Hermann, R., Briggs, R., Smoczyk, G., Bergman, E., and Earle, P. (2015). Reactivated faulting near Cushing, Oklahoma: Increased potential for a triggered earthquake in an area of United States strategic infrastructure. *Geophysical Research Letters*, **42**, 8328–8332. https://doi.org/10.1002/2015GL064669.

Meier, P., Rodríguez, A., and Bethmann, F. (2015). Lessons learned from Basel: New EGS projects in Switzerland using multistage stimulation and a probabilistic traffic light system for the reduction of seismic risk. In *Proceedings World Geothermal Congress 2015*, Melbourne, Australia.

Bibliography

Menin, A., Salomoni, V., Santagiuliana, R., Simoni, L., Gens, A., and Schrefler, B. (2008). A mechanism contributing to subsidence above gas reservoirs and its application to a case study. *International Journal for Computational Methods in Engineering Science and Mechanics*, **9**, 270–287. https://doi.org/10.1080/15502280802225234.

Mignan, A., Broccardo, M., Wiemer, S., and Giardini, D. (2017). Induced seismicity closed-form traffic light system for actuarial decision-making during deep fluid injections. *Scientific Reports*, **7**. https://doi.org/10.1038/s41598-017-13585-9.

Miller, S. (2015). Modeling enhanced geothermal systems and the essential nature of large-scale changes in permeability at the onset of slip. *Geofluids*, **15**, 338–349. https://doi.org/10.1111/gfl.12108.

Miller, S. and Nur, A. (2000). Permeability as a toggle switch in fluid-controlled crustal processes. *Earth and Planetary Science Letters*, **183**, 133–146. https://doi.org/10.1016/S0012-821X(00)00263-6.

Minner, W., Wright, C., Stanley, G., de Pater, C., Gorham, T., Eckerfield, L., and Hejl, K. (2002). Waterflood and production-induced stress changes dramatically affect hydraulic fracture behavior in Lost Hills infill wells. In *SPE Annual Technical Conference and Exhibition, 29 September - 2 October, San Antonio Texas*.

Mitchell, S., Kuske, R., and Peirce, A. (2007). An asymptotic framework for the analysis of hydraulic fractures: The impermeable case. *Journal of Applied Mechanics*, **74**, 365–372.

Morrow, C., Bo-Chong, Z., and Byerlee, J. (1986). Effective pressure law for permeability of Westerly Granite under cyclic loading. *Journal of Geophysical Research*, **91**, 3870–3876. https://doi.org/10.1029/JB091iB03p03870.

Moukhtari, F., Lecampion, B., and Zia, H. (2019). Propagation of a planar hydraulic fracture perpendicular to the isotropy plane of a transversely isotropic material. In *Proceedings: The 53rd US Rock Mechanics/Geomechanics Symposium held in New York, NY, USA, 23–26 June 2019*.

Narteau, C., Byrdina, S., Shebalin, P., and Schorlemmer, D. (2009). Common dependence on stress for the two fundamental laws of statistical seismology. *Nature*, **462**, 642–645. https://doi.org/10.1038/nature08553.

Nicot, J. and Scanlon, B. (2012). Water use for shale-gas production in Texas, U.S. *Environmental Science & Technology*, **46**, 3580–3586. https://doi.org/10.1021/es204602t.

Noël, C., Passelègue, F., Giorgetti, C., and Violay, M. (2019a). Fault reactivation during fluid pressure oscillations: Transition from stable to unstable slip. *Journal of Geophysical Research: Solid Earth*, **124**. https://doi.org/10.1029/ 2019JB018517.

Noël, C., Pimienta, L., and Violay, M. (2019b). Time-dependent deformations of sandstone during pore fluid pressure oscillations: Implications for natural and induced seismicity. *Journal of Geophysical Research: Solid Earth*, **124**, 801–821. https://doi.org/10.1029/2018JB016546.

Nolte, K. and Smith, M. (1981). Interpretation of fracturing pressures. *Journal of Petroleum Technology*, **33**, 1767–1775.

Norbeck, J. and Horne, R. (2015). Physical mechanisms related to microseismic-depletion-delineation field tests with application to reservoir surveillance. *SPE Journal*, **21**. https://doi.org/10.2118/178926-PA.

Norbeck, J. and Horne, R. (2018). Maximum magnitude of injection-induced earthquakes: A criterion to assess the influence of pressure migration along faults. *Tectonophysics*, **733**, 108–118. https://doi.org/10.1016/j.tecto.2018.01.028.

Norbeck, J., McClure, M., and Horne, R. (2018). Field observations at the Fenton Hill enhanced geothermal system test site support mixed-mechanism stimulation. *Geothermics*, **74**, 135–149. https://doi.org/10.1016/j.geothermics.2018.03.003.

Nordgren, R. (1972). Propagation of a vertical hydraulic fracture. *Society of Petroleum Engineers Journal*, **12**, 306–314. https://doi.org/10.2118/3009-PA.

Nurmi, R., Kuchuk, F., Cassel, B., Chardac, J., and Maguet, L. (1995). Horizontal highlights. *Schlumberger Middle East Well Evaluation Review*, **16**, 6–25.

Orellana, L., Scuderi, M., Collettini, C., and Violay, M. (2018). Frictional properties of Opalinus Clay: Implications for nuclear waste storage. *Journal of Geophysical Research: Solid Earth*. https://doi.org/10.1002/2017JB014931.

Osif, T. (1988). The effects of salt, gas, temperature, and pressure on the compressibility of water. *SPE Reservoir Engineering*. https://doi.org/10.2118/13174-PA.

Oye, V., Aker, E., Daley, T., Kühn, D., Bohloli, B., and Korneev, V. (2013). Microseismic monitoring and interpretation of injection data from the In Salah CO_2 storage site (Krechba, Algeria. *Energy Procedia*, **37**, 4191–4198. https://doi.org/10.1016/j.egypro.2013.06.321.

Palmer, I. and Carroll, H. (1983). Three-dimensional hydraulic fracture propagation in the presence of stress variations. *Society of Petroleum Engineers Journal*, **23**, 870–878. https://doi.org/10.2118/10849-PA.

Parisio, F., Vilarrasa, V., Wang, W., Kolditz, O., and Nagel, T. (2019). The risks of long-term re-injection in supercritical geothermal systems. *Nature Communications*, **10**. https://doi.org/10.1038/s41467-019-12146-0.

Parsons, T. (2005). Significance of stress transfer in time-dependent earthquake probability calculations. *Journal of Geophysical Research*. https://doi.org/10.1029/2004JB003190.

Pawar, R., Bromhal, G., Carey, W., Foxall, W., Korre, A., Ringrose, P., Tucker, O., Watson, M., and White, J. (2015). Recent advances in risk assessment and risk management of geologic CO_2 storage. *International Journal of Greenhouse Gas Control*, **40**, 292–311. https://dx.doi.org/10.1016/j.ijggc.2015.06.014.

Peaceman, D. (1977). *Fundamentals of Numerical Reservoir Simulation.* Developments in Petroleum Science. Elsevier.

Peaceman, D. (1978). Interpretation of well-block pressures in numerical reservoir simulation. *Society of Petroleum Engineers Journal*, **18**. https://doi.org/10.2118/6893-PA.

Pearson, C. (1981). The relationship between microseismicity and high pore pressures during hydraulic stimulation experiments in low permeability granitic rocks. *Journal of Geophysical Research*, **86**, 7855–7864. https://doi.org/10.1029/JB086iB09p07855.

Peirce, A. (2015). Modeling multi-scale processes in hydraulic fracture propagation using the implicit level set algorithm. *Computer Methods in Applied Mechanics and Engineering*, **283**, 881–908.

Peirce, A. (2016). Implicit level set algorithms for modelling hyraulic fracture propagation. *Philosopshical Transactions of the Royal Society A*, **374**.

Peirce, A. and Detournay, E. (2008). An implicit level set method for modeling hydraulically driven fractures. *Computer Methods in Applied Mechanics and Engineering*, **197**, 2858–2885.

Perkins, T. and Kern, L. (1961). Widths of hydraulic fractures. *Journal of Petroleum Technology*, **13**, 937–949. https://doi.org/10.2118/89-PA.

Petruccelli, A., Schorlemmer, D., Tormann, T., Rinaldi, A., Wiemer, S., Gasperini, P., and Vannucci, G. (2019a). The influence of faulting style on the size-distribution of global earthquakes. *Earth and Planetary Science Letters*, **527**. https://doi.org/10.1016/j.epsl.2019.115791.

Petruccelli, A., Gasperini, P., Tormann, T., Schorlemmer, D., Rinaldi, A., Vannucci, G., and Wiemer, S. (2019b). Simultaneous dependence of the earthquake-size distribution on faulting style and depth. *Geophysical Research Letters*, **46**. https://doi.org/10.1029/2019GL083997.

Pijnenburg, R., Verberne, B., Hangx, S., and Spiers, C. (2018). Deformation behavior of sandstones from the seismogenic Groningen Gas Field: Role of inelastic versus elastic mechanisms. *Journal of Geophysical Research: Solid Earth.* https://doi.org/10.1029/2018JB015673.

Pine, R. and Batchelor, A. (1984). Downward migration of shearing in jointed rock during hydraulic injections. *International Journal of Rock Mechanics and Mining Sciences & Geomechanics Abstracts*, **21**, 249–263. https://doi.org/10.1016/0148-9062(84)92681-0.

Postma, T. and Jansen, J. (2018). The small effect of poroelastic pressure transients on triggering of production-induced earthquakes in the Groningen natural gas field. *Journal of Geophysical Research: Solid Earth.* https://doi.org/10.1002/2017JB014809.

Pratt, W. E. and Johnson, D. W. (1926). Local subsidence of the Goose Creek oil field. *The Journal of Geology*, **34**, 577–590.

Raghavan, R. and Chin, L. (2002). Productivity changes in reservoirs with stress-dependent permeability. *SPE Reservoir Evaluation & Engineering*. https://doi.org/10.2118/88870-PA.

Raleigh, C., Healy, J., and Bredehoeft, J. (1976). An experiment in earthquake control at Rangely, Colorado. *Science*. https://doi.org/10.1126/science.191.4233.1230.

Reasenberg, P. and Simpson, R. (1992). Response of regional seismicity to the static stress change produced by the Loma Prieta Earthquake. *Science*, **255**, 1687–1690. https://doi.org/10.1126/science.255.5052.1687.

Rice, J. and Cleary, M. (1976). Some basic stress diffusion solutions for fluid-saturated elastic porous media with compressible constituents. *Reviews of Geophysics and Space Physics*, **14**, 227–241. https://doi.org/10.1029/RG014i002p00227.

Riffault, J., Dempsey, D., Karra, S., and Archer, R. (2018). Microseismicity cloud can be substantially larger than the associated stimulated fracture volume: The case of the Paralana Enhanced Geothermal System. *Journal of Geophysical Research: Solid Earth*, **123**, 6845–6870. https://doi.org/10.1029/2017JB015299.

Rinaldi, A., Jeanne, P., Rutqvist, J., Cappa, F., and Guglielmi, Y. (2014a). Effects of fault-zone architecture on earthquake magnitude and gas leakage related to CO_2 injection in a multi-layered sedimentary system. *Greenhouse Gas Science and Technology*, **4**, 99–120. https://doi.org/10.1002/ghg.1403.

Rinaldi, A., Rutqvist, J., and Cappa, F. (2014b). Geomechanical effects on CO_2 leakage through fault zones during large-scale underground injection. *International Journal of Greenhouse Gas Control*, **20**, 117–131. https://dx.doi.org/10.1016/j.ijggc.2013.11.001.

Rinaldi, A., Urpi, L., and Karvounis, D. (2016). Effects of asperity distribution on fluid flow and induced seismicity during deep geothermal exploitation. *Energy Procedia*, **97**, 470–477. https://doi.org/10.1016/j.egypro.2016.10.053.

Robinson, E., Potter, R., McInteer, B., Rowley, J., Armstrong, D., and Mills, R. (1971). A preliminary study of the nuclear subterrene.

Rolando, J., Massonnat, G., Grasso, J. R., Odonne, F., and Meftahi, R. (1997). Characterization and modelling of increasing permeability while producing a gas fractured reservoir. *Proceedings: SPE Annual Technical Conference and Exhibition, 5-8 October, San Antonio, Texas*. https://doi.org/10.2118/38711-MS.

Roman, A., Ahmadi, G., Issen, K., and Smith, D. (2012). Permeability of fractured media under confining pressure: A simplified model. *The Open Petroleum Engineering Journal*, **5**, 36–41. https://doi.org/10.2174/1874834101205010036.

Rubinstein, J. and Babaie Mahani, A. (2015). Myths and facts on wastewater injection, hydraulic fracturing, enhanced oil recovery, and induced seismicity. *Seismological Research Letters*, **86**, 1060–1067. https://doi.org/10.1785/0220150067.

Bibliography

Rubinstein, J., Ellsworth, W., McGarr, A., and Benz, H. (2014). The 2001 - present induced earthquake sequence in the Raton Basin of Northern New Mexico and Southern Colorado. *Bulletin of the Seismological Society of America.* https://doi.org/10.1785/0120140009.

Rubinstein, J., Ellsworth, W., and Dougherty, S. (2018). The 2013-2016 induced earthquakes in Harper and Sumner Counties, southern Kansas. *Bulletin of the Seismological Society of America.* https://doi.org/10.1785/0120170209.

Rudnicki, J. (1986). Fluid mass sources and point forces in linear elastic diffusive solids. *Mechanics of Materials*, **5**, 383–393. https://doi.org/10.1016/0167-6636(86)90042-6.

Rutledge, J., Fairbanks, T. D., Albright, J. N., Boade, R. R., Dangerfield, J., and Landa, G. H. (1994). Reservoir seismicity at the Ekofisk oil field. In *SPE/ISRM Rock Mechanics in Petroleum Engineering Conference, Delft, The Netherlands, 29-31 August 1994.*

Rutledge, J. T., Albright, J. N., Fairbanks, T. D., Murphy, M. B., and Roberts, P. M. (1990). Microseismic monitoring of the Chaveroo Oil Field, New Mexico. *SEG Technical Program Expanded Abstracts 1990.* https://doi.org/10.1190/1.1890159.

Rutledge, J. T., Phillips, W. S., and Schuessler, B. K. (1998). Reservoir characterization using oil-production-induced microseismicity, Clinton County, Kentucky. *Tectonophysics.* https://doi.org/10.1016/S0040-1951(97)00312-0.

Rutqvist, J. (2012). The geomechanics of CO_2 storage in deep sedimentary formations. *Geotechnical and Geological Engineering*, **30**, 525–551. https://dx.doi.org/10.1007/s10706-011-9491-0.

Rutqvist, J., Rinaldi, A., Cappa, F., Jeanne, P., Mazzoldi, A., Urpi, L., Guglielmi, Y., and Vilarrasa, V. (2016a). Fault activation and induced seismicity in geological carbon storage - Lessons learned from recent modeling studies. *Journal of Rock Mechanics and Geotechnical Engineering*, **8**, 789–804. https://dx.doi.org/10.1016/j.jrmge.2016.09.001.

Rutqvist, J., Jeanne, P., Dobson, P., Garcia, J., Hartline, C., Hutchings, L., Singh, A., Vasco, D., and Walters, M. (2016b). The Northwestern Geysers EGS Demonstration Project, California - Part 2: Modeling and interpretation. *Geothermics*, **63**, 120–138. https://dx.doi.org/10.1016/j.geothermics.2015.08.002.

Rutqvist, J., Rinaldi, A., and Cappa, F. (2017). Modeling fault activation and seismicity in geologic carbon storage and shale-gas fracturing - under what conditions could a felt seismic event be induced? In *SEG Technical Program Expanded Abstracts 2017*. SEG. https://doi.org/10.1190/segam2017-17749743.1.

Rybach, L. (2010). "The future of geothermal energy" and its challenges. In *Proceedings World Geothermal Congress 2010*, Bali, Indonesia.

Saffer, D. and Marone, C. (2003). Comparison of smectite- and illite-rich gouge frictional properties: application to the updip limit of the seismogenic zone along subduction megathrusts. *Earth and Planetary Science Letters*, **215**, 219–235. https://doi.org/10.1016/S0012-821X(03)00424-2.

Santagiuliana, R., Fabris, M., and Schrefler, B. (2015). Subsidence above depleted gas fields. *Engineering Computations*. https://doi.org/10.1108/EC-12-2013-0308.

Schoenball, M., Müller, T., Müller, B., and Heidbach, O. (2010). Fluid-induced microseismicity in pre-stressed rock masses. *Geophysical Journal International*, **180**, 813–819. https://doi.org/10.1111/j.1365-246X.2009.04443.x.

Schoenball, M., Dorbath, L., Gaucher, E., Wellmann, J., and Kohl, T. (2014). Change of stress regime during geothermal reservoir stimulation. *Geophysical Research Letters*, **41**, 1163–1170. https://doi.org/10.1002/2013GL058514.

Scholz, C. (1968). The frequency-magnitude relation of microfracturing in rock and its relation to earthquakes. *Bulletin of the Seismological Society of America*, **58**, 399–415.

Scholz, C. (1998). Earthquakes and friction laws. *Nature*, **391**, 37–42. https://dx.doi.org/10.1038/34097.

Scholz, C. (2015). On the stress dependence of the earthquake b value. *Geophysical Research Letters*, **42**, 1399–1402. https://dx.doi.org/10.1002/2014GL062863.

Schorlemmer, D., Wiemer, S., and Wyss, M. (2005). Variations in earthquake-size distribution across different stress regimes. *Nature*, **437**, 539–542. https://dx.doi.org/10.1038/nature04094.

Schutjens, P., van Dijk, C., Martin, J., and van den Oord, R. (2000). Compaction of a poorly consolidated quartz-rich reservoir sandstone: Experiments for the prognosis of compaction drive. In *Proc. 6th Int. Symp. on Land Subsidence, Ravenna, Italy*.

Schutjens, P., Hanssen, T., Hettema, M., Merour, J., de Bree, P., Coremans, J., and Helliesen, G. (2004). Compaction-induced porosity/permeability reduction in sandstone reservoirs: data and model for elasticity-dominated deformation. *SPE Reservoir Evaluation & Engineering*. https://doi.org/10.2118/88441-PA.

Segall, P. (1985). Stress and subsidence resulting from subsurface fluid withdrawal in the epicentral region of the 1983 Coalinga Earthquake. *Journal of Geophysical Research*. https://doi.org/10.1029/JB090iB08p06801.

Segall, P. (1989). Earthquakes triggered by fluid extraction. *Geology*, **17**, 942–946. https://doi.org/10.1130/0091-7613(1989)017<0942:ETBFE>2.3.CO;2.

Segall, P. (1992). Induced stresses due to fluid extraction from axisymmetric reservoirs. *Pure and Applied Geophysics*. https://doi.org/10.1007/BF00879950.

Bibliography

Segall, P. (2010). *Earthquake and Volcano Deformation.* Princeton University Press.

Segall, P. and Fitzgerald, S. (1998). A note on induced stress changes in hydrocarbon and geothermal reservoirs. *Tectonophysics*, **289**, 117–128. https://doi.org/10.1016/S0040-1951(97)00311-9.

Segall, P. and Lu, S. (2015). Injection-induced seismicity: Poroelastic and earthquake nucleation effects. *Journal of Geophysical Research: Solid Earth.* https://doi.org/10.1002/2015JB012060.

Segall, P., Grasso, J. R., and Mossop, A. (1994). Poroelastic stressing and induced seismicity near the Lacq gas field, southwestern France. *Journal of Geophysical Research.* https://doi.org/10.1029/94JB00989.

Shapiro, S., Dinske, C., Langenbruch, C., and Wenzel, F. (2010). Seismogenic index and magnitude probability of earthquakes induced during reservoir fluid stimulations. *The Leading Edge*, **29**, 304–309. https://doi.org/10.1190/1.3353727.

Shen, X., Bai, M., and Standifird, W. (2011). *Drilling and Completion in Petroleum Engineering: Theory and Numerical Applications.* Taylor & Francis Group, LLC.

Shiozawa, S. and McClure, M. (2014). EGS designs with horizontal wells, multiple stages, and proppant. In *Proceedings, Thirty-Ninth Workshop on Geothermal Reservoir Engineering*, Stanford, California.

Shtengeolov, E. S. (1980). Effect of well exploitation of the Upper Jurassic Aquifer on the seismicity of the Crimea. *Water Resources*, **7**, 132–139. Translated from Vodnye Resursy, No. 2, pp. 57-65, March-April 1980.

Shuck, L. (1977). Method for selectively orienting induced fractures in subterranean Earth formations. U.S. Patent No. 4005750.

Siebrits, E. and Peirce, A. (2002). An efficient multi-layer planar 3D fracture growth algorithm using a fixed mesh approach. *International Journal for Numerical Methods in Engineering*, **53**, 691–717. https://doi.org/10.1002/nme.308.

Simoni, L., Salomoni, V., and Schrefler, B. (1999). Elastoplastic subsidence models with and without capillary effects. *Computational Methods in Applied Mechanics and Engineering.* https://doi.org/10.1016/S0045-7825(98)00222-9.

Simonson, E., Abou-Sayed, A., and Clifton, R. (1978). Containment of massive hydraulic fractures. *Society of Petroleum Engineers Journal*, **18**, 27–32.

Simpson, D. W. and Leith, W. (1985). The 1976 and 1984 Gazli, USSR, Earthquakes - were they induced? *Bulletin of the Seismological Society of America*, **75**, 1465–1468.

Simpson, R. (1997). Quantifying Anderson's fault types. *Journal of Geophysical Research*, **102**, 17909–17919. https://doi.org/10.1029/97JB01274.

Skoumal, R., Ries, R., Brudzinski, M., Barbour, A., and Currie, B. (2018). Earthquakes induced by hydraulic fracturing are pervasive in Oklahoma. *Journal of Geophysical Research: Solid Earth*, **123**, 10918–10935. https://doi.org/10.1029/2018JB016790.

Smith, M., Bale, A., Britt, L., Klein, H., Siebrits, E., and Dang, X. (2001). Layered modulus effects on fracture propagation, proppant placement, and fracture modeling. *2001 SPE Annual Technical Conference and Exhibition, New Orleans, Louisiana, USA. Sep. 30–Oct. 3*. https://doi.org/10.2118/71654-MS.

Smith-Konter, B. and Sandwell, D. (2009). Stress evolution of the San Andreas fault system: Recurrence interval versus locking depth. *Geophysical Research Letters*. https://doi.org/10.1029/2009GL037235.

Sone, H. and Zoback, M. (2014). Viscous relaxation model for predicting least principal stress magnitudes in sedimentary rocks. *Journal of Petroleum Science and Engineering*, **124**, 416–431. https://doi.org/10.1016/j.petrol.2014.09.022.

Spada, M., Tornmann, T., Wiemer, S., and Enescu, B. (2013). Generic dependence of the frequency-size distribution of earthquakes on depth and its relation to the strength profile of the crust. *Geophysical Research Letters*, **40**, 709–714. https://dx.doi.org/10.1029/2012GL054198.

Stein, R. (1999). The role of stress transfer in earthquake occurrence. *Nature*. https://doi.org/10.1038/45144.

Stein, S. and Wysession, M. (2003). *An Introduction to Seismology, Earthquakes, and Earth Structure*. Blackwell Publishing Ltd.

Stork, A., Verdon, J., and Kendall, J. (2015). The microseismic response at the In Salah Carbon Capture and Storage (CCS) site. *International Journal of Greenhouse Gas Control*, **32**, 159–171. https://dx.doi.org/10.1016/j.ijggc.2014.11.014.

Suckale, J. (2009). Induced seismicity in hydrocarbon fields. *Advances in Geophysics*, **51**, 55–106. https://doi.org/10.1016/S0065-2687(09)05107-3.

Suckale, J. (2010). Moderate-to-large seismicity induced by hydrocarbon production. *The Leading Edge*, **29**, 310–319. https://doi.org/10.1190/1.3353728.

Sumy, D., Cochran, E., Keranen, K., Wei, M., and Abers, G. (2014). Observations of static Coulomb stress triggering of the November 2011 M5.7 Oklahoma earthquake sequence. *Journal of Geophysical Research: Solid Earth*. https://doi.org/10.1002/2013JB010612.

Sze, E., Toksöz, M. N., and Burns, D. R. (2005). Characterization of induced seismicity in a petroleum reservoir: a case study. In *Earth Resources Laboratory Industry Consortia Annual Report*.

Talwani, P. (2014). *Intraplate Earthquakes*. Cambridge University Press.

Bibliography

Tester, J., Anderson, B., Batchelor, A., Blackwell, D., DiPippo, R., Drake, E., Garnish, J., Livesay, B., Moore, M., Nichols, K., Petty, S., Toksöz, M., and Veatch, R. (2006). The Future of Geothermal Energy.

Teufel, L., Rhett, D., and Farrell, H. (1991). Effect of reservoir depletion and pore pressure drawdown on in situ stress and deformation in the Ekofisk Field, North Sea. In J. C. Rogiers, editor, *Rock Mechanics as a Multidisciplinary Science: Proceedings of the 32nd US Symposium on Rock Mechanics*, pages 63–72. Rotterdam, The Netherlands.

Townend, J. and Zoback, M. (2000). How faulting keeps the crust strong. *Geology*, **28**, 399–402. https://doi.org/10.1130/0091-7613(2000)28<399:HFKTCS>2.0.CO;2.

United States Environmental Protection Agency (1994). Determination of maximum injection pressure for class I wells.
https://www.epa.gov/sites/production/files/2015-09/documents/
r5-deepwell-guidance7-determination-maximum-injection-pressure-class1-199401-9pp.
pdf.

Urpi, L., Rinaldi, A., Rutqvist, J., Cappa, F., and Spiers, C. (2016). Dynamic simulation of CO_2-injection-induced fault rupture with slip-rate dependent friction coefficient. *Geomechanics for Energy and the Environment*, **7**, 47–65. https://dx.doi.org/10.1016/j.gete.2016.04.003.

van Eekelen, H. (1982). Hydraulic fracture geometry: Fracture containment in layered formations. *Society of Petroleum Engineers Journal*, **22**, 341–349.

Vanorio, T., Prasad, M., and Nur, A. (2003). Elastic properties of dry clay mineral aggregates, suspensions and sandstones. *Geophysical Journal International*. https://doi.org/10.1046/j.1365-246X.2003.02046.x.

Veldkamp, H. and Boxem, T. (2015). Sector Outlook: Geothermal power increase in the Netherlands by enhancing the capacity.

Verdon, J., Kendall, J., White, D., and Angus, D. (2011). Linking microseismic event observations with geomechanical models to minimise the risks of storing CO_2 in geological formations. *Earth and Planetary Science Letters*, **305**, 143–152. https://dx.doi.org/10.1016/j.epsl.2011.02.048.

Verdon, J., Kendall, J., Stork, A., Chadwick, A., White, D., and Bissell, R. (2013). Comparison of geomechanical deformation induced by megatonne-scale CO_2 storage at Sleipner, Weyburn, and In Salah. *Proceedings of the National Academy of Sciences of the United States of America*, **110**, E2762–E2771. https://doi.org/10.1073/pnas.1302156110.

Vermylen, J. and Zoback, M. (2011). Hydraulic fracturing, microseismic magnitudes, and stress evolution in the Barnett Shale, Texas, USA. In *SPE Hydraulic Fracturing Technology Conference, 24-26 January, The Woodlands, Texas, USA*.

Verruijt, A. (2013). *Theory and Problems of Poroelasticity*. Delft University of Technology.

Victoria State Government (2019). The CarbonNet Project. *Earth Resources.* https://earthresources.vic.gov.au/projects/carbonnet-project.

Vilarrasa, V. (2016). The role of the stress regime on microseismicity induced by overpressure and cooling in geologic carbon storage. *Geofluids*, **16**, 941–953. https://dx.doi.org/10.1111/gfl.12197.

Vilarrasa, V., Olivella, S., Carrera, J., and Rutqvist, J. (2014). Long term impacts of cold CO_2 injection on the caprock integrity. *International Journal of Greenhouse Gas Control*, **24**, 1–13. https://dx.doi.org/10.1016/j.ijggc.2014.02.016.

Vilarrasa, V., Makhnenko, R., and Gheibi, S. (2016). Geomechanical analysis of the influence of CO_2 injection location on fault stability. *Journal of Rock Mechanics and Geotechnical Engineering*, **8**, 805–818. https://dx.doi.org/10.1016/j.jrmge.2016.06.006.

Vilarrasa, V., Makhnenko, R., and Laloui, L. (2017). Potential for fault reactivation due to CO_2 injection in a semi-closed saline aquifer. *Energy Procedia*, **114**, 3282–3290. https://dx.doi.org/10.1016/j.egypro.2017.03.1460.

Villeneuve, M., Heap, M., Kushnir, A., Qin, T., Baud, P., Zhou, G., and Xu, T. (2018). Estimating in situ rock mass strength and elastic modulus of granite from the Soultz-sous-forêts geothermal reservoir (France). *Geothermal Energy*, **6**. https://doi.org/10.1186/s40517-018-0096-1.

Voake, T., Nermoen, A., Korsnes, R., and Fabricius, I. (2017). Induced shear failure by temperature reduction at uni-axial strain conditions. In *19th European Symposium on Improved Oil Recovery 2017: Sustainable IOR in a Low Oil Price World.*

Walsh, J. (1965). The effect of cracks in rocks on poisson's ratio. *Journal of Geophysical Research*, **70**, 5249–5257. https://doi.org/10.1029/JZ070i002p00381.

Walsh III, F. and Zoback, M. (2016). Probabilistic assessment of potential fault slip related to injection-induced earthquakes: Application to north-central Oklahoma, USA. *Geology*, **44**, 991–994. https://dx.doi.org/10.1130/G38275.1.

Wang, H. (2000). *Theory of Linear Poroelasticity with Applications to Geomechanics and Hydrogeology*. Princeton Series in Geophysics. Princeton University Press, Princeton, NJ.

Wang, J., Elsworth, D., and Denison, M. (2018). Hydrualic fracturing with leakoff in a pressure-sensitive dual porosity medium. *International Journal of Rock Mechanics and Mining Sciences*, **107**, 55–68. https://doi.org/10.1016/j.ijrmms.2018.04.042.

Wang, R., Gu, Y., Schultz, R., Zhang, M., and Kim, A. (2017). Source characteristics and geological implications of the January 2016 induced earthquake swarm near Crooked Lake, Alberta. *Geophysical Journal International*, **210**, 979–988. https://dx.doi.org/10.1093/gji/ggx204.

Warpinski, N. and Branagan, P. (1989). Altered-stress fracturing. *Journal of Petroleum Technology*, **41**, 990–997. https://doi.org/10.2118/17533-PA.

Bibliography

Warpinski, N. and Teufel, L. (1989). In-situ stresses in low-permeability, nonmarine rocks. *Journal of Petroleum Technology*, **41**, 405–414.

Warpinski, N., Schmidt, R., and Northrop, D. (1982a). In-situ stresses: the predominant influence on hydraulic fracture containment. *Journal of Petroleum Technology*, **34**, 653–664.

Warpinski, N., Clark, J., Schmidt, R., and Huddle, C. (1982b). Laboratory investigation on the effect of in-situ stresses on hydraulic fracture containment. *Society of Petroleum Engineers Journal*, **22**, 333–340.

Warpinski, N., Branagan, P., Sattler, A., Cipolla, C., Lorenz, J., and Thorne, B. (1990). Case study of a stimulation experiment in a fluvial, tight-sandstone gas reservoir. *SPE Production Engineering*, **5**, 403–410. https://dx.doi.org/10.2118/18258-PA.

Westwood, R., Toon, S., Styles, P., and Cassidy, N. (2017). Horizontal respect distance for hydraulic fracturing in the vicinity of existing faults in deep geological reservoirs: a review and modelling study. *Geomechanics and Geophysics for Geo-Energy and Geo-Resources*, **3**, 379–391. https://doi.org/10.1007/s40948-017-0065-3.

Wetmiller, R. (1986). Earthquakes near Rocky Mountain House, Alberta, and their relationship to gas production facilities. *Canadian Journal of Earth Sciences*. https://doi.org/10.1139/e86-020.

Wiemer, S. (2000). Introducing probabilistic aftershock hazard mapping. *Geophysical Research Letters*, **27**, 3405–3408. https://doi.org/10.1029/2000GL011479.

Wu, R., Bunger, A., Jeffrey, R., and Siebrits, E. (2008). A comparison of numerical and experimental results of hydraulic fracture growth into a zone of lower confining stress. In *The 42nd U.S. Rock Mechanics Symposium (USRMS), 29 June-2 July, San Francisco, California*.

Wu, Y., Chen, S., Huang, T., Huang, H., Chao, W., and Koulakov, I. (2018). Relationship between earthquake b-value and crustal stresses in a young orogenic belt. *Geophysical Research Letters*, **45**, 1832–1837. https://doi.org/10.1002/2017GL076694.

Yeck, W., Weingarten, M., Benz, H., McNamara, D., Bergman, E., Herrmann, R., Rubinstein, J., and Earle, P. (2016). Far-field pressurization likely caused one of the largest injection induced earthquakes by reactivating a large preexisting basement fault structure. *Geophysical Research Letters*. https://doi.org/10.1002/2016GL070861.

Yerkes, R. and Castle, R. O. (1976). Seismicity and faulting attributable to fluid extraction. *Engineering Geology*. https://doi.org/10.1016/0013-7952(76)90017-X.

Yerkes, R. F. and Castle, R. O. (1970). Surface deformation associated with oil and gas field operations in the united states. In *Land subsidence: International Association of the Science of Hydrology*, pages 55–66. UNESCO.

Zang, A., Yoon, J., Stephansson, O., and Heidbach, O. (2013). Fatigue hydraulic fracturing by cyclic reservoir treatment enhances permeability and reduces induced seismicity. *Geophysical Journal International*, **195**, 1282–1287. https://doi.org/10.1093/gji/ggt301.

Zang, A., Oye, V., Jousset, P., Deichmann, N., Gritto, R., McGarr, A., Majer, E., and Bruhn, D. (2014). Analysis of induced seismicity in geothermal reservoirs - An overview. *Geothermics*, **52**, 6–21. https://dx.doi.org/10.1016/j.geothermics.2014.06.005.

Zbinden, D., Rinaldi, A., Urpi, L., and Wiemer, S. (2017). On the physics-based processes behind production-induced seismicity in natural gas fields. *Journal of Geophysical Research: Solid Earth*, **122**, 3792–3812. https://dx.doi.org/10.1002/2017JB014003.

Zhang, L. and Dusseault, M. (1994). Are horizontal wells always better producers than vertical wells? *SPE/CIM/CANMET International Conference on Recent Advances in Horizontal Well Applications, March 20 - 23, Calgary, Canada*. https://dx.doi.org/10.2118/HWC-94-27.

Zhang, Y., Person, M., Rupp, J., Ellett, K., Celia, M., Gable, C., Bowen, B., Evans, J., Bandilla, K., Mozley, P., Dewers, T., and Elliot, T. (2013). Hydrogeologic controls on induced seismicity in crystalline basement rocks due to fluid injection into basal reservoirs. *Groundwater*, **51**, 525–538. https://dx.doi.org/10.1111/gwat.12071.

Zhu, W. and Wong, T. (1996). Permeability reduction in a dilating rock: Network modeling of damage and tortuosity. *Geophysical Research Letters*. https://doi.org/10.1029/96GL03078.

Zhu, W. and Wong, T. (1997). The transition from brittle faulting to cataclastic flow: Permeability evolution. *Journal of Geophysical Research*. https://doi.org/10.1029/96JB03282.

Zia, H. and Lecampion, B. (2017). Propagation of a height contained hydraulic fracture in turbulent flow regimes. *International Journal of Solids and Structures*, **110**, 265–278.

Zia, H. and Lecampion, B. (2019). PyFrac: A planar 3D hydraulic fracture simulator. *Computer Physics Communications*.

Ziagos, J., Phillips, B., Boyd, L., Jelacic, A., Stillman, G., and Hass, E. (2013). A technology roadmap for strategic development of enhanced geothermal systems. In *Thirty-Eighth Workshop on Geothermal Reservoir Engineering*.

Zimmerman, R. (2017). Pore volume and porosity changes under uniaxial strain conditions. *Transport in Porous Media*, **119**, 481–498. https://doi.org/10.1007/s11242-017-0894-0.

Zimmermann, G., Moeck, I., and Blöcher, G. (2010). Cyclic waterfrac stimulation to develop an Enhanced Geothermal System EGS-Conceptual design and experimental results. *Geothermics*, **39**, 59–69. https://doi.org/10.1016/j.geothermics.2009.10.003.

Zimmermann, G., Hofmann, H., Babadagli, T., Yoon, J., Zang, A., Deon, F., Urpi, L., Bloecher, G., Hassanzadegan, A., and Huenges, E. (2015). Multi-fracturing and cyclic hydraulic stimulation scenarios to develop enhanced geothermal systems - feasibility and mitigation

strategies to reduce seismic risk. In *Proceedings World Geothermal Congress 2015*, Melbourne, Australia.

Zoback, M. (1992). First- and second-order patterns of stress in the lithosphere: The World Stress Map Project. *Journal of Geophysical Research*, **97**, 11703–11728. https://doi.org/10.1029/92JB00132.

Zoback, M. (2007). *Reservoir Geomechanics.* Cambridge University Press, Cambridge, UK.

Zoback, M. and Gorelick, S. (2012). Earthquake triggering and large-scale geologic storage of carbon dioxide. *Proceedings of the National Academy of Sciences*, **109**, 10164–10168. https://doi.org/10.1073/pnas.1202473109.

Zoback, M. and Harjes, H. (1997). Injection-induced earthquakes and crustal stress at 9 km depth at the KTB deep drilling site, Germany. *Journal of Geophysical Research*, **102**, 18477–18491. https://doi.org/10.1029/96JB02814.

Zoback, M. and Healy, J. (1992). In situ stress measurements to 3.5 km depth in the Cajon Pass Scientific Research Borehole: Implications for the mechanics of crustal faulting. *Journal of Geophysical Research*. https://doi.org/10.1029/91JB02175.

Zoback, M. and Townend, J. (2001). Implications of hydrostatic pore pressures and high crustal strength for the deformation of intraplate lithosphere. *Tectonophysics*, **336**, 19–30. https://doi.org/10.1016/S0040-1951(01)00091-9.

Zoback, M. and Zinke, J. (2002). Production-induced normal faulting in the Valhall and Ekofisk oil fields. *Pure and Applied Geophysics*, **159**, 403–420. https://doi.org/10.1007/PL00001258.

Zoback, M., Zoback, M., Adams, J., Assumpção, M., Bell, S., E., B., Blüming, P., Brereton, N., Denham, J., Ding, J., Fuchs, K., Gay, N., Gregersen, S., Gupta, H., Gvishiani, A., Jacob, K., Klein, R., Knoll, P., Magee, M., Mercier, J., Müller, B., Paquin, C., Rajendran, K., Stephansson, O., Suarez, G., Suter, M., Udias, A., Xu, Z., and Zhizhin, M. (1989). Gobal patterns of tectonic stress. *Nature*, **341**, 291–298. https://doi.org/10.1038/341291a0.

Zoback, M., Townend, J., and Grollimund, B. (2002). Steady-state failure equilibrium and deformation of intraplate lithosphere. *International Geology Review*, **44**, 383–401. https://doi.org/10.2747/0020-6814.44.5.383.

A Appendix

A.1 Derivation of stress path equations

In order for the stress ratio to not increase, the updated stress ratio must be less than or equal to the original stress ratio,

$$\frac{S_v + \Delta S_v - P_p - \Delta P_p}{S_{hmin} + \Delta S_{hmin} - P_p - \Delta P_p} \leq \frac{S_v - P_p}{S_{hmin} - P_p}. \tag{A.1}$$

The vertical total stress is assumed to remain constant and the change to S_{hmin} is given by Equation 3.2 such that,

$$\frac{S_v - P_p - \Delta P_p}{S_{hmin} + A\Delta P_p - P_p - \Delta P_p} \leq \frac{S_v - P_p}{S_{hmin} - P_p}. \tag{A.2}$$

This equation can be simplified to

$$\Delta P_p \frac{S_v - S_{hmin}}{S_v - P_p} \leq A\Delta P_p. \tag{A.3}$$

In injection scenarios ΔP_p is positive and the resulting expression is,

$$\frac{S_v - S_{hmin}}{S_v - P_p} \leq A, \tag{A.4}$$

which is equivalent to Equation 3.6. In production cases, however, ΔP_p is negative and Equation A.3 simplifies to

$$\frac{S_v - S_{hmin}}{S_v - P_p} \geq A. \tag{A.5}$$

When Equation A.5 is satisfied, production is not expected to result in the destabilization of optimally-oriented faults. If the crust can be assumed to be critically stressed, S_{hmin} can be found using Equation 3.1, resulting in

$$S_{hmin} = P_p + \frac{S_v - P_p}{\left(\sqrt{\mu^2 + 1} + \mu\right)^2}. \tag{A.6}$$

By combining Equation A.6 with Equation A.4, Equation 3.7 can be obtained.

A.2 PyFrac Simulation Data

Table A.1 – Summary of the parameters used during M scaling analysis; b indicates the result of the trial. K1C was set to zero for each trial. An * on the value for b indicates that the fracture had not stopped propagating.

Name	$\Delta\sigma$ [MPa]	H [m]	E' [GPa]	Q_0 [$\frac{m^3}{sec}$]	μ [Pa sec]	Δz [m]	b [m]
M1	4.3	0.025	3.93	1.7×10^{-9}	30.2	0.00125	0.01023*
M2	3.5	0.025	3.93	1.7×10^{-9}	30.2	0.00125	0.01275*
M3	8.0	0.025	3.93	1.7×10^{-9}	30.2	0.00125	0.00520
M4	15.0	0.025	3.93	1.7×10^{-9}	30.2	0.00125	0.00017
M5	6.0	0.025	3.93	1.7×10^{-9}	30.2	0.00125	0.00646*
M6	10.0	0.025	3.93	1.7×10^{-9}	30.2	0.00125	0.00143
M7	12.0	0.025	3.93	1.7×10^{-9}	30.2	0.00125	0.01023
M8	6.0	0.040	3.93	1.7×10^{-9}	30.2	0.00125	0.00404
M9	6.0	0.045	3.93	1.7×10^{-9}	30.2	0.00125	0.00408
M10	3.5	0.025	3.93	1.7×10^{-9}	15.0	0.00125	0.01023*
M11	3.5	0.025	3.93	1.7×10^{-9}	1.0	0.00125	0.00394
M12	15.0	0.025	8.33	1.7×10^{-9}	30.2	0.00125	0.00394
M13	15.0	0.025	16.70	1.7×10^{-9}	30.2	0.00125	0.00772*
M14	12.0	0.025	3.93	1.0×10^{-9}	30.2	0.00125	0.00268
M15	12.0	0.025	3.93	5.0×10^{-10}	30.2	0.00125	0.00017
M16	5.0	10	41.7	3.0×10^{-5}	30.2	0.5	2.58*
M17	5.0	10	41.7	5.0×10^{-5}	30.2	0.5	3.09*
M18	3.0	10	41.7	3.0×10^{-5}	30.2	0.5	4.60*
M19	5.0	10	41.7	3.0×10^{-5}	15.0	0.5	1.58

Table A.2 – Summary of the parameters used during K scaling analysis; b indicates the result of the trial. Viscosity was zero for each trial. An * on the value for b indicates that the fracture had not stopped propagating.

Name	$\Delta\sigma$ [MPa]	H [m]	E' [GPa]	Q_0 [$\frac{m^3}{sec}$]	$K1C$ [$Pa\sqrt{m}$]	Δz [m]	b [m]
K1	4.0	0.146	165	3×10^{-7}	1×10^6	0.00365	0.0122
K2	8.0	0.146	165	3×10^{-7}	1×10^6	0.00365	0.0086
K3	8.0	0.146	165	3×10^{-7}	2×10^6	0.00365	0.0122
K4	4.0	0.146	165	3×10^{-7}	2×10^6	0.00365	0.0196
K5	6.0	0.146	165	3×10^{-7}	2×10^6	0.00365	0.0122
K6	3.0	0.146	165	3×10^{-7}	3×10^6	0.00365	0.0638*
K7	12.0	0.146	165	3×10^{-7}	1×10^6	0.00365	0.0086
K8	5.0	0.146	165	3×10^{-7}	2×10^6	0.00365	0.0159
K9	3.0	0.146	165	3×10^{-7}	2×10^6	0.00365	0.0306*
K10	5.0	0.146	165	3×10^{-7}	3×10^6	0.00365	0.0638*
K11	6.0	0.146	165	3×10^{-7}	1×10^6	0.00365	0.0086
K12	3.5	0.146	165	3×10^{-7}	3×10^6	0.00365	0.0490*
K13	4.0	0.1825	165	3×10^{-7}	3×10^6	0.00365	0.0309*
K14	4.0	0.1095	165	3×10^{-7}	2×10^6	0.00365	0.0451*
K15	5.0	0.1095	165	3×10^{-7}	2×10^6	0.00365	0.0451*
K16	3.6	0.146	165	5×10^{-7}	3×10^6	0.00365	0.0490*
K17	3.6	0.146	250	3×10^{-7}	3×10^6	0.00365	.0454*
K18	1.0	5.0	165	1×10^{-4}	3×10^6	0.125	0.545
K19	2.0	5.0	165	1×10^{-4}	3×10^6	0.125	0.293
K20	1.0	5.0	165	1×10^{-4}	4×10^6	0.125	0.671*
K21	1.75	5.0	25	1×10^{-4}	1×10^6	0.125	0.293

Table A.3 – Summary of the parameters used during $\tilde{M}$ scaling analysis; b indicates the result of the trial. K1C was set to zero for each trial. An * on the value for b indicates that the fracture had not stopped propagating.

Name	$\Delta\sigma$ [MPa]	H [m]	E' [GPa]	Q_0 [$\frac{m^3}{sec}$]	μ [Pa sec]	C' [$\frac{m}{\sqrt{sec}}$]	Δz [m]	b [m]
$\tilde{M}1$	6.00	2.5	41.7	3×10^{-5}	30.2	2.0×10^{-5}	0.0625	0.020
$\tilde{M}2$	2.50	2.5	41.7	3×10^{-5}	30.2	2.0×10^{-5}	0.0625	0.210
$\tilde{M}3$	3.50	2.5	41.7	3×10^{-5}	30.2	2.0×10^{-5}	0.0625	0.147
$\tilde{M}4$	5.00	2.5	41.7	3×10^{-5}	30.2	2.0×10^{-5}	0.0625	0.020
$\tilde{M}5$	4.50	2.5	41.7	3×10^{-5}	30.2	2.0×10^{-5}	0.0625	0.147
$\tilde{M}6$	2.00	2.5	41.7	3×10^{-5}	30.2	2.0×10^{-5}	0.125	0.273*
$\tilde{M}7$	4.00	2.5	41.7	3×10^{-5}	30.2	2.0×10^{-5}	0.0625	0.147
$\tilde{M}8$	4.00	2.5	41.7	3×10^{-5}	30.2	2.5×10^{-5}	0.0625	0.020
$\tilde{M}9$	3.00	2.5	41.7	3×10^{-5}	30.2	2.0×10^{-5}	0.0625	0.210
$\tilde{M}10$	1.50	2.5	41.7	3×10^{-5}	30.2	2.0×10^{-5}	0.0625	0.273*
$\tilde{M}11$	2.25	2.5	41.7	3×10^{-5}	30.2	2.0×10^{-5}	0.0625	0.210*
$\tilde{M}12$	2.75	2.5	41.7	3×10^{-5}	30.2	2.0×10^{-5}	0.0625	0.210

Table A.4 – Summary of the parameters used during $\tilde{K}$ scaling analysis; b indicates the result of the trial. Viscosity was zero for each trial. An * on the value for b indicates that the fracture had not stopped propagating.

Name	$\Delta\sigma$ [MPa]	H [m]	E' [GPa]	Q_0 [$\frac{m^3}{sec}$]	$K1C$ [$Pa\sqrt{m}$]	C' [$\frac{m}{\sqrt{sec}}$]	Δz [m]	b [m]
$\tilde{K}1$	0.10	5	41.7	1×10^{-5}	3×10^5	1×10^{-5}	0.125	0.671*
$\tilde{K}2$	0.05	5	41.7	1×10^{-5}	2×10^5	1×10^{-5}	0.125	1.175*
$\tilde{K}3$	0.20	5	41.7	1×10^{-5}	2×10^5	1×10^{-5}	0.125	0.293
$\tilde{K}4$	0.10	5	41.7	1×10^{-5}	2×10^5	1×10^{-5}	0.125	0.419
$\tilde{K}5$	0.40	5	41.7	1×10^{-5}	2×10^5	2×10^{-5}	0.125	0.293
$\tilde{K}6$	0.04	5	41.7	1×10^{-5}	1×10^5	2×10^{-5}	0.125	0.545
$\tilde{K}7$	0.035	5	41.7	1×10^{-5}	1×10^5	2×10^{-5}	0.125	0.671*
$\tilde{K}8$	0.11	5	41.7	1×10^{-5}	3×10^5	2×10^{-5}	0.125	0.545*
$\tilde{K}9$	0.13	5	41.7	1×10^{-5}	3×10^5	2×10^{-5}	0.125	0.419
$\tilde{K}10$	0.22	5	41.7	1×10^{-5}	3×10^5	2×10^{-5}	0.125	0.293
$\tilde{K}11$	0.05	5	41.7	1×10^{-5}	3×10^5	2×10^{-5}	0.125	1.175*

A.3 Core concepts

While this section gives an overview of some core concepts used in this thesis, many of the larger topics are not covered here in detail. Instead, appropriate references for poroelasticity (Biot, 1941; Rice and Cleary, 1976; Wang, 2000; Verruijt, 2013; Cheng, 2016), hydraulic fracturing (Economides and Nolte, 2000), petroleum engineering (Peaceman, 1977; Dake, 1978; Lake, 1989; Aziz and Settari, 2002), and reservoir geomechanics (Zoback, 2007), and induced earthquakes (Foulger *et al.*, 2018) are provided.

A.3.1 Anisotropic stress changes

Anisotropic stress changes simply means that the magnitude of the stress changes to each of the principal stress directions is not the same. It does not really make sense to distinguish between total or effective stresses for this definition because pore pressure is a scalar.

A.3.2 Aseismic slip

Aseismic slip, or creep, is when shear failure occurs stably. This is as opposed to seismic slip where shear failure is unstable. Aseismic can be thought of as slow propagation without measurable seismic activity. Felt earthquakes are by nature seismic. For more information on what might promote aseismic slip see Section A.3.22, as well as such articles as (Scholz, 1998; Cappa *et al.*, 2018; Cornet, 2019).

A.3.3 (Geologic) basement

The geologic basement just refers to the rocks below the sedimentary cover. These rocks are either metamorphic or igneous in nature. Frequently, the top of the geologic basement is an unconformity, such that that location may have previously been eroded down to the basement (and further) and then later deposits build up the current sedimentary cover. The basement is frequently harder rock than the sedimentary cover, and characterized by higher coefficients of friction (see Blanpied *et al.* (1995); Saffer and Marone (2003); Ikari *et al.* (2011) for examples of coefficients of friction for granite, shale, and sandstone, respectively). This often means it has a higher differential stress (e.g., (McGarr, 1980; Connor *et al.*, 2009). As discussed in Section A.3.14, this means that it is also capable of producing larger earthquakes. Further, given its age, it is also common for the basement rock to be more highly faulted than the sedimentary cover. These two aspects may be behind why large magnitude induced events are frequently in the basement despite the operation being in the sedimentary cover (see Section A.3.32 for examples). Some studies that deal with the basement seismicity include (Zhang *et al.*, 2013; Chang and Segall, 2016a,b, 2017; Urpi *et al.*, 2016). Of course some operations, such as many EGSs, occur in basement rock, making a discussion on the differences between basement rock and sedimentary cover less interesting.

A.3.4 Carbon storage (CCS)

Mankind is emitting anthropogenic CO_2 at a rate of approximately 50 Gigatonnes per year (IPCC, 2014). It is thought that, in order to remain below a 2^oC temperature increase by 2100 relative to 1880, we can only emit a total of 2900 Gt of anthropogenic CO_2 (of which we have already emitted about 1900 Gt) (IPCC, 2014). Clearly, we need to start implementing solutions quickly.

One such solution is Carbon Capture (Utilization) and Storage, or CCS. CCS will likely involve the storage of CO_2 in the subsurface, likely in deep saline aquifers as they are capable of accommodating large volumes of CO_2 and are potentially well distributed with respect to likely sources of CO_2 (Zoback and Gorelick, 2012). The large-scale storage of CO_2 is said to take place at injection rates of at least 800,000 tonnes per year of CO_2 at any given site (Global-CCS-Institute, 2017). At these injection rates, waste water injection into deep basal aquifers has been seen to be capable of causing significant seismicity (e.g. (Ellsworth, 2013) (Keranen *et al.*, 2013) (IEAGHG, 2013)).

Indeed, even in the handful of CCS projects that are currently underway, there have been instances of seismicity. Injection sites such as In Salah (Oye *et al.*, 2013) (Goertz-Allmann *et al.*, 2014) (Stork *et al.*, 2015), Weyburn (Verdon *et al.*, 2011), and Decatur (Goertz-Allmann *et al.*, 2017a) (Goertz-Allmann *et al.*, 2017b) have all been shown to be associated with microseismic events. Although none of the induced events have been large enough to have been felt at the surface or even cause damage, the risk of a large seismic event during CO_2 injection is certainly large enough to warrant some extra attention.

Further, it should be noted that despite over twenty years of large international conferences organized by the IEAGHG, there are essentially no large scale CCS projects that are not set up as either (a) a solution for large amounts of CO_2 that are produced alongside hydrocarbon, (b) part of an Enhanced Oil Recovery (EOR) operation (under certain conditions CO_2 is miscible with hydrocarbon such that residual oil is not left behind in reservoirs) to increase hydrocarbon production. Indeed, note that operators even produce CO_2 out of CO_2 reservoirs such as the Jackson Dome, Mississippi in order to increase the amount of CO_2 available for EOR operations (Denbury Resources produced over 12 million tonnes of CO_2 from Jackson Dome in 2008 (Denbury Resources Inc., 2008)). From the author's personal experience it can be said that the flaring of CO_2 does occur in these fields and that significant leaks (typically associated with poorly abandoned old wells whose whereabouts are frequently unknown to operators) also occur (e.g., (Ernst, 2013)). Also, the similarities in exploration for a CCS reservoir and hydrocarbon pose the question as to whether or not hydrocarbon reservoirs are sometimes accidentally found during exploration for CCS, such as could be imaged to be the case during the large-scale seismic surveys occurring of the eastern coast of Australia in the Gippsland Basin (Geoscience Australia, 2019), which is also one of Australia's most prolific hydrocarbon provinces (Victoria State Government, 2019).

Those who wish to learn more about CCS can attend IEAGHG's next edition of GHGT, GHGT-15,

which will be held in Abu Dhabi. It has not yet been announced if BHP, ExxonMobil, and Total will be again amongst the list of gold-level sponsors, as was the case for GHGT-14.

A.3.5   Compaction

The topic of compaction is covered in Chapter 2 both in the text itself and through the references provided. Broadly speaking though, as mean effective stress increases pore space is reduced. This results in loss of both porosity and permeability. Note that the reduction of pore pressure causes an increase in mean effective stress, so compaction is expected to some degree during fluid production. Compaction may begin as a small, elastic effect, but it can begin to occur inelastically resulting in large changes to porosity and permeability (Schutjens *et al.*, 2004). Compaction also occurs naturally through burial. It is for this reason that deeper reservoirs tend to have less attractive properties. Note that the severity of the compaction also depends on the type of rock, so certain rocks will compact more than others for a given change in stress.

A.3.6   Confining stress

Confining stress refers the minimum principal total stress (see Section A.3.11). This term is used in hydraulic fracturing as the fluid pressure has to overcome the stress in order to propagate.

A.3.7   Coulomb stress

The concept of Coulomb stress (e.g., Stein (1999) and references therein) is that it characterizes how close a given fault is to failure as well as if a given set of pore pressure and stress changes brought a fault closer to or farther from failure. In this way, a positive change in Coulomb stress means the fault is now closer to failure whereas a negative one stabilizes the fault. This makes Coulomb stress a convenient way to characterize the effect of a given event of the seismicity of an area and spatial plots can be made illustrating how the stress changes in that area have increased or decreased the chance of failure of a potential fault. Coulomb stress is used in Chapters 1, 2, and 3 to illustrate the effect of a given action.

A.3.8   Critically-stressed crust

The notion of a critically-stressed crust (Harrison *et al.*, 1954; Brudy *et al.*, 1997; Townend and Zoback, 2000; Zoback and Townend, 2001; Zoback *et al.*, 2002) implies that the crust is a constant state of failure equilibrium, and small changes in stress are capable of causing earthquakes. Evidence of this state of failure equilibrium includes seismicity caused by small changes in fluid pressure, earthquakes triggered by other earthquakes, and in-situ measurements in deep boreholes (see Zoback *et al.* (2002) for further discussion and references).

One of the implications of a critically-stressed crust is that reverse faulting stress regimes are likely to exhibit larger differential stresses than strike-slip faulting regimes, which, in turn, are expected to exhibit larger differential stresses than normal faulting stress regimes. This is supported by natural earthquake data, when on considers the previously mentioned relationship between differential stress and earthquake size distribution (Schorlemmer *et al.*, 2005; Gulia and Wiemer, 2010).

Further, a critically-stressed crust implies that rocks which are more likely to contain faults with lower coefficients of friction are also likely to exhibit lower differential stresses, and that a stress jump may occur between two layers which are characterized by different coefficients of frictions. This feature has been seen in the field (Alberty and McLean, 2001; Gunzburger and Cornet, 2007; Sone and Zoback, 2014). Conveniently for hydraulic fracturing, this implies that shale cap rocks are likely to have a higher minimum principal stress than a typical conventional sandstone/limestone reservoir in normal faulting stress regimes. Therefore, as minimum principal stress exhibits a strong control on hydraulic fracture propagation (Warpinski *et al.*, 1982a,b; van Eekelen, 1982; Warpinski and Teufel, 1989; Sone and Zoback, 2014), it is likely that this stress jump results in a natural fracture barrier in normal faulting stress regimes, helping to contain hydraulic fractures within the target reservoir. However, in reverse faulting stress regimes, no minimum stress jump is expected. Interestingly, in reverse faulting stress regimes, a lower maximum principal stress should be expected in the cap rock than in the reservoir; however, this has not, to my knowledge, been shown in the field and would probably be of limited interest for hydraulic fracturing operations. The implications for a strike-slip faulting stress regime are less clear. The containment of hydraulic fractures due to stress jumps is the focus of Chapter 5.

However, probably the largest implication of a critically-stressed crust is that associated with the notion that even intraplate areas, which can frequently be quiet seismically, are thought to be critically-stressed (Townend and Zoback, 2000). Intraplate areas are seismically quiet due to low strain rates (Zoback, 2007; Zoback and Zinke, 2002), but this does not mean that they are incapable of hosting earthquakes. Over long periods of time many intraplate areas do experience significant levels of seismicity, including many large ($M_w > 7$) events (Zoback and Gorelick, 2012; Talwani, 2014). In fact, the deadliest earthquake in human history occurred in an intraplate region (Talwani, 2014). As intraplate regions are quiet due to a low stressing rate, any action that results in a significant change in stress in the subsurface may be capable of producing an earthquake. In fact, if the stressing rate is low, even small stress changes may produce significant changes in the seismic behaviour of a region (Parsons, 2005). Certain industrial activities are capable of inducing such stress changes and have been seen to be capable of inducing earthquakes, even (or possibly especially) in intraplate areas.

A.3.9 Depletion-induced seismicity

Depletion-induced seismicity refers to seismicity induced by the production of fluids. This can be water production although usually this is in the context of hydrocarbon (both oil and gas) production. The standard model for depletion-induced seismicity comes from poroelasticity and was proposed by (Segall, 1989). What this model essentially says is that pore pressure reduction in the depleted zone causes a contraction of the reservoir (specifically, the gradient of pore pressure acts as an internal force in the momentum balance equation). This contraction is opposed by surrounding layers, inducing stresses in them. The total stress above and below the reservoir increases in the horizontal direction. The stress next to the reservoir decreases in the horizontal direction. Based on the different faulting types, Section A.3.13, and these stress changes we can predict which types of faulting we expect to see in each location. Reverse faulting is expected to occur above and below the reservoir because the horizontal stress, which is the maximum principal stress in a reverse faulting stress regime, increases in these areas. Normal faulting is expected to occur next to the reservoir because the horizontal stress, which is the minimum principal stress in a normal faulting stress regime, decreases in these areas. Examples seen in practice agree quite well with this theory (see the introduction of Chapter 2). Note that this theory is less clear about when to expect strike-slip faulting, but keep in mind that these stress changes are anisotropic in the horizontal direction (discussed in Chapter 2), so some predictions can be made.

Another type of depletion-induced seismicity occurs within the pore pressure depleted zone of the reservoir in high stress path reservoirs. This is explained in Section A.3.15. A large number of examples of depletion induced seismicity (including from water production) are given in Chapters 1 and especially 2. Further examples can be found in (Suckale, 2009, 2010).

A.3.10 Differential stress

The differential stress is simply the difference between the maximum and minimum principal stresses. The primary relevance for this thesis of differential stress is its effective on compaction (see Chapter 2) and its effect on the frequency magnitude distribution of earthquakes (see Section A.3.14).

A.3.11 Effective stress

The effective stress has a number of definitions. The two that will be used here are Terzaghi's effective stress and the Biot effective stress. Terzaghi's effective stress is the total stress minus the pore pressure, without the Biot coefficient. Terzaghi's effective stress is the effective stress used to evaluate shear failure such as on Mohr Coulomb plots for example (Mandl, 2000). The Biot effective stress is the same as the Terzaghi effective stress except pore pressure is multiplied by a Biot coefficient, which has a value between zero and one. The Biot effective stress is used in calculations of stress change in poroelasticity and is therefore the effective

stress used in the poroelastic reservoir simulator used in many parts of the thesis.

A.3.12 Enhanced Geothermal Systems (EGSs)

An EGS is a geothermal reservoir that is not economically viable initially and must be somehow improved such that it can produce geothermal heat at an acceptable rate. Although EGS can be sedimentary rocks and require acid stimulations (e.g., (Evans *et al.*, 2012)), in this thesis I refer exclusively to EGSs in basement rocks, such as granites. These reservoirs are typically stimulated in shear, although in the United States especially sometimes they are hydraulically fractured with injection pressures above the minimum principal stress (e.g., McClure and Horne (2014)). The typical set up is to stimulate two wells, also called doublet wells, such that cold fluid can be injected in one and produced from the other.

EGS faces a few major problems. It is very expensive, it is difficult to achieve the injection/production rates required to make it economical (injection especially is an issue), and it has caused fairly large magnitude induced seismicity on a number of occasions (Basel and Pohang in particular Häring *et al.* (2008); Grigoli *et al.* (2018); Kim *et al.* (2018)). To my knowledge, there is only one truly successful EGS project in the world, Soultz-sous-Forêts (Evans *et al.*, 2005a,b; Evans, 2005). Regarding induced seismicity, the crux of the problem is that the mechanism for stimulation (shear failure) is the same as that of an earthquake. Obviously that is a simple way of looking at things but that is essentially the problem. For this reason, a lot of research is focused on how to have aseismic shear stimulation without incurring large seismic earthquakes (see Section A.3.26). Indeed, achieving this kind of stimulation reliably would be the "holy grain" for EGS stimulation. This was the focus of a large part of Chapter 3 in the thesis. Regardless of whether one agrees with the ideas put forward in that chapter or not, I think a push needs to be made towards thinking about what we know about rock mechanics and designing stimulation treatments in this way, as sometimes the current approaches feel a little more like guesswork, stimulating a body of rock and just waiting to see what happens.

A.3.13 Faulting types

In the early 1900's Anderson described three types of faulting, normal, strike-slip, and reverse. Essentially, which type of faulting occurs depends on the orientation of the fault as well as the prevailing stress regimes. If the maximum principal stress is vertical, optimally-oriented faults fail such that the hanging wall is lowered compared to the footwall and normal faulting is said to have occurred. If the minimum principal stress is vertical, optimally-oriented faults fail such that the hanging wall is raised compared to the footwall and reverse faulting is said to have occurred. If the vertical stress is intermediate, strike-slip faulting occurs. An optimally oriented fault strikes approximately 30 degrees from the maximum principal stress, depending on the coefficient of friction. Note that intermediate faulting types can also occur and that more than one type of faulting may be seen in a given earthquake sequence. More information on faulting types can be found in Simpson (1997); Zoback (2007).

A.3.14 Gutenberg-Richter

The Gutenberg-Richter power law (Gutenberg and Richter, 1944) essentially a rule in seismicity says that, if there are a given number of events larger than a certain magnitude, there will be ten times less events that are larger than a magnitude which is one higher. In practice, this factor is not always ten and is quantified by the *b*-value. A higher *b*-value means relatively more small events and a lower *b*-value means relatively more large events. A *b*-value of 1 corresponds to the standard case where there is a factor of ten between event sizes as described previously. The relationship is further defined by an activity, or *a*, value. This is the intercept of the relation and quantifies the total number of all events above a magnitude of zero. The magnitude of completeness, M_c, which does not feature in the relationship explicitly, is the magnitude above which operators are confident they have recorded all the events. Most seismology textbooks will discuss Gutenberg-Richter to some extent.

Heavy focus has been placed by authors on the relationship between *b*-value and differential stress (Amitrano, 2003; Schorlemmer *et al.*, 2005; Narteau *et al.*, 2009; Gulia and Wiemer, 2010; Goebel *et al.*, 2013; Spada *et al.*, 2013; El-Isa and Eaton, 2014; Scholz, 2015; Wu *et al.*, 2018; Pearson, 1981; Häring *et al.*, 2008; Goertz-Allmann *et al.*, 2011; Layland-Bachmann *et al.*, 2012; Goertz-Allmann and Wiemer, 2013; Kwiatek *et al.*, 2014; Dohmen *et al.*, 2017). Indeed, I have done the same in Chapter 3. This relationship makes sense intuitively, as earthquakes have the tendency to be larger in high stress environments (Schorlemmer *et al.*, 2005; Narteau *et al.*, 2009; Gulia and Wiemer, 2010). This relationship with differential stress can be combined with the idea of a critically-stressed crust to explain why *b*-values are lowest in reverse faulting stress regimes and highest in normal faulting stress regimes (Schorlemmer *et al.*, 2005; Gulia and Wiemer, 2010; El-Isa and Eaton, 2014; Wu *et al.*, 2018).

A.3.15 High stress path reservoirs

A stress path of a reservoir is simply how much the total horizontal stress changes for a given pore pressure change based off of poroelasticity (Chan and Zoback, 2002). A high stress path reservoir, a definition defined around normal faulting stress regimes, means that the total horizontal stress changes are so large during production, where pore pressure and total stress changes are negative (tensile), that the cause instability despite the decreasing pore pressure. One can imagine that the decreasing horizontal total stress (which is the minimum principal stress in normal faulting stress regimes) results in an increased differential stress and a more unstable stress situation. A high stress path means that this aspect in a sense overrides the increased stability associated with the lower pore pressure. See Chapters 1 and 2 for examples of high stress path reservoirs and especially Chapter 3 for a further discussion of high stress path reservoirs. Examples of literature discussing the stress path include Segall and Fitzgerald (1998); Chan and Zoback (2002); Zoback (2007). Note that this concept is really only applicable in cases where the vertical total stress remains constant. This is the case for laterally-extensive reservoirs which are typical in sedimentary layers commonly used in industry.

A.3.16 Hydraulic fracturing

Hydraulic fracturing is the mode I (tensile failure) opening of a subsurface reservoir through the use of pressurized fluids. This fluid can either be water (slickwater frac) or viscous through the use of gels. These gels allow the fluid to support proppant (sand) which acts to hold the fractures open after pressure is reduced. The propped pathways then allow for increased fluid production due to increased permeability and more favorable flow regimes. Hydraulic fractures generally open in a plane normal to the minimum principal stress, which is why horizontal wells are drilled parallel to the minimum principal stress. Hydraulic fracturing has been around since at least the 1950's (Khristianovic and Zheltov, 1955) but has come to the attention of many recently due to the shale gas boom. Due to the ability to drill horizontal wells and hydraulic fracture the well in stages, hydraulic fracturing in shale (source) rocks has become economical. Hydraulic fracturing has received much negative attention and is even banned in many countries, primarily due to concerns over the contamination of fresh water aquifers, indeed the premise of Chapter 5 is the vertical propagation of hydraulic fractures, something that does not even consider the potential for fracture fluids to leak up a wellbore annulus. Note that hydraulic fracturing has also been seen to induce seismicity on a number of occasions (Atkinson *et al.*, 2015; Clarke *et al.*, 2014; Deng *et al.*, 2016; Wang *et al.*, 2017). Hydraulic fracturing represents a large body of literature that can not be adequately covered here. See Chapter 5 for more references and a discussion of models used in hydraulic fracturing, as well as Economides and Nolte (2000); Lecampion *et al.* (2018) and many other references for further information.

Frac-hits

A frac-hit is essentially a term used when a hydraulic fracture propagates towards a previously depleted zone. This is not ideal for operators because it doesn't give them optimal reservoir coverage with their fractures, as a previously depleted zone is obviously less attractive than the fresh reservoir that they try to target. As pointed out by Jin and Zoback (2019) and presumably others, frac-hits occur because of changes in total stress associated with depletion. Depletion will reduce the horizontal stresses primarily which, in a normal faulting scenario, means the minimum principal stress will decrease. As has been shown by Wu *et al.* (2008), for example, hydraulic fractures tend to grow into zones of low confining stress.

Microseismic depletion delineation (MDD)

When a hydraulic fracturing job is performed in stages, it can happen that some stages either are not correctly fractured or simply do not produce as well as other stages. In the case of hydraulic fracturing of shales, the matrix permeability is so low that it takes a significant amount of time for the matrix pressure to change significantly as the result of either injection or production. By producing from the well over a significant period of time, stages that were well fractured achieve a reduction in pore pressure but those that were not well fractured do

not. From poroelasticity we know that changes in pore pressure result in changes in stress. In normal faulting stress regimes, the poroelastic total stress changes will result in larger differential stresses. As pore pressure is low, shear failure does not occur, however.

When operators wish to see which stages produced well, they then inject fluid. This causes pore pressure to increase, in cases which have a large differential stress, the result is seismicity with a low b-value. Note that this injection is not long term enough to significantly affect the matrix pressure, meaning the stress changes are not undone by this injection. By using this methodology, proposed in a series of a papers by Dohmen *et al.* (2013, 2014); Norbeck and Horne (2015); Dohmen *et al.* (2017), operators can then see which stages need refracturing.

A.3.17 In-situ stress state

The in-situ stress state is the virgin state of stress at a given location in the subsurface. Operators have not influenced the stress state at this stage.

A.3.18 Mean (effective) stress

The mean stress is the average value of the three principal total stresses. The mean effective stress is the mean stress minus the value of pore pressure. This can be done either with or without the inclusion of the Biot coefficient. Indeed, there are some examples of inconsistencies (Schutjens *et al.*, 2004). In this thesis, when mean effective stress is used, the Biot coefficient is not included.

A.3.19 Normal (effective) stress

The normal stress is the stress that is normal to a (fault) plane. For a fault, this is the stress that is holding the fault shut, applied normal to the plane of the fault. Normal stress is sometimes seen definition of Mohr-Coulomb failure and also has implications for the potential of a fault to slip aseismically (see Section A.3.22). The normal effective stress is the normal stress minus pore pressure. If normal effective stress is used in this thesis, it is without the Biot coefficient because normal effective stress is generally used in the context of shear failure where the Biot coefficient is not included (see Mandl (2000) and Section A.3.11).

A.3.20 Poroelasticity

While an in-depth look at poroelasticity will not be given here, it may be useful to colloquially introduce what poroelasticity essentially says. Given a porous structure, it can be imagined that by increasing the stress on the structure the structure can be made to deform resulting in a reduced pore space. If there is fluid in that pore space, the reduced volume available to it results in an increase in pore fluid pressure. Conversely, by increasing pore fluid pressure it can be imagined that the structure is pushed against and deformation is induced resulting

in increased pore space, or increased stress if the structure is confined. Poroelasticity, which is essentially Hooke's Law which uses effective stress in the place of general stress, says that this relationship is elastic. The effect of pore pressure changes on structural strain and the effect of structural strain on pore pressure represent the coupling that is frequently present in poroelastic models. This coupling can be one or two ways, depending on the application. For example, there are certain cases where the solid to fluid coupling can be ignored (Wang, 2000). Further details on poroelasticity can be found in Biot (1941); Rice and Cleary (1976); Wang (2000); Verruijt (2013); Cheng (2016).

A.3.21   Principal stresses

Within an object/material/the subsurface it is possible to make a cube of any orientation and measure the normal and shear stresses on that cube. The maximum and minimum principal stresses are the maximum and minimum normal stresses possible from any orientation of cube. They both exist on the same cube. No shear stresses are present on any plane making up this cube. The maximum and minimum principal stresses are in directions which are normal to one another and therefore form a plane. The third principal stress is in the direction normal to the plane made up by the maximum and minimum principal stresses. By defining these three principal stresses and their directions, we completely characterize the stress in any direction at that location.

Generally in the subsurface, one principal stress is vertical (Zoback, 2007). This is because fluids cannot support shear stress, so the surface, which is in contact with a fluid - air, cannot support shear stress. This means that at the surface one principal stress has to be vertical. That one principal stress holds pretty well in most applications. Exceptions to this can occur around faults or other heterogeneities. Salt (which acts quite a bit like a fluid) is also capable of causing unusual stress orientations. In the case that one minimum principal stress is vertical, it is generally referred to as S_v. The horizontal stresses are referred to as S_{hmin} and S_{Hmax} for the minimum and maximum horizontal stress respectively.

The differential stress refers the difference between the maximum and minimum principal stress. The minimum principal stress can usually be characterized by a mini frac test. Source mechanisms from earthquakes can also help characterize the stress state. In fact, these approaches, and others, have been used to create a world stress map (Zoback *et al.*, 1989; Zoback, 1992; Heidbach *et al.*, 2007, 2010, 2018). This body of literature also discusses the different methods of determining the stress state and their fidelity.

A.3.22   Rate and state friction

When a fault slips, the associated slip rate increase causes an increase in friction, known as the direct velocity effect (Scholz, 1998) and represented by the *a* value. After the initial increase, the friction of the fault decreases to a new steady-state value over a characteristic slip distance

(Scholz, 1998). The characteristic slip distance corresponds to the sliding distance required to renew the asperity contacts (Scholz, 1998). This decrease after the initial increase in friction is given by the *b* value (these are not the same *a* and *b* as in Section A.3.14).

The term a-b governs the slip behaviour of the fault. If a-b is positive, the fault exhibits velocity strengthening behaviour and the fault is always stable (Scholz, 1998). If a-b is negative, the fault is either unstable or conditionally stable (Scholz, 1998). In the case of a negative a-b, the fault will be unstable if the effective normal stress is larger than a critical value, given by

$$\bar{\sigma}_c = \frac{k \cdot L}{-(a-b)},$$
(A.7)

where k is stiffness, L is the critical slip distance, and $\bar{\sigma}_c$ is the critical normal stress (Scholz, 1998). After the slip rate is reduced, the coefficient of friction will appear to drop slightly; this is due again to the direct velocity effect. After this, the coefficient of friction recovers with the log of time (Scholz, 1998).

In a sense, a-b determines if the given fault has the potential to slip seismically. In fact, it is reasonable to assume that recordable earthquakes will nucleate in any region with a negative a-b value regardless of how small it is (Marone and Saffer, 2007). In reality there is a lot of uncertainty regarding many of the a-b values found from laboratory studies (e.g., (Lockner, D. and Byerlee, J., 1986)).

A.3.23   Scaling analyses

From Barenblatt (2003), "the term scaling describes a seemingly very simple situation: the existence of a power-law relationship between certain variables". A scaling analysis can be performed on a complex mathematics equation, or multiple equations, with many terms. By gathering terms of an equation into dimensionless groups, typical values can be input into the variables making up these dimensionless groups to see which terms are governing the equation. Alternatively, it can be decided which groups must be important for a given problem, and the values that these variables must be have can be approximated. Note that for this approach it is helpful to introduce the idea of an order of approximation. A zeroth order of approximation is equivalent to saying that the answer is within one order of magnitude to the given number. For example, stating a few thousand when the correct answer is 3,914. A first-order of approximation is done by giving one number exactly, so stating that the answer is 4,000. A scaling analysis' goal is to give the answer to order one precision.

In chapter 5, a scaling analysis was performed for hydraulic fracturing. There, dimensionless quantities were introduced, and the dimensioned variables in the equations were replaced by them. Then, terms were gathered into dimensionless groups, which were then defined as the *G*'s. Each *G* represented a phenomenon of the problem of a propagating hydraulic fracture.

For example, G_K represented fracture toughness, or the energy being expended to break new rock. If G_K was set to one, as was done for the toughness-dominated regime, it was essentially like saying that the energy being used to break the rock was significant and needed to be included. By setting G_K to zero, we were saying that the energy to do this was negligible, and the process was not dominant. There was also a G_e which represented elasticity, G_m, which represented viscous flow, G_C which represented leak-off, G_v which represented storage, and G_σ which represented the stress jump. By assigning G_e, one of either G_m or G_K, and one of either G_v or G_C to one, we could come up with four main regimes where three processes were dominant. Of course, it is also possible to be in between two regimes, where say both viscous flow and toughness are important, but we were primarily interested in the end members. Based on these three G's being one, we could solve for expressions for the characteristic length, L_*, the characteristic width, W_*, and the characteristic pressure, P_*. Time was present in these expressions, so it was possible to see the scaling of these parameters in time. In this way, it was possible to see how fracture half-length/radius, width, and pressure evolved in time (recall that base equations and therefore also the G's change depending on the fracture geometry used); these are the scalings.

G_σ was given by stress jump divided by the characteristic pressure. It is intuitive to think that if the stress jump is much larger than the characteristic pressure, the fracture will not breakthrough because a fracture needs to overcome the minimum principal stress; this case would give a large value for G_σ. An expression for G_σ in terms of known quantities was found by replacing the characteristic pressure with the value of the characteristic pressure at the time of breakthrough. Therefore, the value of G_σ can be known from given parameters about the reservoir/injection, and, as breakthrough is inversely related to breakthrough, it can be qualitatively stated whether a given case will have a large breakthrough. This qualitative result was then made quantitative by matching it to results from a simulator.

More examples of scaling analyses in hydraulic fracturing are given in Chapter 5, and two useful references for scaling analyses in general are Barenblatt (1996, 2003).

A.3.24   Seismicity models

Explicitly modelling faults allows researchers to account for the mechanics of fault behaviour (e.g. (Vilarrasa *et al.*, 2017; Rutqvist *et al.*, 2017; Rinaldi *et al.*, 2016, 2014a,b; Zbinden *et al.*, 2017; Urpi *et al.*, 2016; Cueto-Felgueroso *et al.*, 2017)). However, the highly faulted nature many basement rocks (where induced seismicity frequently occurs) have due to their long tectonic history, the difficulties faced at recognizing faults in the basement rock (Zoback and Gorelick, 2012; Goertz-Allmann *et al.*, 2017a; Walsh III and Zoback, 2016) (as evidenced by the number of large earthquakes occurring on unrecognised faults due to waste water injection (Horton, 2012; Chen *et al.*, 2017; Rubinstein *et al.*, 2014; Rubinstein and Babaie Mahani, 2015; Alt II and Zoback, 2017)), the size of the risk zone, and the general uncertainty surrounding the subsurface mean that the explicit modelling of faults for risk assessment is fraught with

uncertainty and is likely to under predict seismicity. This is worrying for prospects of obtaining and maintaining a social license-to-operate, as even relatively small earthquakes below a moment magnitude of 4, like those seen in Basel in 2006, can be enough to cause public concern to rise to levels that could spell an end to an operation (Evans *et al.*, 2012) (Pawar *et al.*, 2015; Rutqvist, 2012), even if events this size might not be enough to jeopardize the sealing potential of the caprock (Rutqvist *et al.*, 2016a). Microseismicity with moment magnitudes between 2 and 4 can occur on faults less than 1 km in length which can be difficult to detect using geophysical surveys (Vilarrasa *et al.*, 2014; Evans *et al.*, 2012). For this reason, we cannot assume that operators will be aware of all potentially dangerous faults before the start of operations (Pawar *et al.*, 2015). In fact, even if operators were aware of all faults in the area, over long time periods, say 50 years, injection-induced pressure plumes in CCS, for example, (0.1 MPa or more) may exceed tens of kilometers (Vilarrasa *et al.*, 2016). Over these kinds of areas, it may not even be possible to avoid all faults (Rutqvist, 2012; Rutqvist *et al.*, 2016a)

Instead, stochastic models or even better hybrid models which still honor field data and incorporate various mechanisms important for seismicity (e.g., (Layland-Bachmann *et al.*, 2012; Shapiro *et al.*, 2010; Bourne *et al.*, 2014; Gischig and Wiemer, 2013; Gischig *et al.*, 2014; Király *et al.*, 2014, 2016, 2017; Dempsey and Suckale, 2017)) seem like a practical compromise to incorporate mechanical behaviour and still respect the large uncertainties of the problem at hand.

A.3.25 Shear failure

Shear failure, which can either be mode II or mode II depending on its specific nature (this difference is not important for us here), refers to when the two sides of a fracture or shear plane move horizontally to one another. This is the type of failure in an earthquake and is also the method of stimulation in EGS stimulation (see Section A.3.12). There is a large body of literature on shear failure which will not be covered here. See Scholz (1998) and many other references for more information.

A.3.26 "Soft" stimulation

Soft stimulation is a response to the induced seismicity that has been seen to occur in EGS stimulation (see Section A.3.12 and Chapter 3). The goal is to stimulate the reservoir in shear such that permeability is enhanced through either aseismic or low magnitude event slip without any large seismic events being induced. In my view, when author's mention soft stimulation, they are usually referring to cyclic stimulation. In cyclic stimulation, the injection pressure is held high for a period of time, then reduced. Then it is increased and subsequently decreased again. This process is repeated for as many times as the operator chooses. This is as opposed to the classic version of stimulation where injection pressure is simply held high for a period of time. Numerous studies have focused on soft and cyclic stimulation (e.g., Zimmermann *et al.* (2010); Zang *et al.* (2013); Zimmermann *et al.* (2015); Hofmann *et al.* (2018,

2019); Noël *et al.* (2019b,a); Cornet (2019) and others), with mixed results. The idea is that less seismic energy is radiated during cyclic stimulation and therefore smaller earthquakes should take place. This has been interpreted to be the case numerically (Zang *et al.*, 2013); however, experiments have not supported these findings (Noël *et al.*, 2019b,a). Additionally, a truly fair comparison of a soft stimulation treatment to a classical one is quite difficult to accomplish in the field, and it is my view that there aren't strong enough arguments for why soft stimulation should work based on what we know about rock mechanics for numerical results to be accepted. Not to mention that the only large-scale application cyclic soft stimulation was in Pohang, the site of the largest shear stimulation induced earthquake to date (Hofmann *et al.*, 2019). Of course, I am open to being convinced.

Other authors have suggested that cyclic stimulation fatigues the rock thereby reducing the shear modulus of the rock mass (Cornet, 2019). However, it seems to me that from rate and state friction (Scholz, 1998), a decrease in shear modulus should shorten the critical length for a fault and therefore make it more likely to slip seismically. However, I admit that this is an area of research that interests me and is one that I am actively following. It could be that specifically by weakening the fault in this way it is possible to achieve results. Personally, I am not ready to dismiss this idea based solely on the argument I just gave about the shear modulus. However, I do feel that currently the approach to soft stimulation is a little bit too imprecise and unclear and I would like to see some solid arguments based on what we know about rock mechanics as to why it should work.

A.3.27 Stress regime

The a way of describing the prevailing state of stress. A normal faulting stress regime implies that the stresses at that location are conducive to normal faulting. A stress state which is conducive to normal faulting is one where largest principal stress as vertical and the minimum principal stress is horizontal. A reverse faulting stress regime is conducive to reverse faulting such that the minimum principal stress is vertical. Finally, a strike-slip faulting stress regime is conducive to strike-slip faulting and one where the vertical stress is intermediary. See Section A.3.13 for more information on faulting types and Section A.3.21 for more information on principal stresses.

A.3.28 Tensile failure

Tensile, or mode I, failure, is the opening of a two sides of a fracture plane in a direction normal to the plane, with no horizontal movement. In order to achieve tensile failure, the pore pressure must be larger than the minimum principal total stress. Tensile failure is the method of stimulation in hydraulic fracturing.

A.3.29 Thermoelasticity

Thermoelasticity simply describes the way the strain of a structure responds to changes in temperature and the way temperature responds to strain. Similar to poroelasticity, this coupling can be two-way; however, it is common to neglect the strain-temperature coupling. Much more detail is provided in (Cheng, 2016), including details on when it is appropriate to move to one-way coupling. Thermoelasticity is not widely used in this thesis, with the exceptions being Chapters 3 and 4.

A.3.30 Total stress

The total stress is the stress on an object from external sources. In porous media, pore pressure is not included in this definition of stress because it is internal. For example, the total vertical stress is generally taken as the weight of the (rock) overburden, and does not in any way include the effect of any fluids, neither through their weight nor the pressure they exhibit.

A.3.31 Traffic light systems

Traffic light systems are a way of managing seismic hazard and are fairly widely used in EGS stimulation, being first used by Bommer *et al.* (2006). They operate with three levels, which are of course green, yellow, and red. The level that an operation finds itself at is determined by the seismicity that has been induced so far. The cutoffs can be determined by operators/government/etc. as deemed appropriate for that area. An area with a high population density might have low magnitude cutoffs, for example. When the level passes from green (the initial state) to yellow, usually some kind of precaution is taken, such as lowering the injection rate. At red, the operation is generally shut in.

There are a number of problems with traffic light systems. One major being that many of the largest induced events have occurred after shut-in, and some of the largest failures in geothermal have occurred despite the use of a traffic light system. Both Basel and Pohang made use of traffic light systems (e.g., Layland-Bachmann *et al.* (2011); Hofmann *et al.* (2018)).

Traffic light systems are being improved through the addition of hybrid modelling and are now sometimes called adaptive traffic light systems (e.g., Karvounis and Wiemer (2015); Mignan *et al.* (2017); Hofmann *et al.* (2018)). Examples of these hybrid models are given in Section A.3.24.

A.3.32 Wastewater injection

In the United States where the conversation around wastewater is most relevant, large volumes of untreatable water are produced out of hydrocarbon wells and injected into deep subsurface aquifers (most famously into the Arbuckle Formation). Recently, large volumes of injection

have led to induced seismicity. This seismicity is occurring mostly in the basement. Examples of large seismic events (here M_w 5+) associated with wastewater injection include: Chongqing, China 1997 (Lei *et al.*, 2008), Arkansas 2011 (M_w 4.7) (Horton, 2012), Cushing, Oklahoma 2014 (McNamara *et al.*, 2015) Trinidad, Colorado 2011 (Rubinstein *et al.*, 2014), Prague, Oklahoma 2011 (Keranen *et al.*, 2013) (Sumy *et al.*, 2014), Pawnee, Oklahoma 2016 (Chen *et al.*, 2017), Fairview, Oklahoma 2016 (Goebel *et al.*, 2017c) (Yeck *et al.*, 2016). Of these documented cases, only in Keranen *et al.* (2013) (Prague, Oklahoma) did the seismicity occur on a previously identified fault.

Within the topic of wasterwater induced seismicity, a large discussion occurs around the topic of hydraulic fracturing. It is true that there is a degree of misconception here as most of the water is not flowback from hydraulic fracturing. The earthquakes are also not caused by the process of hydraulic fracturing itself (although there are examples of this, see Section A.3.16). However, the hydraulic fracturing/shale boom that has occurred in the US has led to huge increases in production rates (of both hydrocarbon and water). It is this produced water that is being injected in waste water wells and causing the induced seismicity. So, it is a mistake to say that hydraulic fracturing is directly causing the induced seismicity; however, it is dishonest to say that the two are not connected. See Zhang *et al.* (2013); Ellsworth (2013); Keranen *et al.* (2013, 2014) and many others for overviews.

A.4 Details of Mechanical Model

A.4.1 Derivation of Main Equations

Momentum balance

By performing a force balance (so assuming no acceleration) on the 2D body we get that

$$-\sigma_{xx} A_x + \left(\sigma_{xx} + \frac{\partial \sigma_{xx}}{\partial x} \Delta x\right) A_x - \sigma_{yx} A_y + \left(\sigma_{yx} + \frac{\partial \sigma_{yx}}{\partial y} \Delta y\right) A_y + S_x = 0 \qquad (A.8)$$

and

$$-\sigma_{yy} A_y + \left(\sigma_{yy} + \frac{\partial \sigma_{yy}}{\partial y} \Delta y\right) A_y - \sigma_{xy} A_x + \left(\sigma_{xy} + \frac{\partial \sigma_{xy}}{\partial x} \Delta x\right) A_x + S_y = 0. \qquad (A.9)$$

Note that, for example, A_x is the area of the face in the y-z plane. Its normal is in the x-direction.

Here, S is the internal force. By cancelling out some like terms we have

$$\frac{\partial \sigma_{xx}}{\partial x} \Delta x A_x + \frac{\partial \sigma_{yx}}{\partial y} \Delta y A_y + S_x = 0 \tag{A.10}$$

and

$$\frac{\partial \sigma_{yy}}{\partial y} \Delta y A_y + \frac{\partial \sigma_{xy}}{\partial x} \Delta x A_x + S_y = 0. \tag{A.11}$$

Next, if we assume that we have a cube as a control volume, $\Delta y A_y$ and $\Delta x A_x$ are both equivalent to V. S then becomes f, which represents the force per unit volume in that direction. Also, the shear stresses can be written with τ.

$$\frac{\partial \sigma_{xx}}{\partial x} + \frac{\partial \tau_{xy}}{\partial y} + f_x = 0 \tag{A.12}$$

$$\frac{\partial \tau_{xy}}{\partial x} + \frac{\partial \sigma_{yy}}{\partial y} + f_y = 0, \tag{A.13}$$

or

$$\nabla \cdot \sigma = -f \tag{A.14}$$

These equations, when written in matrix form are

$$\begin{bmatrix} \frac{\partial}{\partial x} & 0 & \frac{\partial}{\partial y} \\ 0 & \frac{\partial}{\partial y} & \frac{\partial}{\partial x} \end{bmatrix} \begin{bmatrix} \sigma_{xx} \\ \sigma_{yy} \\ \tau_{xy} \end{bmatrix} = - \begin{bmatrix} f_x \\ f_y \end{bmatrix} \tag{A.15}$$

or simply

$$B^T \sigma = -f. \tag{A.16}$$

It is assumed that displacements are sufficiently small that equilibrium conditions that were established for the initial geometry remain valid. Note that the stresses here are total stresses. In the case where we have pore pressure, we replace total stress with the definition of effective stress, such that our equation becomes

$$\nabla \cdot \left(\sigma' + p \right) = -f. \tag{A.17}$$

This results in

$$\nabla \cdot \sigma' + \nabla p = -f, \tag{A.18}$$

or

$$B^T \sigma' + \nabla p = -f, \tag{A.19}$$

Hooke's Law

Hooke's Law reads,

$$\sigma'_{ij} = \lambda \epsilon_{kk} \delta_{ij} + 2\mu \epsilon_{ij}, \tag{A.20}$$

where σ' is an effective stress. $\lambda = \frac{E\nu}{(1+\nu)(1-2\nu)}$, so

$$\sigma'_{ij} = \frac{E\nu}{(1+\nu)(1-2\nu)} \epsilon_{kk} \delta_{ij} + 2\mu \epsilon_{ij}, \tag{A.21}$$

and $\mu = \frac{E}{2(1+\nu)}$, so

$$\sigma'_{ij} = \frac{E\nu}{(1+\nu)(1-2\nu)}\epsilon_{kk}\delta_{ij} + \frac{E}{(1+\nu)}\epsilon_{ij}. \tag{A.22}$$

Since $\epsilon_{kk} = \epsilon_{xx} + \epsilon_{yy}$ in Cartesian coordinates for plane strain in the x-y plane,

$$\sigma'_{xx} = \frac{E}{(1+\nu)(1-2\nu)}\left((1-\nu)\epsilon_{xx} + \nu\epsilon_{yy}\right), \tag{A.23}$$

$$\sigma'_{yy} = \frac{E}{(1+\nu)(1-2\nu)}\left((1-\nu)\epsilon_{yy} + \nu\epsilon_{xx}\right), \tag{A.24}$$

and

$$\tau_{xy} = \frac{E}{(1+\nu)(1-2\nu)}\frac{1-2\nu}{2}\gamma_{xy}. \tag{A.25}$$

Note that the shear strain here is the engineering shear strain, such that $\gamma_{xy} = 2\epsilon_{xy}$. These equations can be written in matrix form as:

$$\begin{bmatrix} \sigma'_{xx} \\ \sigma'_{yy} \\ \tau_{xy} \end{bmatrix} = \frac{E}{(1+\nu)(1-2\nu)} \begin{bmatrix} 1-\nu & \nu & 0 \\ \nu & 1-\nu & 0 \\ 0 & 0 & \frac{1-2\nu}{2} \end{bmatrix} \begin{bmatrix} \epsilon_{xx} \\ \epsilon_{yy} \\ \gamma_{xy} \end{bmatrix} \tag{A.26}$$

Note that σ_{zz} is not necessarily zero and in some cases we will solve for it. When we couple to the flow model we need volumetric strain, but note that strain is zero in the z-direction (because we are plane strain). However, currently, this was the case of no pore pressure. For the case of a fluid pore pressure, the analogous law to Hooke's Law reads (Segall, 2010) (Detournay and Cheng, 1993),

$$2\mu\epsilon_{ij} = \sigma_{ij} - \frac{\nu}{1+\nu}\sigma_{kk}\delta_{ij} - \frac{(1-2\nu)\alpha}{1+\nu}p\delta_{ij}, \tag{A.27}$$

where σ is the total stress, positive in compression. The poroelastic constants used are for a

drained material because when $p = 0$ the equation reduces to the original Hooke's Law (Segall, 2010). Note that this equation is exactly the same as the original Hooke's Law if the stresses are assumed to be effective in the original (as we did here). By writing out Equation A.27, we can retrieve Equation A.26. The effective stress is related to the total stress by

$$\sigma^{'}_{ij} = \sigma_{ij} - \alpha p \delta_{ij}. \tag{A.28}$$

This can then be written for stresses (Detournay and Cheng, 1993), by first making the following replacement (with a sign switch due this derivation being positive in compression) (Segall, 2010)

$$\sigma_{kk} = 3K\epsilon_{kk} + 3\alpha P, \tag{A.29}$$

such that,

$$2\mu\epsilon_{ij} = \sigma_{ij} - \frac{\nu}{1+\nu}\left(3K\epsilon_{kk} + 3\alpha p\right)\delta_{ij} - \frac{(1-2\nu)\alpha}{1+\nu}p\delta_{ij}. \tag{A.30}$$

Then, the bulk modulus, K, can be replaced,

$$K = \frac{E}{3(1-2\nu)}, \tag{A.31}$$

yielding,

$$2\mu\epsilon_{ij} = \sigma_{ij} - \frac{\nu}{1+\nu}\left(\frac{E}{1-2\nu}\epsilon_{kk} + 3\alpha p\right)\delta_{ij} - \frac{(1-2\nu)\alpha}{1+\nu}p\delta_{ij}. \tag{A.32}$$

This can be rearranged and simplified such that,

$$\sigma_{ij} = 2\mu\epsilon_{ij} + \frac{E\nu}{(1+\nu)(1-2\nu)}\epsilon_{kk}\delta_{ij} + \frac{3\nu}{1+\nu}\alpha p\delta_{ij} + \frac{(1-2\nu)\alpha}{1+\nu}p\delta_{ij}. \tag{A.33}$$

The pressure terms then simplify

$$\sigma_{ij} = 2\mu\epsilon_{ij} + \frac{E\nu}{(1+\nu)(1-2\nu)}\epsilon_{kk}\delta_{ij} + \alpha p \delta_{ij}. \tag{A.34}$$

By then replacing the shear modulus we get that,

$$\sigma_{ij} - \alpha p \delta_{ij} = \frac{E}{(1+\nu)}\epsilon_{ij} + \frac{E\nu}{(1+\nu)(1-2\nu)}\epsilon_{kk}\delta_{ij}. \tag{A.35}$$

This is the same as the original Hooke's Law presented in Equation A.22 when we consider the relationship between total and effective stress (and using engineering shear strain again). Meaning we can use

$$\begin{bmatrix} \sigma'_{xx} \\ \sigma'_{yy} \\ \tau_{xy} \end{bmatrix} = \frac{E}{(1+\nu)(1-2\nu)} \begin{bmatrix} 1-\nu & \nu & 0 \\ \nu & 1-\nu & 0 \\ 0 & 0 & \frac{1-2\nu}{2} \end{bmatrix} \begin{bmatrix} \epsilon_{xx} \\ \epsilon_{yy} \\ \gamma_{xy} \end{bmatrix} \tag{A.36}$$

which can also be written as

$$\sigma' = D\epsilon \tag{A.37}$$

Rewriting the Strains

The definition for ϵ under the assumption of small strains is

$$\epsilon = \frac{\Delta L}{L}. \tag{A.38}$$

The limit as the length of our system goes to zero causes

$$\lim_{L \to 0} \frac{\Delta L}{L} = \frac{du}{dx}. \tag{A.39}$$

This can be done for both directions such that

$$\epsilon_{xx} = \frac{\partial u_x}{\partial x} \tag{A.40}$$

and

$$\epsilon_{yy} = \frac{\partial u_y}{\partial y}. \tag{A.41}$$

The engineering shear strain, γ_{ij}, for small displacement gradients is given by

$$\gamma_{xy} = \frac{\partial u_x}{\partial y} + \frac{\partial u_y}{\partial x}. \tag{A.42}$$

These equations can then be written in matrix form yielding

$$\begin{bmatrix} \epsilon_{xx} \\ \epsilon_{yy} \\ \gamma_{xy} \end{bmatrix} = - \begin{bmatrix} \frac{\partial}{\partial x} & 0 \\ 0 & \frac{\partial}{\partial y} \\ \frac{\partial}{\partial y} & \frac{\partial}{\partial x} \end{bmatrix} \begin{bmatrix} u_x \\ u_y \end{bmatrix} \tag{A.43}$$

or simply

$$\widetilde{\epsilon} = -B\widetilde{u} \tag{A.44}$$

and also

$$\epsilon = -Bu \tag{A.45}$$

Terms with a tilde are continuous whereas when displacement and strain are written without a tilde it means that they are nodal values.

Setting Up The System Of Equations

By combining Equations A.19, A.37, and A.45 we get

$$B^T DB\widetilde{u} = f + \nabla p \tag{A.46}$$

Basis Functions

The displacement, $\widetilde{u}$, can be found at any point in the element through the use of the values at the nodes and basis functions such that

$$\widetilde{u} = N_1 u_1 + N_2 u_2 + N_3 u_3 + N_4 u_4 \tag{A.47}$$

for an element with four points or, more generally in matrix form,

$$\widetilde{u} = Nu. \tag{A.48}$$

Here, N represents the basis functions and u represents the value of displacement (in both x and y) at the nodes. For an element with four nodes, this looks like

$$\widetilde{u} = \begin{bmatrix} N_1 & 0 & N_2 & 0 & N_3 & 0 & N_4 & 0 \\ 0 & N_1 & 0 & N_2 & 0 & N_3 & 0 & N_4 \end{bmatrix} \begin{bmatrix} u_{x1} \\ u_{y1} \\ u_{x2} \\ u_{y2} \\ u_{x3} \\ u_{y3} \\ u_{x4} \\ u_{y4} \end{bmatrix} \tag{A.49}$$

For a square element with linear basis functions with the node numbering beginning in the upper left and moving horizontally before vertically, the basis functions are

$$N_1 = \left(1 - \frac{x}{a}\right)\left(1 - \frac{y}{b}\right) \tag{A.50}$$

$$N_2 = \frac{x}{a}\left(1 - \frac{y}{b}\right) \tag{A.51}$$

$$N_3 = \left(1 - \frac{x}{a}\right)\frac{y}{b} \tag{A.52}$$

$$N_4 = \frac{x}{a}\frac{y}{b} \tag{A.53}$$

Here, a is the length of the element in the x direction and b is the length of the element in the y direction. Now, Equation A.46, which we had previously, is written like

$$B^T DBNu = f + \nabla p. \tag{A.54}$$

Including Body Forces and Pore Pressures

Multiplying the above result by the transpose of the basis functions yields:

$$N^T B^T DBNu = N^T f + N^T \nabla p \tag{A.55}$$

Recall that f is a stress per length. This multiplied by the basis functions is a stress per length in a given direction at a given location. The integral of this over x and y is the force per length (where the length is into the plane) at any given location (matching the location of the displacement which will be at the nodes). The basis function for pore pressure is just one everywhere because the pore pressure is constant in each element. Pore pressure is also turned into a distributed load, then multiplied by the length of the element side along which it is applied. This yields a force per length (recalling that we are in plane strain and the length is into the plane).

$$\int_0^a \int_0^b N^T B^T DBNu \partial\xi\partial\eta = \int_0^a \int_0^b N^T f \partial\xi\partial\eta + \int_0^a \int_0^b N^T \nabla p \partial\xi\partial\eta \tag{A.56}$$

$$\int_0^a \int_0^b N^T B^T DBNu\partial\xi\partial\eta = F + P \tag{A.57}$$

Here, P is basically the pressure of each element times the length of the side of the element in the direction in which the force is being applied times the Biot coefficient. F is similar. As an example, see Figure A.1.

The force due to pore pressure, P_{Ax}, on node A in the x-direction would then be given by

$$P_{Ax} = \alpha \frac{dy}{2}(P_1 + P_3 - P_2 - P_4) \tag{A.58}$$

The same principle is applied for adding distributed loads. Body forces (which again in plane strain are actually a force per length where the length is going into the plane) are simply applied as a two single values, one for the x and one for the y directions.

Setting Up The Final Equation

Also recall that this has been done for one element. These integrals can now be performed for an element by evaluating a stiffness matrix, k_m which is defined as

$$k_m = \int_0^a \int_0^b N^T B^T DBN\partial\xi\partial\eta \tag{A.59}$$

This will yield an 8x8 matrix (for quadrilateral elements). The definitions of N, B, and D (for plane strain) are listed below and the values of each element of the resulting matrix are shown in the table (for quadrilateral elements and linear basis functions). This can also be done with Gauss Integration.

$$D = \frac{E}{(1+v)(1-2v)}\begin{bmatrix} 1-v & v & 0 \\ v & 1-v & 0 \\ 0 & 0 & \frac{1-2v}{2} \end{bmatrix} \tag{A.60}$$

$$BN = \begin{bmatrix} \frac{\partial N_1}{\partial x} & 0 & \frac{\partial N_2}{\partial x} & 0 & \frac{\partial N_3}{\partial x} & 0 & \frac{\partial N_4}{\partial x} & 0 \\ 0 & \frac{\partial N_1}{\partial y} & 0 & \frac{\partial N_2}{\partial y} & 0 & \frac{\partial N_3}{\partial y} & 0 & \frac{\partial N_4}{\partial y} \\ \frac{\partial N_1}{\partial y} & \frac{\partial N_1}{\partial x} & \frac{\partial N_2}{\partial y} & \frac{\partial N_2}{\partial x} & \frac{\partial N_3}{\partial y} & \frac{\partial N_3}{\partial x} & \frac{\partial N_4}{\partial y} & \frac{\partial N_4}{\partial x} \end{bmatrix} \tag{A.61}$$
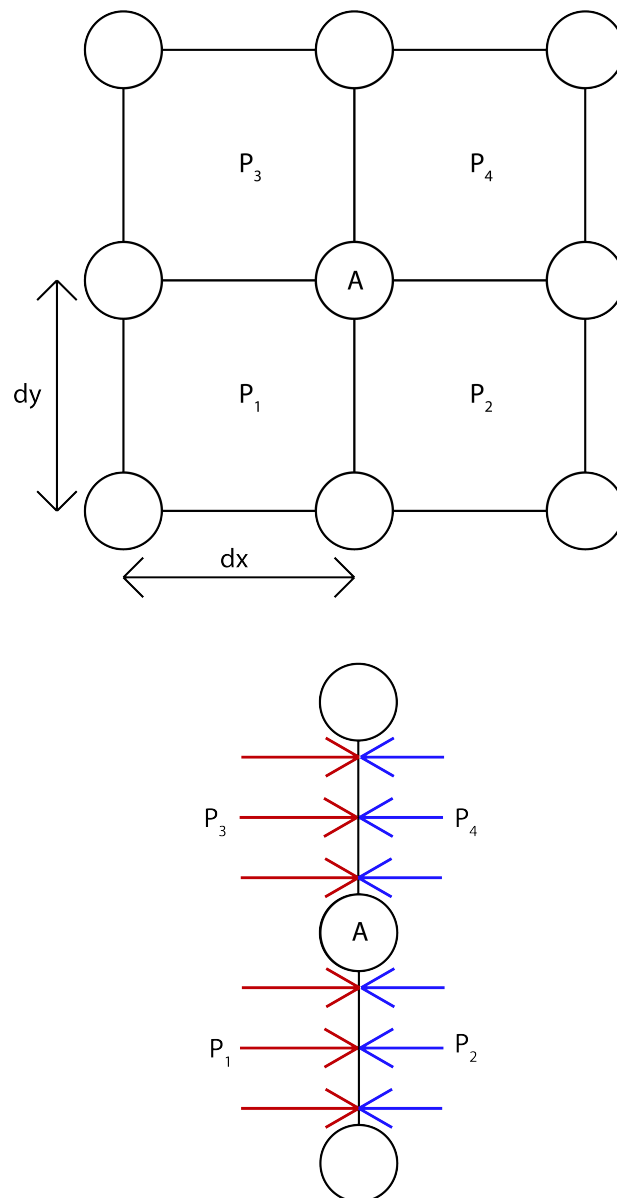
Figure A.1 – How pore pressures are applied for the x-force

Realize that $N^T B^T = (BN)^T$. Now, for example, $k_m(1,1)$ can be found as:

$$k_m(1,1) = \frac{E}{(1+v)(1-2v)} \int_0^a \int_0^b \left[(1-v)\left(\frac{\partial N_1}{\partial x}\right)^2 + \frac{1-2v}{2}\left(\frac{\partial N_1}{\partial y}\right)^2 \right] \partial \xi \partial \eta \tag{A.62}$$

where the basis functions can be directly plugged in and integrated. This can usually not be done analytically and typically Gauss quadrature is used to solve the integrals and build the stiffness matrix. It is possible to take each derivative manually and fill up the local (and ultimately the global) stiffness matrix in this way. Note that the displacements weren't involved in the integral because these are displacements at the node locations and these values are only at the nodes. Their integral over an area is therefore a constant.

Now the equation looks like

$$k_m u = (F + P) \tag{A.63}$$

and can be solved for displacements

$$u = k_m^{-1}(F + P) \tag{A.64}$$

Solving For Strains

Recall that

$$\epsilon = -Bu. \tag{A.65}$$

However, what we actually do is

$$\epsilon = BNu. \tag{A.66}$$

so that we can solve for strains at any location in the element by plugging in different values of the shape functions into the shape functions.

So, to solve for strains all we need to do is build a B matrix. This can be done by solving for the

Jacobian, which is shown below:

$$J = \begin{bmatrix} \frac{\partial x}{\partial \xi} & \frac{\partial y}{\partial \xi} \\ \frac{\partial x}{\partial \eta} & \frac{\partial y}{\partial \eta} \end{bmatrix}.$$

(A.67)

These values can be found by averaging the difference in x-locations between nodes (i.e., the x distances along the lines connecting the nodes) and dividing by the the length of the local coordinate.

Next, the derivatives required for the B matrix are found my taking the inverse of the Jacobian and multiplying by the derivative of the shape functions in the local coordinates. For example,

$$\frac{\partial N_1}{\partial x} = \frac{\partial N_1}{\partial \xi} \frac{\partial \xi}{\partial x}.$$

(A.68)

Then, the BN matrix is creating by placing the correct derivatives in the correct place such that

$$BN = \begin{bmatrix} \frac{\partial N_1}{\partial x} & 0 & \frac{\partial N_2}{\partial x} & 0 & \frac{\partial N_3}{\partial x} & 0 & \frac{\partial N_4}{\partial x} & 0 \\ 0 & \frac{\partial N_1}{\partial y} & 0 & \frac{\partial N_2}{\partial y} & 0 & \frac{\partial N_3}{\partial y} & 0 & \frac{\partial N_4}{\partial y} \\ \frac{\partial N_1}{\partial y} & \frac{\partial N_1}{\partial x} & \frac{\partial N_2}{\partial y} & \frac{\partial N_2}{\partial x} & \frac{\partial N_3}{\partial y} & \frac{\partial N_3}{\partial x} & \frac{\partial N_4}{\partial y} & \frac{\partial N_4}{\partial x} \end{bmatrix}.$$

(A.69)

Finally, the strains can be solved for using

$$\epsilon = BNu.$$

(A.70)

Again, the strains are evaluated at the location corresponding to the local coordinates used in N.

Solving For Stresses

The stresses can then simply be solved for in the following manner:

$$\sigma' = D\epsilon$$

(A.71)

and total stress can be found with

$$\sigma = \sigma^{'} + \alpha p \tag{A.72}$$

A.4.2 Coding

The full details of the coding will not be provided here, and instead a general overview will be given.

Stiffness matrix

It is recommended to build the stiffness matrix before starting the simulation. The disadvantage of this is that the mechanical properties can therefore not change during the course of the simulation. It is possible to perform all double integrals of the basis functions manually (there are 64 in the case of quadratic elements) and add them one by one into the stiffness matrix if this is easier.

Adding forces

Each time the elastic simulator is called, the force vector needs to be made. This should consist of body forces and pore pressures. Pore pressures are applied to each of the four nodes touching their cell. Be sure to include the Biot coefficient. The forces should be in the x and y directions as we are 2-D. An example of a force applied in the x-direction on a node would be, $F_x = \alpha P \frac{\Delta y}{2}$.

Boundary conditions

Fixed displacement boundary conditions are applied by setting the corresponding row in the stiffness matrix to zero (except for a one in the diagonal) and also setting the force on that node to zero. This results in a displacement of 0 when the displacements are solved for.

Solving for displacements

Displacements are simply solved for by performing $u = K_m^{-1} F$. Depending on how you wrote the code, the top of the vector of displacements corresponds to x-displacements and the bottom to y-displacements.

Solving for strains

First build two matrices, E', which is the size of $[Ne,4]$ in the case of quadratic elements. One matrix is for the x-displacements, the other for the y-displacements. For each element (each row) add the displacements of each node in that element. I placed the bottom left in column one, bottom right in column 2, top left in column 3, and top right in column 4.

Next make two more matrices, Loc, that are exactly the same as the E's except they contain the exact original locations of all the nodes.

Start a for loop over all elements. Now build the elasticity matrix, given in Equation A.36. Do this within the for loop. Next build a 4x2 martrix, $coord$, which takes the x and y locations of the nodes in this element. Build a 1x8 matrix, $disp$, which contains the displacements of the nodes in this element.

Now build the basis function matrix, dN, which is a 2x4 matrix. Each node is a column. For example,

$$dN(1,1) = -\frac{1}{4}\left(1-\eta\right), \tag{A.73}$$

and

$$dN(2,1) = -\frac{1}{4}\left(1-\xi\right), \tag{A.74}$$

note that here, η and ξ are taken as zero throughout. These are the local coordinates.

Next, build the Jacobian by $J = dN * coord$. The derivatives for the B matrix are then $deriv = Jac^{-1}dN$. Now, build the BN matrix. This matrix is 3x8 and can be found in Equation A.69. Finally, solve for strains via $\epsilon = -B * disp'$. This matrix is $3xNe$. Note that if you want to solve for σ_{zz} as well, simply add a row of strains under ϵ_{yy} and make them all zeros; this is ϵ_{zz}.

Solving for effective stresses

Effective stress changes can be found by performing $\sigma' = DE\epsilon$.

Solving for total stresses

To solve for total stress changes simply take the effective stresses and add back the pore pressure times the Biot coefficient.
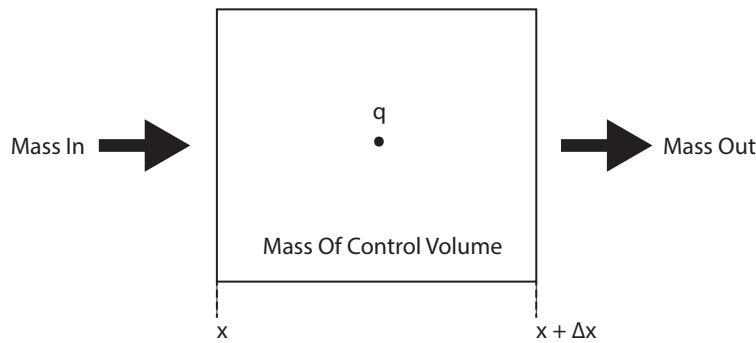
Figure A.2 – Control volume defined to develop mass balance equation.

Solving for volumetric strain

The volumetric strain is simply the sum of ϵ_{xx} and ϵ_{yy}. Recall ϵ_{zz} is zero because we are plane strain.

A.5 Details of Flow + Temperature Model

A.5.1 Deriving the Continuity Equation

Beginning with a control volume, Figure A.2, it is possible to derive a continuity equation for mass balance.

Because mass can neither be created or destroyed, the mass conservation for this control volume can be described as

$$\underbrace{\text{Mass Final} - \text{Mass Initial}}_{\text{Accumulation}} = \underbrace{\text{Mass In} - \text{Mass Out}}_{\text{Convection}} + \underbrace{\text{Generation}}_{\text{Source}}, \tag{A.75}$$

which can be stated as

$$\underbrace{m \cdot V \Big|_{t+\Delta t} - m \cdot V \Big|_{t}}_{\text{Accumulation}} = \underbrace{F \cdot \Delta t \cdot A \Big|_{x} - F \cdot \Delta t \cdot A \Big|_{x+\Delta x}}_{\text{Convection}} + \underbrace{q \cdot \Delta t \cdot V}_{\text{Source}}. \tag{A.76}$$

Here, m is the mass density of the control volume, F is the mass flux (convection), V is the volume of the control volume, Δt is the change in time, and A is the cross-sectional area

orthogonal to the direction of Δx. By dividing this equation by the Δt and V, one obtains

$$\frac{m}{\Delta t}\bigg|_{t+\Delta t} - \frac{m}{\Delta t}\bigg|_{t} = \frac{F}{\Delta x}\bigg|_{x} - \frac{F}{\Delta x}\bigg|_{x+\Delta x} + q, \tag{A.77}$$

which can be reformulated as

$$\frac{m\big|_{t+\Delta t} - m\big|_{t}}{\Delta t} = \frac{F\big|_{x} - F\big|_{x+\Delta x}}{\Delta x} + q. \tag{A.78}$$

Next, the limit is taken as Δt and Δx go to zero, i.e.,

$$\lim_{\substack{\Delta t \to 0 \\ \Delta x \to 0}} \left(\frac{m\big|_{t+\Delta t} - m\big|_{t}}{\Delta t} = \frac{F\big|_{x} - F\big|_{x+\Delta x}}{\Delta x} + q \right), \tag{A.79}$$

resulting in

$$\frac{\partial m}{\partial t} = -\frac{\partial F}{\partial x} + q. \tag{A.80}$$

Note that this equation, representing the conservation of total mass, is also called the Continuity Equation. In general form, the equation can be stated as

$$\frac{\partial m}{\partial t} = -\nabla \cdot F + q. \tag{A.81}$$

The m (mass density of fluid) of the left term can be replaced like

$$\frac{\partial (\phi \rho)}{\partial t} = -\nabla \cdot F + q. \tag{A.82}$$

The F (mass flux in units of $\frac{kg}{m^3}\frac{m}{sec}$) can be replaced like

$$\frac{\partial(\phi\rho)}{\partial t} = -\nabla \cdot (\rho \cdot u) + q. \tag{A.83}$$

Next, by assuming that velocity is entirely governed by advection and can be described by Darcy's Law, the continuity equation is given by

$$\frac{\partial(\phi\rho)}{\partial t} - \nabla \cdot \left(\frac{k}{\mu}\rho\,(\nabla P)\right) = q. \tag{A.84}$$

A.5.2 Solution strategy

Basically, this begins with the continuity equation from mass balance:

$$\frac{\partial(\phi\rho)}{\partial t} - \nabla \cdot \left(\frac{k}{\mu}\rho\,(\nabla P)\right) = q \tag{A.85}$$

Assuming an incompressible matrix, the equation is then discretized in a finite volume framework in space and a finite difference framework in time such that in 1-D,

$$V_i\phi_i\frac{(\rho_i^\nu - \rho_i^n)}{\Delta t} + A_i\left[\left(\frac{k\rho}{\mu}\right)_{i+\frac{1}{2}}^\nu \cdot \left(\frac{P_i^\nu - P_{i+1}^\nu}{\Delta x}\right) - \left(\frac{k\rho}{\mu}\right)_{i-\frac{1}{2}}^\nu \cdot \left(\frac{P_{i-1}^\nu - P_i^\nu}{\Delta x}\right)\right] = Q_i^\nu. \tag{A.86}$$

Note that all interface properties are upstreamed. Then, this equation is set up in a residual framework,

$$r_i^\nu = V_i\phi_i\frac{(\rho_i^\nu - \rho_i^n)}{\Delta t} + A_i\left[\left(\frac{k\rho}{\mu}\right)_{i+\frac{1}{2}}^\nu \cdot \left(\frac{P_i^\nu - P_{i+1}^\nu}{\Delta x}\right) - \left(\frac{k\rho}{\mu}\right)_{i-\frac{1}{2}}^\nu \cdot \left(\frac{P_{i-1}^\nu - P_i^\nu}{\Delta x}\right)\right] - Q_i^\nu, \tag{A.87}$$

and then solved fully implicitly like,

$$r^{n+1} = r^{\nu+1} \approx r^\nu + \frac{\partial r}{\partial P}^\nu \Delta P^{\nu+1} = 0 \tag{A.88}$$

$$\frac{\partial r}{\partial P}^{v} \Delta P^{v+1} = -r^{v} \qquad\qquad (A.89)$$

The update to pressure can then be found. This process is repeated until convergence. The permeability used between two cells is harmonically averaged. The fluid properties at the interfaces (ρ, μ and their derivatives) are upstreamed. They are also upstreamed at the wells.

A.5.3 Two-phase flow

The continuity equation presented in Equation A.84, and repeated here,

$$\frac{\partial \left(\phi \rho \right)}{\partial t} - \nabla \cdot \left(\frac{k}{\mu} \rho \left(\nabla P \right) \right) = q, \qquad\qquad (A.90)$$

can be extended to two phase flow such that it reads,

$$\frac{\partial \left(\phi \rho_\alpha S_\alpha \right)}{\partial t} - \nabla \cdot \left(\frac{k k_{r\alpha}}{\mu_\alpha} \rho_\alpha \left(\nabla P \right) \right) = q_\alpha. \qquad\qquad (A.91)$$

Here, α represents the phase. Note that this formulation is immiscible with no state changes and therefore phase conservation is valid. The relative permeability is found using Corey functions; viscosities are considered to remain constant. This continuity equation is repeated for each phase as each phase is conserved in this formulation.

The equations are then discretized in a similar fashion to the single phase continuity equation and then solved for pressure and one saturation with

$$\frac{\partial r}{\partial P}^{v} \Delta P^{v+1} + \sum_{\alpha=1}^{N_\alpha - 1} \frac{\partial r}{\partial S_\alpha}^{v} \Delta S_\alpha^{v+1} = -r^{v}, \qquad\qquad (A.92)$$

where N_α is the number of phases. The final saturation is found through unity, i.e.,

$$\sum_{\alpha=1}^{N_\alpha} S = 1. \qquad\qquad (A.93)$$

Together the two mass balance equations form a system of equations that can be written as

$$
\overbrace{\begin{bmatrix} \dfrac{\partial r_1}{\partial P} & \dfrac{\partial r_1}{\partial S_1} \\[2ex] \dfrac{\partial r_2}{\partial P} & \dfrac{\partial r_2}{\partial S_1} \end{bmatrix}}^{\nu} \underbrace{}_{2N \times 2N} \overbrace{\begin{bmatrix} \Delta P \\[2ex] \Delta S_1 \end{bmatrix}}^{\nu+1} \underbrace{}_{2N \times 1} = - \overbrace{\begin{bmatrix} r_1 \\[2ex] r_2 \end{bmatrix}}^{\nu} \underbrace{}_{2N \times 1}.
$$

A.5.4 Dual-Porosity model

A dual porosity model for ubiquitos fractures in a porous media is defined. As in Khalili and Valliappan (1996); Wang *et al.* (2018), the continuity equation for mass balance is defined both for the matrix,

$$
\frac{\partial \left(\phi_m \rho_m \right)}{\partial t} - \nabla \cdot \left(\frac{k_m}{\mu} \rho_m \left(\nabla P_m - \nabla \left(\rho_m g z \right) \right) \right) = q_{fm}, \tag{A.94}
$$

and the fracture,

$$
\frac{\partial \left(\phi_f \rho_f \right)}{\partial t} - \nabla \cdot \left(\frac{k_f}{\mu} \rho_f \left(\nabla P_f - \nabla \left(\rho_f g z \right) \right) \right) = q - q_{fm}, \tag{A.95}
$$

where ϕ is the porosity, k the permeability, ρ the fluid density, μ the fluid viscosity, P the fluid pressure, g the acceleration due to gravity, z the depth, q the mass source term due to injection/production, and q_{fm} the flow between the fracture and the matrix. The subscripts m and f designate whether the property is defined for the matrix or for the fracture, respectively. In order to calculate the flow between the fracture and the matrix, q_{fm} is then defined as (Khalili and Valliappan, 1996; Wang *et al.*, 2018)

$$
q_{fm} = \gamma \rho \left(P_f - P_m \right), \tag{A.96}
$$

where γ is the leakage parameter and ρ is the upstreamed fluid density. The leakage parameter

is defined as (Wang *et al.*, 2018)

$$\gamma = \frac{\pi^2}{s^2} \frac{k_m}{\mu}, \qquad (A.97)$$

where s is the fracture spacing, here taken as the the stage length. Before the fracture has opened, γ is set to a very large number to ensure equilibrium between the fracture and matrix systems. Equations A.94 and A.95 are discretized in a fully implicit finite volume framework and solved for two primary variables, the two pressures.

A.5.5 Energy Balance

In order to model temperature changes, a new equation has to be added. This is the energy balance based on (Li and Laloui, 2016),

$$\frac{\partial H_m}{\partial t} + \nabla \cdot \Gamma + \nabla \cdot f_t = 0, \qquad (A.98)$$

where H_m is the enthalpy of the entire medium, Γ is the heat conduction, and f_T is the convection. Together, Γ and f_T make up the heat transfer whereas the first term is the heat storage. The thermal conduction is given by

$$\Gamma = -\left(\sum_{\alpha=1}^{N_\alpha} \left(\phi S_\alpha \lambda_\alpha \right) + \left(1 - \phi \right) \lambda_s \right) \nabla T, \qquad (A.99)$$

where α denotes the phase and λ is the thermal conductivity. Note that here fluid properties are upstreamed on the basis of temperature and not flow potential. The thermal convection is given by

$$f_T = \sum_{\alpha=1}^{N_\alpha} c_{p,\alpha} \left(T - T_0 \right) \rho_\alpha q_\alpha, \qquad (A.100)$$

where c_p is the specific heat capacity. Finally, the enthalpy of the entire medium is given by

$$H = \left(1 - \phi\right) \rho_s c_{p,s} \left(T - T_0\right) + \phi \sum_{\alpha=1}^{N_\alpha} c_{p,\alpha} \left(T - T_0\right) S_\alpha \rho_\alpha. \tag{A.101}$$

Thermal equilibrium of the mixture is assumed. For simplicity, it is said that a change in temperature only affects T and μ (neglecting compressibility in the solid and liquid with respect to temperature). However, this equation itself is dependent on pressure (q, ρ, ϕ) and saturation (S), meaning the Jacobian of this equation will contain derivatives for all three primary variables (with temperature now being a primary variable as well).

The conservation of enthalpy equation is then discretized in a finite volume in space and finite difference in time framework and written in residual form such that

$$r_3^v = V \frac{H_m^v - H_m^n}{\Delta t} + V \nabla \cdot \Gamma^v + V \nabla \cdot f_t^v, \tag{A.102}$$

This conservation of enthalpy equation is the used in combination with two (in the case of two phases) mass balance equations presented earlier such each conservation equation's update is calculated as

$$\frac{\partial r}{\partial P}^v \Delta P^{v+1} + \sum_{\alpha=1}^{N_\alpha - 1} \frac{\partial r}{\partial S_\alpha}^v \Delta S_\alpha^{v+1} + \frac{\partial r}{\partial T}^v \Delta T^{v+1} = -r^v. \tag{A.103}$$

This ultimately leads to the full system of equations being written as

$$\overbrace{\begin{bmatrix} \frac{\partial r_1}{\partial P} & \frac{\partial r_1}{\partial S_1} & \frac{\partial r_1}{\partial T} \\[2ex] \frac{\partial r_2}{\partial P} & \frac{\partial r_2}{\partial S_1} & \frac{\partial r_2}{\partial T} \\[2ex] \frac{\partial r_3}{\partial P} & \frac{\partial r_3}{\partial S_1} & \frac{\partial r_3}{\partial T} \end{bmatrix}}^{v}_{\underbrace{\qquad\qquad}_{3N \times 3N}} \overbrace{\begin{bmatrix} \Delta P \\[2ex] \Delta S_1 \\[2ex] \Delta T \end{bmatrix}}^{v+1}_{\underbrace{\quad}_{3N \times 1}} = - \overbrace{\begin{bmatrix} r_1 \\[2ex] r_2 \\[2ex] r_3 \end{bmatrix}}^{v}_{\underbrace{\quad}_{3N \times 1}},$$

where r_1 and r_2 are given by the residuals of components 1 and 2 respectively whereas r_3 is

given by the residual of the conservation of enthalpy equation. i.e.,

$$r_1^v = V \frac{(\phi^v \rho_1^v S_1^v - \phi^n \rho_1^n S_1^n)}{\Delta t} + V\nabla \cdot \left(\frac{k k_{r,1}^v}{\mu_1^v} \rho_1^v \left(\nabla P^v - \nabla \left(\rho_1^v g z \right) \right) \right) - Q_1^v, \tag{A.104}$$

and

$$r_3^v = V \frac{H_m^v - H_m^n}{\Delta t} + V\nabla \cdot \Gamma^v + V\nabla \cdot f_t^v, \tag{A.105}$$

Viscosity's dependence on temperature is given by (Likhachev, 2003),

$$\mu = \mu_0 e^{aP + \frac{E-bP}{R(T-\theta-cP)}}, \tag{A.106}$$

where, for water, $a = 4.42 \cdot 10^{-9} \left[\frac{1}{Pa} \right]$, $b = 9.565 \cdot 10^{-6} \left[\frac{J}{molPa} \right]$, $c = 1.24 \cdot 10^{-7} \left[\frac{K}{Pa} \right]$, $E = 4753$ $\left[\frac{J}{mol} \right]$, $\theta = 139.7 \, [K]$, and R is the molar gas constant.

A.5.6 Details

Boundary conditions

Boundary conditions here are always no-flow (Neumann). This is done by setting the transmissibility of the interfaces at the boundaries equal to be zero. Constant pressure boundaries can also be used in the simulator's current state; however, this is done simply by placing a well in the cell closest to the desired border. The injectivity of the well is then set to a very high value, effectively fixing the pressure of the cell to be the well pressure.

Density

The definition of isothermal fluid compressibility is

$$c_f = \frac{1}{\rho} \left(\frac{\partial \rho}{\partial P} \right)_T. \tag{A.107}$$

This can be rearranged such that

$$c_f \partial P = \frac{\partial \rho}{\rho}.$$ (A.108)

Assuming a constant, small compressibility, this can then be integrated from a reference pressure and density to the pressure of interest such that

$$\int_{P_0}^{P} c_f \partial P = \int_{\rho_0}^{\rho} \frac{\partial \rho}{\rho}.$$ (A.109)

Which the solves as

$$c_f (P - P_0) = ln\left(\frac{\rho}{\rho_0}\right).$$ (A.110)

This then in turn reduces to,

$$\rho = \rho_0 \cdot e^{[c_f(P-P_0)]},$$ (A.111)

which is the density formulation used in the simulators.

Gravity

Gravity can be included in the convection term, changing the continuity equation to

$$\frac{\partial\left(\phi\rho_\alpha S_\alpha\right)}{\partial t} - \nabla \cdot \left(\frac{kk_{r\alpha}}{\mu_\alpha}\rho_\alpha\left(\nabla P - \nabla\left(\rho_\alpha g z\right)\right)\right) = q_\alpha.$$ (A.112)

The density used in the gravity term is taken as the average as the densities of the two cells forming each interface. Derivatives are taken according to this convention as well.

Initialization

Pressure and saturation both need to be initialized. Ideally, this is done by assigning reasonable in-situ values, which for saturation is fairly straight forward, but requires a little bit of math for pressure (in the case of a compressible fluid with gravity). By starting with the equation for hydrostatic pressure,

$$\partial P = \rho g \partial z, \tag{A.113}$$

we can then separate variables and integrate from the surface ($z = 0$) to each depth in the reservoir to find the pressure, i.e.,

$$\int_{P=P_{surf}}^{P} \frac{\partial P}{\rho} = \int_{z=0}^{z=z} g \partial z. \tag{A.114}$$

It will be assumed that the surface pressure, P_{surf}, is equal to zero such that pressure is the gauge pressure. Then, we can substitute in the relationship for density presented earlier,

$$\int_{P=0}^{P} \frac{\partial P}{\rho_0 e^{[c_f(P-P_0)]}} = \int_{z=0}^{z=z} g \partial z. \tag{A.115}$$

From here, we have that

$$-\frac{1}{\rho_0 c_f} e^{[-c_f(P-P_0)]} \bigg|_{P=0}^{P} = g z, \tag{A.116}$$

which yields,

$$P = P_0 - \frac{1}{c_f} \ln\left[1 - g z \rho_0 c_f\right]. \tag{A.117}$$

Note that generally after this has been performed the model is further initialized by setting the permeability to very large values and allowing the simulation to run for a while with no wells.

Wells

Constant pressure wells are modelled with the Peaceman well model (Peaceman, 1978),

$$Q_\alpha = WI \cdot \left(P_{wf} - P\right) \cdot \lambda_\alpha \cdot \rho_\alpha, \tag{A.118}$$

where WI is the well index, which determines how productive the well is, and P_{wf} is the well bore flowing pressure, which is assigned for each well. All fluid properties are upstreamed in this calculation.

For constant flow rate wells, the flow rate into or out of the cell is simply assigned for injectors. For producers, the total flow rate can be assigned but then fractional flow must be used to determine how much of each fluid is produced. Care should be taken when handling the derivatives of the flow rate with respect to pressure and saturation as these two cases are handled differently in this regard. For injectors, these derivatives are zero.

Mechanics coupling

Poroelastic coupling can be ignored in the case that (Cheng, 2016)

$$\alpha B_{sk} \ll 1, \tag{A.119}$$

where B_{sk} is the Skempton coefficient; however, this is generally not the case. Here, the mechanics coupling is performed using the definition of porosity from Coussy (2007), which is

$$\phi = -\epsilon_{kk}\alpha + \frac{P\left(\alpha - \phi_0\right)}{k_s} + \phi_0. \tag{A.120}$$

Here, ϵ_{kk} is the volumetric strain, positive in extension, α is the Biot coefficient, ϕ is the current porosity, ϕ_0 is the reference porosity at zero pressure and strain, P is the pore pressure, and k_s is the grain bulk modulus. The volumetric strain is simply a sum of the axial strains.

I initialize by first assigning a fixed value of porosity to perform the pressure initialization (such that I can achieve hydrostatic pressure for compressible flow). Then, I assume a typical lithostatic gradient (usually 2.3 times hydrostatic) to calculate the predicted vertical stress. This is then multiplied by the Young's Modulus of each layer to get a predicted vertical strain. The vertical strain is then taken as the initial volumetric strain and this is then used in the equation above to calculate porosity. The initial volumetric strain is then stored and applied

each time porosity is calculated (because the mechanics simulator subtracts the forces applied by the initial hydrostatic stress field so that it can calculate stress changes from the initial condition). In this way porosity can be seen to be decreasing with depth (assuming a high enough bulk modulus for the grains). Note that it is important to assign the same initial reference porosity within each layer so that porosity's gradient with respect to pressure is constant within that layer.

The flow and mechanics model are iterated each time step until convergence (determined by change in pressure) before moving on to the next time step. At the beginning of the time step, the new volumetric strain is applied. This changes the porosity, so the pressure has to be adjusted such that the mass of each phase is conserved.

Thermoelastic coupling

Here, the thermoelastic coupling can ignored in certain cases(i.e. heat does not cause solids to deform and the solid deformation does not generate heat). This is generally the case for most geomaterials (Cheng, 2016) and is the case for geomaterials where

$$\frac{K\beta_d^2}{m_d} \ll 1. \tag{A.121}$$

In the case that one-way flow to solid coupling is to be included, the thermal strain, ϵ_T,

$$\epsilon_T = \alpha_T \Delta T, \tag{A.122}$$

is added to the mechanical strains before the computation of stress changes. Here, α_T is the coefficient of linear thermal expansion and T is the temperature.

Dual-Porosity mechanical model

The mechanical model begins with the conservation of momentum,

$$\nabla \cdot \sigma' + \nabla \left(\alpha_1 P_m + \alpha_2 P_f \right) = -f_b, \tag{A.123}$$

where σ' is the effective stress and f_b the body forces. As defined by Khalili and Valliappan (1996), α_1 and α_2 are the effective stress parameters for the matrix and fracture pressures

respectively and are equivalent to

$$\alpha_1 = \frac{c_p}{c} - \frac{c_s}{c}, \qquad \alpha_2 = 1 - \frac{c_p}{c}. \tag{A.124}$$

Here, c_s is the compressibility of the solid grains, c_p is the compressibility of the porous blocks, and c is the compressibility of the fissured porous medium. The conservation of momentum equation is then combined with the linear theory of poroelasticity extended for a dual porosity system (Biot, 1941; Rice and Cleary, 1976; Khalili and Valliappan, 1996; Wang, 2000),

$$S_{ij} - \alpha_1 P_m \delta_{ij} - \alpha_2 P_f \delta_{ij} = \frac{E}{(1+\nu)} \epsilon_{ij} + \frac{E\nu}{(1+\nu)(1-2\nu)} \epsilon_{kk} \delta_{ij}, \tag{A.125}$$

where S is defined as the total stress, E is the drained Young's Modulus, ν is the drained Poisson's Ratio, ϵ is the strain, and δ_{ij} is the Kronecker delta. The combination of these equations is then discretized in a finite element framework.

Dual-Porosity coupling

The poroelastic coupling between the mechanical model and matrix flow model can be performed using (Coussy, 2007),

$$\phi_m = -\epsilon_{kk}\alpha_1 + \frac{P_m\left(\alpha_1 - \phi_{m,0}\right)}{K_s} + \phi_{m,0}. \tag{A.126}$$

where $\phi_{m,0}$ represents the reference matrix porosity and K_s is the grain bulk modulus. For simplicity, the fracture porosity is assumed to have a constant value of one. However, the permeability of the fractures is assumed to permanently increase when the pore pressure exceeds the minimum principal stress during stimulation, an approach used in numerical fracture models (e.g., Wang *et al.* (2018)) and seen in field studies (e.g., Warpinski *et al.* (1982a)). An opened fracture is assumed to have a permeability that is three orders of magnitude larger than that of the matrix. The coupling from the flow model to the mechanical model occurs via the inclusion of pore pressures as internal forces in the momentum balance equation.

A.5.7 An alternate approach, the Pressure Diffusion Equation

Starting with the continuity equation of mass balance for a single phase:

$$\frac{\partial(\phi\rho)}{\partial t} - \nabla \cdot \left(\frac{k}{\mu}\rho\,(\nabla P)\right) = q \tag{A.127}$$

Note that, as mentioned above, the diffusion of mass in this equation has already been neglected (because velocity was replaced by Darcy's Law which does not account for diffusion). To account for the diffusion of mass something like Fick's Law must be used in combination. Therefore, when using Darcy's Law the convection term is simply made up of advection. Assuming that k and μ are constant:

$$\frac{\partial(\phi\rho)}{\partial t} - \frac{k}{\mu}\nabla \cdot \left(\rho\,(\nabla P)\right) = q \tag{A.128}$$

Then using the chain rule on the left-hand side.

$$\rho\frac{\partial(\phi)}{\partial t} + \phi\frac{\partial(\rho)}{\partial t} - \frac{k}{\mu}\nabla \cdot \left(\rho\,(\nabla P)\right) = q \tag{A.129}$$

Next, using the definition of isothermal fluid compressibility, which is

$$c_f = \frac{1}{\rho}\left(\frac{\partial\rho}{\partial P}\right)_T, \tag{A.130}$$

and the chain rule, which yields

$$\frac{\partial\rho}{\partial t} = \frac{\partial\rho}{\partial P}\frac{\partial P}{\partial t} = c_f \cdot \rho\frac{\partial P}{\partial t}, \tag{A.131}$$

we find that

$$\rho\frac{\partial(\phi)}{\partial t} + \phi \cdot c_f \cdot \rho\frac{\partial P}{\partial t} - \frac{k}{\mu}\nabla \cdot \left(\rho\,(\nabla P)\right) = q \tag{A.132}$$

Next, given that rock compressibility is defined as

$$c_r = \frac{1}{\phi}\left(\frac{\partial\phi}{\partial P}\right)_T \tag{A.133}$$

and using that

$$\frac{\partial\phi}{\partial t} = \frac{\partial\phi}{\partial P}\frac{\partial P}{\partial t} = c_r \cdot \phi \frac{\partial P}{\partial t}, \tag{A.134}$$

we can also write

$$\rho \cdot c_r \cdot \phi \frac{\partial P}{\partial t} + \phi \cdot c_f \cdot \rho \frac{\partial P}{\partial t} - \frac{k}{\mu}\nabla\cdot\left(\rho\left(\nabla P\right)\right) = q \tag{A.135}$$

or

$$\rho \cdot \phi\left(c_r + c_f\right)\frac{\partial P}{\partial t} - \frac{k}{\mu}\nabla\cdot\left(\rho\left(\nabla P\right)\right) = q \tag{A.136}$$

Now we can expand the second term:

$$\rho \cdot \phi\left(c_r + c_f\right)\frac{\partial P}{\partial t} - \frac{k}{\mu}\left(\rho\nabla^2 P + \nabla P \cdot \nabla\rho\right) = q \tag{A.137}$$

The second term within the second term can be replaced with

$$\nabla P \cdot \nabla\rho = c_f \cdot \rho \cdot \nabla^2 P \tag{A.138}$$

The reason for this can be most easily seen in a 1D example:

$$\frac{\partial P}{\partial x}\frac{\partial\rho}{\partial x} = \frac{\partial P}{\partial x}\frac{\partial\rho}{\partial P}\frac{\partial P}{\partial x} = \frac{\partial\rho}{\partial P}\left(\frac{\partial P}{\partial x}\right)^2 = c_f \cdot \rho \cdot \left(\frac{\partial P}{\partial x}\right)^2 \tag{A.139}$$

Anyway, this term is usually neglected (because $c_f \cdot \rho$ is much smaller than ρ) leaving us with:

$$\rho \cdot \phi \left(c_r + c_f \right) \frac{\partial P}{\partial t} - \frac{k}{\mu} \rho \nabla^2 P = q \qquad\qquad \text{(A.140)}$$

The compressibilities can be combined to yield a total compressibility c_t.

$$\rho \cdot \phi \cdot c_t \frac{\partial P}{\partial t} - \frac{k}{\mu} \rho \nabla^2 P = q \qquad\qquad \text{(A.141)}$$

The equation be divided by the terms in front of the derivative in the left-most term,

$$\frac{\partial P}{\partial t} - \frac{k}{\mu} \frac{1}{\phi \cdot c_t} \nabla^2 P = \frac{q}{\rho \cdot \phi \cdot c_t} \qquad\qquad \text{(A.142)}$$

These terms can be lumped together. This yields the final version of the pressure diffusion equation,

$$\frac{\partial P}{\partial t} - D \nabla^2 P = Q, \qquad\qquad \text{(A.143)}$$

where

$$D = \frac{k}{\mu \phi c_t}. \qquad\qquad \text{(A.144)}$$

Note that although the pressure term in the diffusion equation is Laplacian and therefore a diffusive term, it is important to note that the fundamental process behind this is not diffusion. What I mean here is that this equation comes from the continuity equation for mass balance with Darcy's Law, which describes advection (see derivation). That equation does not, therefore, describe the diffusion of mass it describes the advection of mass. Pressure is diffusive here, mass is not, and the diffusion equation comes from mass balance.

A.6 Validation

A.6.1 Validation of flow model

Pressure validation

To solve the heat equation,

$$\frac{\partial^2 v}{\partial x^2} - \frac{1}{\kappa} \frac{\partial v}{\partial t} = -Q \tag{A.145}$$

Carslaw and Jaeger (1959) derived the following equation

$$v = \frac{Vx}{l} + \frac{2V}{\pi} \sum_{n=1}^{\infty} \frac{(-1)^n}{n} e^{-\frac{k \cdot n^2 \cdot \pi^2 \cdot t}{l^2}} sin\left(\frac{n\pi x}{l}\right) \tag{A.146}$$

for a finite region $0 < x < l$ with zero initial temperature, no flow of heat at $x = 0$ and $x = l$ maintained at temperature V, which is constant at $t > 0$. The equation is valid for small values of time. Note that it is not important how the Q in the first equation is actually defined for my purposes, just that it supplies the right amount of mass/heat to maintain the constant value at the boundary.

One important point to note is that the locations of the boundary conditions can be switched by removing the negative sign from the -1 just after the summation. This will be done in our case when we have an injector on the left-hand side.

The first equation has the same form as the mass balance equation,

$$\frac{\partial (\phi\rho)}{\partial t} - \nabla \cdot \left(\frac{k}{\mu}\rho\,(\nabla P)\right) = q, \tag{A.147}$$

when it is written as the pressure diffusion equation (see Section A.5.7),

$$\frac{\partial P}{\partial t} - D\nabla^2 P = Q. \tag{A.148}$$

Note the big differences between the two is that the pressure diffusion equation assumes constant k and μ. Also, the density formulation that I typically use for the other one is different.

221

Regardless, this new equation has the same form as the heat equation when it is written as

$$\frac{\partial^2 P}{\partial x^2} - \frac{1}{D}\frac{\partial P}{\partial t} = -Q. \tag{A.149}$$

in 1-D. This means the analytical solution from Carslaw and Jaeger still holds. However, in this case $\kappa = D$ and V equals the new Dirichlet boundary condition. Finally, the equation has been scaled up to an initial pressure P_i, i.e.

$$P = P_i + (P_R - P_i)\frac{x}{l} + (P_R - P_i)\frac{2}{\pi}\sum_{n=1}^{\infty}\frac{(-1)^n}{n}e^{-\frac{D\cdot n^2\cdot\pi^2\cdot t}{l^2}}sin\left(\frac{n\pi x}{l}\right) \tag{A.150}$$

If you would like the higher pressure boundary to be on the left-hand side the equation reads,

$$P = P_i + (P_i - P_R)\frac{x}{l} + (P_i - P_R)\frac{2}{\pi}\sum_{n=1}^{\infty}\frac{1}{n}e^{-\frac{D\cdot n^2\cdot\pi^2\cdot t}{l^2}}sin\left(\frac{n\pi x}{l}\right) \tag{A.151}$$

This second equation is the one that was used for my validation. I assigned a constant pressure well in the left-most cell and gave the well a very high well index, effectively making the cell a constant pressure. The results are as shown in Figure A.3.

At late times it is clear there is a large difference. This is because Carlaw and Jaeger's result is for small times only. As soon as the pressure reaches the boundary it is not valid. There are also smaller differences among curves before that point. I feel these differences are small enough considering also that I am using a different density formulation, i.e.

$$\rho = \rho_0 e^{c_f(P-P_0)} \tag{A.152}$$

which is valid for slightly compressible fluids.
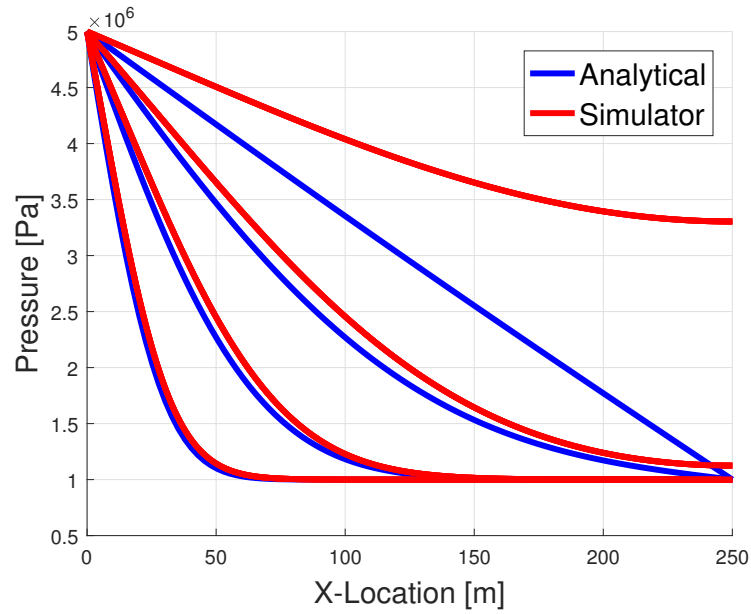
Figure A.3 – Pressure solution on 30x30 grid cells

Validation of two phase flow

Buckley-Leverett (BL) theory begins with the continuity equation for the mass balance of water,

$$\frac{\partial\left(\phi\rho S_w\right)}{\partial t} - \frac{\partial}{\partial x}\cdot\left(\frac{k\cdot k_r}{\mu}\rho\left(\nabla P\right)\right) = 0. \tag{A.153}$$

Since one of the assumption of BL theory is incompressible fluids, density can be removed from the partial derivatives,

$$\rho\frac{\partial\left(\phi S_w\right)}{\partial t} - \rho\frac{\partial}{\partial x}\cdot\left(\frac{k\cdot k_r}{\mu}\left(\nabla P\right)\right) = 0. \tag{A.154}$$

It can then be cancelled out,

$$\frac{\partial\left(\phi S_w\right)}{\partial t} - \frac{\partial}{\partial x}\cdot\left(\frac{k\cdot k_r}{\mu}\left(\nabla P\right)\right) = 0. \tag{A.155}$$

Reversing the implementation of Darcy's Law such that we are using velocity and not pressure

gradient yields

$$\frac{\partial(\phi S_w)}{\partial t} - \frac{\partial}{\partial x} \cdot (u_w) = 0. \tag{A.156}$$

This velocity can be replaced with the total velocity multiplied by the fractional flow of water,

$$u_w = \frac{q_t}{A} \cdot f_w. \tag{A.157}$$

By substituting this relation in we have,

$$\frac{\partial(\phi S_w)}{\partial t} - \frac{\partial}{\partial x} \cdot \left(\frac{q_t}{A} \cdot f_w \right) = 0. \tag{A.158}$$

Because flow is incompressible, volume flow rate is constant throughout the system. Additionally, the porosity is assumed to remain constant, yielding

$$\phi \frac{\partial(S_w)}{\partial t} - \frac{q_t}{A} \frac{\partial}{\partial x} \cdot (f_w) = 0. \tag{A.159}$$

Rearrangement yields,

$$\frac{\partial S_w}{\partial t} = \frac{q_t}{A \cdot \phi} \frac{\partial f_w}{\partial x}. \tag{A.160}$$

Now use chain rule,

$$dS_w = \left(\frac{\partial S_w}{\partial t} \right)_x dt + \left(\frac{\partial S_w}{\partial x} \right)_t dx. \tag{A.161}$$

For constant saturation we have

$$0 = \left(\frac{\partial S_w}{\partial t} \right)_x dt + \left(\frac{\partial S_w}{\partial x} \right)_t dx. \tag{A.162}$$

This yields through rearrangement

$$\left(\frac{dx}{dt}\right)_{S_w} = -\frac{\left(\frac{\partial S_w}{\partial t}\right)_x}{\left(\frac{\partial S_w}{\partial x}\right)_t}. \tag{A.163}$$

Combining the above equation with Equation A.160

$$\left(\frac{dx}{dt}\right)_{S_w} = \frac{q_t}{A \cdot \phi} \frac{\partial f_w}{\partial x} \frac{1}{\left(\frac{\partial S_w}{\partial x}\right)_t} \tag{A.164}$$

This reduces to

$$\left(\frac{dx}{dt}\right)_{S_w} = \frac{q_t}{A \cdot \phi} \frac{\partial f_w}{\partial S_w}. \tag{A.165}$$

Now this equation can be made dimensionless by recognizing that

$$x_D = \frac{x}{L} \tag{A.166}$$

and

$$t_D = \frac{q \cdot t}{A \cdot \phi \cdot L} \tag{A.167}$$

leaving us with

$$x_D\left(S_w\right) = \left.\frac{\partial f_w}{\partial S_w}\right|_{S_w} t_D. \tag{A.168}$$

The definition of fraction flow is

$$f_w(S_w) = \frac{\lambda_w}{\lambda_w + \lambda_{nw}}.$$
(A.169)

Here, mobility is defined as

$$\lambda_w = \frac{kr_w}{\mu_w}.$$
(A.170)

Therefore, we can solve Equation A.165 (rewritten in a different form here) using the relations for fractional flow and mobility to find the velocity of each value of saturation,

$$u_w(S_w) = \frac{Q}{A\phi} \frac{df_w}{dS_w}.$$
(A.171)

Additionally, Equation A.168 can be used to solve for the locations of all of the values of saturation at various times. Care should be taken to ignore the invalid results caused by the shock front. Effectively, the highest values of water saturation will have lower velocities than some of the lower values of water saturation. For non-water injection into an initially water saturated reservoir this is not physical. Therefore these values of water saturation should be ignored and replaced by the shock front. This approach can be used to validate the two phase flow of a system, but as two phase flow was not used for any of the projects in the thesis, we will not perform the validation here.

A.6.2   Validation of mechanical model
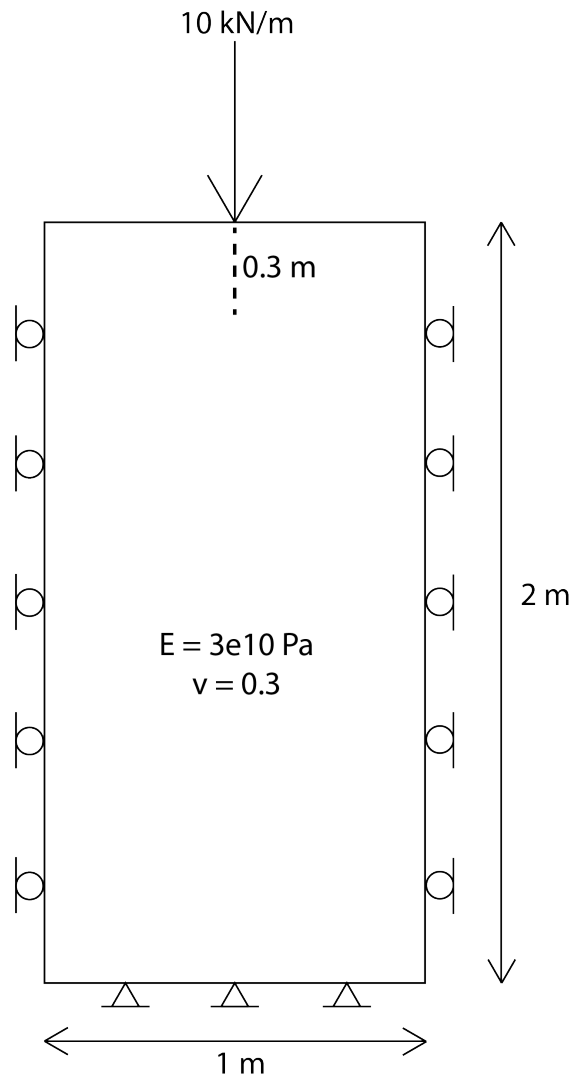
Figure A.4 – Validation Against Flamant Analytical Solution Setup

Validation using Flamant

Flamant presented analytical solutions for point loads. Helwany (2007) used these solutions for the validation of an FEM simulator. One such problem he presented is below.

The analytical Flamant solution for plane strain due to a line load is:

$$\Delta\sigma_z = \frac{2qz^3}{\pi\left(x^2 + z^2\right)^2} \tag{A.172}$$
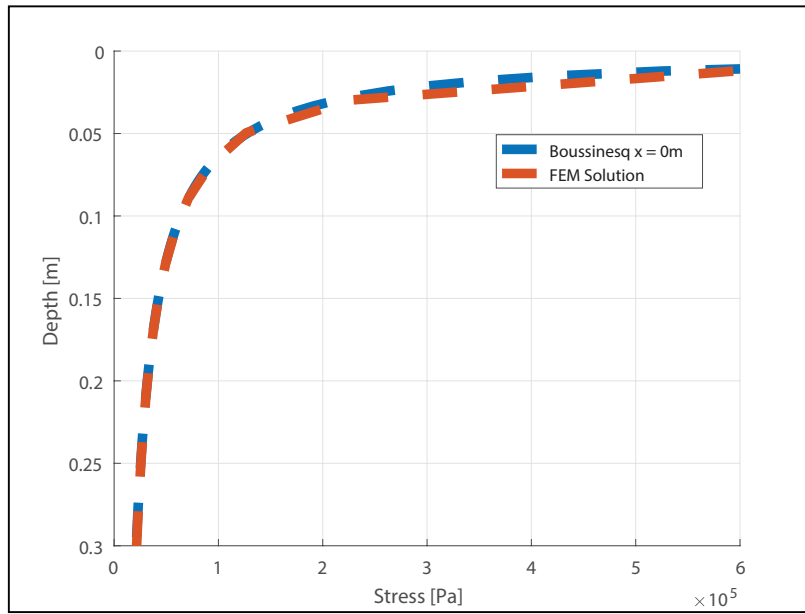
Figure A.5 – Validation Against Flamant Analytical Solution

which reduces to

$$\Delta\sigma_z = \frac{2q}{\pi \cdot z} \tag{A.173}$$

if we set x to be equal to zero and just look at how stress changes with depth, Figure A.4. This was then compared against my FEM solution and the results are shown in Figure A.5.

Validation using definition of plane strain

By applying a load across the top of a block of $-1000 \left[\frac{N}{m}\right]$ (which corresponds to placing a force of $-1000 \cdot \frac{L_x}{N_x} [N]$ on each node in the middle of the system and half this force on the edge nodes), Figure A.6, we expect a vertical stress of $-1000 [Pa]$ throughout the system. The horizontal and shear stresses should be zero. This is what we find, Figures A.7 and A.8.

Next, if we take a look at the plane strain formulation,

$$\begin{bmatrix} \sigma_{xx} \\ \sigma_{yy} \\ \tau_{xy} \end{bmatrix} = \frac{-E}{(1+\nu)(1-2\nu)} \begin{bmatrix} 1-\nu & \nu & 0 \\ \nu & 1-\nu & 0 \\ 0 & 0 & \frac{1-2\nu}{2} \end{bmatrix} \begin{bmatrix} \epsilon_{xx} \\ \epsilon_{yy} \\ \gamma_{xy} \end{bmatrix}, \tag{A.174}$$
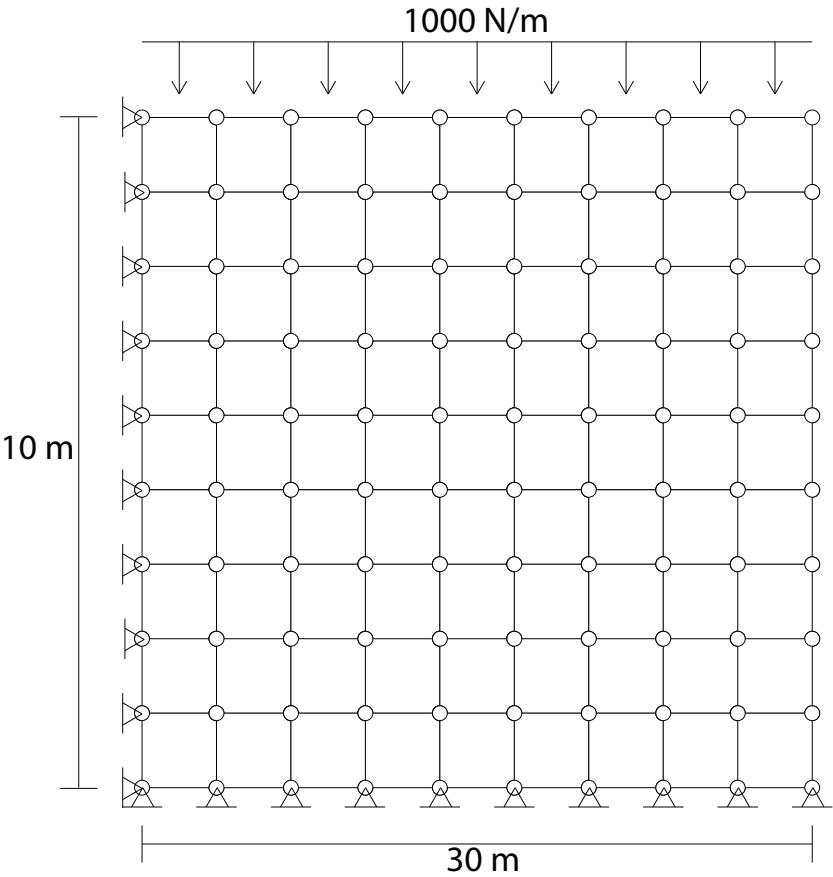
Figure A.6 – Setup
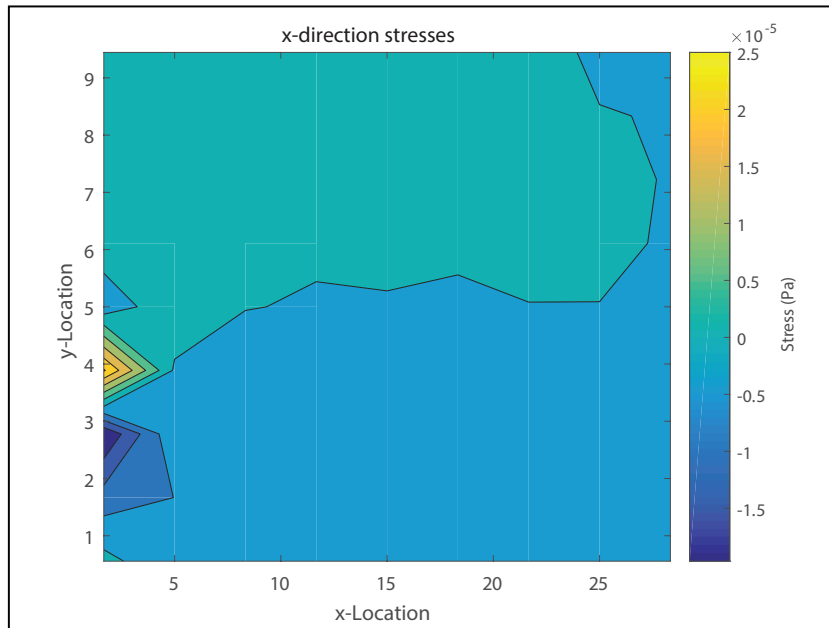
Figure A.7 – X-Stresses, equal to zero everywhere

we can plug in values for a given problem. For example, if the force was applied such that the stress equals $-1000\,[Pa]$, Young's Modulus equals $1 \times 10^9\,[Pa]$, and Poisson's ratio equals 0.3, we get the following system of equations:

$$\begin{bmatrix} 0 \\ -1000 \\ 0 \end{bmatrix} = \frac{-1 \times 10^9}{(1.3)(0.4)} \begin{bmatrix} 0.7 & .3 & 0 \\ 0.3 & 0.7 & 0 \\ 0 & 0 & 0.2 \end{bmatrix} \begin{bmatrix} \epsilon_{xx} \\ \epsilon_{yy} \\ \gamma_{xy} \end{bmatrix}, \tag{A.175}$$

or

$$0 = -1.9231 \times 10^9 \left(0.7 \cdot \epsilon_{xx} + 0.3 \epsilon_{yy} \right) \tag{A.176}$$

$$-1000 = -1.9231 \times 10^9 \left(0.3 \cdot \epsilon_{xx} + 0.7 \epsilon_{yy} \right) \tag{A.177}$$

$$0 = -1.9231 \times 10^9 \cdot 0.2 \cdot \epsilon_{xy}. \tag{A.178}$$
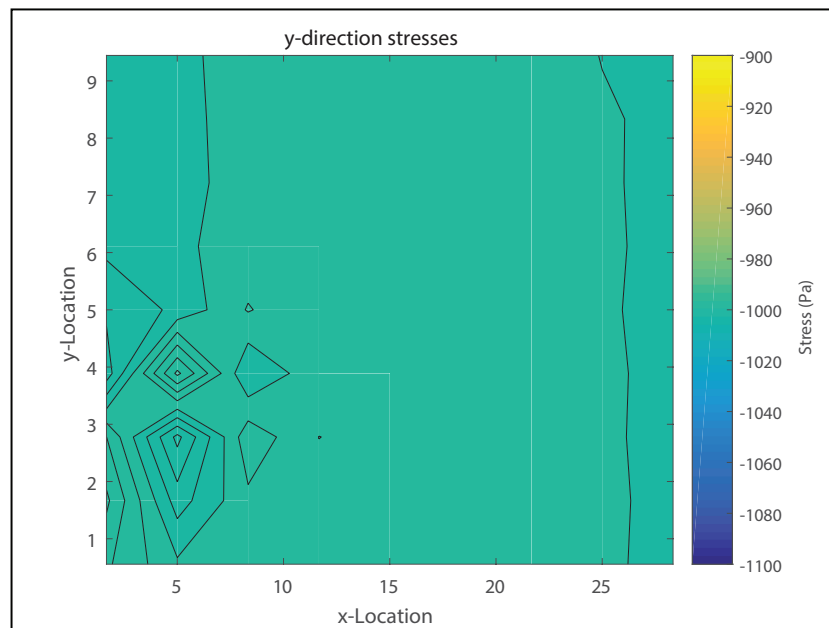
Figure A.8 – Y-Stresses, equal to -1000 Pa everywhere

We could, in theory, solve for the expected strains. Alternatively, we could run the problem in our simulator and simply plug in our values of strain and see if they satisfy the equations. This is what I did. I found that $\epsilon_{xx} = 3.9 \times 10^{-7}$, Figure A.9, and $\epsilon_{yy} = -9.1 \times 10^{-7}$, Figure A.10. These values satisfy the equations.

Also we can note that the maximum displacement in the y-direction (occurring where the forces are applied) is equal to the strain multiplied by the length in the y-direction, Figure A.11. The same check holds for the x-displacement at the right-hand edge, Figure A.12.

Validation using ABAQUS

Next, the problem depicted in Figure A.13 was run both in ABAQUS and my simulator. As it is difficult to depict the results in a comparative manner in 2-D, a cut was made along the red dashed line, as seen in Figure A.13, and stresses were analyzed along this line for both the ABAQUS results and mine, Figures A.14, A.15, and A.16.

A.6.3   Validation of poroelastic model

Terzaghi

Terzaghi's consolidation problem consists of a confined sample (on three sides) filled with water. The sample is assumed to be in plane strain conditions. A distributed load, q, in $[Pa]$ is applied to the top of the sample. Unlike Terzaghi's original work, the analytical solutions taken from Verruijt (2013) and Cheng (2016) will be compressible. A constant pressure of zero
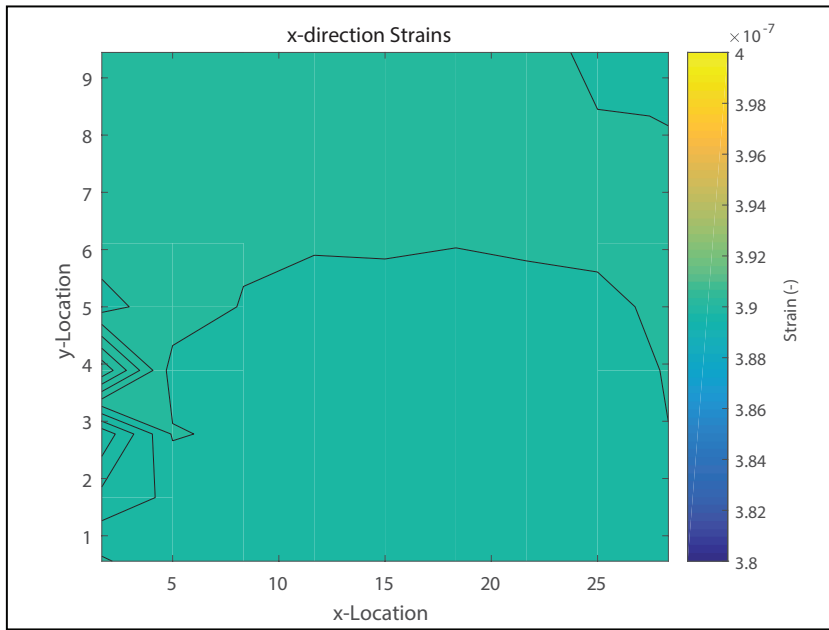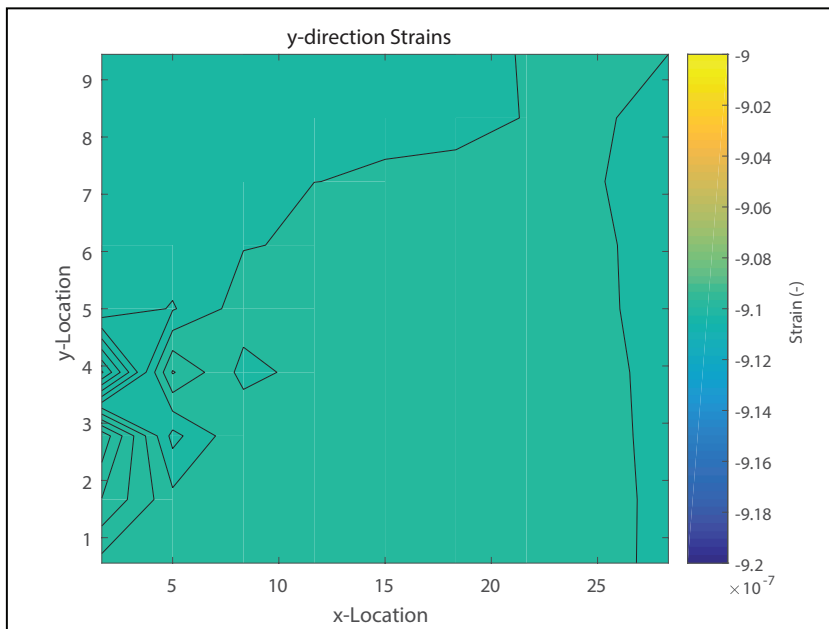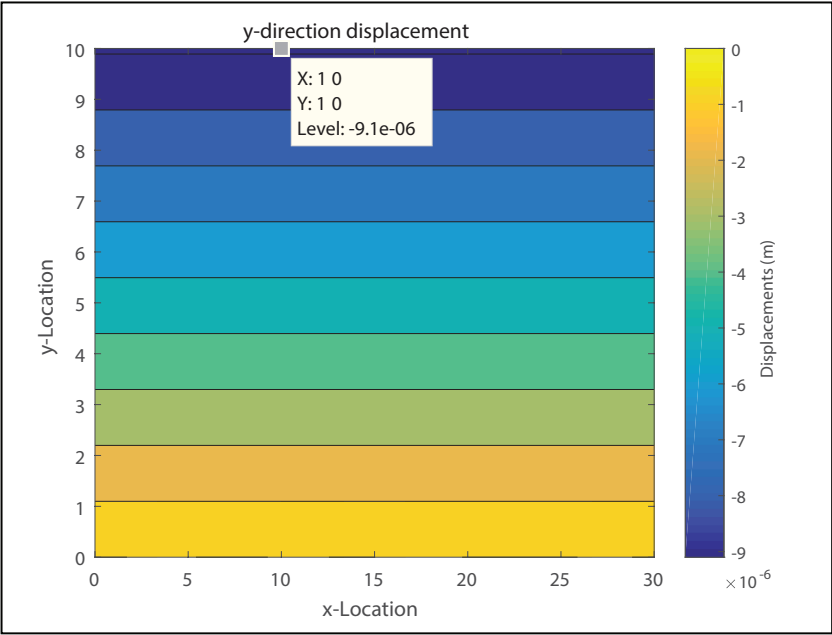
Figure A.9 – X-Strains

Figure A.10 – Y-Strains

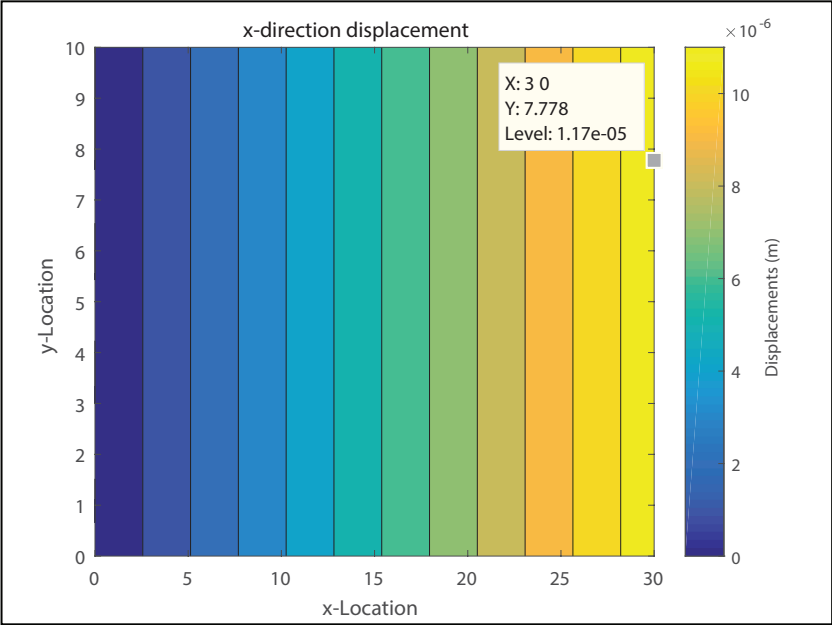Figure A.11 – Y-Displacements, maximum value of the strain times the length of the side

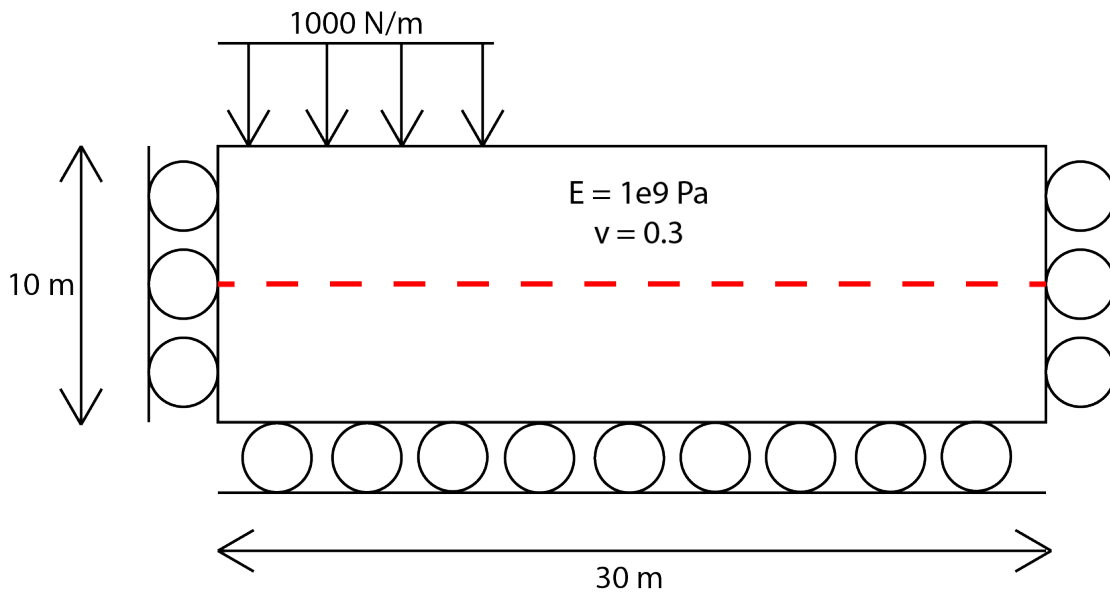Figure A.12 – X-Displacements, maximum value of the strain times the length of the side

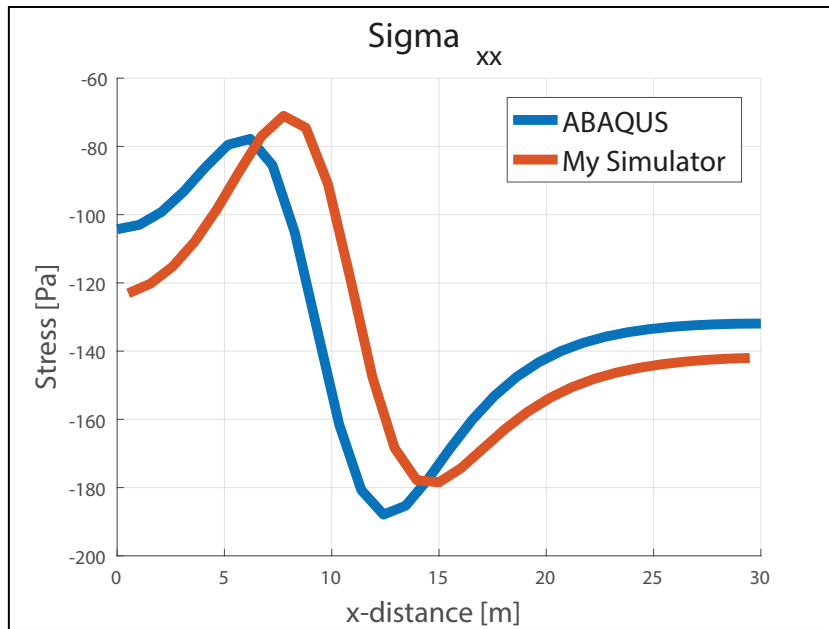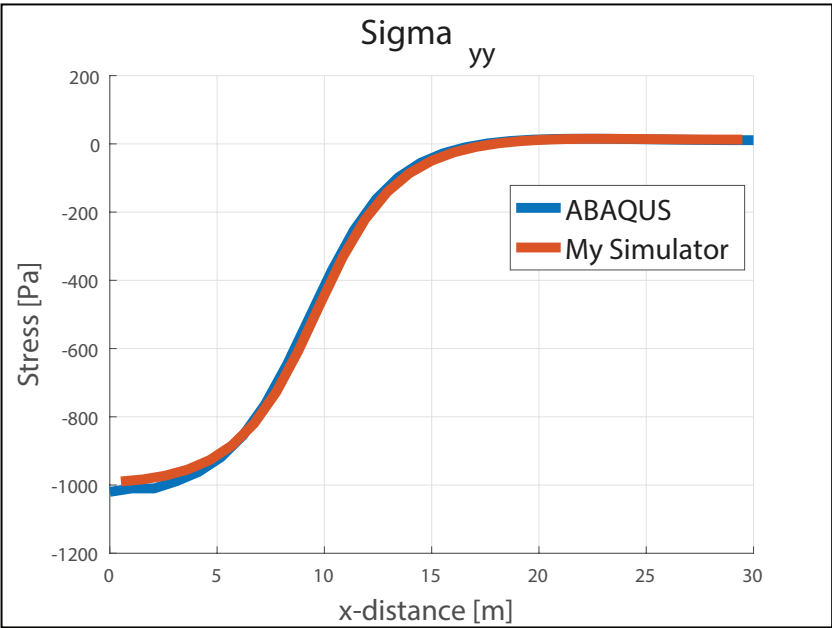Figure A.13 – FEM Setup for ABAQUS validation

Figure A.14 – Comparison of σ_{xx}
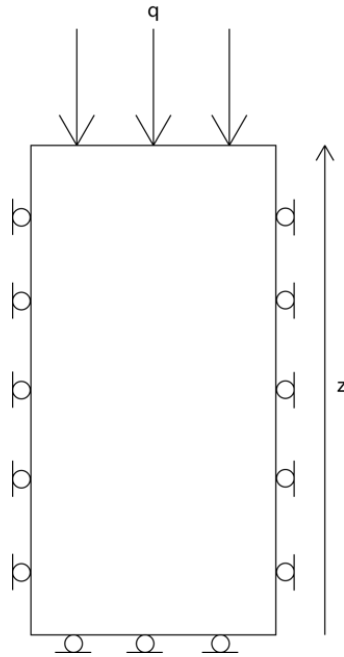
Figure A.15 – Comparison of σ_{yy}
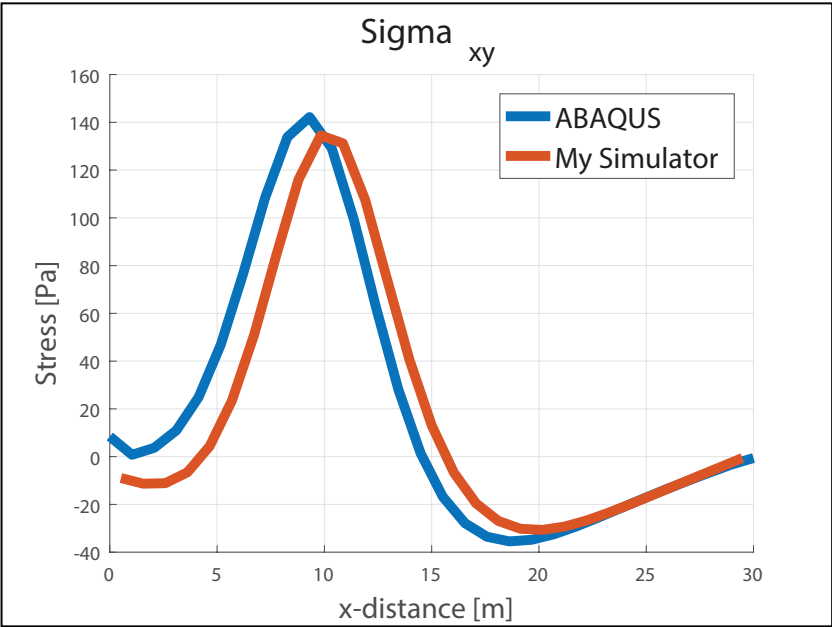
Figure A.16 – Comparison of σ_{xy}

Figure A.17 – Terzaghi experiment setup

(atmospheric) is assumed at the top of the sample; no flow boundaries are defined for the other three edges. Additionally, these edges are assumed to be fixed and are defined in my model to have zero displacement. The top edge is allowed to move freely. A schematic can be seen in Figure A.17.

The significant parameters defined in my model are the drained Poisson's ratio, v, the drained Young's Modulus, E, the bulk modulus of the grains, K_s, the initial porosity, ϕ, the fluid compressibility, c_f, the permeability, k, and the fluid viscosity, μ_f.

To begin the analytical calculation for pore pressure from Verruijt (2013), first the compressibility of the solid material is calculated

$$C_s = \frac{1}{K_s} \tag{A.179}$$

along with the shear modulus,

$$G = \frac{E}{2\left(1 + v\right)}. \tag{A.180}$$

This is then used to calculate the drained bulk modulus,

$$K = \frac{2G(v+1)}{3(1-2v)} \tag{A.181}$$

which is in turn used to calculate the compressibility of the porous medium

$$C_m = \frac{1}{K}. \tag{A.182}$$

Then, the Biot Coefficient can be calculated,

$$\alpha = 1 - \frac{C_s}{C_m}. \tag{A.183}$$

This allows for the calculation of the storativity,

$$S = \phi c_f + (\alpha - \phi) C_s \tag{A.184}$$

which can be used in combination with the confined compressibility of the porous medium,

$$m_v = \frac{1}{K + \frac{4}{3}G} \tag{A.185}$$

to calculate the consolidation coefficient,

$$c_v = \frac{k_f}{\gamma_f (S + \alpha^2 m_v)}. \tag{A.186}$$

At this point, the initial pressure increase seen everywhere in the sample at the application of the load can be calculated,

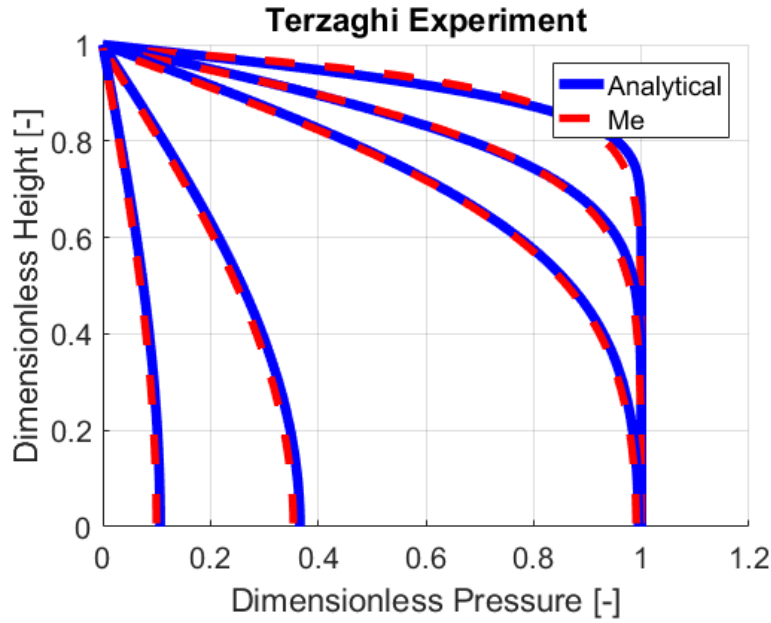$$p_0 = \frac{\alpha m_v}{S + \alpha^2 m_v} q. \tag{A.187}$$

Figure A.18 – Comparison of P_p with an analytical solution for Terzaghi's problem

Finally, the dimensionless pressure throughout the sample at a given time and location can be found,

$$\frac{p}{p_0} = \frac{4}{\pi} \sum_{k=1}^{\infty} \frac{(-1)^{k-1}}{2k-1} cos\left[(2k-1)\frac{\pi}{2}\frac{z}{h}\right] \exp\left[-(2k-1)^2\frac{\pi^2}{4}\frac{c_v t}{h^2}\right] \tag{A.188}$$

The comparison between this analytical solution and my simulator's results can be seen in Figure A.18 for various times.

To calculate the displacements analytically, we will follow (Cheng, 2016). To begin the Biot Modulus must be calculated using Castelletto *et al.* (2015),

$$M = \left(\frac{\alpha - \phi_0}{K_s} + \frac{\phi}{K_f}\right)^{-1}. \tag{A.189}$$

Then, the Skempton coefficient can be calculated (Castelletto *et al.*, 2015),

$$B = \frac{\alpha M}{K + \alpha^2 M} \tag{A.190}$$

This can be used to calculate the undrained Poissons ratio (Castelletto *et al.*, 2015),

$$\nu_u = \frac{3\nu + \alpha B (1 - 2\nu)}{3 - \alpha B (1 - 2\nu)} \tag{A.191}$$

Together with the hydraulic conductivity ($k_h = \frac{k}{\mu_f}$), the Terzaghi consolidation coefficient can be calculated (Cheng, 2016),

$$c = \frac{c k_h G (1 - \nu)(\nu_u - \nu)}{\alpha^2 (1 - 2\nu)^2 (1 - \nu_u)}. \tag{A.192}$$

Next, Cheng (2016) defines $z^* = \frac{z}{L}$ and $t^* = \frac{cT}{4L^2}$ before presenting the equation for the vertical displacement

$$u_z(z, t) = \frac{qL(1 - 2\nu_u)}{2G(1 - \nu_u)}\left(1 - z^*\right) + \frac{qL(\nu_u - \nu)}{2G(1 - \nu_u)(1 - \nu)} F_2\left(z^*, t^*\right), \tag{A.193}$$

where

$$F_2\left(z^*, t^*\right) = \sum_{m=1,3,\cdots}^{\infty} \frac{8}{m^2 \pi^2} \cos\left(\frac{m\pi z^*}{2}\right)\left(1 - \exp\left[-m^2 \pi^2 t^*\right]\right). \tag{A.194}$$

The comparison of the analytical results and the results from my simulator can be seen in Figure A.19.

Mandel

Mandel's problem is a sample confined on two sides (top and bottom) by an impermeable membrane. The sides are left open and at atmospheric pressure. A force is applied on the top and bottom members which is equally distributed and equal to $2F$. This is a force per unit length in the z-direction (into the plane in this plane strain problem). Because of the symmetry of the problem, only the top right quadrant needs to be simulated. Then, the bottom and left boundaries are no-flow no-displacement. The fluid and grains are compressible. The schematic of the setup can be seen in Figure A.20.

Here, a similar process is adopted as in Terzaghi's problem. First, the shear modulus, drained bulk modulus, Biot's coefficient, the fluid bulk modulus, Biot's modulus, and the Skempton
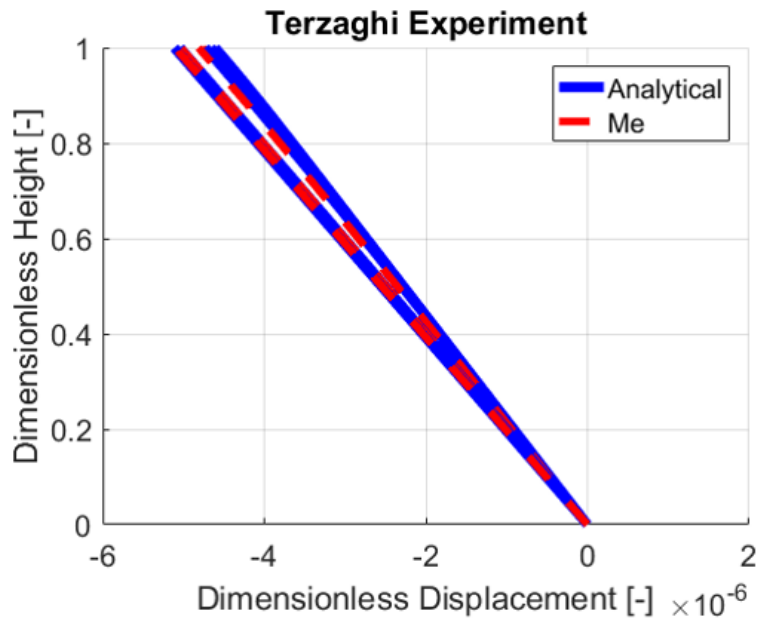
Figure A.19 – Comparison of u_z with an analytical solution for Terzaghi's problem
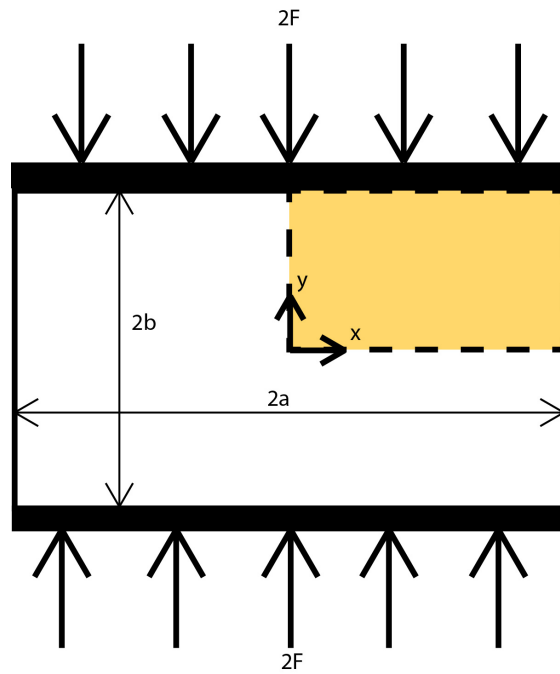

Figure A.20 – Mandel experiment setup

coefficient are all calculated in that order. Next, the undrained Poisson's ratio is calculated (Castelletto *et al.*, 2015),

$$\nu_u = \frac{3\nu + \alpha B (1 - 2\nu)}{3 - \alpha B (1 - 2\nu)}. \tag{A.195}$$

Then, the uniaxial drained bulk modulus is found (Castelletto *et al.*, 2015),

$$K_\nu = \frac{2G (1 - \nu)}{(1 - 2\nu)}. \tag{A.196}$$

Next, the fluid diffusivity coefficient is calculated (Castelletto *et al.*, 2015),

$$c_\nu = k_h M \frac{K_\nu}{K_\nu + \alpha^2 M}. \tag{A.197}$$

Next, an auxiliary elastic constant is calculated using (Castelletto *et al.*, 2015)

$$\xi = \frac{1 - \nu}{\nu_u - \nu}. \tag{A.198}$$

This is used to find all of the positive roots, β_n, that satisfy (Castelletto *et al.*, 2015),

$$\tan(\beta_n) = \xi \beta_n \tag{A.199}$$

Dimensionless pore pressure can the be found using (Castelletto *et al.*, 2015)

$$\frac{p}{p_0} = 2 \sum_{n=1}^{\infty} \frac{\sin(\beta_n)}{\beta_n - \sin(\beta_n)\cos(\beta_n)} \left(\cos\left(\frac{\beta_n x}{a}\right) \cos(\beta_n) \right) \exp\left(-\frac{\beta_n^2 c_\nu t}{a^2}\right), \tag{A.200}$$

with (Castelletto *et al.*, 2015)

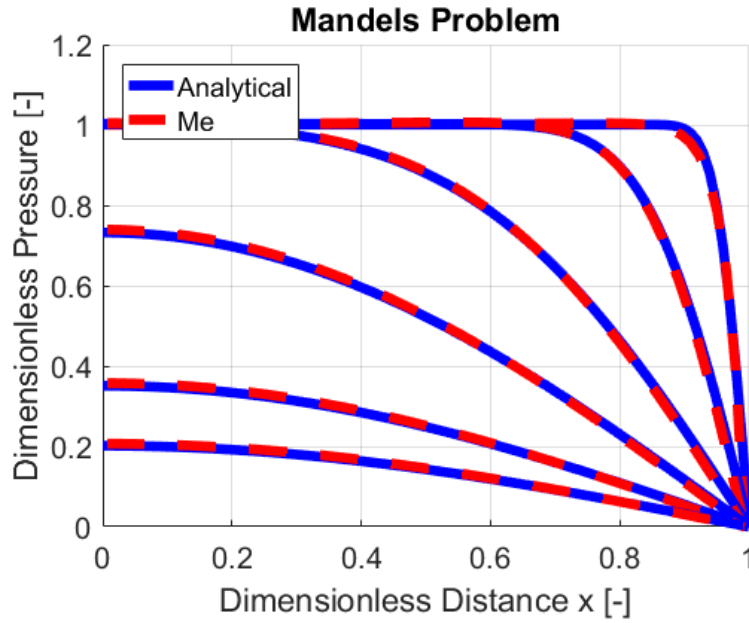$$p_0 = \frac{B}{3a} (1 + \nu_u) F. \tag{A.201}$$

241

Figure A.21 – Comparison of pressure with an analytical solution for Mandel's problem

This matches well with my simulator, Figure A.21.

Next, the displacement in the y-direction can be calculated using (Castelletto *et al.*, 2015),

$$u_y = \left[-\frac{F(1-\nu)}{2Ga} + \frac{F(1-\nu_u)}{Ga} \sum_{n=1}^{\infty} \frac{\sin(\beta_n)\cos(\beta_n)}{\beta_n - \sin(\beta_n)\cos(\beta_n)} \exp\left(-\frac{\beta_n^2 c_v t}{a^2}\right) \right] y. \tag{A.202}$$

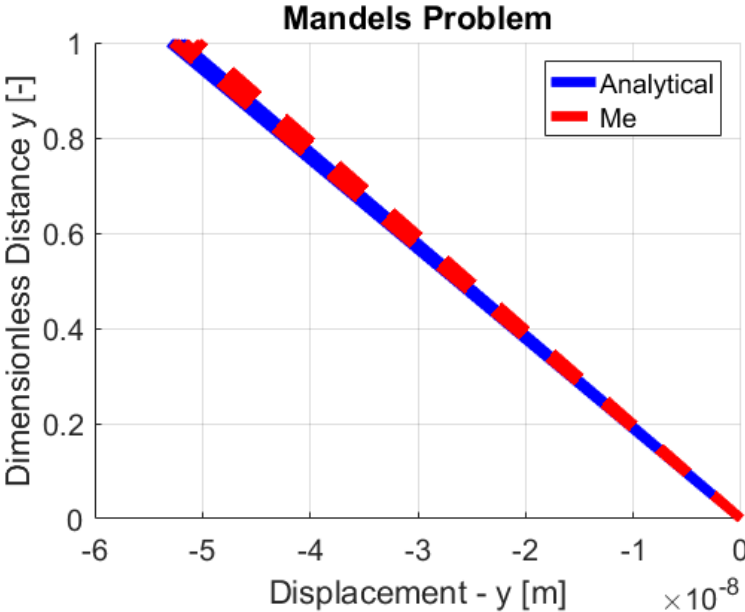It can be seen that this matches well with my simulator, Figure A.22.

Figure A.22 – Comparison of u_y with an analytical solution for Mandel's problem

Barnaby Fryer

Curriculum Vitae

▬▬▬ Education

2014–2016	**Master of Science**, *Applied Earth Sciences, Reservoir Geology Track*, Delft University of Technology.
2010–2014	**Bachelor of Science**, *Petroleum Engineering with Honors*, The University of Texas, Austin, Minor in German.

▬▬▬ Experience

Scholastic

2017– **PhD**, Laboratory of Soil Mechanics, EPFL, Lausanne, Switzerland, *Stress management in the context of induced seismicity in subsurface reservoirs*.

Using knowledge of how industrial operations can affect stress levels in the subsurface and fundamental ideas related to induced seismicity, I developed ideas which aim to reduce the risk of induced seismicity during fluid production, injection, and EGS operations. Built poroelastic reservoir model to investigate these proposals.

Vocational

2013 **Summer Intern**, Activa Resources, San Antonio, Texas.

Worked as both an office and field intern for a small San Antonio based oil company. Part of a 3-person field-based team to convert a shallow oil field from pumping units to an air pump system. Involved many hands-on tasks such as running pumps and tubing into wells by hand.

2012 **Summer Intern**, Denbury Resources, Tinsley, Mississippi.

Worked as a field intern at a CO_2 EOR facility producing approximately 10,000 bbls per day. Performed cost savings analysis on new well monitoring system. Responsible for routine well checks and understanding the processes taking place at the plant.

Miscellaneous

2011–2014 **Physics and Calculus Tutor**, *Sanger Learning Resources*, Austin, Texas.

Tutored individual students in Physics and Calculus. Lead group tutoring sessions of up to 20 students in Physics.

Journal Publications

Under Review **B. Fryer**, X. Ma, G. Siddiqi, L. Laloui. Critically-stressed reservoir stimulation direction via stress preconditioning in horizontal EGS doublets. *Geothermics*

In Press **B. Fryer**, G. Siddiqi, L. Laloui. Injection-induced seismicity: Strategies for reducing risk using high stress path reservoirs and temperature-induced stress preconditioning. *Geophysical Journal International*, doi:10.1093/gji/ggz490

2019 **B. Fryer**, G. Siddiqi, L. Laloui. Compaction-induced permeability loss's effect on induced seismicity during reservoir depletion. *Pure and Applied Geophysics*, 176:4277-4296, 2019. doi:10.1007/s00024-019-02198-0

2018 **B. Fryer**, G. Siddiqi, L. Laloui. Reservoir stimulation's effect on depletion-induced seismicity. *Journal of Geophysical Research: Solid Earth*, 132:7806-7823, 2018. doi:10.1029/2018JB016009

2017 M. Cusini, **B. Fryer**, C. van Kruijsdijk, H. Hajibeygi. Algebraic Dynamic Multilevel Method for compositional flow in heterogeneous media. *Journal of Computational Physics*, 354:593-612, 2017. doi:10.1016/j.jcp.2017.10.052

Awards

2018 Awarded the Swiss Association of Energy Geoscientists' Student Grant

2016 Passed *Dutch As Second Language* (NT2 II) exam for people looking to "work or study at a university level"

2015 Xodus - Sergio Ottochian Scholarship for Reservoir Simulation

2013 Chevron Workforce Initiative Scholarship

2012 & 2013 Petroleum and Geosystems Engineering Departmental Scholarship

2012 Kenneth B. and Jane Stroud Ford Endowed Scholarship in Petroleum Engineering

Computer skills

Proficient MATLAB, LATEX, Microsoft Office, Adobe Illustrator, WordPress

Familiar COMSOL, Petrel, C++, Interactive Petrophysics, InDesign

Languages

English **Native**

Dutch **Professional Working Proficiency**

French **Good Command**